

# **[M(salen)]-Based Conducting Polymer Films**

A thesis submitted for the degree of

Doctor of Philosophy

at the University of Leicester

by

**Joao Andre da Costa Tedim**

Department of Chemistry

University of Leicester



**June 2008**

UMI Number: U601246

All rights reserved

INFORMATION TO ALL USERS

The quality of this reproduction is dependent upon the quality of the copy submitted.

In the unlikely event that the author did not send a complete manuscript and there are missing pages, these will be noted. Also, if material had to be removed, a note will indicate the deletion.



UMI U601246

Published by ProQuest LLC 2013. Copyright in the Dissertation held by the Author.  
Microform Edition © ProQuest LLC.

All rights reserved. This work is protected against  
unauthorized copying under Title 17, United States Code.



ProQuest LLC  
789 East Eisenhower Parkway  
P.O. Box 1346  
Ann Arbor, MI 48106-1346

# **[M(*salen*)]-Based Conducting Polymer Films**

by

Joao Andre da Costa Tedim

## **Abstract**

This thesis reports the preparation and characterisation of poly[M(*salen*)] (M=Ni) conducting films bearing crown ether receptors, which were prepared via oxidative polymerisation of the [Ni(*salen*)] monomer. Electrochemical techniques showed that the resulting modified electrodes are electroactive, and that the electrochemical response is ligand-based. Moreover, this response was found to change irreversibly in the presence of metal cations ( $\text{Cs}^+$ ,  $\text{Mg}^{2+}$  and  $\text{Ba}^{2+}$ ), indicating the potential use of these films as sensing systems.

The local structure around Ni atoms was studied by X-ray absorption spectroscopy, and found to remain unchanged regardless of the sample physical state, occurrence of polymerisation, and changes in the polymer doping state or ion uptake. For films bearing a small and ‘rigid’ pseudo-crown, data show that  $\text{Ba}^{2+}$  uptake occurs by allocation of the cation *within* the pseudo-crown. However, for films bearing the large and flexible crown ether macrocycles,  $\text{Ba}^{2+}$  is coordinated to a very low number of oxygen donor atoms, which is unexpected according to solution complexation concepts. This allows more  $\text{Ba}^{2+}$  to bind to the polymer at the cost of less selectivity towards analyte size.

Acoustic wave sensor and microscopic techniques showed that the mechanical properties of films bearing crown ether macrocycles depends on the amount of deposited electroactive material. Thin films ( $\Gamma < 15 \text{ nmol cm}^{-2}$ ) consist of a uniform layer of polymer with monodisperse, small polymer islands on the top, whereas thick films ( $\Gamma > 100 \text{ nmol cm}^{-2}$ ) are rough, with an underlying uniform layer decorated with large heterogeneous islands of polymer. These large islands are mechanically quite different (more liquid-like) from the dense, inner layer.

Finally, the incorporation of multi-walled carbon nanotubes in the poly[Ni(*salen*)] matrix enhances the electronic/electrochemical properties of the conducting polymer, opening a new route towards the optimisation of these systems.

**Dedicated to Claudia, Mum and Dad**



## ACKNOWLEDGEMENTS

In the first place, I thank *Fundação para a Ciência e a Tecnologia* for the PhD grant.

I would like to express my thanks to my supervisor Prof. A. R. Hillman for his guidance, support and, above all, for his patience with me.

Many thanks to Dr. Cristina Freire for her guidance and teaching me the joy of doing science.

I am thankful to Dr. Steve J. Gurman for his help and fruitful discussions about XAS.

Thanks to Dr. Karl Ryder for lending his potentiostat and his readiness to help. I am also grateful to the guys in the workshop for constructing my electrochemical cells, and to my lab colleagues, for their insight and helpful suggestions.

Thanks to my Portuguese friends for all their understanding, support and companionship.

Special thanks to my brother Tiago and sister Rita, for their love and for always giving me a good laugh.

My deepest gratitude goes to my loving parents, for all the sacrifices they have made for me, and to my wife Claudia, for her love and support. Without them I wouldn't have made it.

# LIST OF CONTENTS

<b>Acknowledgements</b>	<b>ii</b>
<b>List of Symbols</b>	<b>xix</b>
<b>Chapter 1: Introduction – Conducting Polymers</b>	<b>1</b>
1.1 Conducting Polymers	2
1.2 Conjugated Polymers: an Overview	3
1.3 Excitons in Conjugated Polymers	6
1.4 [M( <i>salen</i> )] Complexes as Precursors of Poly(heterocycles)	7
1.5 Incorporation of Ion Recognition Functionalities in Conjugated Polymers	12
1.5.1 Poly(heterocycles) bearing polyether recognition functionalities	14
1.5.2 Conjugated polymers incorporating metal derived substituents and recognition sites	21
1.5.3 Molecular design of poly[M( <i>salen</i> )] electroactive films	23
1.6 Aim	24
References	26
<b>Chapter 2: Techniques</b>	<b>35</b>
2.1 Electrochemical Methods	36
2.1.1 Cyclic voltammetry (CV)	36
2.1.1.1 Mass-transfer-controlled reactions at planar electrodes	37
2.1.1.2 Different contributions for the measured current	39
2.1.1.3 Cyclic voltammetry at planar electrodes	40
(i) Solution species	40
(ii) Surface immobilised species	42
2.1.1.4 Experimental	43
2.1.2 Electrochemical Impedance Spectroscopy (EIS)	44
2.1.2.1 Theory	45
2.1.2.2 Equivalent circuit of a cell	47
2.1.2.3 Instrumentation	49
2.2 Spectroscopic Methods	50
2.3 Acoustic Wave Methods	51

2.3.1 Extraction of rheological parameters for real systems	53
2.3.1.1 General case	53
2.3.1.2 Particular case: viscoelastic layer	55
2.3.2 Rheological characteristics and the effect of frequency	58
2.3.3 Experimental	59
<b>2.4 X-Ray Techniques</b>	<b>60</b>
2.4.1 X-ray photoelectron spectroscopy (XPS)	60
2.4.1.1 Instrumentation	61
2.4.1.2 Accuracy of electron binding energies	62
2.4.1.3 Surface sensitivity	62
2.4.2 X-ray absorption spectroscopy (XAS)	63
2.4.2.1 EXAFS theory	64
2.4.2.2 Experimental	66
<b>2.5 Imaging Techniques</b>	<b>69</b>
2.5.1 Scanning electron microscopy (SEM)	69
2.5.1.1 Instrumentation	70
2.5.2 Atomic force microscopy (AFM)	71
<b>References</b>	<b>73</b>
 <b>Chapter 3: Experimental</b>	 <b>77</b>
3.1 Chemicals	78
3.2 Preparation and Characterisation of Modified Electrodes by Cyclic Voltammetry	78
3.2.1 Instrumentation	78
3.2.2 Electropolymerisation	79
3.2.3 Cyclic voltammetry of modified electrodes	79
3.2.4 Determination of oxidation degree and surface coverage	79
3.2.5 Ion recognition studies	79
3.3 UV-Vis Transmission Spectroscopy	80
3.3.1 Instrumentation	80
3.3.2 Electropolymerisation	81
3.3.3 Characterisation of modified electrodes	81
3.3.4 Ion recognition studies	81
3.4 Compositional Characterisation of Poly[M( <i>salen</i> )] Films by X-Ray Photoelectron Spectroscopy (XPS)	81
3.4.1 Instrumentation	81
3.4.2 Preparation and characterisation of modified electrodes	82

3.5 Structural Characterisation of Poly[M( <i>salen</i> )] Films by X-Ray Absorption Spectroscopy (XAS)	82
3.5.1 Instrumentation	82
3.5.2 Design of electrochemical cell for XAS applications	83
3.5.3 XAS Measurements	84
3.5.3.1 Poly[Ni(3-MeOsaltMe)]	84
3.5.3.2 Poly[Ni( <i>salen</i> )(crown ether)]	85
3.5.5 EXAFS data analysis	85
3.6 Rheological Characterisation of Poly[M( <i>salen</i> )] Films by Electrochemical Quartz Crystal Microbalance (EQCM) / Crystal Impedance	86
3.6.1 Instrumentation	86
3.6.2 Electropolymerisation	87
3.6.3 Characterisation of modified electrodes	88
3.7 Imaging and Morphology Characterisation of Poly[M( <i>salen</i> )] Films by Atomic Force Microscopy (AFM) and Scanning Electron Microscopy (SEM)	88
3.7.1 Instrumentation	88
3.7.2 Preparation of modified electrodes	88
3.8 Preparation and Characterisation of Nanocomposites Based on Poly[M( <i>salen</i> )] Films and Multi-walled Carbon Nanotubes (MWCNTs)	89
3.8.1 Functionalisation of carbon nanotubes	89
3.8.2 Instrumentation used in the preparation of composites	89
3.8.3 Preparation of composites based on [M( <i>salen</i> )] and MWCNT's	90
3.8.4 Electrochemical characterisation of composites	90
3.8.5 Morphology characterisation of composites by SEM	90
References	91

<b>Chapter 4: Preparation and Characterisation of Poly[Ni(3-Mesalophen-b15-c5)] by Cyclic Voltammetry and UV-Vis Spectroscopy</b>	<b>92</b>
4.1 Introduction	93
4.2 Preparation and Characterisation of Poly[Ni(3-Mesalophen-b15-c5)] by Cyclic Voltammetry	93

4.2.1 Electropolymerisation	93
4.2.2 Characterisation of the modified electrodes in background electrolyte	95
4.2.2.1 Determination of oxidation degree and electroactive surface coverage	97
4.2.2.2 Dynamics of charge transfer processes	99
4.3 Ion Recognition Studies of Poly[Ni(3-Mesalophen-b15-c5)]	102
4.3.1 Qualitative analysis of the voltammetric response of poly[Ni(3-Mesalophen-b15-c5)] in the presence of alkali and alkaline earth metal ions	102
4.3.2 Quantitative analysis of the voltammetric response of poly[Ni(3-Mesalophen-b15-c5)] in the presence of alkali and alkaline earth metal ions	108
4.3.2.1 Dynamic studies	108
4.3.2.2 Analysis of $E_{pal}$	112
4.3.2.3 Analysis of $i_{pcll}$	115
4.3.2.4 Reversibility	118
4.4 Characterisation of Poly[Ni(3-Mesalophen-b15-c5)] by <i>In Situ</i> UV-Vis Spectroscopy	119
4.4.1 Electropolymerisation of [Ni(3-Mesalophen-b15-c5)]	119
4.4.2 Spectroscopic characterisation of poly[Ni(3-Mesalophen-b15-c5)]	120
4.4.2.1 Determination of extinction coefficients associated with the UV-Vis bands	122
4.4.2.2 Charge carriers and the polaron model	124
4.4.3 UV-Vis properties of poly[Ni(3-Mesalophen-b15-c5)] in the presence of metal cations - ion recognition studies	125
Concluding Remarks	130
References	132

## **Chapter 5: Compositional and Structural Studies of Poly[M(salen)] Films by X-ray Techniques: XPS and XAS**

5.1 Introduction	135
5.2 Compositional Studies of Poly[Ni(3-Mesalophen-b15-c5)] by XPS	137
5.2.1 Deconvolution of XPS data	140
5.3 Structural Studies of Poly[M(salen)] Films by XAS	147

5.3.1 Poly[Ni(3-MeOsaltMe)]: polymeric films bearing pseudo crown receptors	147
5.3.1.1 Electrochemical characterisation	147
5.3.1.2 Structural characterisation by XAS	149
5.3.1.3 XAS and XPS: bulk vs. surface probes	156
5.3.2 Poly[Ni( <i>salen</i> )(crown ether)]: polymeric films bearing crown ether receptors	160
5.3.2.1 Electrochemical characterisation	161
5.3.2.2 Structural characterisation by XAS	164
5.3.2.3 XAS quantitative analysis	170
5.3.2.4 Rationalisation of Ba <sup>2+</sup> binding process	173
Concluding Remarks	176
References	178
 <b>Chapter 6: Interfacial and Rheological Properties of Poly[Ni(3-Mesalophen-b15-c5)]</b>	 <b>181</b>
6.1 Introduction	182
6.2 Characterisation of the Potentiodynamic Deposition of Poly[Ni(3-Mesalophen-b15-c5)]	183
6.2.1 Acoustically thin film	185
6.2.2 Acoustically thick film	186
6.2.3 Morphological Analysis	188
6.3 Variation of Rheological Properties in Background Electrolyte	193
6.3.1 Effect of doping state	193
6.3.1.1 EQCM studies – acoustically thin films	194
6.3.1.2 Acoustically thick films and the ‘thin film’ approach	196
6.3.2 Effect of Ba <sup>2+</sup> addition	199
6.3.2.1 Acoustically thin films	199
6.3.2.2 Acoustically thick films	200
6.3.3 Effect of the resonating frequency	202
Concluding Remarks	205
References	207
 <b>Chapter 7: Introductory Studies of Composites Based on Poly[Ni(3-Mesalophen-b15-c5)] and Multi-Walled Carbon Nanotubes</b>	 <b>208</b>
7.1 Composites Based on Conducting Polymers and Carbon Nanotubes	209

7.2 Preparation and Characterisation of Composites Based on Poly[Ni(3-Mesalophen-b15-c5)] and Multi-Walled Carbon Nanotubes	212
7.2.1 Functionalisation of carbon nanotubes	212
7.2.2 Preparation and characterisation of composites by cyclic voltammetry	213
7.2.3 Characterisation of the composites by electrochemical impedance spectroscopy	221
7.2.4 Structural/morphologic characterisation of composites by scanning electron microscopy	229
7.3 Correlation of Composite Electrochemical Properties and Morphology	232
Concluding Remarks	235
References	236
<b>Final Conclusions and Future Directions</b>	<b>238</b>

## LIST OF FIGURES

1.1	Conduction mechanisms in <b>a)</b> ion conducting, <b>b)</b> redox and <b>c)</b> conjugated polymers.	3
1.2	Structures of <b>a)</b> <i>trans</i> -polyacetylene, <b>b)</b> polypyrrole and <b>c)</b> polythiophene.	4
1.3	<b>a)</b> Soliton in <i>trans</i> -polyacetylene, <b>b)</b> structural relaxation of the soliton, <b>c)</b> band diagrams for positive and negative solitons associated with electronic transitions.	6
1.4	Structures of negative <b>a)</b> polaron and <b>b)</b> bipolaron in poly( <i>p</i> -phenylene). Band diagrams for positive and negative <b>c)</b> polarons and <b>d)</b> bipolarons associated with electronic transitions.	7
1.5	<b>a)</b> Aromatic and <b>b)</b> quinoid structures of poly( <i>p</i> -phenylene).	8
1.6	Mechanism of polymerisation of poly(heterocycles).	8
1.7	Structures of <b>a)</b> <i>salen</i> ligands and <b>b)</b> [M( <i>salen</i> )] complexes.	10
1.8	<b>a)</b> 15-crown-5, <b>b)</b> 18-crown-6 and <b>c)</b> benzo-15-crown-5	13
1.9	Monomers <b>1</b> and <b>2</b> .	15
1.10	Monomers <b>3-7</b> .	16
1.11	Monomers <b>8</b> and <b>9</b> .	17
1.12	Monomer <b>10</b> .	18
1.13	Monomer <b>11</b> .	18
1.14	Monomers <b>12</b> and <b>13</b> .	19
1.15	Monomers <b>14-18</b> .	20
1.16	Monomer <b>19</b> .	22
1.17	Monomer <b>20</b> .	22
1.18	Monomer <b>21</b> .	23
2.1	Excitation signals for potential scan voltammetry: <b>a)</b> linear sweep and <b>b)</b> cyclic voltammetries.	36
2.2	Typical cyclic voltammogram.	37
2.3	Voltammogram for a system characterised by the Langmuir Isotherm.	42
2.4	Three electrode cell configuration.	44
2.5	Nyquist plots for different equivalent circuits.	46
2.6	<b>a)</b> Randles equivalent circuit and <b>b)</b> approximations used for $Z_f$ .	47
2.7	Nyquist plot for a simple electrochemical cell.	49
2.8	Lumped-element model.	53



2.9	Frequency dependency of (—) $G'$ and (---) $G''$ predicted by <b>a)</b> the Voigt model and <b>b)</b> the Maxwell model.	59
2.10	Schematic view of crystal impedance measurement set-up.	60
2.11	Example of XAS spectrum.	63
2.12	Absorption spectra for <b>a)</b> free atom ( $\mu_0$ ) and <b>b)</b> atom within a sample ( $\mu$ ).	65
2.13	Experimental setup for EXAFS measurements in both transmission and fluorescent modes.	68
2.14	Schematic view of a SEM instrument.	71
2.15	Typical setup of an AFM.	72
3.1	<b>a)</b> Electrochemical cell (machined from Teflon) for <i>in situ</i> XAS experiments and <b>b)</b> with the adjustable container for film polymerisation.	84
3.2	Electrochemical cell for crystal impedance measurements.	87
4.1	Voltammograms obtained during the oxidative polymerisation of [Ni(3-Mesalophen-b15-c5)] at $0.1 \text{ V s}^{-1}$ , by cycling the potential between $-0.3 \text{ V}$ and $1.3 \text{ V}$ . Number of deposition cycles <b>a)</b> 1, <b>b)</b> 5, <b>c)</b> 35 and <b>d)</b> 100. Arrows in panel <b>a</b> indicate the direction of potential cycling; in panels <b>b</b> , <b>c</b> and <b>d</b> arrows indicate the increase of anodic/cathodic current intensity as a result of deposition of electroactive species. The peak potentials associated with the redox features $a/a'$ , $b/b'$ , $c/c'$ and $d$ are shown in Table 4.1; $b^*$ corresponds to the monomer oxidation.	94
4.2	Voltammetric response of modified electrodes poly[Ni(3-Mesalophen-b15-c5)] prepared with <b>a)</b> 1, <b>b)</b> 5, <b>c)</b> 35 and <b>d)</b> 100 cycles, and acquired in $0.1 \text{ mol dm}^{-3}$ TBAP/ $\text{CH}_3\text{CN}$ at $0.1 \text{ V s}^{-1}$ from $-0.3$ to $1.3 \text{ V}$ . Arrows indicate the direction of potential cycling.	96
4.3	Dependence of electroactive surface coverage on the number of deposition cycles.	98
4.4	Voltammetric response of two poly[Ni(3-Mesalophen-b15-c5)] modified electrodes ( $\Gamma=1.7 \text{ nmol cm}^{-2}$ panels <b>a</b> and <b>b</b> ; $\Gamma=86 \text{ nmol cm}^{-2}$ panels <b>c</b> and <b>d</b> ), acquired at different scan rates: $0.01$ , $0.02$ and $0.05 \text{ V s}^{-1}$ (panels <b>a</b> and <b>c</b> ) and $0.1$ , $0.2$ and $0.5 \text{ V s}^{-1}$ (panels <b>b</b> and <b>d</b> ). Arrows indicate the increase of current intensity as a result of the scan rate increase.	100
4.5	Dependence of peak potential $E_{pH}$ on scan rate $v$ of two poly[Ni(3-Mesalophen-b15-c5)] modified electrodes, <b>a)</b> $\Gamma=1.7 \text{ nmol cm}^{-2}$ and <b>b)</b> $\Gamma=86 \text{ nmol cm}^{-2}$ .	100
4.6	Dependence of $\log i_{pH} $ on $\log v$ for two poly[Ni(3-Mesalophen-b15-c5)] modified electrodes, <b>a)</b> $\Gamma=1.7 \text{ nmol cm}^{-2}$ and <b>b)</b> $\Gamma=86 \text{ nmol cm}^{-2}$ .	101

- 4.7 Voltammetric response of poly[Ni(3-Mesalophen-b15-c5)],  $\Gamma \approx 10 \text{ nmol cm}^{-2}$ , acquired in  $0.1 \text{ mol dm}^{-3}$  TBAP/ $\text{CH}_3\text{CN}$ : (—) before, ( ) between successive metal cation additions and (—) after the last addition. Responses in panels **a**, **c** and **e** were obtained following the addition of  $5 \text{ } \mu\text{mol dm}^{-3}$  aliquots of  $\text{X}(\text{ClO}_4)_y$  ( $\text{X}=\text{Cs}^+$ ,  $\text{Mg}^{2+}$  and  $\text{Ba}^{2+}$ ) to the electrolyte solution; response in panel **b** was obtained after the addition of  $10 \text{ } \mu\text{mol dm}^{-3}$  of  $\text{CsClO}_4$  and in **d** and **f** after the addition of  $100$  and  $500 \text{ } \mu\text{mol dm}^{-3}$  of  $\text{X}(\text{ClO}_4)_2$  ( $\text{X}=\text{Mg}^{2+}$  and  $\text{Ba}^{2+}$ ). Arrows indicate the evolution of the electrochemical features with metal addition and redox-switching. 104
- 4.8 Voltammetric response of poly[Ni(3-Mesalophen-b15-c5)], acquired in  $0.1 \text{ mol dm}^{-3}$  TBAP/ $\text{CH}_3\text{CN}$ : (—) before, ( ) between successive metal cation additions and (—) after the last addition. Additions consisted of  $10 \text{ } \mu\text{mol dm}^{-3}$  aliquots of  $\text{CsClO}_4$  (panels **a** and **b**) and  $100$  and  $500 \text{ } \mu\text{mol dm}^{-3}$  aliquots of  $\text{X}(\text{ClO}_4)_2$  ( $\text{X}=\text{Mg}^{2+}$  and  $\text{Ba}^{2+}$ ) (panels **c** to **f**). Films surface coverage: panels **a**, **c**, **e**  $\Gamma \approx 20\text{-}35 \text{ nmol cm}^{-2}$ ; panels **b**, **d**, **f**  $\Gamma \approx 80\text{-}100 \text{ nmol cm}^{-2}$ . Arrows indicate the evolution of the electrochemical features with metal addition and redox-switching. 106
- 4.9 Voltammetric response of poly[Ni(3-Mesalophen-b15-c5)], acquired in  $0.1 \text{ mol dm}^{-3}$  TBAP/ $\text{CH}_3\text{CN}$ : (—) before and (—) after an addition of  $100 \text{ mmol dm}^{-3}$  of  $\text{X}(\text{ClO}_4)_2$  ( $\text{X}=\text{Mg}^{2+}$  and  $\text{Ba}^{2+}$ ); ( ) response acquired 15, 30 and 45 minutes after the addition. Films surface coverage: panels **a**, **b**  $\Gamma \approx 10 \text{ nmol cm}^{-2}$ ; panels **c**, **d**  $\Gamma \approx 20\text{-}35 \text{ nmol cm}^{-2}$ ; panels **e**, **f**  $\Gamma \approx 60\text{-}90 \text{ nmol cm}^{-2}$ . Arrows indicate the evolution of the electrochemical features with metal addition and redox-switching. 107
- 4.10 Voltammetric response of poly[Ni(3-Mesalophen-b15-c5)],  $\Gamma=19.3 \text{ nmol cm}^{-2}$ , cycled at different scan rates following  $\text{Cs}^+$  additions: **a**)  $0.01, 0.02, 0.05, 0.1 \text{ V s}^{-1}$  and **b**)  $0.1, 0.2, 0.5$  and  $1 \text{ V s}^{-1}$ . Arrows indicate the increase of current intensity as a result of the scan rate increase. 108
- 4.11 Dependence of  $\log|i_{pII}|$  on  $\log v$  for two poly[Ni(3-Mesalophen-b15-c5)] modified electrodes in the presence of  $\text{Mg}^{2+}$ , **a**)  $\Gamma=26 \text{ nmol cm}^{-2}$  and **b**)  $\Gamma=99 \text{ nmol cm}^{-2}$ . 109
- 4.12 Graphic representation of  $E_{pal}$  vs.  $\log|\text{cation}|$  for small (panels **a**, **c** and **e**) and intermediate additions (panels **b**, **d** and **f**). Different symbols (■ ○ ▲ \* ◇) correspond to different films, prepared with different  $\Gamma$ . 113
- 4.13 Graphic representation of  $\Delta E_{pal}$  vs.  $\Gamma$  following the addition of a  $100 \text{ mmol dm}^{-3}$  aliquot of  $\text{X}(\text{ClO}_4)_2$  ( $\text{X}=\text{Mg}^{2+}$ ,  $\text{Ba}^{2+}$ ). 115
- 4.14 Graphic representation of  $i_{pII}$  vs.  $|\text{cation}|$  (panels **a**, **c** and **e**) and  $i_{pII} \Gamma^{-1}$  vs.  $|\text{cation}|$  (panels **b**, **d** and **f**). Different symbols (■ ● ○ ▲ △ \*) correspond to different films (prepared with different  $\Gamma$ ). 116
- 4.15 Graphic representation of  $\Delta i_{pII}$  vs.  $\Gamma$  following the addition of a  $100 \text{ mmol dm}^{-3}$  aliquot of  $\text{X}(\text{ClO}_4)_2$  ( $\text{X}=\text{Mg}^{2+}$ ,  $\text{Ba}^{2+}$ ). 117

4.16	Voltammetric response of poly[Ni(3-Mesalophen-b15-c5)] recorded in metal cation-free 0.1 mol dm <sup>-3</sup> TBAP/CH <sub>3</sub> CN, before and after cation addition studies: $I \approx 25$ nmol cm <sup>-2</sup> (panels <b>a</b> , <b>c</b> and <b>e</b> ) and $I \approx 90$ nmol cm <sup>-2</sup> (panels <b>b</b> , <b>d</b> and <b>f</b> ).	118
4.17	UV-Vis spectra collected and referenced to 0.1 mol dm <sup>-3</sup> TBAP/CH <sub>3</sub> CN solution during the 5 <sup>th</sup> deposition cycle.	119
4.18	UV-Vis spectra of [Ni(3-Mesalophen-b15-c5)] and reduced poly[Ni(3-Mesalophen-b15-c5)] referenced to 0.1 mol dm <sup>-3</sup> TBAP/CH <sub>3</sub> CN solution. <b>a</b> ) 280-1100 nm and <b>b</b> ) 600-1100 nm.	120
4.19	UV-Vis spectra of poly[Ni(3-Mesalophen-b15-c5)] acquired in 0.1 mol dm <sup>-3</sup> TBAP/CH <sub>3</sub> CN from <b>a</b> ) -0.3 to 1.3 V and <b>b</b> ) 1.3 to -0.3 V. The spectra are referenced to 0.1 mol dm <sup>-3</sup> TBAP/CH <sub>3</sub> CN and different colours (grey scale) correspond to different intervals of potential (Figure 4.20).	121
4.20	Voltammetric response of poly[Ni(3-Mesalophen-b15-c5)] acquired in 0.1 mol dm <sup>-3</sup> TBAP/CH <sub>3</sub> CN by cycling the potential between -0.3 and 1.3 V. Arrows indicate the direction of potential sweep.	121
4.21	Differential of UV-Vis spectra depicted in Figure 4.19: <b>a</b> ) spectra acquired from -0.3 to 0.3 V and referenced to poly[Ni(3-Mesalophen-b15-c5)] at -0.3 V; <b>b</b> ) spectra acquired from 0.3 to 0.9 V referenced to poly[Ni(3-Mesalophen-b15-c5)] at 0.3 V and <b>c</b> ) spectra acquired from 0.9 to 1.3 V referenced to poly[Ni(3-Mesalophen-b15-c5)] at 0.9 V; <b>d</b> ) variation of absorbance with the applied potential for a complete voltammetric cycle (absorbance referenced to poly[Ni(3-Mesalophen-b15-c5)] at -0.3 V).	122
4.22	Dependence of absorbance (referenced to the polymer at -0.3 V) on $q_{redox} = Q_{redox}/A$ at <b>a</b> ) $\lambda_{max} = 315$ nm, <b>b</b> ) $\lambda_{max} = 382$ nm, <b>c</b> ) $\lambda_{max} = 435$ nm, <b>d</b> ) $\lambda_{max} = 508$ nm and <b>e</b> ) $\lambda_{max} = 945$ nm.	123
4.23	Assignment of electronic transitions for poly[Ni(3-Mesalophen-b15-c5)], based on the polaron model (VB = valence band; CB = conduction band).	125
4.24	UV-Vis spectra of poly[Ni(3-Mesalophen-b15-c5)] acquired in 0.1 mol dm <sup>-3</sup> TBAP/CH <sub>3</sub> CN at -0.3 V after the addition of 200 $\mu$ L of <b>a</b> ) 5 mmol dm <sup>-3</sup> CsClO <sub>4</sub> /0.1 mol dm <sup>-3</sup> TBAP/CH <sub>3</sub> CN and <b>b</b> ), <b>c</b> ) 0.05 mol dm <sup>-3</sup> X(ClO <sub>4</sub> ) <sub>2</sub> (X= Mg <sup>2+</sup> , Ba <sup>2+</sup> ) / 0.1 mol dm <sup>-3</sup> TBAP/CH <sub>3</sub> CN. The spectra are referenced to 0.1 mol dm <sup>-3</sup> TBAP/CH <sub>3</sub> CN. Arrows indicate variation of absorbance (vertical) and wavelength (horizontal).	127
4.25	UV-Vis spectra of poly[Ni(3-Mesalophen-b15-c5)] acquired in 0.1 mol dm <sup>-3</sup> TBAP/CH <sub>3</sub> CN at 0.9 V ( <b>a</b> , <b>c</b> and <b>e</b> ) and at 1.3 V ( <b>b</b> , <b>d</b> and <b>f</b> ) after the addition of 200 $\mu$ L of <b>a</b> ) and <b>b</b> ) 5 mmol dm <sup>-3</sup> CsClO <sub>4</sub> /0.1 mol dm <sup>-3</sup> TBAP/CH <sub>3</sub> CN and <b>c</b> ) to <b>f</b> ) 0.05 mol dm <sup>-3</sup> X(ClO <sub>4</sub> ) <sub>2</sub> (X= Mg <sup>2+</sup> , Ba <sup>2+</sup> ) / 0.1 mol dm <sup>-3</sup> TBAP/CH <sub>3</sub> CN. The spectra are referenced to 0.1 mol dm <sup>-3</sup> TBAP/CH <sub>3</sub> CN. Arrows indicate variation of absorbance (vertical) and wavelength (horizontal).	128

5.1	XPS spectra of poly[Ni(3-Mesalophen-b15-c5)] ( $\Gamma \approx 14 \text{ nmol cm}^{-2}$ , reduced state) with (—) and without (—) $\text{Ba}(\text{ClO}_4)_2$ , in the regions of <b>a)</b> C 1s, <b>b)</b> O 1s, <b>c)</b> N 1s, <b>d)</b> Ni 2p, <b>e)</b> Cl 2p and <b>f)</b> Ba 3d.	138
5.2	Deconvolution of raw XPS spectra for films in the absence (panels <b>a</b> , <b>c</b> and <b>e</b> ) and presence (panels <b>b</b> , <b>d</b> and <b>f</b> ) of $\text{Ba}(\text{ClO}_4)_2$ . Numbers of the fitted peaks for the C 1s spectral line (panels <b>a</b> and <b>b</b> ) are assigned to the carbon atoms as shown in Figure 5.3 (see next page).	141
5.3	Different chemical environments of carbon in poly[Ni(3-Mesalophen-b15-c5)].	142
5.4	<b>a)</b> Oxidative polymerisation of $1 \text{ mmol dm}^{-3}$ [Ni(3-MeOsaltMe)] in $0.1 \text{ mol dm}^{-3}$ TBAP/ $\text{CH}_3\text{CN}$ , between 0.0 and 1.3 V at $0.1 \text{ V s}^{-1}$ (10 deposition cycles) and <b>b)</b> redox switching of the modified electrode poly[Ni(3-MeOsaltMe)] ( $\Gamma = 46 \text{ nmol cm}^{-2}$ ) in $0.1 \text{ mol dm}^{-3}$ TBAP/ $\text{CH}_3\text{CN}$ between 0.0 and 1.3 V at $0.1 \text{ V s}^{-1}$ . Arrows indicate time sequence of cycles.	148
5.5	Voltammetric response of poly[Ni(3-MeOsaltMe)] ( $\Gamma = 5.0 \text{ nmol cm}^{-2}$ ) acquired after successive additions of $10 \text{ }\mu\text{L}$ aliquots of $2.5 \text{ mmol dm}^{-3}$ $\text{Ba}(\text{ClO}_4)_2/0.1 \text{ mol dm}^{-3}$ TBAP/ $\text{CH}_3\text{CN}$ to $0.1 \text{ mol dm}^{-3}$ TBAP/ $\text{CH}_3\text{CN}$ .	149
5.6	XANES spectra in the region near Ni K-edge: <b>a)</b> Ni metal, $50 \text{ mmol dm}^{-3}$ $\text{Ni}(\text{NO}_3)_2/\text{H}_2\text{O}$ , and [Ni(3-MeOsaltMe)] powder; <b>b)</b> <b>1</b> [Ni(3-MeOsaltMe)] powder; <b>2</b> $20 \text{ mmol dm}^{-3}$ [Ni(3-MeOsaltMe)]/ $\text{CH}_3\text{CN}$ ; <b>3</b> $20 \text{ mmol dm}^{-3}$ [Ni(3-MeOsaltMe)]/ $20 \text{ mmol dm}^{-3}$ $\text{Ba}(\text{ClO}_4)_2/\text{CH}_3\text{CN}$ ; <b>4</b> poly[Ni(3-MeOsaltMe)] in $0.1 \text{ mol dm}^{-3}$ TBAP/ $\text{CH}_3\text{CN}$ at 0.0 V; <b>5</b> poly[Ni(3-MeOsaltMe)] in $0.1 \text{ mol dm}^{-3}$ TBAP/ $\text{CH}_3\text{CN}$ at 1.3 V; <b>6</b> poly[Ni(3-MeOsaltMe)] + $\text{Ba}^{2+}$ in $0.1 \text{ mol dm}^{-3}$ TBAP/ $\text{CH}_3\text{CN}$ at 0.0 V.	150
5.7	XANES spectra in the region of Ba K-edge for <b>1</b> $0.05 \text{ mol dm}^{-3}$ $\text{Ba}(\text{ClO}_4)_2/\text{CH}_3\text{CN}$ and <b>2</b> poly[Ni(3-MeOsaltMe)] + $\text{Ba}^{2+}$ at 0.0 V.	151
5.8	Structural environment around the Ni atom - initial parameters for the fitting of EXAFS function.	152
5.9	<b>a)</b> EXAFS functions (—) data and ( $\circ$ ) fitting, and <b>b)</b> Fourier transforms for <b>1</b> [Ni(3-MeOsaltMe)] powder; <b>2</b> $20 \text{ mmol dm}^{-3}$ [Ni(3-MeOsaltMe)]/ $\text{CH}_3\text{CN}$ ; <b>3</b> $20 \text{ mmol dm}^{-3}$ [Ni(3-MeOsaltMe)] / $20 \text{ mmol dm}^{-3}$ $\text{Ba}(\text{ClO}_4)_2/\text{CH}_3\text{CN}$ ; <b>4</b> poly[Ni(3-MeOsaltMe)] in $0.1 \text{ mol dm}^{-3}$ TBAP/ $\text{CH}_3\text{CN}$ at 0.0 V; <b>5</b> poly[Ni(3-MeOsaltMe)] in $0.1 \text{ mol dm}^{-3}$ TBAP/ $\text{CH}_3\text{CN}$ at 1.3 V; <b>6</b> poly[Ni(3-MeOsaltMe)] + $\text{Ba}^{2+}$ in $0.1 \text{ mol dm}^{-3}$ TBAP/ $\text{CH}_3\text{CN}$ at 0.0 V.	153
5.10	Structural environment around $\text{Ba}^{2+}$ - initial parameters for the fitting of EXAFS function. <b>a)</b> Schematic view of $\text{Ba}^{2+}$ coordinated to the pseudo-crown; <b>b)</b> result of DFT calculations for the complex [Ni(3-MeOsaltMe)] + $\text{Ba}^{2+}$ .	155
5.11	<b>a)</b> EXAFS functions (—) data and ( $\circ$ ) fitting, and <b>b)</b> Fourier transforms for <b>1</b> $50 \text{ mmol dm}^{-3}$ $\text{Ba}(\text{ClO}_4)_2$ ; <b>2</b> poly[Ni(3-MeOsaltMe)] + $\text{Ba}^{2+}$ in $0.1 \text{ mol dm}^{-3}$ TBAP/ $\text{CH}_3\text{CN}$ at 0.0 V.	156
5.12	Structures of the [Ni( <i>salen</i> )] complexes studied by XAS.	160

5.13	Voltammetric response acquired during <b>a), c)</b> polymerisation and <b>b), d)</b> redox-switching processes for <b>a), b)</b> [Ni(3-Mesalophen)] and <b>c), d)</b> [Ni(3-Mesalophen-b18-c6)] at 0.1 V s <sup>-1</sup> . Arrows indicate time sequence of cycles.	162
5.14	Voltammetric response of poly[Ni(3-Mesalophen-b15-c5)] ( $\Gamma = 5.4 \text{ nmol cm}^{-2}$ ) acquired in background electrolyte at 0.1 V s <sup>-1</sup> (—) before Ba <sup>2+</sup> additions, ( ) following each Ba <sup>2+</sup> addition and (- - -) at the end of Ba <sup>2+</sup> additions.	163
5.15	XANES spectra in the region of Ni K-edge for films poly[1], poly[2], poly[3] and complex [4]; (*)XAS spectra were not obtained for poly[4] due to experimental problems.	164
5.16	Optimised structures of [Ni(3-Mesalophen-b15-c5)]+Ba <sup>2+</sup> and [Ni(3-Mesalophen-b18-c6)]+Ba <sup>2+</sup> obtained by DFT calculations.	165
5.17	(—) Experimental data and (○) fitting of <b>a), c)</b> EXAFS functions, and <b>b), d)</b> Fourier transforms; <b>a), b)</b> monomers as powders and <b>c), d)</b> monomer <b>2</b> (powder), poly[2] and poly[2]+Ba <sup>2+</sup> .	167
6.1	Polymerisation of [Ni(3-Mesalophen-b15-c5)] at 0.01 V s <sup>-1</sup> (film <b>A</b> ). <b>a)</b> Cyclic voltammogram (— first deposition cycle; — subsequent cycles); <b>b)</b> admittance spectra (— admittance spectrum of QCM in solution and — admittance spectra acquired at the end of each deposition cycle). Arrows indicate <b>a)</b> the increase of current intensity and <b>b)</b> the decrease of frequency and admittance with progressive cycling.	183
6.2	<b>a)</b> Admittance spectra acquired during the polymerisation of [Ni(3-Mesalophen-b15-c5)] at 0.02 V s <sup>-1</sup> (film <b>B</b> ) (— admittance spectrum of QCM in solution and — admittance spectra acquired at the end of each deposition cycle); <b>b)</b> variation of admittance vs. variation of resonant frequency for film <b>A</b> (□) and film <b>B</b> (▲). Arrows indicate the decrease of frequency and admittance.	184
6.3	Variation of the resonant frequency with respect to the bare electrode, as a function of deposition charge $Q_{dep}$ (□ film <b>A</b> : $R^2=0.9994$ ; and ▲ film <b>B</b> : $R^2=0.9945$ ).	184
6.4	Polymerisation of [Ni(3-Mesalophen-b15-c5)] at 0.02 V s <sup>-1</sup> (film <b>B</b> ): variation of film thickness ( $h_f$ ) with the applied potential (○ 1st deposition cycle; ■ subsequent cycles). Arrows indicate the direction of potential sweep.	186
6.5	Shear moduli values vs. $h_f$ fitted for the polymerisation process of film <b>A</b> ( $\rho_f=1.2 \text{ g cm}^{-3}$ ); ■ $G'$ , ○ $G''$ and ▲ $ G $ values.	187
6.6	SEM images acquired for two films prepared on ITO electrodes at different scan rates: 5 cycles at 0.1 V s <sup>-1</sup> (film <b>C</b> , $\Gamma = 9.76 \text{ nmol cm}^{-2}$ , panels <b>a</b> and <b>c</b> ), and 5 cycles at 0.005 V s <sup>-1</sup> (film <b>D</b> , $\Gamma = 162 \text{ nmol cm}^{-2}$ , panels <b>b</b> and <b>d</b> ).	189
6.7	AFM images of films prepared on ITO electrodes at 0.02 V s <sup>-1</sup> with 3 cycles (film <b>E</b> , $\Gamma = 13.1 \text{ nmol cm}^{-2}$ , panels <b>a</b> and <b>c</b> ) and 35 deposition cycles (film <b>F</b> , $\Gamma = 194 \text{ nmol cm}^{-2}$ , panels <b>b</b> and <b>d</b> ).	191
6.8	Estimate of $h_f$ at the cut edge of <b>a)</b> film <b>E</b> and <b>b)</b> film <b>F</b> using AFM software.	191

6.9	AFM images of an acoustically thin film prepared on QCM with 10 cycles at $0.02 \text{ V s}^{-1}$ (film <b>G</b> ), $\Gamma = 55.7 \text{ nmol cm}^{-2}$ .	192
6.10	Voltammetric response of poly[Ni(3-Mesalophen-b15-c5)] (film <b>A</b> ) acquired in $0.1 \text{ mol dm}^{-3}$ TBAP/ $\text{CH}_3\text{CN}$ between $-0.3$ and $1.3 \text{ V}$ .	194
6.11	<b>a)</b> Admittance spectra acquired during the polymerisation of [Ni(3-Mesalophen-b15-c5)] at $0.02 \text{ V s}^{-1}$ (film <b>H</b> ) ( $\blacksquare$ admittance spectrum of QCM in solution and $\square$ admittance spectra acquired at the end of each deposition cycle); <b>b)</b> variation of the peak admittance (film <b>H</b> ) with the applied potential in background electrolyte (arrows indicate the direction of potential sweep).	194
6.12	Plot of <b>a)</b> $Q_{\text{redox}}$ and $h_f$ vs. the applied potential and <b>b)</b> $\Delta M'$ vs. $Q_{\text{redox}}$ for film <b>H</b> , in $0.1 \text{ mol dm}^{-3}$ TBAP/ $\text{CH}_3\text{CN}$ . 'I' is the slope in the anodic half-cycle and 'II' for the cathodic counterpart ( $\blacksquare$ ).	195
6.13	<b>a)</b> Film thickness profile $h_f(E)_{\text{thick}}$ used in the fitting process and <b>b)</b> variation of shear moduli values with the applied potential (film <b>A</b> ). Arrows indicate the direction of potential sweep.	198
6.14	Plots of <b>a)</b> $Q$ vs. $E$ and <b>b)</b> shear moduli vs. $Q$ , for film <b>A</b> .	198
6.15	<b>a)</b> Variation of $h_f$ (film <b>H</b> ) before and after addition of $\text{Ba}(\text{ClO}_4)_2$ (final concentration $2 \text{ mmol dm}^{-3}$ ) to the background electrolyte; <b>b)</b> $\Delta M'$ vs. $Q_{\text{redox}}$ for film <b>H</b> after $\text{Ba}^{2+}$ addition. 'I' is the slope in the anodic half-cycle and 'II' for the cathodic counterpart ( $\blacksquare$ ). Arrows indicate the direction of potential sweep.	199
6.16	<b>a)</b> Variation of shear moduli values with the applied potential (film <b>A</b> ). Comparisons between <b>b)</b> storage, <b>c)</b> loss and <b>d)</b> modulus moduli, before and after $\text{Ba}^{2+}$ addition (final concentration $2 \text{ mmol dm}^{-3}$ ).	201
6.17	Storage (panels <b>a</b> , <b>b</b> ) and loss (panels <b>c</b> , <b>d</b> ) moduli before (panel <b>a</b> , <b>c</b> ) and after ( <b>b</b> , <b>d</b> ) $\text{Ba}^{2+}$ addition (final concentration $2 \text{ mmol dm}^{-3}$ ). Resonant frequency: $10 \text{ MHz}$ ( $\blacktriangle$ ), $30 \text{ MHz}$ ( $\circ$ ), $50 \text{ MHz}$ ( $\blacksquare$ ), $70 \text{ MHz}$ ( $\diamond$ ) and $90 \text{ MHz}$ ( $\times$ ).	202
6.18	Logarithmic dependence of $G'$ and $G''$ on frequency, before (panels <b>a</b> and <b>b</b> ) and after (panels <b>c</b> and <b>d</b> ) $\text{Ba}^{2+}$ addition.	203
6.19	Ratio of $h_f(\text{Ba}^{2+})/h_f$ at different resonant frequencies (film <b>A</b> ).	204
7.1	Schematic view of entrapment of MWCNTs within the poly[Ni(3-Mesalophen-b15-c5)] matrix during the polymerisation step and nomenclature used to describe composite/solvent systems. The detailed description of MWCNTs functionalisation is presented in Chapter 3.	211
7.2	Cyclic voltammograms acquired during polymerisation of [Ni(3-Mesalophen-b15-c5)] in $0.1 \text{ mol dm}^{-3}$ TBAP/ $\text{CH}_3\text{CN}$ at $0.005 \text{ V s}^{-1}$ . Arrows indicate the increase of current intensity with progressive cycling.	215

7.3	Cyclic voltammograms of polymerisation of [Ni(3-Mesalophen-b15-c5)] in 0.1 mol dm <sup>-3</sup> TBAP/CH <sub>2</sub> Cl <sub>2</sub> at 0.005 V s <sup>-1</sup> . Arrows indicate the increase of current intensity with progressive cycling.	216
7.4	Redox switching of the composite-modified electrodes of Figure 7.2 in 0.1 mol dm <sup>-3</sup> TBAP/CH <sub>3</sub> CN at 0.01 V s <sup>-1</sup> .	218
7.5	Redox switching of the composite-modified electrodes of Figure 7.3 in 0.1 mol dm <sup>-3</sup> TBAP/CH <sub>2</sub> Cl <sub>2</sub> at 0.01 V s <sup>-1</sup> .	219
7.6	Nyquist representations obtained for <b>a)</b> polymer, <b>b)</b> MWCNT-T0, <b>c)</b> MWCNT-T1, <b>d)</b> MWCNT-T2 and <b>e)</b> MWCNT-T3 in 0.1 mol dm <sup>-3</sup> TBAP/CH <sub>3</sub> CN. Lines of unit slope are provided as a guide to the eye.	222
7.7	Nyquist representations obtained for <b>a)</b> polymer, <b>b)</b> MWCNT-T0, <b>c)</b> MWCNT-T1, <b>d)</b> MWCNT-T2 and <b>e)</b> MWCNT-T3 in 0.1 mol dm <sup>-3</sup> TBAP/CH <sub>2</sub> Cl <sub>2</sub> . Lines of unit slope are provided as a guide to the eye.	223
7.8	Modified Randles circuit and limiting cases.	224
7.9	Estimate of charge transfer resistance ( $R_{CT}$ ) at 0.2 V (average of duplicate determinations). Annotated percentage figures indicate variation of value for composite from corresponding pure polymer value.	226
7.10	Double layer capacitance ( $C_{DL}$ ) at -0.3 V and 0.2 V for polymers and composites in <b>a)</b> 0.1 mol dm <sup>-3</sup> TBAP/CH <sub>3</sub> CN and <b>b)</b> 0.1 mol dm <sup>-3</sup> TBAP/CH <sub>2</sub> Cl <sub>2</sub> .	227
7.11	Faradaic capacitance ( $C_{redox}$ ) estimated at 0.2 V and 0.9 V for polymers and composites in <b>a)</b> 0.1 mol dm <sup>-3</sup> TBAP/CH <sub>3</sub> CN and <b>b)</b> 0.1 mol dm <sup>-3</sup> TBAP/CH <sub>2</sub> Cl <sub>2</sub> . Values are normalised by the polymer coverage, $\Gamma$ , and geometric area of the electrode.	228
7.12	SEM images of poly[Ni(3-Mesalophen-b15-c5)] (pure polymer) prepared in CH <sub>3</sub> CN. <b>a)</b> The film shows distinctive uniform vs. heterogeneous regions ( <b>I</b> and <b>II</b> , respectively); <b>b)</b> is a magnification of a heterogeneous region.	230
7.13	SEM images of MWCNT-T0 prepared in <b>a)</b> 0.1 mol dm <sup>-3</sup> TBAP/CH <sub>3</sub> CN and <b>b)</b> 0.1 mol dm <sup>-3</sup> TBAP/CH <sub>2</sub> Cl <sub>2</sub> . Solid circles correspond to regions of superficial MWCNT; dashed circles correspond to regions of lower amounts of MWCNT in the surface.	231
7.14	SEM images of MWCNT-T0 prepared in 0.1 mol dm <sup>-3</sup> TBAP/CH <sub>2</sub> Cl <sub>2</sub> . <b>a)</b> Carbon nanotubes individually covered are inserted in the polymeric matrix; <b>b)</b> solid squares highlight regions where the presence of nanotubes can be inferred beneath a uniform layer of polymer.	231
7.15	SEM images of the composites <b>a)</b> MWCNT-T0, <b>b)</b> MWCNT-T1, <b>c)</b> MWCNT-T2 and <b>d)</b> MWCNT-T3 prepared in 0.1 mol dm <sup>-3</sup> TBAP/CH <sub>3</sub> CN and <b>e)</b> MWCNT-T1, <b>f)</b> MWCNT-T2, <b>g)</b> MWCNT-T3 prepared in 0.1 mol dm <sup>-3</sup> TBAP/CH <sub>2</sub> Cl <sub>2</sub> .	233

## LIST OF TABLES

1.1	Structures of the $[M(salen)]$ complexes studied.	25
4.1	Peak potentials associated with redox features observed during oxidative polymerisation of $[Ni(3-Mesalophen-b15-c5)]$ in $0.1 \text{ mol dm}^{-3}$ TBAP/ $CH_3CN$ .	95
4.2	Peak potentials associated with redox features of $poly[Ni(3-Mesalophen-b15-c5)]$ , by cycling $E$ between $-0.3$ and $1.3 \text{ V}$ at $0.1 \text{ V s}^{-1}$ , in $0.1 \text{ mol dm}^{-3}$ TBAP/ $CH_3CN$ (5 <sup>th</sup> scan).	97
4.3	Results obtained from dynamics studies of $poly[Ni(3-Mesalophen-b15-c5)]$ .	101
4.4	Dynamic studies of $poly[Ni(3-Mesalophen-b15-c5)]$ in the presence of $Mg(ClO_4)_2$ – intermediate additions.	110
4.5	Dynamic studies of $poly[Ni(3-Mesalophen-b15-c5)]$ in the presence of $Ba(ClO_4)_2$ – intermediate additions.	110
4.6	Dynamic studies of $poly[Ni(3-Mesalophen-b15-c5)]$ in the presence of $Mg(ClO_4)_2$ – large additions.	111
4.7	Dynamic studies of $poly[Ni(3-Mesalophen-b15-c5)]$ in the presence of $Ba(ClO_4)_2$ – large additions.	111
4.8	Values of $CD^{1/2}$ and $D$ estimated using voltammetric data and the Randles-Sevcik equation.	112
4.9	Slopes of $E_{pol}$ vs. $\log cation $ plots.	114
4.10	Extinction coefficients $\epsilon_\lambda$ associated with the electronic transitions.	124
4.11	Response of extinction coefficients $\epsilon_\lambda$ , associated with the electronic transitions, to cation additions.	129
5.1	Atomic proportions of the elements present in films prepared with $\Gamma \approx 14 \text{ nmol cm}^{-2}$ (scan rate of polymerisation $\nu = 0.05 \text{ V s}^{-1}$ ), in the absence and presence of $Ba(ClO_4)_2$ ( $0.002 \text{ mol dm}^{-3}$ ). The precision is generally 0.1 atomic %.	139
5.2	Atomic proportions of the elements present in films prepared with $\Gamma \approx 8 \text{ nmol cm}^{-2}$ (scan rate of polymerisation $\nu = 0.1 \text{ V s}^{-1}$ ), in the absence and presence of $Ba(ClO_4)_2$ ( $0.05 \text{ mol dm}^{-3}$ ). The precision is generally 0.1 atomic %.	140
5.3	Corrected binding energy values for XPS spectra presented in Figure 5.2.	143
5.4	Normalised areas and proportion of C atoms in $poly[Ni(3-Mesalophen-b15-c5)]$ .	144
5.5	Structural information obtained from EXAFS analysis near the Ni K-edge.	154
5.6	Structural information obtained from EXAFS analysis near the Ba K-edge.	156
5.7	Quantitative analysis of XANES for $[Ni(3-MeOsaltMe)]$ systems (Ni K-edge).	157
5.8	Atomic percentages and ratios of relevant elements for $[Ni(3-MeOsaltMe)]$ . The precision is generally 0.1 atomic %.	159



5.9	Peak potentials associated with the redox features of modified electrodes in 0.1 mol dm <sup>-3</sup> TBAP/CH <sub>3</sub> CN.	163
5.10	Interatomic distances determined by DFT for [Ni( <i>salen</i> )] complexes in the absence and presence of Ba <sup>2+</sup> .	166
5.11	Structural information obtained from EXAFS analysis near the Ni K-edge.	168
5.12	Structural information obtained from EXAFS analysis near the Ba K-edge.	170
5.13	Quantitative analysis based on Ni K-edge steps (fluorescence spectra) and coulometry.	172
5.14	Quantitative analysis based on Ba K-edge steps (transmission spectra) and coulometry.	172
6.1	Film thickness ( $h_f$ ), decay length ( $\delta$ ) and phase shift ( $\varphi$ ) obtained from the fitting of the shear moduli, for a film density of $\rho_f = 1.2 \text{ g cm}^{-3}$ .	188
6.2	Estimate of film thickness and effective concentrations in the outer film region ( $C_{\text{outer}}$ ).	193
6.3	Determination of molar mass associated with the slopes of Figure 6.12b.	196
6.4	Determination of molar mass associated with the slopes of Figure 6.15b.	200
7.1	Textural properties of MWCNTs.	212
7.2	Summary of voltammetric responses (peak potentials) in CH <sub>3</sub> CN during polymer / composite electrodeposition as a function of MWCNT pre-treatment.	217
7.3	Summary of voltammetric responses (peak potentials) in CH <sub>2</sub> Cl <sub>2</sub> during polymer / composite electrodeposition as a function of MWCNT pre-treatment.	217
7.4	Summary of voltammetric responses (peak potentials) of modified electrodes in background electrolyte shown in Figure 7.4; solvent system as for deposition (CH <sub>3</sub> CN, Figure 7.2).	220
7.5	Summary of voltammetric responses (peak potentials) of modified electrodes in background electrolyte shown in Figure 7.5; solvent system as for deposition (CH <sub>2</sub> Cl <sub>2</sub> , Figure 7.3).	220
7.6	Electroactive coverage of the composite-modified electrodes, expressed in terms of Ni-complex monomer units. Data in columns 3 and 4 refer to different films prepared and characterised in a single solvent.	221
7.7	'Knee' frequency estimated from Nyquist representations.	229

## LIST OF SYMBOLS

Symbol	Meaning
$A$	Area
$A_w$	Atomic weight
$A_{Ox}(\lambda)$	Absorbance of species $Ox$ at wavelength $\lambda$
$b$	$\alpha Fv/RT$
$C$	a) Capacitance b) Concentration
$C_{dl}, C_d$	Double-layer capacitance
$C_0$	Static capacitance (BvD model)
$C_p$	Parasitic capacitance (BvD model)
$C_0^*$	$C_0 + C_p$ (BvD model)
$C_l$	Capacitance representing mechanical elasticity in the TSM resonator (BvD model)
$C_{redox}$	Faradaic (redox) pseudocapacitance (Modified Randles circuit)
$C_s$	Pseudocapacitance (Modified Randles circuit)
$C_i$	Concentration of species $i$
$C_i(x)$	Concentration of species $i$ at distance $x$
$C_i(x=0)$	Concentration of species $i$ at the electrode surface
$C_i(x,t)$	Concentration of species $i$ at distance $x$ at time $t$
$C_i(0,t)$	Concentration of species $i$ at the electrode surface at time $t$
$C_i^*$	Bulk concentration of species $i$
$C_{inner}$	Concentration of redox sites within the inner layer
$C_{outer}$	Concentration of redox sites in the outer layer
$c_1$	$-2f_0^2/\sqrt{(\mu_q \rho_q)}$
$D_i$	Diffusion coefficient of species $i$
$e$	Polarization vector of the electric field
$E$	Potential of an electrode vs. a reference
$\bar{E}$	Voltage or potential phasor
$\langle E(j) \rangle$	Potential mean value associated with the $j^{\text{th}}$ redox process ( $j=I, II, III, IV$ )
$E^0$	Formal potential of an electrode
$E_{1/2}$	Measured or expected half-wave potential in voltammetry
$E_{end}$	End potential
$E_{start}$	Starting potential
$E_s, E_s'$	Switching potential
$E_p$	Peak potential
$E_{pa}$	Anodic peak potential
$E_{pa,j}$	Anodic peak potential associated with the $j^{\text{th}}$ redox feature ( $j=I, II, III, IV$ )

$E_{pc}$	Cathodic peak potential
$E_{pcj}$	Cathodic peak potential associated with the $j^{th}$ redox feature ( $j=I, II, III, IV$ )
$\Delta E_p$	$ E_{pa}-E_{pc} $
$\Delta E_{pal}$	$E_{pal}$ (after addition) - $E_{pal}$ (before addition)
$E(t)$	a) AC voltage (electrochemical impedance spectroscopy) b) Variation of the applied potential during a linear sweep or cyclic voltammetry experiment, $E(t)=E_{start}+vt$
$E_0$	a) Amplitude of an AC voltage (electrochemical impedance spectroscopy) b) Binding energy, $E_0=\Phi$ (X-ray photoelectron spectroscopy) c) The energy offset which corresponds to the Fermi energy (X-ray absorption spectroscopy)
$E_K$	Photoelectron kinetic energy
$E_v$	Photon energy
$F$	Faraday constant; charge on one mole of electrons
$f$	a) $F/RT$ b) Frequency
$\Delta f$	Variation of quartz resonant frequency
$f_0$	Quartz resonant frequency
$ f_m(\pi, k) $	Backscattering factor
$G$	Shear modulus
$G^{(n)}$	Shear modulus associated with the $n^{th}$ viscoelastic layer
$G'$	Storage modulus
$G''$	Loss modulus
$h_f$	Film thickness (solvated polymer)
$h_f^0$	Polymer thickness (unsolvated polymer)
$h_s$	Solvent thickness within the film, $h_s=h_f-h_f^0$
$h_f^Q$	Estimate of film thickness based on coulometric data
$h_f^{grav}$	Estimate of film thickness based on gravimetric data
$h_{finner}$	Thickness of the film inner layer
$h_{fouter}$	Thickness of the film outer layer
$h_f(E)_{thick}$	Variation of thickness with potential for an acoustically thick film
$h_f(E)_{thin}$	Variation of thickness with potential for an acoustically thin film
$\langle h_f \rangle$	Average thickness of an acoustically thin film
$h_f(pol)$	Thickness of an acoustically thick film at the end of the polymerisation
$h_f(E)_{thickBa}$	Variation of thickness with potential for an acoustically thick film after $Ba^{2+}$ addition
$h_f(E)_{thinBa}$	Variation of thickness with potential for an acoustically thin film after $Ba^{2+}$ addition
$\cdot h_f \cdot_{Ba}$	Average thickness of an acoustically thin film after $Ba^{2+}$ addition
$i$	Current

$I$	Current phasor
$i(t)$	a) Current at time $t$ (cyclic voltammetry) b) AC current (electrochemical impedance spectroscopy)
$i_c$	Charging current
$i_f$	Faradaic current
$i_d$	Diffusion limited current
$i_p$	Peak current
$i_{pa}$	Anodic peak current
$i_{pa}^j$	Anodic peak current associated with the $j^{\text{th}}$ redox feature ( $j=I, II, III, IV$ )
$i_{pc}$	Cathodic peak current
$i_{pc}^j$	Cathodic peak current associated with the $j^{\text{th}}$ redox feature ( $j=I, II, III, IV$ )
$i_0$	Amplitude of an AC current
$\Delta i_{pcII}$	$i_{pcII}(\text{after addition}) - i_{pcII}(\text{before addition})$
$I$	Intensity
$I_0$	Incident intensity
$-dI$	Variation of intensity due to absorption processes
$j$	$\sqrt{-1}$
$J_i(x)$	Flux of species $i$ at location $x$
$J_i(x,t)$	Flux of species $i$ at location $x$ at time $t$
$k$	Photoelectron momentum vector, $k=2\pi/\lambda$
$k^\circ$	Standard heterogeneous rate constant
$k_{ox}$	Heterogeneous rate constant for reduction
$l_m(k)$	Electron free mean path
$L_1$	Inductance representing the inertial mass in a TSM resonator (BvD model)
$L_2$	Inductance associated with the imaginary part of $Z_s$ , which represents mechanical energy storage at the surface of TSM resonator (BvD model)
$m_e$	Electron mass
$\Delta m$	Areal mass density
$M, m'$	Molar mass
$\Delta M'$	Mass variation
$n$	a) Stoichiometric number of electrons involved in an electrode reaction b) Oxidation degree in poly[M( <i>salen</i> )] films, $n=2y+x$
$n_d$	Atomic density
$N$	Number of atoms per volume unit
$N_A$	Avogadro's number
$N_m$	Number of neighbouring atoms in the $m^{\text{th}}$ shell
$Ox$	Oxidised form of the standard system $Ox + ne^- \leftrightarrow Re$
$q$	Charge density, $q=Q/A$

$Q$	Charge
$Q_{pol}, Q_{dep}$	Charge passed in polymerisation
$Q_{redox}$	Charge passed in redox-switching
$r$	a) Electron coordinate b) Interatomic distance between the absorbing atom and neighbours in the $m^{th}$ shell
$R$	a) Gas constant b) Resistance
$R_{\Omega}$	Ohmic solution resistance
$R_{solution}$	Solution resistance
$R_{CT}$	Charge-transfer resistance
$R_s$	a) Resistance (Modified Randles circuit) b) Solution resistance
$R_f$	Resistance representing the dissipation of energy in a TSM resonator (BvD model)
$R_s$	Element associated with the real part of $Z_s$ , which represents mechanical power dissipation at the surface of TSM resonator (BvD model)
$R_m$	Interatomic distance between the absorbing atom and neighbours in the $m^{th}$ shell
$Re$	Reduced form of the standard system $Ox + ne^- \leftrightarrow Re$
$S$	Strain
$S'$	Charge accumulated on the sample surface during XPS measurements
$S_i^{-2}(k)$	Amplitude reduction factor associated with energy loss
$t$	a) Time b) Thickness
$T$	a) Temperature b) Stress
$T_m$	Type of neighbours in the shells around the absorbing atom
$T_{xy}$	Surface stress
$v$	Linear potential scan rate
$v(x)$	Velocity with which a volume element moves along the $x$ direction
$v_x$	Particle velocity
$V_m$	Molar volume
$x$	Distance from a planar electrode
$Z$	a) Impedance b) Atomic number
$Z_0$	a) Magnitude of $Z$ , $Z_0 = E_0/i_0$ (electrochemical impedance spectroscopy) b) Mechanical impedance of a viscoelastic layer (crystal impedance)
$Z_0^{(n)}$	Characteristic impedance of the $n^{th}$ viscoelastic layer
$Z_0^{(n+1)}$	Characteristic impedance of the $n^{th}+1$ viscoelastic layer
$Z'$	Real part of $Z$

$Z''$	Imaginary part of $Z$
$Z_l$	General impedance element ( Modified Randles circuit)
$Z_e$	Complex impedance element, $Z_e = R_2 + j\omega L_2$ (BvD model)
$Z_f$	General impedance describing a faradaic process (Randles equivalent circuit)
$Z_l$	Mechanical impedance associated with a semi-infinite Newtonian fluid
$Z_m$	Mechanical impedance associated with an ideal mass layer
$Z_q$	Quartz shear-wave characteristic impedance
$Z_W$	Warburg element
$Z_s$	Shear mechanical impedance associated with a loading
$Z_s^{(n)}$	Shear mechanical impedance associated with the $n^{\text{th}}$ layer of a loading
$z_i, z$	Charge of species $i$
$z$	Sample depth
$dz$	Infinitesimal thickness
$\alpha$	Transfer coefficient
$\beta$	Association constant
$\Gamma, \Gamma_p, \Gamma(Q_{redox})$	Electroactive surface coverage
$\Gamma_{inner}$	Surface concentration of redox sites in the inner layer
$\Gamma_{outer}$	Surface concentration of redox sites in the outer layer
$\gamma$	$j\omega(\rho/G)^{1/2}$
$\delta$	Decay length
$\delta_l$	Phase shift with which the photoelectron leaves the atom
$\varepsilon(\lambda)$	Extinction coefficient associated with the electronic transition at wavelength $\lambda$
$\eta_l$	Liquid viscosity
$\eta_f$	Film viscosity
$\theta_m$	Phase shift of the backscatter atom in the $m^{\text{th}}$ shell
$\lambda$	Wavelength
$\lambda_{max}$	Wavelength at which the absorbance is maximum
$\mu$	Absorption coefficient, $\mu = N\sigma_a$
$\mu_0$	Absorption coefficient of a free atom
$\mu_f$	Film stiffness
$\mu_q$	Quartz shear modulus
$\nu$	Frequency of electromagnetic radiation
$\rho$	Mass density
$\rho_f$	Film density (solvated polymer)
$\rho_f^{(n)}$	Density of the $n^{\text{th}}$ viscoelastic layer
$\rho_f(z)$	Variation of film density with depth
$\rho_f^0$	Polymer density (unsolvated polymer)
$\rho_l$	Fluid density

$\rho_m$	Mass per area of layer
$\rho_q$	Quartz density
$\rho_s$	Solvent density
$\sigma$	a) $nFv/RT$ (cyclic voltammetry) b) $\sigma = \frac{RT}{n^2 F^2 A \sqrt{2}} \left( \frac{1}{D_{ox}^{1/2} C_{ox}^*} + \frac{1}{D_{red}^{1/2} C_{red}^*} \right)$ (electrochemical impedance spectroscopy)
$\sigma_a$	Absorption cross-section
$\Delta\sigma_a$	Variation of the absorption cross-section at the edge
$\sigma_m^2, \sigma^2$	Debye-Waller factor
$\tau$	a) Time constant, $\tau = R_{CT} C_{dl}$ and $\tau = R_s C_d$ b) Relaxation time, $\tau = \eta/\mu_f$
$\varphi$	Phase shift
$\Phi_{Fermi}$	Binding energy with respect to the Fermi level
$\Phi_{vacuum}$	Binding energy with respect to vacuum
$\phi$	Electrostatic potential
$\chi$	EXAFS function
$\chi(bt)$	Normalised current for a totally irreversible system (linear sweep and cyclic voltammetries)
$\chi(\sigma t)$	Normalised current for a reversible system (linear sweep and cyclic voltammetries)
$\psi_{sample}$	Sample work function, $\psi_{sample} = \Phi_{Fermi} - \Phi_{vacuum}$
$\psi_{spectrometer}$	Spectrometer work function
$\omega$	Angular frequency of a sinusoidal oscillation, $2\pi f$

# Chapter 1

## *INTRODUCTION-CONDUCTING POLYMERS*



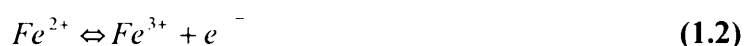
## 1.1 CONDUCTING POLYMERS

Polymeric systems with the ability to conduct charge are generically termed *conducting polymers*. This broad yet simple definition includes such a vast range of systems that numbering all the groups and sub-groups of materials would be impracticable, risking an artificial compartmentalisation. However, some ‘figures of merit’ must be used in order to distinguish and rationalise the characteristics of these materials. For instance, electroactive materials can be classified depending on the type of charge carriers and conduction mechanisms. When the conductivity arises from ionic mobility *only*, the polymers are designated as *ion conducting polymers* and may be regarded as ‘solutions of ionic salts in polymeric matrices’<sup>1</sup>. The most representative example is poly(ethylene oxide) (PEO), whose interaction with salts was first reported by Doscher and colleagues<sup>2</sup> in 1951. Cationic and anionic species are both mobile, but only the cation seems to be responsible for conduction since it interacts with heteroatoms from the flexible network of the polymeric matrix, whereas the anion is found as ion paired (non-conducting) units<sup>3-7</sup> (Figure 1.1a). Other systems, provided with redox active species (organic molecules, organometallic or coordination complexes), may undergo redox reactions enabling the creation of mobile charge carriers. These polymers are designated as *electrically conducting polymers*<sup>8</sup>, and can be divided into two subcategories: (i) *redox* and (ii) *conjugated polymers*. Both contain electronic states that can be reversibly occupied/emptied by doping, though processes by which conduction proceeds differ.

Redox polymers possess localised redox sites and the mechanism of electron transfer is by *electron hopping*<sup>9-13</sup> (Figure 1.1b): the redox sites act as ‘traps’ that can be oxidised (occupied by a hole) or reduced (occupied by an electron), and the electronic mobility is a result of self-exchange reactions:



This reaction is a bimolecular process, thus requiring the presence of both oxidised and reduced sites. In this sense, fully oxidised or reduced states are not conducting, whereas an oxidised:reduced sites ratio of 1:1 results in maximum conductivity (the polymer must be ‘mixed valent’<sup>14</sup>). Polyvinylferrocene (PVF) is a well known example of a redox polymer, whose oxidation process consists of removal of electrons from Fe sites (Equation 1.2), which are transported through the film by electron hopping<sup>15</sup>.



Contrastingly, conjugated polymers comprise polymeric chains of extended  $\pi$ -conjugated systems. In this case, conduction is a result of charge carriers created upon doping with an ability to move within the delocalised  $\pi$ -systems (Figure 1.1c). Due to the intrinsic nature of the conduction mechanism, conjugated polymers have higher electronic conductivity when compared to redox polymers. For example, the electronic conductivity of conjugated polymer polypyrrole (PPy) is up to  $10^8$  times higher than that of PVF<sup>8</sup>.

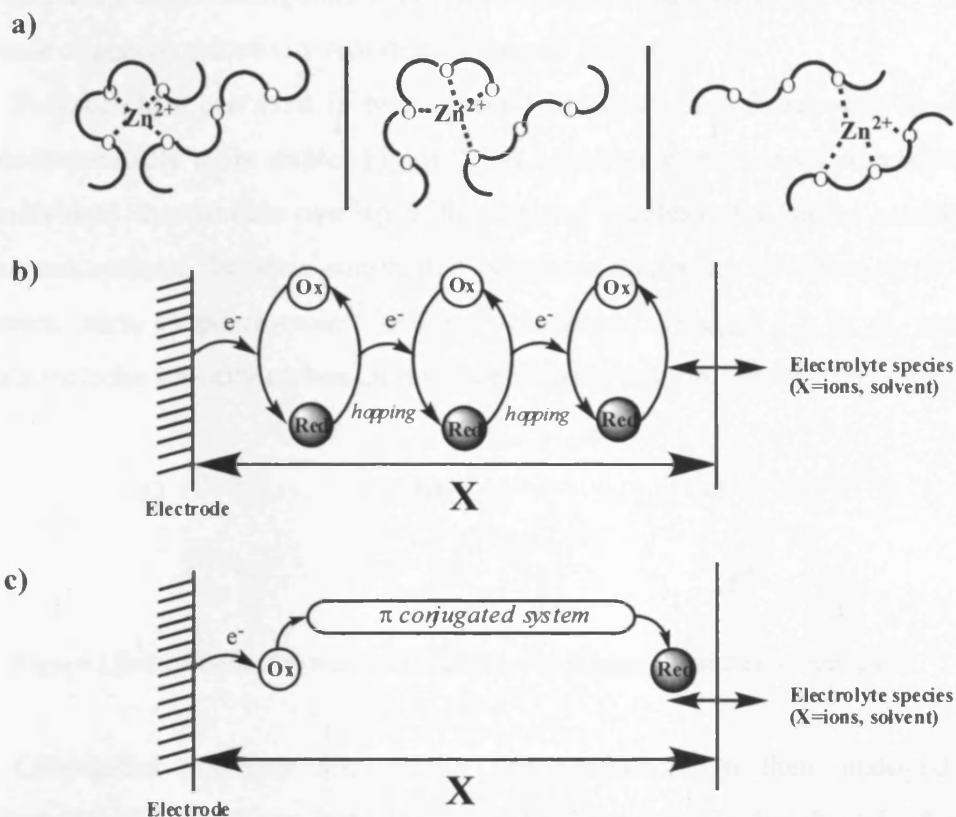


**Figure 1.1:** Conduction mechanisms in a) ion conducting, b) redox and c) conjugated polymers.

## 1.2 CONJUGATED POLYMERS: AN OVERVIEW

Prior to the 1970s, organic polymers were generically regarded as non relevant materials in the context of electronic applications<sup>16</sup>. This assumption was based on the fact that saturated organic polymers are insulators. On the other hand, little attention was devoted to polyconjugated systems and both their molecular and electronic structures in undoped states were not well understood<sup>17</sup>.

In 1977, Heeger, MacDiarmid, Shirakawa and co-workers showed that polyacetylene can be turned into a conductive polymer upon doping, over the full range from insulator to metal<sup>18,19</sup>. This discovery marked the beginning of a new generation of polymers<sup>20</sup>, leading to more than 20 years of research which culminated with the award of the Nobel Prize of Chemistry in 2000 to Heeger, MacDiarmid and Shirakawa. More recently, Shon and co-workers showed that the conjugated polymer poly(3-hexylthiophene) used in a field-effect transistor configuration becomes a superconductor at 2.35 K<sup>21</sup>. This was the first case of superconductivity reported in organic polymers.

Polyacetylene can exist in two isomeric forms, *cis* and *trans*, with the latter being thermodynamically more stable (Figure 1.2a). Carbon atoms are  $sp^2$  hybridised, whereas the individual  $2p_z$  orbitals overlap with those of neighbouring atoms establishing a  $\pi$ -conjugated system. In other conjugated polymers consisting of heterocyclic conjugated polymers, such as polypyrrole<sup>22</sup> and polythiophene<sup>23</sup> (Figure 1.2 b, c), overlap of  $p_z$  orbitals includes not only carbon atoms but also heteroatoms such as nitrogen or sulphur.

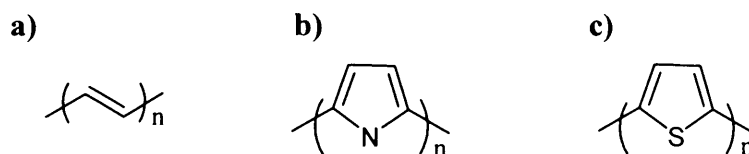


**Figure 1.2:** Structures of a) *trans*-polyacetylene, b) polypyrrole and c) polythiophene.

Conjugated polymers are usually semiconductors in their undoped states. In polyacetylene the band gap between  $\pi$ -bonding (or *valence band*) and  $\pi^*$ -antibonding bands (or *conduction band*) is 1.5 eV<sup>24</sup>, which is due to the non-equivalence of single vs. double bonds (so-called Peierls Instability). Since the band gap depends on the molecular/monomeric structure, it is possible to adjust the gap by careful design of the monomer. In this context, there are several studies reporting the narrowing of the band gap when donor/acceptor groups are introduced in the polymer backbone<sup>25-27</sup>. Organic semiconductors offer the advantage of easier processing when compared to inorganic conductors, and can be used in the preparation of low-cost, large-area flexible electronic components. Their application in electronics as semiconductors has been extended over different areas: (i) light-emitting diodes (LEDs)<sup>28,29</sup>, (ii) optically pumped conjugated

based lasers<sup>30-32</sup>, (iii) plastic photovoltaic cells<sup>33-35</sup> and (iv) polymer-based field effect transistors (FETs)<sup>36,37</sup>.

As mentioned earlier, the conductivity of conjugated polymers can be dramatically increased by doping, in some cases reaching the conductivity of metals<sup>19,38,39</sup>. Since they show electronic, electrical, magnetic and optical properties typical of metals together with processability, mechanical and other properties typical of polymeric materials, these polymers are commonly designated as *intrinsically conducting polymers* (ICPs) or *synthetic metals*<sup>16,40</sup>.

Doping introduces mobile charge carriers into the electronic structure of polymers and it can be achieved in different ways: redox-doping, doping involving no dopant ions, and non-redox doping. Redox doping includes chemical (charge transfer reactions)<sup>18,19</sup> and electrochemical doping<sup>41</sup>. It is classified as *p*-doping when there is partial removal of electronic density from the  $\pi$ -backbone (oxidation) or *n*-doping in the case of partial reduction. Redox doping is considered to induce 'permanent' electrical conductivity until the carriers are chemically compensated by insertion of counterions or removed by 'undoping'. Electrochemical doping additionally offers the advantage of being effective in controlling doping levels, especially in intermediate states<sup>17,41</sup>. Doping involving no ions includes (i) photodoping<sup>42</sup>, which corresponds to the excitation of electrons with photons of greater energy than the band gap to the conduction band, and (ii) charge injection at a metal-semiconductor polymer (MS) interface<sup>43</sup>. The longevity of redox doping contrasts with the transient character of photodoping and MS excitations: photoconductivity lasts only until the excitons are either trapped or decay back to the ground state, whereas in the case of MS excitations conductivity endures only as long as a bias is applied<sup>16</sup>. Doping by acid-base chemistry<sup>44</sup> is a non-redox type of doping, which occurs in polymers possessing strong basic atoms within the  $\pi$ -backbone. In this case, the increase in conductivity is a result of protonation and not changes in the number of electrons. The most representative example of conduction by protonation is polyaniline, though it may also be doped by redox processes<sup>45,46</sup>.

Doped conjugated polymers have been applied in a wide range of scientific areas: (i) organic conductors in conductive layers<sup>47</sup>, (ii) fibres<sup>48,49</sup>, (iii) heterogeneous catalysis<sup>50,51</sup>, (iv) membranes for gas and liquid separations<sup>52,53</sup>, (v) corrosion inhibition<sup>54</sup>, (vi) lithium batteries<sup>55</sup>, (vii) electrochromic devices<sup>56,57</sup> and (viii) sensors<sup>58,59</sup>.

### 1.3 EXCITONS IN CONJUGATED POLYMERS

Doping or charge injection results in the formation of charge carriers responsible for the electrical conductivity of conjugated polymers. These charge carriers consist of localised structural distortions, corresponding to the occurrence of electronic states in the gap between valence and conduction bands<sup>60</sup>.

If the ground-state of the polymer is degenerate (e.g., *trans*-polyacetylene) doping results in structural relaxation of polymeric chains, which leads to a localisation of charge called a *soliton*. The soliton is a domain boundary between two degenerate ground-state configurations (Figure 1.3a), and is both topological and mobile due to translational symmetry of the chain<sup>16</sup>. Theoretical predictions<sup>60</sup> and experimental data show, however, that structural relaxation in the vicinity of the domain boundary (as well as the spin and charge of the soliton) extends over approximately seven carbon atoms (Figure 1.3b). The localised electronic state associated with the soliton is a nonbonding state situated between  $\pi$  and  $\pi^*$  bands (Figure 1.3c). The soliton can be neutral and have spin (e.g., found as defects from the synthesis of undoped material), or can be negatively/positively charged and spinless (created by doping). *Anti-soliton* is the designation given to the reverse boundary of a soliton.

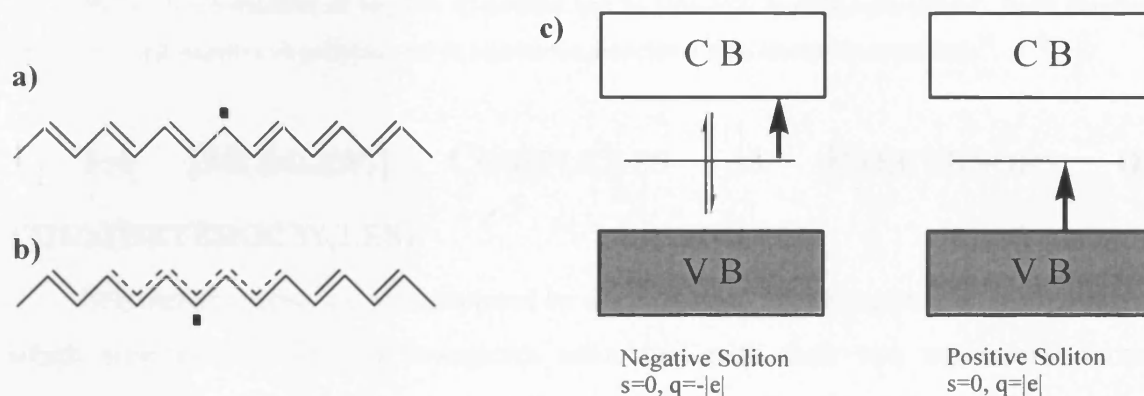


**Figure 1.3:** a) Soliton in *trans*-polyacetylene, b) structural relaxation of the soliton, c) band diagrams for positive and negative solitons associated with electronic transitions<sup>16</sup>.

In the case of polymers such as polythiophene or poly(*p*-phenylene) the ground-state is nondegenerate, meaning that there are two energetically different bond alternation patterns and the charge carriers are called *polarons* and *bipolarons*<sup>61,62</sup>. A polaron can be understood as a bound state consisting of a charged soliton and a neutral soliton whose

electronic states hybridise, giving rise to bonding and antibonding levels (Figure 1.4 a, c). A positive (negative) polaron is a radical cation (anion) with a single positive (negative) charge and spin  $1/2$ . A bipolaron can be envisaged as a bound state of two charged solitons of identical charge (or two polarons whose neutral solitons annihilate each other); it is a spinless dication (dianion)<sup>16</sup> (Figure 1.4 b, d).

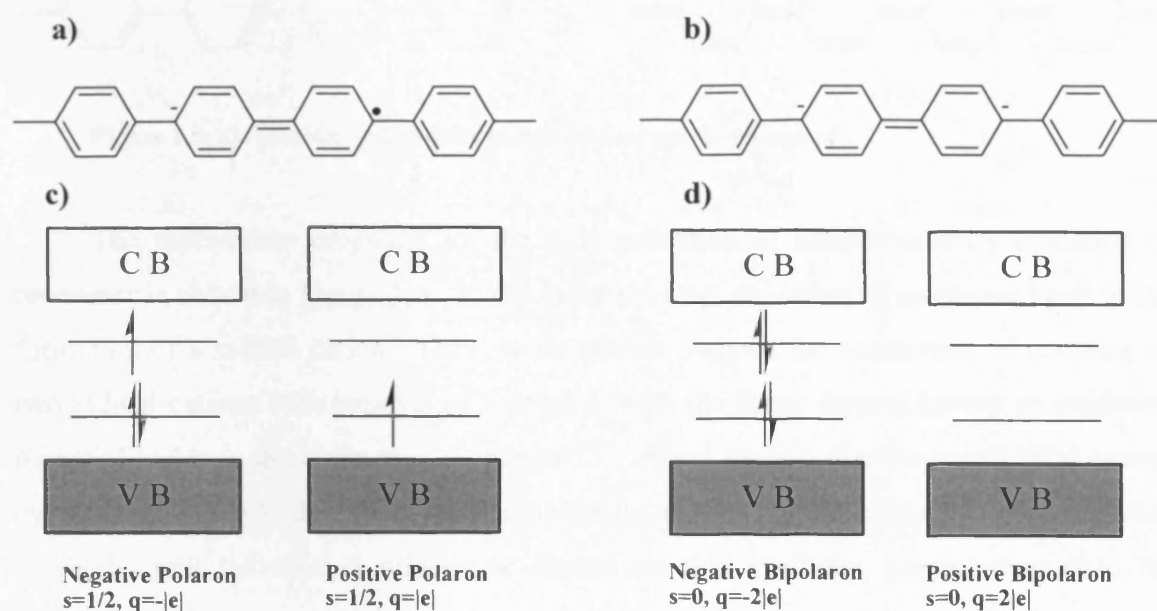


**Figure 1.4:** Structures of negative **a)** polaron and **b)** bipolaron in poly(*p*-phenylene). Band diagrams for positive and negative **c)** polarons and **d)** bipolarons associated with electronic transitions<sup>16</sup>.

## 1.4 [M(SALEN)] COMPLEXES AS PRECURSORS OF POLY(ETEROCYCLES)

Poly(heterocycles) are characterised by the existence of nondegenerate ground states, which arise due to different energetics associated with their two mesomeric forms, aromatic and quinoid structures (Figure 1.5). Compared to polyacetylene, poly(heterocycles) are environmentally more stable and their structural versatility allows design at the molecular level for modulation of the polymer electronic properties<sup>63</sup>. The discovery in 1979 that heterocyclic conjugated polymers can be prepared electrochemically as highly conductive, homogeneous films by the oxidative polymerisation of monomer<sup>22</sup> prompted a renewed interest in this class of materials for potential applications<sup>55,56</sup>. Electrochemical techniques provide easier routes for preparation of conjugated polymers

when compared to chemical/synthetic methods, particularly of materials required as a thin film deposited on a metal surface. This is obviously convenient for electrochemical applications.

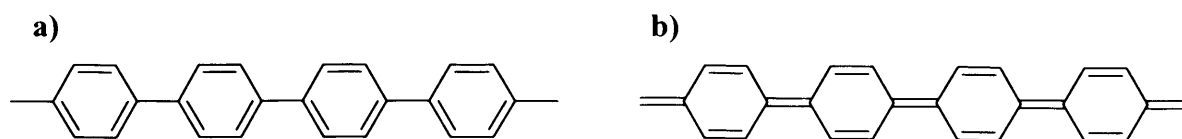


**Figure 1.5:** a) Aromatic and b) quinoid structures of poly(*p*-phenylene).

The mechanism proposed for the polymerisation of heterocycles by oxidation of monomer is shown in [Figure 1.6](#). In the initiation step, oxidation of monomer leads to the formation of a radical cation. Then, some authors suggest the occurrence of coupling of two radical cations with removal of 2 protons, with the dimer formed having an oxidation potential lower so the chain may propagate<sup>64,65</sup>; others suggest that the propagation occurs by electrophilic addition of a neutral molecule to the radical cation<sup>66,67</sup>. Propagation proceeds until the formed oligomeric chains become insoluble, precipitating onto the electrode surface.

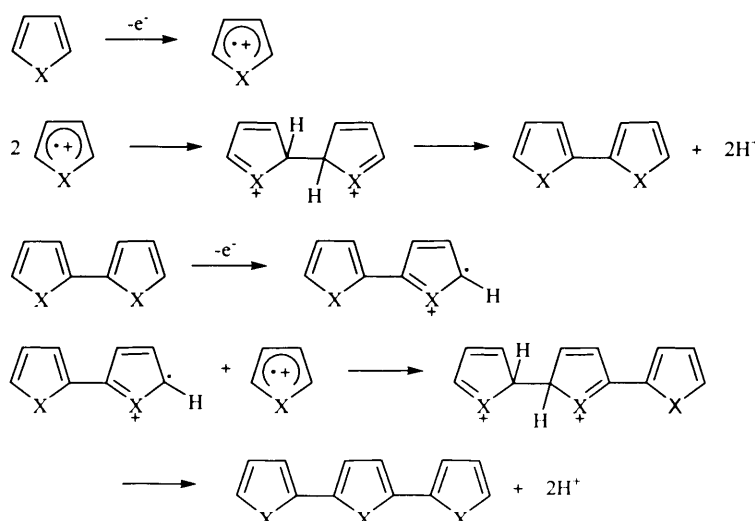


**Figure 1.6:** Mechanism of polymerisation of poly(heterocycles)<sup>63</sup>.

The model that describes charge transport in these conjugated polymers is the *polaron-hopping model*<sup>68-70</sup>. When they are in their neutral form, the band gap between valence (full) and conduction (empty) bands is high and electrons are not free to move; the

structure of the polymer is aromatic. Nonetheless, when non-degenerate oxidation (*p*-doping) occurs, the polymer loses an electron (the valence band is no longer filled) and assumes a quinoid structure, which originates the formation of a new electronic state (polaron), becoming conductive. The removal of a second electron can lead to two different situations: formation of another polaron, or removal of the electron from the polaronic level (bipolaron). The electrons can also travel between different chains by an electron hopping mechanism.

The conductivity in organic-based polymers can be, nonetheless, limited by the existence of defects which may interrupt charge carrier mobility. One strategy to overcome this limitation is the introduction of redox-active centres such as transition metals, either as functional groups along the polymer backbone or as units incorporated within the polymer backbone<sup>71</sup>. In the latter case, overlapping of metal orbitals with those of  $\pi$  conjugated system of the polymer may occur and provide efficient charge transport pathways, which may result in enhancement of conductivity. The incorporation of metal centres in pre-formed polymeric networks is not an easy task since it is necessary to create reactive sites in the polymer in order to insert them<sup>72</sup>. A more straightforward way of preparing polymeric films with metal centres is to use monomeric species containing the metal, such as metal complexes or organometallic species, and then prepare the supramolecular structures.

*Salen* ligands (Figure 1.7a) are important structures in the context of coordination chemistry because they are chemically robust, can accommodate a variety of different metals and form coordinatively unsaturated metal complexes<sup>71</sup>. Transition metal complexes based on *salen* ligands are here designated [M(*salen*)] (Figure 1.7b). Nickel complexes based on *salen* ligands, [Ni(*salen*)], are known for their application as catalysts in homogenous reduction of alkyl and aryl halides<sup>73-75</sup>.

The oxidation of [Ni<sup>II</sup>(*salen*)] is quite sensitive to the nature of the solvent: in strongly donating solvents such as *N,N'*-dimethylformamide or (CH<sub>3</sub>)<sub>2</sub>SO, the nickel centre is oxidised and the complex becomes hexacoordinated [Ni<sup>III</sup>(*salen*)L<sub>2</sub>]<sup>+</sup>, where L is a solvent molecule<sup>76-81</sup>; in moderate/weak donor solvents such as CH<sub>3</sub>CN or CH<sub>2</sub>Cl<sub>2</sub> the oxidation results in the formation of polymeric electroactive films deposited on the electrode surface<sup>82-99</sup>.



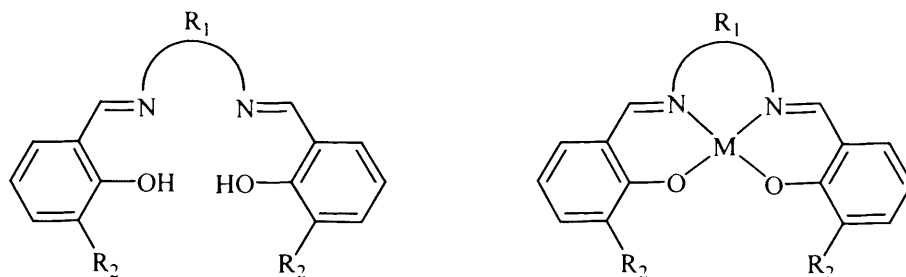


**Figure 1.7** Structures of **a)** *salen* ligands and **b)** [M(*salen*)] complexes.

The first studies of [M(*salen*)] (M=Ni, Cu) modified electrodes were reported by Goldsby and colleagues<sup>82-84</sup> in the late 1980s. In these studies electroactive films were deposited on different substrates (Pt and ITO electrodes) and characterised by cyclic voltammetry, electron spectroscopy and scanning electron microscopy. According to these authors, the polymerisation process may occur by linkage of phenyl groups at *para* positions. This was confirmed by inhibition of the polymerisation process when methyl groups were introduced in the referred positions of [M(*salen*)]<sup>82,83</sup>. Audbert's group<sup>86</sup> also reached the same findings by analysis of products resulting from cleavage of the films in acidic media. Based on these findings, Goldsby<sup>84</sup> and Audbert<sup>86-88</sup> proposed that polymerisation of these electroactive films is *ligand-based*, via a radical-radical coupling mechanism similar to that occurring for oxidation of phenol. Moreover, Audbert noticed that the change of metal centre (Ni or Cu) has little effect in the conductivity of the resulting polymers, and that they are conducting even in dry states. It was proposed that the electrochemical response associated with these systems is based on delocalisation of charge towards the ligand. Nonetheless, it was admitted that the metal centre might be oxidised to some extent<sup>88,89</sup>.

This view, however, was not uniformly accepted. Dahm and co-workers<sup>90-92</sup> also studied electroactive films based on [Ni(*salen*)] complexes deposited on Pt, glassy carbon electrodes and optically transparent tin oxide electrodes, and characterised them by cyclic voltammetry, spectroelectrochemistry techniques and scanning electron microscopy. Regarding the polymerisation process, Dahm<sup>92</sup> proposed that in a first stage the metal centre is oxidised, followed by irreversible establishment of bonds between phenyl rings; the electrochemical response of the modified electrode is metal centred.

In 1997 Vilas-Boas and co-workers<sup>93</sup> used *in situ* FTIR and UV-Vis spectroscopies to study the structure and electronic properties of electroactive [Ni(*salen*)] films as a

function of doping state; *ex situ* EPR was also used to analyse oxidised species during polymerisation and redox switching processes. Their findings showed that the polymerisation process is ligand-based, taking place at both *ortho* and *para* positions of the phenyl rings. Furthermore, the chemical and physical properties of these electroactive films are typical of polyphenylene compounds, with the metal centre acting solely as a bridge between biphenylene moieties. At moderate doping levels, charge carriers were identified as being paramagnetic radicals with electronic states situated in the mid gap (polarons), whereas at higher doping states formation of diamagnetic bipolarons occurs. A similar idea was proposed by Mathis<sup>72</sup>: films based on palladium-pyrrole complexes behave like polypyrrole, mainly because their HOMO orbitals are essentially a result of pyrrole  $\pi$  orbital overlap. Nevertheless, and unlike organic polymers such as polypyrrole or polyphenylene, non-metallated *salen* ligands cannot be used to prepare stable electroactive films<sup>98</sup>, thereby revealing the key role of the metal centre in the preparation of these polymeric films.

In spite of these findings, there is still no general consensus regarding the ligand-based response of poly[M(*salen*)]. In particular, Timonov's group<sup>100-102</sup> suggested that poly[M(*salen*)] possesses redox conductivity in liquid media and polaron conductivity in the dry state. In solution, charge transport takes place via electron hopping between adjacent metal centres through the  $\pi$ -conjugated system.

The first applications of modified electrodes based on [Ni(*salen*)] were reported by Dahm and co-workers<sup>90,91</sup>. These polymers were found to exhibit catalytic activity for reduction of alkyl halides. Losada and co-workers<sup>103</sup> prepared electroactive films based on [Ni(*salen*)] complexes using the *salen* ligand functionalised with a pyrrole unit, and found that they catalyse the reduction of carbon dioxide, and the oxidation of methanol and hydrazine. Momandre's group<sup>104</sup> reported catalytic properties of films based on [Fe(*salen*)] for the electroreduction of hydrogen peroxide and oxygen. More recently, Voituriez and co-workers<sup>105</sup> prepared [M(*salen*)] electroactive films (M=Ni, Cu, Cr and Co) based on chiral thiophene-containing ligands and studied them for applications in heterogeneous asymmetric catalysis. Other heterogeneous catalysts based on [M(*salen*)] include Langmuir films<sup>106,107</sup>, and [Co(*salen*)] complexes supported on glassy carbon electrode modified with a poly(estersulfonate) ionomer<sup>108</sup>.

In the context of chemical sensors, electropolymerised films based on [M(*salen*)] (M=Ni, Fe, Co, Cu and Mn) and Nafion were used for the detection of nitric oxide by Mao and co-workers<sup>109,110</sup>. The results showed that the characteristics of sensors did not change significantly with the metal centre, indicating that the electrochemical catalytic activity of the polymer should not be ascribed to the metal centre. Other applications of [M(*salen*)] complexes include luminescence phenomena<sup>111-113</sup>.

There were two studies reported in 2003 worthy of mention, demonstrating the development of poly[M(*salen*)] systems in new directions: (i) preparation of processible polymers and (ii) preparation of nanostructured materials with improved conductivities. The first, by Sukwattanasinitt and co-workers<sup>114</sup>, reports the preparation of soluble poly[M(*salen*)] (M=Ni, Mn, V) by introduction of glycolic chains between chiral *salen* ligands. These polymers can be used in the preparation of modified electrodes for electrochemical sensing purposes. The second, by Timonov's group<sup>102</sup>, reports the first work on template-based electrochemical methods for preparation of poly[M(*salen*)] with nanowire dimensions (diameters of 20-200 nm). These nanostructures were found to have conductivities one order of magnitude greater than the bulk polymers.

## 1.5 INCORPORATION OF ION RECOGNITION FUNCTIONALITIES IN CONJUGATED POLYMERS

Among the most important and widely studied applications of conjugated polymers is chemical sensing. In fact, chemical sensing was the first reported application of conjugated polymers, when free-standing polymer polyacetylene was used to detect and measure the presence of vapour dopants within the polymer, by changes in its conductivity<sup>18,19,115-117</sup>. Systems to be used as chemical sensors must fulfil two important requirements: (i) recognition of the analyte at the molecular level and (ii) transduction of the chemical interaction into a detectable and measurable signal<sup>58,117,118</sup>.

Due to their intrinsic electronic, electrochemical and optical properties, conjugated polymers can be used in chemical and/or biological sensors as transducers: they are able to convert the chemical interaction into electrical, electrochemical, optical, gravimetric/viscoelastic or thermal signals. Additionally, the interaction with the analyte at molecular level causes changes in the collective properties of the supramolecular systems - *recognition amplifiers*<sup>119</sup>.

There are several strategies to incorporate recognition sites within conjugated polymers: physical adsorption, physical occlusion during electropolymerisation, and covalent methods<sup>117</sup>. Physical adsorption is a simple and quick method but the resulting systems lack stability due to the occurrence of desorption processes and consequent loss of selectivity/specificity. The use of charged recognition species as ionic dopants (electrolyte) during the electropolymerisation process is not only a more efficient method of incorporation but also a ready way of preparing modified electrodes showing recognition properties, with the electrochemical techniques allowing precise control of film thickness and morphology. Disadvantages of this methodology are associated with the ionic nature of polymer-recognition site interaction, namely the possible egress of recognition sites, which is facilitated by the polymer doping/undoping process. This problem can be overcome when the recognition functionalities are covalently attached to the polymer backbone. Chemical modification and derivatization of the pre-formed electrode is a possible route but it is costly, synthetically complex, and usually functionalisation results in a decrease of polymer conductivity and poorer mechanical properties<sup>117</sup>. In this regard, the attachment of functional groups to the primary repeat unit prior to polymerisation seems to be an easier route for this purpose.

Species that can be used as a recognition site or indicator include catalysts (inorganic, organic and enzymes), binding molecules such as macrocycles, antibodies, DNA/RNA fragments, proteins or peptide chains. Polyether macrocycles, also known as *crown ethers*, are amongst the most studied macrocycles in the context of ion complexation (Figure 1.8).

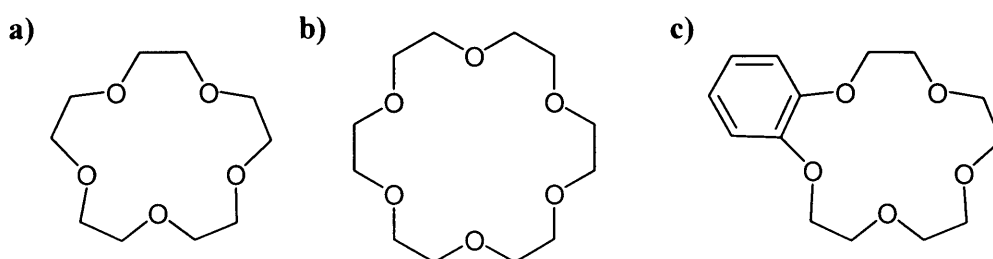


**Figure 1.8** a) 15-crown-5, b) 18-crown-6 and c) benzo-15-crown-5.

In 1967, Pedersen reported the synthesis of several polyether cycles, as well as ion complexation studies of these macrocycles with cations including alkali and alkaline earth metals in solution<sup>120,121</sup>. The interactions between metal and macrocycles were suggested

to be ion-dipole in nature, and several factors that could influence the stability of a polyether-ion complex were highlighted: relative sizes of ion and hole in the macrocycle ring, number, coplanarity, symmetrical placement and basicity of donor atoms, steric hindrance in the ring, ion solvation and cation charge. The stoichiometry of polyether ring-cation complex was suggested to be 1:1, regardless of the metal valence. Three years later Pedersen reported a more detailed (X-ray) analysis of the stoichiometry associated with the complexation of some of these crown ethers with  $\text{Na}^+$ ,  $\text{K}^+$ ,  $\text{Rb}^+$ ,  $\text{Cs}^+$ ,  $\text{NH}_4^+$  and  $\text{Ba}^{2+}$ <sup>122</sup>. In this work, salts of the complexes were analysed and the results were interpreted considering the *hole size-cation diameter relationship*. When the ionic diameter of the cation fits into the diameter of the macrocycle ring, the cation is found in a proportion of 1:1; when the cation is too large to fit within the ring, ‘sandwich structures’ in proportion 2:1 (macrocycle:cation) and in some cases 3:2 were proposed. Frensdorff determined stability constants for 1:1 complexes, by potentiometry in water and methanol<sup>123</sup>. The constants in methanol were found to be considerably higher than in water, implying that ion solvation plays an important role and limits complexation. The same trend was found in terms of ion size and ring diameter as previously reported by Pedersen. Additionally, substitution of oxygen atoms by nitrogen and sulphur atoms resulted in a decrease in affinity of polyether cycles towards alkali ions. Since these early studies a lot of research has been done in this area and several reviews listing the successful synthesis of new macrocycles, as well as the compilation of thermodynamic and kinetic data for ion-macrocycle complexation, have been published<sup>124-128</sup>.

### 1.5.1 Poly(heterocycles) bearing polyether recognition functionalities

The incorporation of polyethers in a heterogeneous phase for recognition purposes has been reported for a wide range of self-assembled monolayers<sup>129-133</sup>, Langmuir-Blodgett films<sup>134-136</sup> and conducting polymers<sup>137,138</sup>. The first report on conjugated polymers functionalised with polyalkyl ethers was by Roncali and co-workers in 1989<sup>139,140</sup> (Figure 1.9, monomer 1), and the voltammetric response of this polymer was studied in the presence of tetrabutylammonium and  $\text{Li}^+$  electrolytes. In tetrabutylammonium electrolyte the system exhibited two redox processes around 0.5 V and 0.8 V vs. SCE. The insertion of increasing amounts of  $\text{Li}^+$  resulted in the shift of potential associated with the redox processes to less positive potentials and narrowing of the redox features. This was

attributed to the complexation of  $\text{Li}^+$  cations with the polyalkylether substituent. Based on more detailed spectroscopic studies of poly $\mathbf{1}$ <sup>141,142</sup>, the same authors suggested that complexation of  $\text{Li}^+$  with the polyether substituent had two effects: to planarise the polymer backbone and increase its rigidity by pseudo-cross-linking between chains. Moreover, the effect associated with the extension of the ethylene oxide group towards the polythiophene group was also studied<sup>143</sup>. The peak current associated with the first redox feature (0.40 V vs. SCE) increased in the presence of  $\text{Li}^+$ . This was suggested to result from an increase of ionic conductivity.

However, polyalkylether chains lack differentiation abilities towards ions and the use of crown ether macrocycles as pendant groups may result in ionoselective responses. Bartlett and co-workers prepared a polymer based on pyrrole and benzo-15-crown-5 by electrochemical routes (monomer  $\mathbf{2}$ )<sup>144</sup>. Cyclic voltammetry carried out in the presence of different cations ( $\text{Li}^+$ ,  $\text{Na}^+$ ,  $\text{K}^+$  and tetraethylammonium) revealed no selective binding towards  $\text{Na}^+$ . This was explained in terms of steric barriers arising due to the close packing of the crown ethers within the polymer, thereby preventing the complexation of the solvated ion.

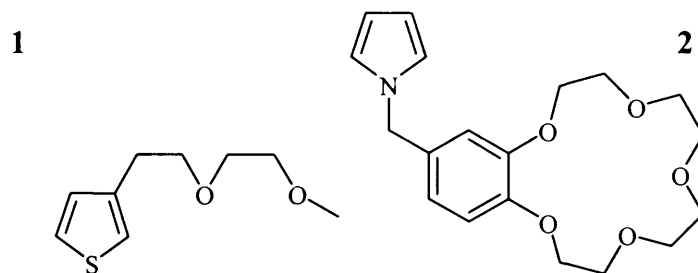


**Figure 1.9** Monomers  $\mathbf{1}$  and  $\mathbf{2}$ .

Since 1993, several works related to the preparation of ionoselective systems with conjugated polymers and crown ethers have been reported. Bauerle and co-workers studied the sensitivity of several polythiophene films bearing crown ethers towards  $\text{Li}^+$ ,  $\text{Na}^+$  and  $\text{K}^+$  cations (Figure 1.10, structures  $\mathbf{3}$  to  $\mathbf{7}$ ). Poly $\mathbf{3}$  and poly $\mathbf{4}$  bear 12-crown-4 substituents, linked to the thiophene rings via alkyl chains. They were found to show a differentiated electrochemical response, with the highest sensitivity observed for  $\text{Li}^+$  and the lowest for  $\text{K}^+$ <sup>145,146</sup>. These results are consistent with the hole size-cation diameter relationship, since  $\text{Li}^+$  fits within the 12-crown-4 ring<sup>147</sup>. Upon metal cation addition, the voltammetric response was characterised by a decrease in current and displacement of

redox features towards higher potentials, an evidence of progressive difficulties in oxidising the polymers.

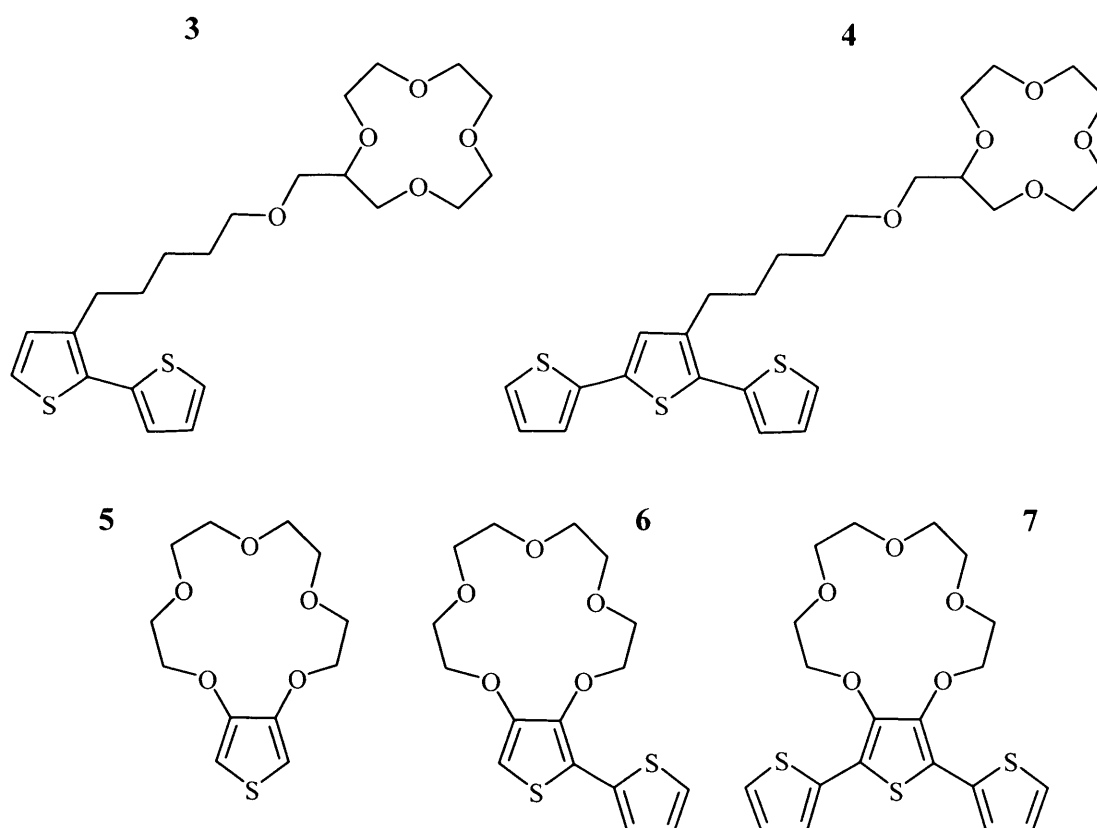


**Figure 1.10:** Monomers 3-7.

Polymers based on monomers **5**, **6** and **7**, showed selective response towards  $\text{Na}^+$ <sup>148</sup>, as expected considering the match between the diameter of the ether derivative ring (similar to the benzo-15-crown-5) and the size of the cation. The changes in the voltammetric responses were qualitatively similar to those observed for poly**3** and poly**4** in the presence of metal cations. The greatest effects were observed for poly**5** and poly**6** in the presence of  $\text{Na}^+$ , whereas for poly**7** small variations were detected and attributed to the lower number of macrocycle rings per repeat unit. Another report by Bauerle's group focused on the study of oligothiophenes with fused 15-crown-5, 18-crown-6, as well as pendant polyalkylether chains<sup>149</sup>. Analysis of the voltammetric response showed, again, correlation between macrocycle ring and cation relative sizes. The largest effects were observed for 18-crown-6 derived oligomers in the presence of  $\text{K}^+$ . Also, polymers with polyalkylether pendant groups showed the best responses for  $\text{Li}^+$ , which was attributed to the ability of these substituents to adapt easily and wrap around the ion. The addition of

$\text{Ba}^{2+}$  resulted in the highest anodic displacements of redox features for all the oligomers studied, even in the presence of monovalent cations; some degree of selectivity towards  $\text{Ba}^{2+}$  was suggested. Similar systems based on bithiophene units bearing crown ethers and ethylene oxide groups have been studied<sup>150</sup>, and in the presence of alkali metal ions the observed loss in electroactivity was suggested to be associated with hindrance of the diffusion of anions inside the polymer films.

Sannicolo and colleagues synthesised cyclopentadithiophenes containing crown ether moieties and studied the resulting polymers prepared by anodic polymerisation<sup>151</sup>. The monomers were designed in such a manner that crown ether moieties (16- and 15-crown-5) were placed far from the coupling sites of bithiophene moieties. Furthermore, the ‘spacers’ introduced between crowns and bithiophene were rigid and short to maximise the cation-sensing interaction. The effect of crown ether orientation was also studied by preparing monomers with crown ethers both co-planar and perpendicular with respect to the bithiophene moiety ([Figure 1.11](#)). Poly**8** was found to show a differentiated response in the presence of  $\text{Li}^+$  and  $\text{Na}^+$ , with the latter cation imparting greater changes in the electrochemical response in acetonitrile solution. For repeat units with parallel crown ethers (monomer **8**)  $\pi$ -dimerization occurs upon oxidation, which favours ion coordination in sandwich mode and consequent loss of the cations in excess. In polymers with perpendicular crown ethers (monomer **9**) dimerisation does not occur and no cations are released.

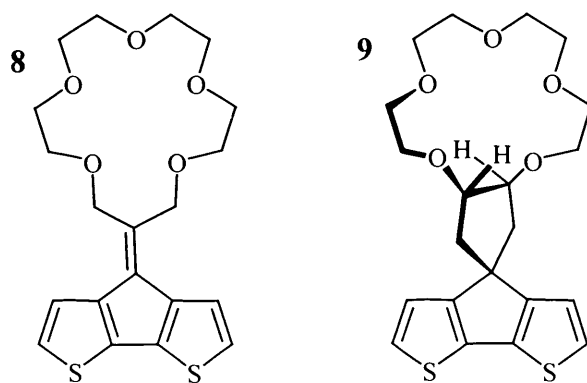


**Figure 1.11:** Monomers **8** and **9**.

Fabre and co-workers reported the preparation of polythiophenes in which the repeat unit consists of two thiophene units linked by a crown ether ([Figure 1.12](#))<sup>152</sup>. The polymer



can be either *p*-doped or *n*-doped, and in the presence of  $K^+$  the redox processes are displaced to more positive potentials. This change in the electrochemical response cannot be observed for  $Li^+$  or  $Na^+$  and was explained in terms of the relative size of metal cation and ring diameter of the crown.

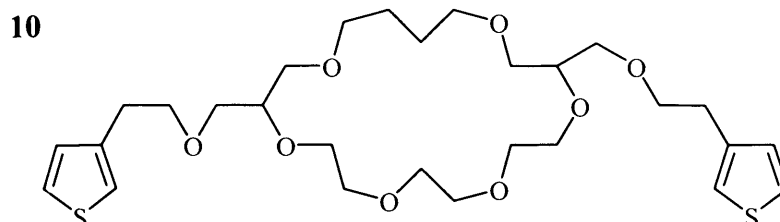


**Figure 1.12:** Monomer 10.

More recently, Si and colleagues reported the synthesis of a monomer based on a thiophene unit and benzo-15-crown-5 (Figure 1.13), and studied its electrochemical polymerisation and self-assembly on Au (111) surfaces<sup>153</sup>. The polymerisation was found to lead to the formation of nanoparticles or clusters spread all over the Au (111) electrode and the polymer was found to be attached to the surface by sulphur-gold interactions. The potentiometric response of the system in presence of  $K^+$  was also investigated, with the polymer revealing a Nernstian dependence, both in aqueous and organic solutions, over 4 orders of magnitude. Furthermore, the electrochemical response of the polymer was studied in the presence of other cations, including  $Li^+$ ,  $Na^+$ ,  $NH_4^+$ ,  $Mg^{2+}$  and  $Ca^{2+}$ , and found to be  $K^+$ -selective.

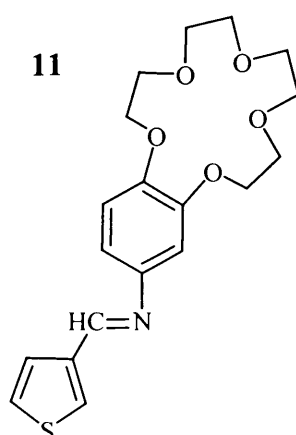


**Figure 1.13:** Monomer 11.

Garnier and co-workers prepared and studied polypyrrole films bearing monoaza-12-crown-4 and monoaza-18-crown-6 groups (Figure 1.14)<sup>154-156</sup>. In aqueous solution, the cyclic voltammogram did not change in the presence of  $\text{Li}^+$ ,  $\text{Na}^+$  or  $\text{K}^+$ . Similar results were obtained for poly**12** in  $\text{CH}_3\text{CN}$  solution, but for poly**13** the response changed when  $\text{Na}^+$  or  $\text{K}^+$ -based electrolytes were added to a  $\text{Li}^+$ -based electrolyte. More specifically, the anodic feature was shifted towards more positive potentials, whereas no changes in its cathodic counterpart were observed (irreversible process). The size of the crown in poly**12** is too small to accommodate any of the three cations, which explains the absence of alterations; on the other hand, poly**13** shows the ability to complex  $\text{Na}^+$  and  $\text{K}^+$  in  $\text{CH}_3\text{CN}$  but not  $\text{Li}^+$  because the latter is too small to be stabilised within the monoaza-18-crown-6 ring. In aqueous solution the undifferentiated response of poly**13** was assumed to result from the stronger solvation of cations and low binding constant of the crown.

Pernaut and colleagues also prepared 14-crown-4 derived pyrrole films by electropolymerisation<sup>157</sup>. The electrochemical response of the polymer was found to be sensitive to both the nature ( $\text{Li}^+$  is favoured over  $\text{Na}^+$  and  $\text{Mg}^{2+}$ ) and concentration of the cation.

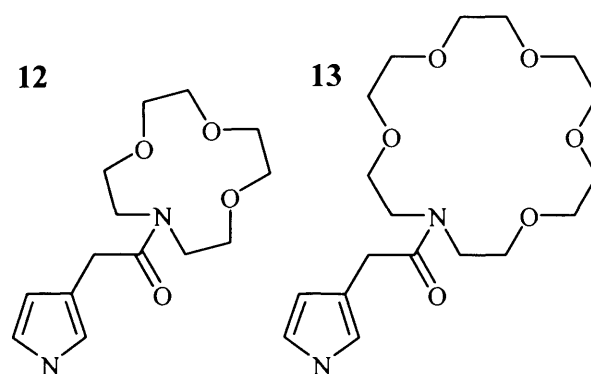


**Figure 1.14:** Monomers **12** and **13**.

Although extensive electrochemical studies have been reported in the context of ion recognition, other techniques with particular relevance to optical-based ones have been used. The factors associated with changes in the redox potential of electroactive polymers upon cation addition can be due either to electronic effects resulting from the presence of those species or conformational changes imposed by their presence. While

electrochemical-based techniques cannot provide a clear distinction between these factors, optical-based procedures can be applied to overcome this difficulty, since optical changes depend only on conformational variations<sup>138</sup>.

Marsella and Swager reported the preparation of conjugated polymers by chemical coupling reactions, with bithiophene units integrating part of the crown ether<sup>158-162</sup> (Figure 1.15). These polymers exhibited ion-specific UV-Vis responses, proving that the binding process regulates polymer conformation. As a result, intra- and interchain conductions are affected, by reduction of conjugation length and by decrease of polymer ability to pack, respectively. Additionally, the complexation of electron deficient species by donor atoms from the crown, which are also part of the polymer  $\pi$  system, raises the local redox potential and increases the band gap by lowering the HOMO energy<sup>137</sup>.

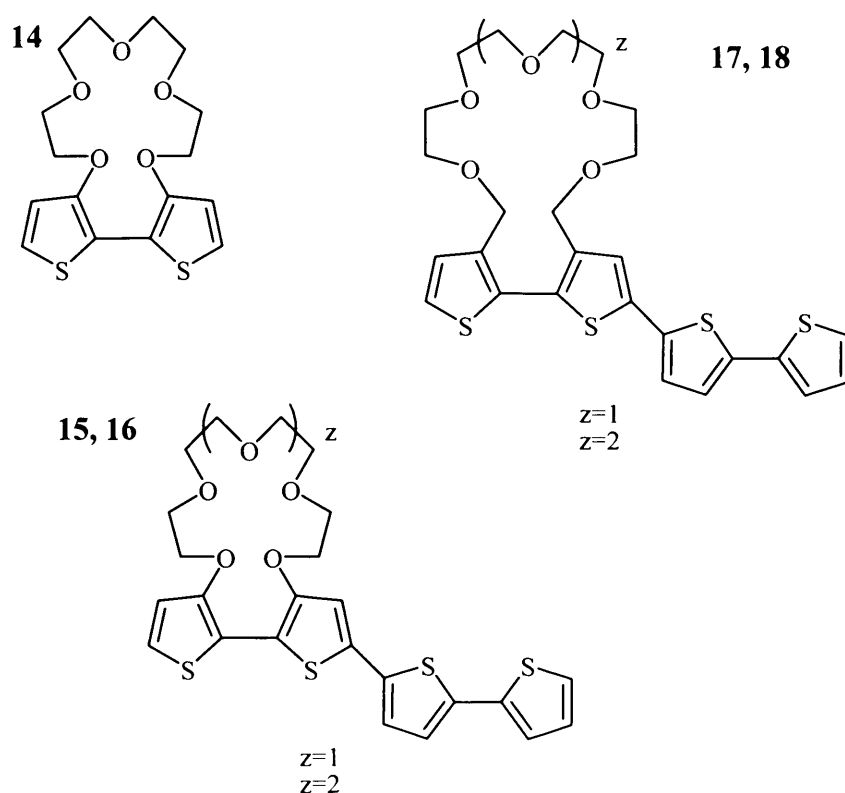


**Figure 1.15:** Monomers 14-18.

Leclerc and colleagues have also focused their effort on the study of optical properties of regioregular polythiophene systems with polyalkylether and crown ether macrocycles, and the effect of alkali metal cations in them<sup>163-167</sup>. Interestingly, the major changes detected by UV-Vis and fluorescence spectroscopies were found for polymers

whose pendant groups were too small to fit the cations, therefore forcing the polymer into conformational changes; in some cases formation of inter- and intramolecular sandwich complexes were suggested.

In another work, Swager and colleagues prepared poly(*p*-phenylene ethylene)s bearing 15-crown-5 and explored the 1:2 sandwich complex between  $K^+$  and this crown ether to impart aggregation between vicinal chains and use this process as a new transducing mechanism<sup>168</sup>. Both UV-Vis and fluorescence spectroscopy evidenced interpolymer  $\pi$ -stacking aggregation in the presence of  $K^+$ , but not for  $Na^+$  or  $Li^+$ .

Recently, selective and reversible responses were found for poly-(*p*-phenylene ethynylene) conjugated polymers containing pseudo-crowns attached to the backbone<sup>169</sup>. Changes in the optical properties of polymers in the presence of metal ions are due to induced conformational changes, and are sensitive to metal cation concentration. The small responses obtained in the presence of  $K^+$  were attributed to the larger size of this cation when compared to  $Li^+$  and  $Na^+$ . Ion binding was found to be reversible and selectivity towards  $Li^+$  was obtained by manipulating the composition of polymer side-chains (introduction of ethylene oxide chains in phenyl rings next to the rings bearing pseudo-crowns).

### **1.5.2 Conjugated polymers incorporating metal derived substituents and recognition sites**

The first report on conjugated polymer bearing polyalkylether substituents, as well as ‘metal-derived’ substituents, was by Ion in 1997<sup>170</sup>. The system consisted of a electropolymerised polypyrrole film, functionalised with a ferrocene-crown ether receptor (Figure 1.16). The addition of  $Ba^{2+}$  resulted in a decrease of the redox feature associated with ferrocene/ferricinium couple at  $E_{1/2} = 0.56$  V, whilst a new redox wave occurred at  $E_{1/2} = 0.68$  V. The current associated with the latter feature eventually saturates and for excessive amounts of  $Ba^{2+}$  the wave at  $E_{1/2} = 0.56$  V disappears. Similar behaviour was found in the presence of  $Ca^{2+}$ , but the response of the system is about 10 times more sensitive to  $Ba^{2+}$  than  $Ca^{2+}$ . Addition of  $Mg^{2+}$ ,  $Li^+$ ,  $Na^+$  and  $K^+$  cations did not influence the electrochemical response of the polymer.

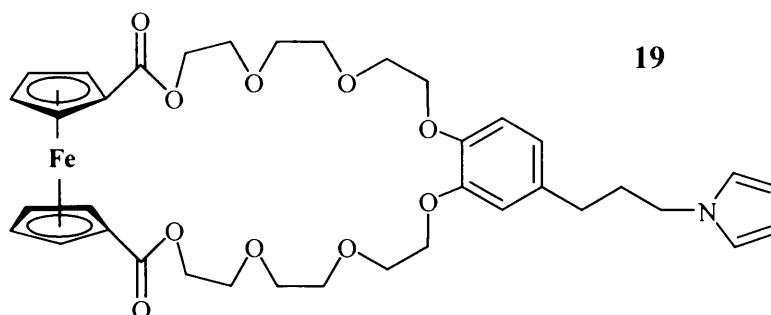


**Figure 1.16: Monomer 19.**

In 1998, Reddinger and Reynolds reported the preparation and characterisation of new polythiophene-based films able to bind both ionic and uncharged molecular analytes<sup>171</sup> (Figure 1.17). The repeat unit consists of a poly(terthiophene)-Schiff base metal complex monomer. Cyclic voltammetry was used to study its recognition properties for  $\text{Li}^+$ ,  $\text{Na}^+$ ,  $\text{Mg}^{2+}$ ,  $\text{Ba}^{2+}$ , pyridine and triphenylphosphine. The addition of metal cations to background electrolyte resulted in positive displacements of  $E_{1/2}$  in the order  $\text{Li}^+ < \text{Na}^+ < \text{Mg}^{2+} < \text{Ba}^{2+}$ . Additionally, in the presence of  $\text{Li}^+$  and  $\text{Na}^+$  the redox waves become narrowed, which was attributed to the higher mobility of these species with respect to divalent cations. The addition of divalent cations induced irreversible electrochemical changes in the polymer.

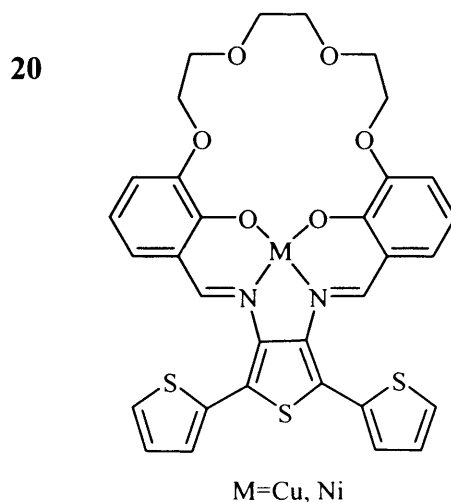


**Figure 1.17: Monomer 20.**

Tarabek and co-workers designed and characterised new electroactive polymers based on *salen* units<sup>172</sup> (Figure 1.18). Polymers based on monomer 21 and its copolymer with pyrrole, were prepared by electrosynthesis and characterised using

spectroelectrochemical techniques including *in situ* ESR, ESR/UV–Vis–NIR and FTIR. Both the polymer and copolymer were demetallised and then immersed in solutions containing  $\text{Ni}^{2+}$ . In the case of the polymer, the loss of  $\text{Ni}^{2+}$  species results in loss of electroactivity (insulating film); subsequent addition of  $\text{Ni}^{2+}$  ions does not provoke any increase of conductivity. For the copolymer, addition of successive amounts of  $\text{Ni}^{2+}$  to the demetallised but still partially conductive copolymer resulted in an increase of conductivity near the oxidation potentials of pyrrole and *salen* groups. Potentiometric studies also showed the possibility of using these systems for  $\text{Ni}^{2+}$  detection.

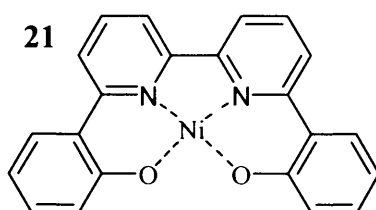


**Figure 1.18:** Monomer 21.

### 1.5.3 Molecular design of poly[M(*salen*)] electroactive films

Following the work by Vilas-Boas and colleagues in 1997<sup>93</sup>, the group leaded by Freire in collaboration with Hillman has devoted the last 10 years of research to molecular design of  $[\text{Ni}(\textit{salen})]$  complexes, in order to tune the properties of the resulting poly $[\text{Ni}(\textit{salen})]$  films<sup>94-97</sup> in a *bottom-up* fashion. The strategy has consisted of keeping the backbone of the main structure intact in order to obtain the same type of materials with generic properties (*i.e.*, conducting polymers, electrochemical properties typical of ligand-based redox processes), whilst changing the substituents in the imine bridge (position  $\text{R}_1$ , recall [Figure 1.7](#)) and/or in the phenyl rings (position  $\text{R}_2$ ). In a first stage, different diimine bridges, were incorporated in the complexes via synthetic routes and the corresponding films characterised<sup>94-97</sup>. The results showed that, among the films prepared, poly $[\text{Ni}(\text{saltMe})]$  was the most stable. The latter was extensively studied to provide an understanding of redox activity and charge transport<sup>94</sup>, electronic structure<sup>96</sup> and ion/solvent motion<sup>95</sup>, and to assess the potentialities of these systems in charge transfer mediation processes<sup>97</sup>. Subsequently, methoxy groups were incorporated as substituents in the phenyl rings of the  $[\text{Ni}(\text{saltMe})]$  complex<sup>98</sup> ( $[\text{Ni}(3\text{-MeOsaltMe})]$ , [Table 1.1](#)), and the electrochemical properties of the resulting film were found to change dramatically when

compared to those of poly[Ni(saltMe)]. More recently, the influence of the metal centre in polymers with the same ligand network was reported<sup>173</sup>, with the spectroelectrochemical properties of poly[Cu(salen)] films being similar when compared to their nickel analogues. The long term goal of such efforts is to refine the properties of poly[M(salen)] in two different yet complementary aspects: (i) improvement of properties related to general requirements for their application in nanotechnology such as stability, durability and reproducibility of the response and (ii) preparation of materials for specific purposes, namely ion recognition/sensing systems<sup>99</sup>.

## 1.6 AIM

The aim of the work presented in this thesis is the preparation and characterisation of poly[M(salen)] films (Table 1.1), exploring their potential as sensing systems for alkali and alkaline earth metal electroinactive cations.

A ‘multi-dimensional’ approach was followed: in some studies *different techniques* were used to characterise the *same poly[M(salen)] film*, whereas in others *different but structurally related poly[M(salen)] films* were investigated using the *same technique*. The purpose is to correlate electrochemical, electronic and optical properties with composition, structure and morphology, in order to establish patterns for a more comprehensive conception of these systems.

The next chapters are divided as follows:

Chapter 2: description and theory associated with the techniques used;

Chapter 3: description of experimental procedures;

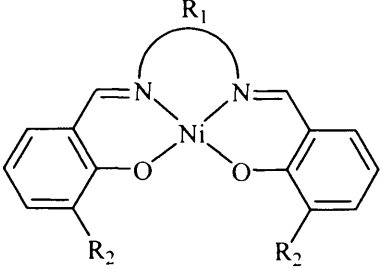
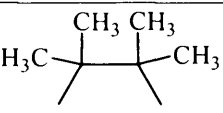
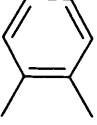
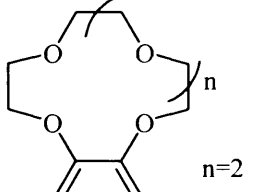
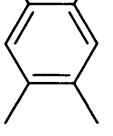
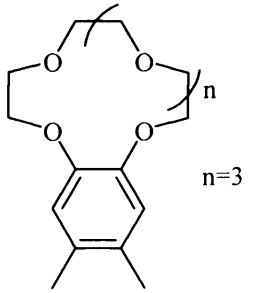
Chapter 4: electrochemical characterisation of poly[Ni(3-Mesalophen-b15-c5)] and ion recognition studies by cyclic voltammetry and UV-Vis spectroscopy;

Chapter 5: compositional and structural studies of poly[M(salen)] films by X-ray techniques (X-ray photoelectron and X-ray absorption spectroscopies);

Chapter 6: study of interfacial and viscoelastic properties of poly[Ni(3-Mesalophen-b15-c5)] by quartz crystal impedance, atomic force and scanning electron microscopies;

Chapter 7: introductory studies of composites based on poly[Ni(3-Mesalophen-b15-c5)] and carbon nanotubes by cyclic voltammetry, electrochemical impedance and scanning electron microscopy;

**Table 1.1:** Structures of the [M(*salen*)] complexes studied.

<b>[Ni(<i>salen</i>)] complexes</b>		
		
Complex	R <sub>1</sub>	R <sub>2</sub>
[Ni(3-MeOsaltMe)]		CH <sub>3</sub> O-
[Ni(3-Mesalophen)]		CH <sub>3</sub> -
[Ni(3-Mesalophen-b15-c5)]		CH <sub>3</sub> -
[Ni(3-MeOsalophen-b15-c5)]		CH <sub>3</sub> O-
[Ni(3-Mesalophen-b18-c6)]		CH <sub>3</sub> -



## REFERENCES

1. Linford, R. G. In *Applications of Electroactive Polymers*; Scrosati, B., Ed.; Chapman & Hall: London, 1993; p 1.
2. Doshier, T. M.; Myers, G. C.; Atkins, D. C. Jr. *J. Colloid Sci.* **1951**, 6, 223.
3. Chadwick, A. V.; Worboys, M. R. In *Polymer Electrolyte Reviews 1*; MacCallum, J. R., Vincent, C. A., Eds.; Elsevier Applied Science: London, 1987; p 203.
4. Linford, R. G. In *Electrochemical Science and Technology of Polymers 2*; Elsevier Applied Science: London, 1990; p 281.
5. Bruce, P. G.; Vincent, C. A. *Faraday Discuss. Chem. Soc.* **1989**, 88, 43.
6. Cameron, G. G.; Ingram, M. D.; Harvie, J. L. *Faraday Discuss. Chem. Soc.* **1989**, 88, 55.
7. Andrews, K. C.; Cole, M.; Latham, R. J.; Linford, R. G.; Williams, H. M.; Dobson, B. R. *Solid State Ionics* **1988**, 28-30, 929.
8. Smyrl, W. H.; Lien, M. In *Applications of Electroactive Polymers*; Scrosati, B., Ed.; Chapman & Hall: London, 1993; p 29.
9. Dalton, E. F.; Surridge, N. A.; Jernigan, J. C.; Wilburn, K. O.; Facci, J. S.; Murray, R. W. *Chem. Phys.* **1990**, 141, 143.
10. Doblhofer, K.; Durr, W.; Jauch, M. *Electrochim. Acta* **1982**, 27, 677.
11. Mortimer, R. J.; Anson, F. C. *J. Electroanal. Chem.* **1982**, 138, 325.
12. Oh, S. M.; Faulkner, L. R. *J. Electroanal. Chem.* **1989**, 269, 77.
13. Forster, R. J.; Kelly, A. J.; Vos, J. G.; Lyons, M. E. G. *J. Electroanal. Chem.* **1989**, 270, 365.
14. Pickup, P.G.; Murray, R.W. *J. Am. Chem. Soc.* **1983**, 105, 4510.
15. Daum, P.; Murray, R.W. *J. Phys. Chem.* **1981**, 85, 389.
16. Heeger, A. J. *J. Phys. Chem. B* **2001**, 105, 8475.
17. Pron, A.; Rannou, P. *Prog. Polym. Sci.* **2002**, 27, 135.
18. Shirakawa, H.; Louis, E. J.; MacDiarmid, A. G.; Chiang, C. K.; Heeger, A.J. *J. Chem. Soc., Chem. Commun.* **1977**, 578.
19. Chiang, C. K.; Fincher Jr., C. R.; Park, Y. W.; Heeger, A. J.; Shirakawa, H.; Louis, E. J., Gau, S. C.; MacDiarmid, A. G. *Phys. Rev. Lett.* **1977**, 39, 1098.

20. Ranby, B. In *Conjugated Polymers and Related Materials: The Interconnection of Chemical and Electronic Structures*; Salaneck, W. R., Lundstrom, I., Ranby, B., Eds.; Oxford University Press: Oxford, U. K., 1993; Chapter 3.
21. Shon, J. H.; Dodabalapur, A.; Bao, Z.; Kloc, C.; Schencker, G.; Batlogg, B. *Nature* **2001**, *410*, 189.
22. Diaz, A. F.; Kanazawa, K. K.; Gardini, G. P. *J. Chem. Soc., Chem. Commun.* **1979**, 635.
23. Tourillon, G.; Garnier, F. *J. Electroanal. Chem.* **1982**, *135*, 173.
24. Heeger, A. J. In *Handbook of Conducting Polymers*, 1st ed.; Skotheim, T. A., Ed.; Marcel Dekker: New York, 1986; Vol. 2, p 729.
25. Wudl, F.; Kobayashi, M.; Heeger, A. J. *J. Org. Chem.* **1984**, *49*, 3382.
26. Roncali, J. *Chem. Rev.* **1997**, *97*, 173.
27. Pomerantz, M. In *Handbook of Conducting Polymers*, 2nd ed.; Skotheim, T. A., Elsenbaumer, R. L., Reynolds, J. R., Eds.; Marcel Dekker: New York, 1998; p 277.
28. Friend, R. H.; Greenham, N. C. In *Handbook of Conducting Polymers*, 2nd ed.; Skotheim, T. A., Elsenbaumer, R. L., Reynolds, J. R., Eds.; Marcel Dekker: New York, 1998; p 823.
29. Leising, G.; Tash, S.; Graupner, W. In *Handbook of Conducting Polymers*, 2nd ed.; Skotheim, T. A., Elsenbaumer, R. L., Reynolds, J. R., Eds.; Marcel Dekker: New York, 1998; p 847.
30. Hide, F.; Diaz-Garcia, M. A.; Schwartz, B. J.; Heeger, A. J. *Acc. Chem. Res.* **1997**, *30*, 430.
31. Tessler, N. *Adv. Mater.* **1999**, *11*, 363.
32. McGehee, M. D.; Heeger, A. J. *Adv. Mater.* **2000**, *12*, 1655.
33. Brabec, C. J.; Sariciftci, N. S.; Hummelen, J. C. *Adv. Funct. Mater.* **2001**, *11*, 15.
34. Yu, G.; Gao, J.; Hummelen, J. C.; Wudl, F.; Heeger, A. J. *Science* **1995**, *270*, 1789.
35. Roman, L. S.; Inganas, O.; Granlund, T.; Nyberg, T.; Svensson, M.; Andersson, M. R.; Hummelen, J. C. *Adv. Mater.* **2000**, *12*, 189.
36. Fuchigami, H.; Tsumura, A.; Koezuka, H. *Appl. Phys. Lett.* **1993**, *63*, 1372.
37. Sirringhaus, H.; Tessler, N.; Friend, R. H. *Science* **1998**, *280*, 1741.
38. Reghu, M.; Cao, Y.; Moses, D.; Heeger, A. J. *Phys. Rev. B* **1993**, *47*, 1758.
39. Yoon, C. O.; Reghu, M.; Moses, D.; Heeger, A. J., *Phys. Rev. B* **1994**, *49*, 10851.

40. MacDiarmid, A. G. *Angew. Chem. Int. Ed.* **2001**, *40*, 2581.
41. Nigrey, P. J.; MacDiarmid, A. G.; Heeger, A. J. *J. Chem. Soc., Chem. Commun.* **1979**, 594.
42. Sariciftci, N. S. In *Primary Photoexcitations in Conjugated Polymers*; World Scientific Publishing Co.: Singapore, 1998.
43. Burroughes, J. H.; Bradley, D. D. C.; Brown, A. R.; Marks, R. N.; Friend, R. H.; Burns, P. L.; Holmes, A. B. *Nature* **1990**, *347*, 539.
44. Salaneck, W. R.; Lundstrom, I.; Haung, W.-S.; McDiarmid, A. G. *Synth. Met.* **1986**, *13*, 291.
45. Chiang, J.-C.; MacDiarmid, A. G. *Synth. Met.* **1986**, *13*, 193.
46. MacDiarmid, A. G.; Chiang, J.-C.; Richter, A. F.; Epstein, A. J. *Synth. Met.* **1987**, *18*, 285.
47. Kudoh, Y.; Akami, K.; Matsuya, Y. *Synth. Met.* **1999**, *102*, 973.
48. Thieblemont, J. C.; Planche, M. F.; Petrescu, C.; Bouvier, J. M.; Bidan, G. *Synth. Met.* **1993**, *59*, 81.
49. Pomfret, S. J.; Adams, P. N.; Comfort, N. P.; Monkman, A. P. *Polymer* **2000**, *41*, 2265.
50. Missono, M. *J. Chem. Soc., Chem. Commun.* **2001**, *13*, 1141.
51. Pozniczek, J.; Bielanski, A.; Kulszewicz-Bajer, I.; Zagorska, M.; Kruczala, K.; Dyrek, K.; Pron, A. *J. Mol. Catal.* **1991**, *69*, 223.
52. Conklin, J. A.; Su, T. M.; Huang, S.-C.; Kaner, R. In *Handbook of Conducting Polymers*, 2nd ed.; Skotheim, T. A., Elsenbaumer, R. L., Reynolds, J. R., Eds.; Marcel Dekker: New York, 1998; p 945.
53. Stolarczyk, A.; Lapkowski, M. *Synth. Met.* **2001**, *121*, 1385.
54. Zarras, P.; Anderson, N.; Webber, C.; Irvin, D. J.; Irvin, J. A.; Guenthner, A.; Stenger-Smith, J. D. *Rad. Phys. Chem.* **2003**, *68*, 387.
55. Furukawa, N.; Nishio, K. In *Applications of Electroactive Polymers*; Scrosati, B., Ed.; Chapman & Hall: London, 1993; p 150.
56. Mastragostino, M. In *Applications of Electroactive Polymers*; Scrosati, B., Ed.; Chapman & Hall: London, 1993; p 223.
57. Somani, P. R.; Radhakrishnan, S. *Mater. Chem. Phys.* **2002**, *77*, 117.

58. Gerard, M.; Chaubey, A.; Malhotra, B. D. *Biosensors & Bioelectronics* **2002**, *17*, 345.
59. Jurs, P. C.; Bakken, G. A.; McClelland, H. E. *Chem. Rev.* **2000**, *100*, 2649.
60. Heeger, A. J.; Kivelson, S.; Schrieffer, J. R.; Su, W. P. *Rev. Mod. Phys.* **1988**, *60*, 781.
61. Fesser, K.; Bishop, A. R.; Campbell, D. K. *Phys. Rev. B* **1983**, *27*, 4804.
62. Brazovski, S. A.; Kirova, N. *JETP* **1981**, *33*, 4.
63. Roncali, J. *Chem. Rev.* **1992**, *92*, 711.
64. Genies, E. M.; Bidan, G.; Diaz, A. F. *J. Electroanal. Chem.* **1983**, *149*, 101.
65. Waltman, R. J.; Bargon, J.; Diaz, A. F. *J. Phys. Chem.* **1983**, *87*, 1459.
66. Wey, Y.; Jang, G.-W.; Chan, C.-C. *J. Polym. Sci., Part C: Polym. Lett.* **1990**, *28*, 219.
67. Wei, Y.; Chan, C. C.; Tiang, J.; Jang, G. W.; Hsueh, K. F. *Chem. Mater.* **1991**, *3*, 888.
68. Lyons, M. E. G. In *Electroactive Polymer Electrochemistry Part 1: Fundamentals*; Lyons, M. E. G., Ed.; Plenum: New York, 1994; Chapter 1.
69. Bredas, J. In *Handbook of Conducting Polymers*, 1st ed.; Skotheim, T. A., Ed.; Marcel Dekker: New York, 1986; Vol. 2, Chapter 25.
70. Bredas, J. L.; Scott, J. C.; Yakushi, K.; Street, G. B. *Phys. Rev. B* **1984**, *30*, 1023.
71. Holliday, B. J.; Swager, T. M. *Chem. Commun.* **2005**, 23.
72. Mathis, M.; Harsha, W.; Hanks, T. W.; Bailey, R. D.; Schimek, G. L.; Pennington, W. T. *Chem. Mater.* **1998**, *10*, 3568.
73. Gosden, C.; Healy, K. P.; Pletcher, D. *J. Chem. Soc., Dalton Trans.* **1978**, 972.
74. Gosden, C.; Pletcher, D. *J. Organomet. Chem.* **1980**, *186*, 401.
75. Gosden, C.; Kerr, J. B.; Pletcher, D.; Rosas, R. *J. Electroanal. Chem.* **1981**, *117*, 101.
76. Freire, C.; de Castro, B. *Inorg. Chem.* **1990**, *29*, 5113.
77. Freire, C.; de Castro, B. *J. Chem. Soc., Dalton Trans.* **1998**, 1491.
78. C. Freire; de Castro, B. *Polyhedron* **1998**, *17*, 4227.
79. Azevedo, F.; Carronto, M. A. A. F. C. T.; de Castro, B.; Convery, M.; Domingues, D.; Freire, C.; Duarte, M. T.; Nielsen, K.; Santos, I. C. *Inorg. Chim. Acta* **1994**, *219*, 43.

80. Carronto, M. A. A. F. C. T.; de Castro, B.; Coelho, A. M.; Domingues, D.; Freire, C.; Morais, J. *Inorg. Chim. Acta* **1993**, *205*, 157.
81. Santos, I. C.; Vilas-Boas, M.; Piedade, M. F. M.; Freire, C.; Duarte, M. T.; de Castro, B. *Polyhedron* **2000**, *19*, 655.
82. Goldsby, K. A. *J. Coord. Chem.* **1988**, *19*, 83.
83. Goldsby, K. A.; Blaho, J. K.; Hoferkamp, L. A. *Polyhedron* **1989**, *8*, 113.
84. Hoferkamp, L. A.; Goldsby, K. A. *Chem. Mater.* **1989**, *1*, 348.
85. Bedioui, F.; Labbe, E.; Gutierrez-Granados, S.; Devynck, J. *J. Electroanal. Chem.* **1991**, *301*, 267.
86. Audebert, P.; Capdevielle, P.; Maumy, M. *New J. Chem.* **1991**, *15*, 235.
87. Audebert, P.; Capdevielle, P.; Maumy, M. *Synth. Met.* **1991**, *43*, 3049.
88. Audebert, P.; Capdevielle, P.; Maumy, M. *New J. Chem.* **1992**, *16*, 697.
89. Audebert, P.; Hapiot, P.; Capdevielle, P.; Maumy, M. *J. Electroanal. Chem.* **1992**, *338*, 269.
90. Dahm, C. E.; Peters, D. G. *Anal. Chem.* **1994**, *66*, 3117.
91. Dahm, C. E.; Peters, D. G. *J. Electroanal. Chem.* **1996**, *406*, 119.
92. Dahm, C. E.; Peters, D. G.; Simonet, J. *J. Electroanal. Chem.* **1996**, *410*, 163.
93. Vilas-Boas, M.; Freire, C.; de Castro, B.; Christensen, P. A.; Hillman, A. R. *Inorg. Chem.* **1997**, *36*, 4919.
94. Vilas-Boas, M.; Freire, C.; de Castro, B.; Hillman, A. R. *J. Phys. Chem. B* **1998**, *102*, 8533.
95. Vilas-Boas, M.; Henderson, M. J.; Freire, C.; Hillman, A. R.; Vieil, E. *Chem. -Eur. J.* **2000**, *6*, 1160.
96. Vilas-Boas, M.; Freire, C.; de Castro, B.; Christensen, P. A.; Hillman, A. R. *Chem. -Eur. J.* **2001**, *7*, 139.
97. Vilas-Boas, M.; Pereira, E. M.; Freire, C.; Hillman, A. R. *J. Electroanal. Chem.* **2002**, *538-539*, 47.
98. Vilas-Boas, M.; Santos, I. C.; Henderson, M. J.; Freire, C.; Hillman, A. R.; Vieil, E. *Langmuir* **2003**, *19*, 7460.
99. Martins, M.; Freire, C.; Hillman, A. R. *Chem. Commun.* **2003**, 434.
100. Hamnett, A.; Abel, J.; Eameaim, J.; Christensen, P.; Timonov, A.; Vasilyeva, S. *Phys. Chem. Chem. Phys.* **1999**, *1*, 5147.

101. Vasilieva, S. V.; Tchepournaya, I. A.; Logvinov, S. A.; Gamankov, P. V.; Timonov, A. M. *Russ. J. Electrochem.* **2003**, *39*, 310.
102. Tchepournaya, I.; Vasilieva, S.; Logvinov, S.; Timonov, A.; Amadelli, R.; Bartak, D. *Langmuir* **2003**, *19*, 9005.
103. Losada, J.; del Peso, I.; Beyer, L. *J. Electroanal. Chem.* **1998**, *447*, 147.
104. Miomandre, F.; Audebert, P.; Maumy, M.; Uhl, L. *J. Electroanal. Chem.* **2001**, *516*, 66.
105. Voituriez, A.; Mellah, M.; Schulz, E. *Synth. Met.* **2006**, *156*, 166.
106. Pasc-Banu, A.; Sugisaki, C.; Gharsa, T.; Marty, J.-D.; Gascon, I.; Pozzi, G.; Quici, S.; Rico-Lattes, I.; Mingotaud, C., *Angew. Chem. Int. Ed.* **2004**, *43*, 6174.
107. Pasc-Banu, A.; Sugisaki, C.; Gharsa, T.; Marty, J.-D.; Gascon, I.; Kramer, M.; Pozzi, G.; Desbat, B.; Quici, S.; Rico-Lattes, I.; Mingotaud, C. *Chem. -Eur. J.* **2005**, *11*, 6032.
108. Buriez, O.; Moretto, L. M.; Ugo, P. *Electrochim. Acta* **2006**, *52*, 958.
109. Mao, L.; Tian, Y.; Shi, G.; Liu, H.; Jin, L.; Yamamoto, K.; Tao, S.; Jin, J. *Anal. Lett.* **1998**, *31*, 1991.
110. Mao, L.; Yamamoto, K.; Zhou, W.; Jin, L. *Electroanalysis* **2000**, *12*, 72.
111. Mitchell-Koch, J. T.; Borovik, A. S. *Chem. Mater.* **2003**, *15*, 3490.
112. Galbrecht, F.; Yang, X. H.; Nehls, B. S.; Neher, D.; Farrell, T.; Scherf, U. *Chem. Commun.* **2005**, 2378.
113. Cardoso, M. R.; Neves, U. M.; Misoguti, L.; Ye, Z.; Bu, X. R.; Mendonça, C.R. *Opt. Mater.* **2006**, *28*, 1118.
114. Sukwattanasinitt, M.; Nantalaksakul, A.; Potisatityuenyong, A.; Tuntulani, T.; Chailapakul, O.; Praphairakait, N. *Chem. Mater. Commun.* **2003**, *15*, 4337.
115. Seeger, K.; Gill, W. D.; Clarke, T. C.; Street, G. B. *Solid State Commun.* **1978**, *28*, 873.
116. Kwak, J. F.; Clarke, T. C.; Greene, R. L.; Street, G. B. *Solid State Commun.* **1979**, *31*, 355.
117. Elie, A. G.; Wallace, G. G.; Matsue, T. In *Handbook of Conducting Polymers*, 2nd ed.; Skotheim, T. A., Elsenbaumer, R. L., Reynolds, J. R., Eds.; Marcel Dekker: New York, 1998; p 963.
118. Bobacka, J.; Ivaska, A.; Lewenstam, A. *Electroanalysis* **2003**, *15*, 366.

119. Swager, T. M. *Acc. Chem. Res.* **1998**, *31*, 201.
120. Pedersen, C. J. *J. Am. Chem. Soc.* **1967**, *89*, 7017.
121. Pedersen, C. J. *J. Am. Chem. Soc.* **1967**, *89*, 2495.
122. Pedersen, C. J. *J. Am. Chem. Soc.* **1970**, *92*, 386.
123. Frensdorff, H. K. *J. Am. Chem. Soc.* **1971**, *93*, 600.
124. Christensen, J. J.; Eatough, D. J.; Izzat, R. M. *Chem. Rev.* **1974**, *74*, 351.
125. Izzat, R. M.; Bradshaw, J. S.; Nielsen, S. A.; Lamb, J. D.; Christensen, J. J.; Sen, D. *Chem. Rev.* **1985**, *85*, 271.
126. Izzat, R. M.; Pawlak, K.; Bradshaw, J. S.; Bruening, R. L. *Chem. Rev.* **1991**, *91*, 1721.
127. Christensen, J. J.; Hill, J. O.; Izzat, R. M. *Science* **1971**, *174*, 459.
128. Poonia, N. S.; Bajaj, A. V. *Chem. Rev.* **1979**, *79*, 389.
129. Steinberg, S.; Tor, Y.; Sabatani, E.; Rubinstein, I. *J. Am. Chem. Soc.* **1991**, *113*, 5176.
130. Steinberg, S.; Rubinstein, I. *Langmuir* **1992**, *8*, 1183.
131. Arias, F.; Godinez, L. A.; Wilson, S. R.; Kaifer, A. E.; Echegoyen, L. *J. Am. Chem. Soc.* **1996**, *118*, 6086.
132. Moore, A. J.; Goldenberg, L. M.; Bryce, M. R.; Petty, M. C.; Moloney, J.; Howard, J. A. K.; Joyce, M. J.; Port, S. N. *J. Org. Chem.* **2000**, *65*, 8269.
133. Zhang, S.; Cardona, C. M.; Echegoyen, L. *Chem. Comm.* **2006**, 4461.
134. Nagase, S.; Kataoka, M.; Naganawa, R.; Komatsu, R.; Odashima, K.; Umezawa, Y. *Anal. Chem.* **1990**, *62*, 1252.
135. Wang, S.; Leblanc, R. M.; Arias, F.; Echegoyen, L. *Langmuir* **1997**, *13*, 1672.
136. Goldenberg, L. M.; Biernat, J. F.; Petty, M. C. *Langmuir* **1998**, *14*, 1236.
137. McQuade, D. T.; Pullen, A. E.; Swager, T. M. *Chem. Rev.* **2000**, *100*, 2537.
138. Fabre, B.; Simonet, J. *Coord. Chem. Rev.* **1998**, *178-180*, 1211.
139. Roncali, J.; Garreau, R.; Delabouglise, D.; Garnier, F.; Lemaire, M., *J. Chem. Soc., Chem. Commun.* **1989**, 679.
140. Shi, L. H.; Garnier, F.; Roncali, J. *Synth. Met.* **1991**, *41*, 547.
141. Roncali, J.; Shi, L. H.; Garnier, F. *J. Phys. Chem.* **1991**, *95*, 8983.
142. Shi, L. H.; Garnier, F.; Roncali, J. *Solid State Commun.* **1991**, *77*, 811.

143. Lemaire, M.; Garreau, R.; Roncali, J.; Delabougliise, D.; Youssoufi, H. K.; Garnier, F. *New J. Chem.* **1989**, *13*, 863.
144. Bartlett, P. N.; Benniston, A. C.; Chung, L.-Y.; Dawson, D. H.; Moore, P. *Electrochim. Acta* **1991**, *36*, 1377.
145. Bauerle, P.; Scheib, S. *Adv. Mater.* **1993**, *5*, 848.
146. Bauerle, P.; Gotz, G.; Hiller, M.; Scheib, S.; Fisher, T.; Segelbacher, U.; Bennati, M.; Grupp, A.; Mehring, M.; Stoldt, M.; Seidel, C.; Geiger, F.; Schweizer, H.; Umbach, E.; Schmelzer, M.; Roth, S.; Egelhaaf, H. J.; Oelkrug, D.; Emele, P.; Port, H. *Synth. Met.* **1993**, *61*, 71.
147. Bradshaw, J. S.; Izzat, R. M.; Bordunov, A. V.; Zhu, C. Y.; Hathaway, J. K. In *Comprehensive Supramolecular Chemistry*; Pergamon: Oxford, 1996; Vol. 1, Chapter 2.
148. Bauerle, P.; Scheib, S. *Acta Polym.* **1995**, *46*, 124.
149. Rimmel, G.; Bauerle, P. *Synth. Met.* **1999**, *102*, 1323.
150. Scheib, S.; Bauerle, P. *J. Mater. Chem.* **1999**, *9*, 2139.
151. Sanniccolo, F.; Brenna, E.; Benincori, T.; Zotti, G.; Zecchin, S.; Schiavon, G.; Pilati, T. *Chem. Mater.* **1998**, *10*, 2167.
152. Fabre, B.; Marrec, P.; Simonet, J. *J. Electroanal. Chem.* **2000**, *485*, 94.
153. Si, P.; Chi, Q.; Li, Z.; Ulstrup, J.; Moller, P. J.; Mortensen, J. *J. Am. Chem. Soc.* **2007**, *129*, 3888.
154. Youssoufi, H. K.; Hmyene, M.; Garnier, F.; Delabougliise, D. *J. Chem. Soc., Chem. Commun.* **1993**, 1550.
155. Youssoufi, H. K.; Yassar, A.; Baiteche, S.; Hmyene, M.; Garnier, F. *Synth. Met.* **1994**, *67*, 251.
156. Garnier, F.; Youssoufi, H. K.; Hmyene, M.; Yassar, A. *Polym. Prepr.* **1994**, *35*, 205.
157. Pernaut, J.-M.; Zong, K.; Reynolds, J. R. *Synth. Met.* **2002**, *130*, 1.
158. Swager, T. M.; Marsella, M. J. *Adv. Mater.* **1994**, *6*, 595.
159. Marsella, M. J.; Swager, T. M. *J. Am. Chem. Soc.* **1993**, *115*, 12214.
160. Swager, T. M.; Marsella, M. J.; Bicknell, L. K.; Zhou, Q. *Polym. Prepr.* **1994**, *35*, 206.
161. Marsella, M. J.; Swager, T. M. *Polym. Prepr.* **1994**, *35*, 271.
162. Marsella, M. J.; Newland, R. J.; Swager, T. M. *Polym. Prepr.* **1995**, *36*, 594.



163. Faid, K.; Frechette, M.; Ranger, M.; Mazerolle, L.; Levesque, I.; Leclerc, M.; Chen, T.-A.; Rieke, R. D. *Chem. Mater.* **1995**, 7, 1390.
164. Levesque, I.; Leclerc, M. *J. Chem. Soc., Chem. Commun.* **1995**, 2293.
165. Levesque, I.; Leclerc, M. *Chem. Mater.* **1996**, 8, 2843.
166. Levesque, I.; Leclerc, M. *Synth. Met.* **1997**, 84, 203.
167. Boldea, A.; Levesque, I.; Leclerc, M. *J. Mater. Chem.* **1999**, 9, 2133.
168. Kim, J.; McQuade, D. T.; McHugh, S. K.; Swager, T. M. *Angew. Chem. Int. Ed.* **2000**, 39, 3868.
169. Chen, Z.; Xue, C.; Shi, W.; Luo, F.-T.; Green, S.; Chen, J.; Liu, H. *Anal. Chem.* **2004**, 76, 6513.
170. Ion, A.; Ion, I.; Popescu, A.; Ungureanu, M.; Moutet, J.-C.; Saint-Aman, E. *Adv. Mater.* **1997**, 9, 711.
171. Reddinger, J. L.; Reynolds, J. R. *Chem. Mater.* **1998**, 10, 3.
172. Tarabek, J.; Rapta, P.; Jahne, E.; Ferse, D.; Adler, H.-J.; Maumy, M.; Dunsch, L. *Electrochim. Acta* **2005**, 50, 1643.
173. Martins, M.; Vilas-Boas, M.; de Castro, B.; Hillman, A. R.; Freire, C. *Electrochim. Acta* **2005**, 51, 304.

# Chapter 2

## *TECHNIQUES*

## 2.1 ELECTROCHEMICAL METHODS

### 2.1.1 Cyclic voltammetry (CV)

The electrochemical behaviour of a system can be fully described using three-dimensional  $i$ - $t$ - $E$  surfaces<sup>1</sup>. One way to accomplish this is by using voltammetric techniques where the current  $i$  is recorded as a function of time  $t$ , as the applied potential  $E$  is controlled and linearly varied<sup>2</sup>. The way in which  $E$  is varied defines the type of voltammetry (Figure 2.1): when  $E$  is varied linearly the experiment is designated as *linear sweep voltammetry* (LSV); if  $E$  is a triangular, symmetrical waveform the experiment is termed *cyclic voltammetry* (CV). The plot of  $i$  vs.  $E$  is a voltammogram.

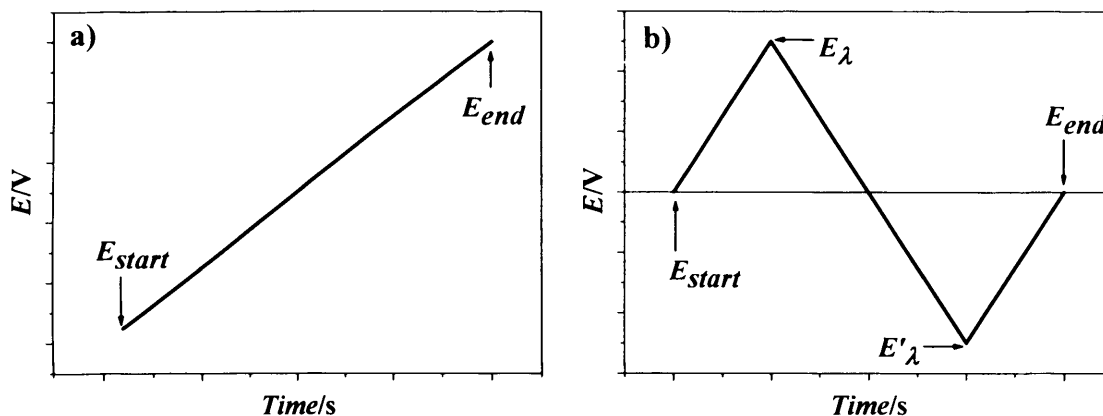


**Figure 2.1:** Excitation signals for potential scan voltammetry: a) linear sweep and b) cyclic voltammetries<sup>2</sup>.

In a cyclic voltammetric experiment the applied potential is swept from a starting potential  $E_{start}$  at a scan rate  $v = dE/dt$  until reaching the so-called ‘switching’ potential  $E_{\lambda}$ . At this point the potential is swept in opposite direction (scan rate  $-v$ ) until either a second switching potential  $E'_{\lambda}$  or a potential value  $E_{end}$  corresponding to the end of the experiment is attained ( $E_{end}$  may or may not coincide with  $E_{start}$ ).

Consider a system characterised by a reversible reaction involving the  $Ox/Re$  couple, whose voltammogram is depicted in Figure 2.2. The potential cycle starts from a value negative with respect to  $E^{0'}$ . Here only nonfaradaic currents flow. When the potential reaches the vicinity of  $E^{0'}$ , oxidation begins and faradaic current starts to flow. As the potential continues to increase, the current increases exponentially until a point where concentration of  $Re$  decays nearly to zero; then, mass transfer of  $Re$  species from the bulk solution to the electrode surface starts to be slower than the rate of consumption, and the

voltammetric response is governed by diffusion. Reversing the potential, similar behaviour can be observed with *Ox* species predominating near the surface electrode. This description is actually rather simplistic, since several factors may affect the electrode reaction rate and current, such as: (i) mass transfer of species between the bulk solution and the electrode surface, (ii) rate of electron transfer at the electrode surface, (iii) chemical reactions (homogenous/heterogeneous) preceding or following the electron transfer and (iv) other surface processes such as adsorption/desorption and electrodeposition.

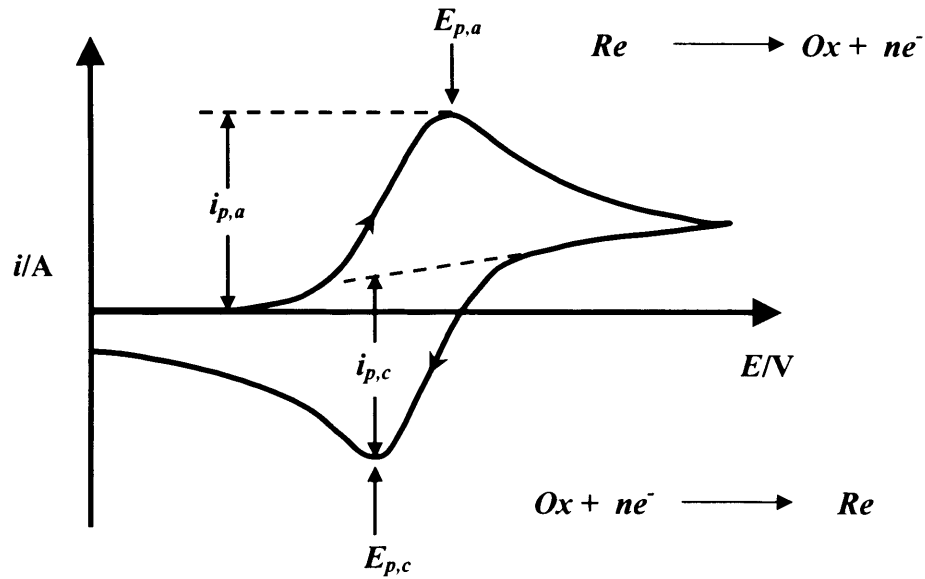


**Figure 2.2:** Typical cyclic voltammogram.

#### 2.1.1.1 Mass-transfer-controlled reactions at planar electrodes

Mass transfer may occur as a result of differences in electrical or chemical potentials between two regions, or by movement of a volume element of solution<sup>3</sup>. The modes of mass transfer are *migration* (electrical potential gradient), *diffusion* (concentration gradient) and *convection*.

Mass transfer to an electrode is given by the Nernst-Planck equation, which for one-dimension (as for planar electrodes), is given by:

$$J_i(x) = -D_i \frac{\partial C_i(x)}{\partial x} - \frac{z_i F}{RT} D_i C_i \frac{\partial \phi(x)}{\partial x} + C_i v(x) \quad (2.1)$$

where  $J_i(x)$  is the flux of species  $i$  ( $\text{mol s}^{-1} \text{cm}^{-2}$ ) at distance  $x$  from the surface,  $D_i$  is the diffusion coefficient ( $\text{cm}^2 \text{s}^{-1}$ ),  $\partial C_i(x)/\partial x$  is the concentration gradient at distance  $x$ ,  $\partial \phi/\partial x$  is the potential gradient,  $z_i$  and  $C_i$  are the charge and concentration ( $\text{mol cm}^{-3}$ ) of species  $i$ , and  $v(x)$  is the velocity ( $\text{cm s}^{-1}$ ) with which a volume element in solution moves along the axis.

### *Diffusion controlled reactions*

For a system without stirring and in the presence of supporting electrolyte, the effects of convection and migration are negligible and mass-transfer is restricted to diffusion. In these conditions, Fick's laws of diffusion can be used to describe the flux of a substance and its concentration as a function of time and position. *Fick's first law* states that the flux of a species  $i$  is proportional to the concentration gradient  $\partial C_i/\partial x$ :

$$-J_i(x,t) = D_i \frac{\partial C_i(x,t)}{\partial x} \quad (2.2)$$

Taking the space derivative of Equation 2.2 yields *Fick's second law*:

$$-\frac{\partial J_i(x,t)}{\partial x} = \frac{\partial C_i(x,t)}{\partial t} = D_i \left( \frac{\partial^2 C_i(x,t)}{\partial x^2} \right) \quad (2.3)$$

Consider an experiment involving an instantaneous change in potential from a value where no electrolysis occurs to a value in the mass-transfer controlled region, due to the application of a large-amplitude potential step. In a system where only  $Ox$  species are initially present, the reaction  $Ox + ne^- \rightarrow Re$  will occur, regardless of whether the kinetics of the process are facile or sluggish, so that the concentration of  $Ox$  at the electrode surface will become effectively zero. In these conditions the diffusion limited current  $i_d$  can be derived solving the linear diffusion equation (Equation 2.3) together with the boundary conditions:

$$\text{i) Initial condition: } C_{Ox}(x,0) = C_{Ox}^* \quad (2.4)$$

$$\text{ii) Semi-infinite condition: } \lim_{x \rightarrow \infty} C_{Ox}(x,t) = C_{Ox}^* \quad (2.5)$$

$$\text{iii) } C_{Ox}(0,t) = 0 \text{ (for } t > 0) \quad (2.6)$$

The current-time response is given by Equation 2.7, known as the *Cottrell equation*:

$$i(t) = i_d(t) = \frac{nFAD_{Ox}^{1/2} C_{Ox}^*}{\pi^{1/2} t^{1/2}} \quad (2.7)$$

where  $F$  is the Faraday constant,  $A$  is the electrode area, and  $C_{Ox}^*$  is the bulk concentration of  $Ox$ . This equation shows that the diffusion limited current is a function of  $t^{-1/2}$ .

### 2.1.1.2 Different contributions for the measured current

The measured current results from the combination of (i) *faradaic current*  $i_f$ , associated with the system under the study (due to the electrode reaction occurring at the working electrode); (ii) *residual currents*, arising due to the presence of  $O_2$  not conveniently removed and/or the presence of impurities in the solvent/background electrolyte; (iii) *non-faradaic current*  $i_c$ , capacitive contribution of the double layer charging at the electrode/solution interface.

For a system where no residual currents flow, the total current is given by:

$$i = i_f + i_c = i_f + C_d \frac{dE}{dt} = i_f + \nu C_d \quad (2.8)$$

where  $C_d$  is the capacitance associated with the double layer charging and  $\nu$  is the scan rate. Equation 2.8 shows that the contribution of double layer charging increases linearly with the scan rate.

#### *Double layer charging and solution resistance*

The electric response of a cell consisting of an *ideal polarized electrode* (IPE) and a reversible electrode (reference electrode) can be explained in terms of electrical components as a series  $RC$  circuit, in which  $R_s$  is the solution resistance and  $C_d$  the double layer capacitance. When a voltage ramp or linear potential sweep  $E$  is applied to the  $R_s C_d$  circuit, the voltage of the system is given by:

$$E = E_{start} + \nu t = R_s \frac{dQ}{dt} + \frac{Q}{C_d} \quad (2.9)$$

where  $\nu$  is the scan rate,  $i = dQ/dt$  is the current passing through the system and  $Q/C_d$  the voltage associated with the capacitor  $C_d$ . The solution of this differential equation for  $Q=0$  at  $t=0$  is:

$$i = \nu C_d + \left[ \left( \frac{E_{start}}{R_s} - \nu C_d \right) \exp(-t / R_s C_d) \right] \quad (2.10)$$

This expression contains two terms, the first constant over time and the second corresponding to a transient current which can be neglected after an interval of time  $\tau = R_s C_d$ .

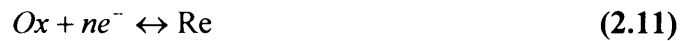
### 2.1.1.3 Cyclic voltammetry at planar electrodes

#### (i) Solution species

Potential  $E$  plays a decisive role in the response of the system: not only does it provide the driving force for the electrochemical reactions to occur ( $\Delta G = -nFE$ ), but also the activation/kinetic parameters show an Arrhenius-like dependence on  $E$ . Depending on the experimental timescales, thermodynamic or kinetic features may define the shape of the  $i$ - $E$  curve. The characterisation of different types of electrochemical responses is presented below.

#### *Nernstian (Reversible) systems*

A reversible system is one in which the kinetics of the  $Ox/Re$  couple are rapid, so the  $|C_{Ox}|/|C_{Re}|$  ratio is given by the *Nernst equation* (Equation 2.12) at all times/potentials (assuming semi-infinite linear diffusion, Equations 2.13 and 2.14)<sup>1</sup>:



$$E = E^0 + \frac{RT}{nF} \ln \frac{|C_{Ox}|}{|C_{Re}|} \quad (2.12)$$

$$\frac{\partial C_{Ox}(x,t)}{\partial t} = D_{Ox} \frac{\partial^2 C_{Ox}(x,t)}{\partial x^2} \quad (2.13) \quad \frac{\partial C_{Re}(x,t)}{\partial t} = D_{Re} \frac{\partial^2 C_{Re}(x,t)}{\partial x^2} \quad (2.14)$$

These equations, together with the boundary conditions, enable the determination of the current variation:

$$i = nFAC_{Ox} * (\pi D_{Ox} \sigma)^{1/2} \chi(\sigma t) \quad (2.15)$$

where  $\sigma = \frac{nFv}{RT}$ . At any given point  $\chi(\sigma t)$  is a pure number<sup>4-10</sup>, so that Equation 2.15 gives the functional relationship between the current and the other variables ( $\chi(\sigma t)$  is the normalised current). The function  $\pi^{1/2} \chi(\sigma t)$ , and consequently the current, reaches a maximum at  $\pi^{1/2} \chi(\sigma t) = 0.4463$ . The resulting equation:

$$i_p = 0.4463 nFAC_{Ox} \left( \frac{nF}{RT} \right)^{1/2} D_{Ox}^{1/2} v^{1/2} \quad (2.16)$$

is known as the *Randles-Sevcik equation*<sup>11</sup>. According to this expression, the peak current  $i_p$  is proportional to  $v^{1/2}$ . At 25 °C, for  $A$  in  $\text{cm}^2$ ,  $D_{Ox}$  in  $\text{cm}^2 \text{ s}^{-1}$ ,  $C_{Ox}^*$  in  $\text{mol cm}^{-3}$  and  $v$  in  $\text{V s}^{-1}$ , the current peak  $i_p$  in amperes is:

$$i_p = (2.69 \times 10^5) n^{3/2} A C_{Ox}^* D_{Ox}^{1/2} v^{1/2} \quad (2.17)$$

The potential at which  $i_p$  occurs is independent of the scan rate and is given by:

$$E_p = E^0 - \frac{RT}{nF} \left[ \ln \left( \frac{D_{Ox}}{D_{Re}} \right)^{1/2} + 1.109 \right] \quad (2.18)$$

### *Totally irreversible systems*

When the reaction is kinetically slow in one direction, it is described as “irreversible” and the Nernst equation no longer applies. The boundary equation for a one-step, one-electron reaction  $Ox + e^- \xrightarrow{k_{ox}} Re$  is given by:

$$\frac{i}{FA} = D_{Ox} \left[ \frac{\partial C_{Ox}(x,t)}{\partial x} \right]_{x=0} = k_{Ox}(t) C_{Ox}(0,t) \quad (2.19)$$

In this case  $E_p$  changes with the scan rate and the current is given by:

$$i = F A C_{Ox}^* (\pi D_{Ox} b)^{1/2} \chi(bt) \quad \text{or by:} \quad (2.20)$$

$$i = F A C_{Ox}^* (\pi D_{Ox} b)^{1/2} \chi(bt)$$

where  $b = \alpha f v = \alpha \frac{Fv}{RT}$ ,  $\alpha$  is the transfer coefficient, and  $\chi(bt)$  is a mathematical function (different from  $\chi(\sigma t)$ ) describing the normalised current for a totally irreversible system.

### *Quasi-reversible systems*

There are systems characterised by moderately fast kinetics, but insufficiently so to maintain the equilibrium. The treatment of these systems was described for the first time by Matsuda and Ayabe<sup>7</sup>. In this case the boundary condition is given by:

$$D_{Ox} \left[ \frac{\partial C_{Ox}(x,t)}{\partial x} \right]_{x=0} = k^0 e^{-\alpha f [E(t) - E^0]} \left[ C_{Ox}(0,t) - C_{Re}(0,t) e^{f [E(t) - E^0]} \right] \quad (2.21)$$

where  $k^0$  is the standard rate constant. This intermediate behaviour depends on the scan rate, with the system switching between Nernstian (slow scan rates) and totally irreversible (high scan rates) behaviours.



## (ii) Surface immobilised species

### Monolayers

The systems described in the previous section involve redox reactions between reactants and products that are both soluble in solution. When only the adsorbed forms of *Ox* and/or *Re* are electroactive, and the reaction is Nernstian, the voltammetric peaks are sharp and symmetrical (Figure 2.3). The current rises from zero to a maximum value, and falls again to zero; the difference of potential between the cathodic and anodic peaks is negligible. The values of  $i_p$ ,  $E_p$  and the peak width depend on the isotherms involved.

For a system (monolayer) whose processes are described by the Langmuir isotherm,  $E_{pa} = E_{pc}$  and  $i_{pa} = -i_{pc}$ . The peak current is given by<sup>12</sup>:

$$i_p = \frac{n^2 F^2 A \Gamma}{4RT} v \quad (2.22)$$

In this case the peak current is linearly related to the scan rate (in the case of soluble species  $i_p$  is proportional to  $v^{1/2}$ ).  $\Gamma$  is the surface coverage, and is determined by measuring the area ( $\propto Q$ ) under the peak:

$$\Gamma = \frac{Q}{nFA} \quad (2.23)$$

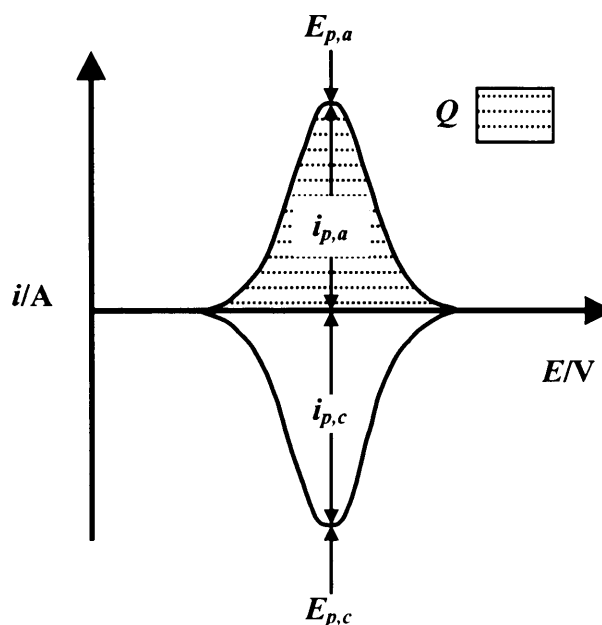


**Figure 2.3:** Voltammogram for a system characterised by the Langmuir Isotherm.

### *Multi-layer systems*

In the case of multi-layer modified electrodes more complex theoretical models have to be used. Kinetics and mass transport occurring *within* the film must also be considered.

Consider a uniform film (both in composition and thickness) exhibiting diffusional charge transport. If the rate of charge transport is faster than the experimental timescale, the film will be uniformly oxidised/reduced, and thus in thermodynamic equilibrium with the applied potential. In this case, the cyclic voltammograms will have a symmetrical shape. However, if the rate of charge transport is slower than the experimental timescale, there is no uniformity in oxidation/reduction current responses. A diffusional-type response occurs, and the rate-limiting step is the flux of species in the film<sup>13-15</sup>. The predominating regime can be determined by recording *i*-*E* curves at different scan rates: for fast diffusion of electrolyte species within the film, the current changes linearly with the scan rate  $\nu$  (this trend is usually found for thin films - [Equation 2.22](#)); if mass transport along the film is the limiting step, the current changes linearly with  $\nu^{1/2}$ , and according to the Randles-Sevcik equation<sup>11</sup> the diffusion coefficient can be estimated.

#### **2.1.1.4 Experimental**

The electrochemical cell commonly used in voltammetric experiments consists of a sealed vessel to prevent contact between air and solution, and a tube connected to the cell that allows saturation of solution with an inert gas (N<sub>2</sub> or Ar)<sup>16</sup>. Inert gas bubbling removes O<sub>2</sub> to prevent currents that may arise due to its reduction. The cell has a standard cell configuration ([Figure 2.4](#)) with three electrodes immersed in electrolyte solution: the working electrode (WE) where the redox processes associated with the system occur, the counter electrode (CE) that is important to the flow of current in the system and the reference electrode (RE). The WE potential is controlled with respect to RE *via* a potentiostat. A waveform generator imposes the desired waveform at WE, and the current flowing between WE and CE is measured as the potential drop  $V$  across a resistor, which is connected in series with the two electrodes. The *i* vs. *E* curve is then acquired; the system is controlled by a computer.

Application of voltammetric techniques to real systems is limited by several factors: oxidation or reduction of the electrolyte, working electrode or impurities present in the electrolyte<sup>2</sup>. Together, these factors determine the *potential window*, the potential range

where only redox reactions associated with the analyte under study may occur. Additionally, the starting potential must be selected in a region where no current flows. This potential can be determined by measuring the potential of the open circuit ( $i=0$ ). The analyte must be homogeneously distributed in the electrolyte in order to ensure that distortion of voltammetric response does not occur due to diffusive phenomena. The choice of the switching potential influences the peaks occurring in the reverse half-scan, but there is no general trend to be followed.

In organic solvents and at high scan rates,  $iR$  drop and double layer effects have to be considered. The use of electrodes with small areas can be used to minimise the  $iR$  drop and background subtraction may be used to remove double layer effects from the voltammogram.

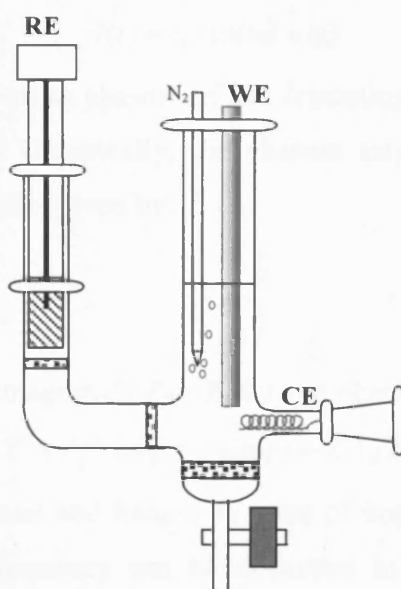


**Figure 2.4:** Three electrode cell configuration.

### 2.1.2 Electrochemical Impedance Spectroscopy (EIS)

The techniques presented in previous sections involve a large perturbation that drives the system far from equilibrium<sup>17,18</sup>. Another approach is the application of a very small perturbation (alternating voltage signals of small magnitude) and thus observation of the system near steady state conditions. This approach yields high-precision data since it is possible to average the response over long periods of time. It also allows measurement of the system characteristics over a wide range of frequencies (timescales) -  $10^{-4}$  to  $10^6$  Hz. The small perturbation amplitude allows one to theoretically treat the response by

linearized current-potential characteristics. Working in conditions close to equilibrium precludes the need for detailed knowledge of the  $i$ - $E$  curve over wide intervals of potential, thereby simplifying issues associated with kinetics and diffusion.

### 2.1.2.1 Theory

In electrochemical impedance spectroscopy the cell impedance is measured as a function of frequency for a sinusoidal voltage  $E(t)$ :

$$E(t) = E_0 \sin \omega t \quad (2.24)$$

where  $E_0$  is the voltage amplitude and  $\omega$  the angular frequency  $2\pi f$ , with  $f$  the frequency. The current  $i(t)$  (response to the perturbation) is a sinusoidal signal with the same frequency  $f$ , amplitude  $i_0$  and displaced with respect to  $E(t)$  by a phase shift  $\varphi$ :

$$i(t) = i_0 \sin(\omega t + \varphi) \quad (2.25)$$

These signals can be depicted as phasors ( $\vec{E}$  and  $\vec{I}$ ) rotating at the same frequency and separated by a phase angle  $\varphi$ . Generically, the phasors may have real and imaginary components, and the impedance  $Z$  is given by:

$$Z = \frac{\vec{E}}{\vec{I}} \quad (2.26)$$

$Z$  is a complex quantity of magnitude  $Z_0 = (E_0/i_0)$  and phase  $\varphi$ :

$$Z = Z_0(\cos \varphi + j \sin \varphi) = Z' + jZ'' \quad (2.27)$$

with  $j = \sqrt{-1}$ , and  $Z'$  and  $Z''$  the real and imaginary parts of impedance, respectively. The variation of impedance with frequency can be displayed in several ways, namely by plotting  $\log|Z|$  and  $\varphi$  vs.  $\log \omega$  (*Bode plot*), or by plotting  $-Z''$  vs.  $Z'$  (*Nyquist plot*).

#### *Impedance response of a pure resistor, $R$*

Application of a sinusoidal voltage to a pure resistor of value  $R$ , results in an impedance with  $Z_0 = R$  and  $\varphi = 0$ , i.e.,  $Z = Z' = R$ . In the Nyquist plot  $R$  is a point which intersects the  $Z'$  axis ([Figure 2.5a](#)).

#### *Impedance of a pure capacitor, $C$*

The impedance of a pure capacitor of capacitance  $C$  to which a sinusoidal voltage was applied is given by:

$$Z = -\frac{j}{\omega C} \quad (2.28)$$

where  $Z_0 = \frac{1}{\omega C}$  and  $\varphi = -\pi/2$ . The impedance of a pure capacitor is a function of frequency and only has an imaginary term (Figure 2.5b).

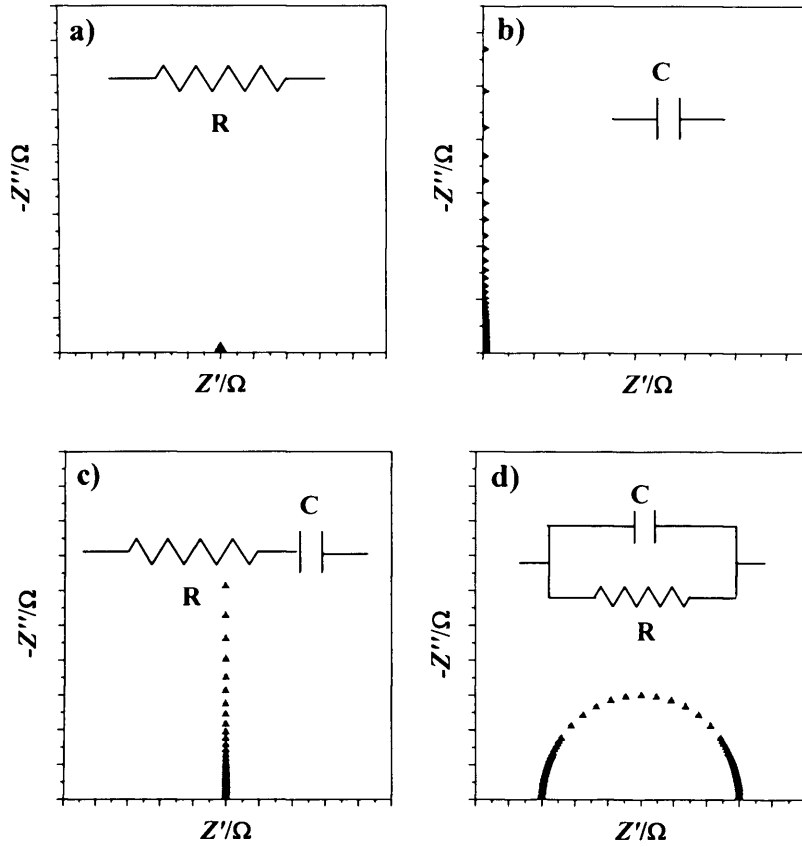


**Figure 2.5:** Nyquist plots for different equivalent circuits.

#### *Impedance of R and C in series*

The impedance of a system composed by  $R$  and  $C$  in series equals the sum of the impedance associated with the individual components:

$$Z = R - \frac{j}{\omega C} \quad (2.29)$$

with  $Z_0 = \sqrt{\left(R^2 + \frac{1}{\omega^2 C^2}\right)}$  and  $\varphi = \arctan\left(-\frac{1}{R\omega C}\right)$ . In the Nyquist plot, it is depicted as a vertical line intersecting the  $Z'$  axis at  $Z'=R$  (Figure 2.5c).

### Impedance of $R$ and $C$ in parallel

For a system composed by  $R$  and  $C$  in parallel, the inverse of the impedance equals the sum of the inverse of each individual component:

$$\frac{1}{Z} = \frac{1}{R} - \frac{\omega C}{j} \text{ or } Z = \left( \frac{1}{R} - \frac{\omega C}{j} \right)^{-1} \quad (2.30)$$

with  $Z_0 = \left( \frac{1}{R^2} + \omega^2 C^2 \right)^{-1/2}$  and  $\varphi = \arctan(-R\omega C)$ . In the complex plane diagram the impedance of this system shows the shape of a semicircle (Figure 2.5d)

#### 2.1.2.2 Equivalent circuit of a cell

The electrochemical cell can be represented by an impedance for small sinusoidal excitations. Consequently, its response may be represented in terms of *equivalent circuits* of capacitors and resistors that mimic the real cell. Figure 2.6 depicts an equivalent circuit often used, the *Randles equivalent circuit*<sup>19</sup>, which accounts for capacitive or charging current  $i_c$ , and faradaic current  $i_f$ .

The double layer capacitance is nearly a pure capacitance, here represented by the element  $C_{DL}$ . The faradaic process is depicted by a general element  $Z_f$ .  $R_\Omega$  represents the solution resistance through which all the current must pass.

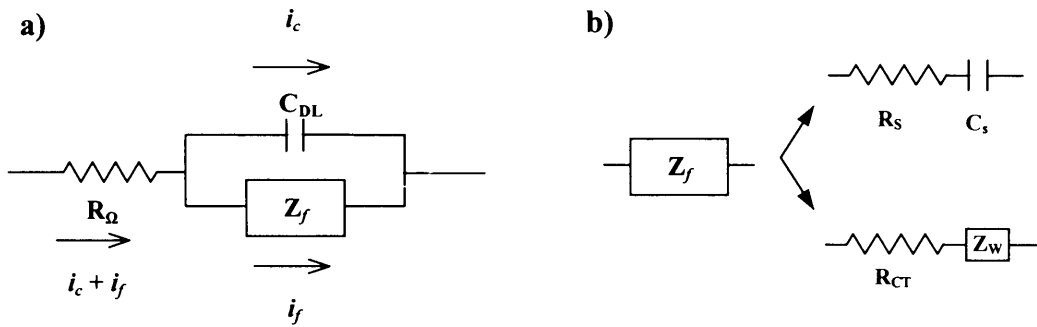


**Figure 2.6:** a) Randles equivalent circuit and b) approximations used for  $Z_f$ .

The simplification of the faradaic element  $Z_f$  has been considered in different ways. In some cases,  $Z_f$  is assumed as a series combination of a resistance  $R_s$  and a pseudocapacitance  $C_s$  (low frequencies). The alternative is to separate  $Z_f$  into a pure resistance  $R_{CT}$  in series with another general element  $Z_w$ , called the *Warburg element*<sup>20</sup> (high frequencies).  $R_{CT}$  is associated with charge-transfer resistance, whilst  $Z_w$  accounts

for resistance associated with mass transfer. Although  $C_{DL}$  and  $R_Q$  are nearly ideal elements, the same is not true for  $Z_f$ , which is a function of the frequency. Therefore, a given equivalent circuit that represents the system at a specific frequency may not be the best choice for all the frequencies.

AC-impedance measurements performed at different frequencies can be used to identify different circuit components. For instance, at very high frequencies the impedance associated with double layer capacitance becomes very small and the impedance of the system is basically given by  $R_Q$ . In the Nyquist diagram this corresponds to the intersection of the semicircle with the real axis, as presented in [Figure 2.7](#). The decrease of frequency results in an increase of the impedance associated with  $C_{DL}$ . At sufficiently low frequencies, the impedance of  $C_{DL}$  becomes larger than  $R_{CT}$ , and the impedance of the system is given by the sum of  $R_Q$  with  $R_{CT}$ ;  $R_{CT}$  is the diameter of the semicircle. The frequency at the top of the semicircle is given by:

$$\omega_{\max} = \frac{1}{R_{CT}C_{DL}} \quad (2.31)$$

where  $\tau = R_{CT}C_{DL}$  is the time constant for the faradaic process.

The Warburg impedance  $Z_W$  is associated with faradaic processes and related to mass transfer/diffusion phenomena. Consider a system where a simple charge-transfer reaction occurs ([Equation 2.11](#)), and both species are present in solution with bulk concentrations  $C_{Ox}^*$  and  $C_{Re}^*$ . Assuming semi-infinite linear diffusion ([Equations 2.13 and 2.14](#)), the Warburg impedance is given by<sup>17,18</sup>:

$$Z_W = \frac{\sigma}{\omega^{1/2}} - j \frac{\sigma}{\omega^{1/2}} \quad (2.32)$$

where  $\sigma = \frac{RT}{n^2 F^2 A \sqrt{2}} \left( \frac{1}{D_{Ox}^{1/2} C_{Ox}^*} + \frac{1}{D_{Re}^{1/2} C_{Re}^*} \right)$ . Since the  $Z_W' = -Z_W''$ , the Warburg element in a Nyquist plot is depicted by a straight line with phase angle of 45°.

This simple approach can be used to estimate the double layer capacitance, as well as charge transfer resistance or even determine whether the response is diffusion controlled. On the other hand, the use of commercial software packages for fitting AC-impedance data is a more accurate method for determination of values for the equivalent circuit elements, but requires very good estimates of the initial parameters.

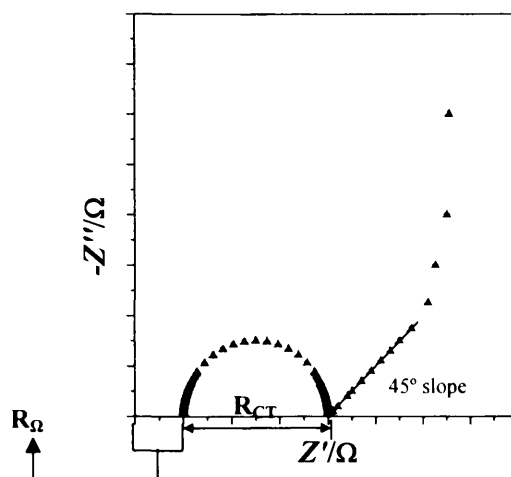


**Figure 2.7:** Nyquist plot for a simple electrochemical cell.

### 2.1.2.3 Instrumentation

Impedance test equipment usually comprises an AC measurement unit and a potentiostat or galvanostat<sup>18</sup>. The potentiostat is important when the system under study possesses high impedance, due to its high-input impedance and good current sensitivity.

The techniques commonly used in AC measurements can be divided into two main groups: single-sine (measurement at fixed frequency) and multiple-sine techniques (measurement at different frequencies simultaneously). The latter are used to reduce the effects of systems changing during the measurement.

*Frequency response analysis* is a single-sine technique widely used for impedance testing; it enables the extraction of small signals from a very high background of noise, rejecting DC and harmonic responses. The frequency response analyser (FRA) has a sine wave generator which outputs a voltage signal of small-amplitude to the system under study. The response signals are then fed into input channels, digitized and then integrated over several cycles in order to reject noise. These response signals are usually the voltage measured between two reference points in the electrochemical cell and a voltage signal proportional to the current flowing through the cell.



## 2.2 SPECTROSCOPIC METHODS

UV-Vis spectroelectrochemistry enables the establishment of a bridge between the intrinsic electronic properties of materials and how they are mirrored in the electrochemical features of the system.

Consider the system  $Ox/Re$  couple, involving the reaction  $Re \rightarrow Ox + ne^-$ . If  $Ox$  is the only chromophore at the probing wavelength, absorbance  $A_{Ox}$  arising due to this species will be the sum of all the absorbances  $dA_{Ox}$  over small distances  $dx$  in the optical path  $x$ . Therefore,  $A_{Ox}$  is:

$$A_{Ox}(\lambda) = A_t(\lambda) = \varepsilon(\lambda) \int_0^{\infty} |Ox|_{x,t} dx \quad (2.33)$$

The integral represents the total amount of  $Ox$  present per unit of area at time  $t$ , *i.e.*  $\Gamma$ . Equation 2.33 can be written as:

$$A_t(\lambda) = \varepsilon(\lambda)\Gamma = \varepsilon(\lambda) \frac{Q}{nFA} \quad (2.34)$$

Experimentally, there are different modes for collection of spectral data, the most simple and widely employed being transmission mode. The radiation beam is passed through the working electrode and changes in the beam intensity due to depletion/generation of chromophores are measured directly. Transmission mode implies the use of *optically transparent electrodes* (OTE's), which can be divided into three classes: (i) metal minigrids, (ii) thin coatings of semiconductors or metal on glass and (iii) reticulated vitreous carbon<sup>21</sup>. Minigrids are made of Pt, Au, Ag and comprise several hundred wires per centimetre. These electrodes allow transmittance of the incident light up to 80 % and can be used in both UV-Vis and IR cells. A disadvantage is the limitation in time to acquire spectral data: the diffusion layers around each wire must overlap for the minigrid to behave like a planar electrode. Thin layers of metals or carbon may result in planar surfaces. However, there is a trade-off between conductivity and transmittance. Thin layers of certain oxides, such as In/SnO<sub>2</sub> on glass (ITO), are metallic and transparent in the visible region: conductivity arises from extensive doping of the oxide whereas transparency results from the material band gap being situated in the UV.

Short-lived species can be measured when rapid-scanning spectrometers like diode-array instruments are employed. When the absorbance of electrogenerated species is very

small, signal-averaging or phase-sensitive detection may be required to improve the signal-to-noise ratio.

## 2.3 ACOUSTIC WAVE METHODS

The *thickness-shear mode* (TSM) resonator consists of an AT-cut quartz crystal disc coated with metal electrodes on both sides. Due to the piezoelectric properties and crystalline orientation, the application of voltage between the electrodes results in shear deformation of the crystal. When an alternating electric field is applied perpendicular to the crystal plane, the deformation will oscillate at the frequency of that electric field, and the amplitude of the oscillation will be maximum at the mechanical resonant frequency of the crystal. Resonance occurs when there is constructive interference from the wave fronts propagating from the upper and lower surfaces of the resonator, a criterion satisfied when the crystal thickness corresponds to half of the acoustic wavelength<sup>22</sup>. If the quartz crystal is placed in contact with any medium or material (air, liquid, polymer), there will be mechanical interaction, altering the electrical properties of the TSM resonator. Therefore, the measurement of the electrical properties of the loaded crystal can give information about the mechanical properties of the contacting medium.

When the TSM resonator is used as a gravimetric probe, it is commonly referred to as the *quartz crystal microbalance* (QCM). In this case, only the frequency associated with the acoustic wave changes upon loading, and the Sauerbrey approximation<sup>23</sup> is applicable. According to this, the variation of quartz resonant frequency  $\Delta f$  is proportional to the mass of deposited material per unit of area  $\Delta m$ :

$$\Delta f = \frac{-2f_0^2}{\sqrt{\mu_q \rho_q}} \Delta m, \Delta m = h_f \rho_f \quad (2.35)$$

where  $\mu_q$ ,  $\rho_q$  and  $f_0$  are the quartz shear modulus, density, and resonant frequency, respectively;  $\rho_f$  and  $h_f$  are the film density and thickness. Mechanically, this corresponds to the coupling of rigid material that oscillates synchronously with the quartz crystal (changes in the amplitude and phase are negligible). This behaviour is usually observed for thin films and solid/gas phase situations. At the other extreme, when a liquid is placed in contact with a TSM resonator, the acoustic wave propagates with considerable energy dissipation. Initially, it was commonly assumed that the extent of dissipation would be so great that the attenuation of the wave would damp the oscillation to such an extent that it

would prevent the use of QCM *in situ*. In the early 1980s, Nomura and Iijima showed that the fluid damping is not so great as to prohibit the use of the QCM *in situ*<sup>24</sup>. The QCM and its electrochemical extension, the EQCM<sup>25</sup>, have since been used in the characterisation of solid/liquid interfaces and electroactive films.

Many systems, due to their intrinsic characteristics, are not rigidly coupled to the TSM resonator, and are termed ‘viscoelastic’. The loading of a quartz crystal with viscoelastic material results in the decrease of both the frequency and peak admittance, corresponding to a phase shift and damping in the amplitude of the acoustic wave launched from the quartz crystal. In this case, the gravimetric approximation can no longer be used, and more complex models are required to extract the rheological properties of the loading material.

Due to the piezoelectric properties of the quartz crystal, the coupling between the crystal and loading material can be equivalently described in terms of electrical or mechanical parameters. The former can be accomplished in a similar way to that of electrochemical impedance. The electrical driving and response functions are related by the mechanical impedance of the loading. The system response can then be represented by equivalent circuits where capacitors, resistors and inductors represent physical components of the system. The mechanical impedance of the loading  $Z_S$  is given by the quotient of the surface stress  $T_{xy}$  and the particle velocity  $v_x$  at the resonator surface:

$$Z_S = \frac{T_{xy}}{v_x} \bigg|_{y=0} \quad (2.36)$$

Two of the most commonly used equivalent circuits are the *transmission-line model* (TLM)<sup>26</sup> and the *lumped-element model* (LEM)<sup>27</sup> (also referred to as the Butterworth-van Dyke, BvD, model). The transmission-line model is more accurate, but the lumped-element model is easier to visualise and requires less effort to extract parameters<sup>28</sup>.

Bandey and colleagues<sup>28,29</sup> presented a method for the case of finite and semi-infinite viscoelastic films exposed to Newtonian fluids, describing a general transmission-line model for these cases, and showing that the simpler lumped-element model is in fact a low loading limiting case of the former. The lumped-element model was found to be a very good approximation (within 1 %) near the resonant frequency and when  $|Z_S|/Z_q \leq 0.2$ , where  $Z_q$  is the impedance of the unloaded crystal<sup>30</sup>. Generically, for most practical

loading conditions, the deviation between these two models does not exceed 3%<sup>31</sup>. Therefore, the scope of the following section will be the description of the LEM model.

In the lumped-element model (Figure 2.8), a static capacitance  $C_0$  is attributed to the presence of the electrode thin films on each side of the quartz disc (in practice there is also a parasitic capacitance that is included in the term  $C_0^* = C_0 + C_p$ ), and an additional motional contribution arises as a result of the electromechanical coupling ( $L_1$ ,  $C_1$ ,  $R_1$ ). Here,  $C_1$  represents the mechanical elasticity of the system,  $R_1$  the dissipation of energy and  $L_1$  the inertial mass. According to this model,  $C_0^*$  dominates the response for frequencies away from resonance whilst the motional contribution becomes dominant in the vicinity of resonance.

If there is any loading material in contact with one of the quartz faces, the impedance will increase. This corresponds to an extra contribution to the impedance  $Z_e = R_2 + jaL_2$ , where  $R_2$  and  $L_2$  are related to the real and imaginary part of the shear mechanical impedance of the device surface  $Z_s$ , respectively.

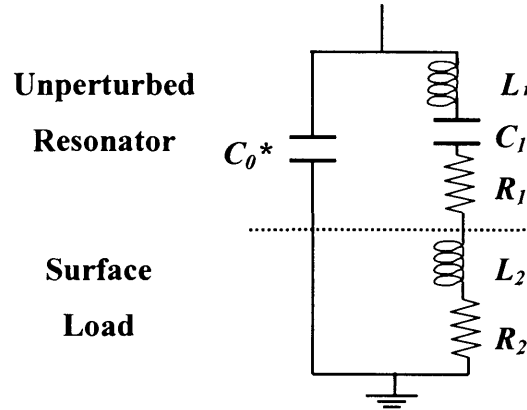


**Figure 2.8:** Lumped-element model.

## 2.3.1 Extraction of rheological parameters for real systems

### 2.3.1.1 General case

The most general case that can be found is a system in which the quartz resonator is in contact with an ideal mass layer, multiple viscoelastic layers of finite thickness and a semi-infinite Newtonian fluid. The mechanical impedance associated with a semi-infinite Newtonian fluid is given by<sup>28</sup>:

$$Z_L = \left( \frac{\omega \rho_L \eta_L}{2} \right)^{1/2} (1 + j) \quad (2.37)$$

where  $\rho_L$  is the density and  $\eta_L$  the viscosity of the fluid.

An ideal mass is a layer of sufficiently thin and rigid material, for which no acoustic phase shift occurs across its thickness. The mechanical impedance is given by:

$$Z_m = j\omega\rho_m \quad (2.38)$$

where  $\rho_m$  is the mass per area of the layer. This component is of particular relevance when rough, unpolished crystals are used, since the material deposits in the interstices of the crystal. In this case, the material resonates synchronously with the crystal.

The surface mechanical impedance of a finite viscoelastic layer is given by:

$$Z_0 = (G\rho_f)^{1/2} \tanh(\gamma h_f) \quad (2.39)$$

where  $G = G' + jG''$  is called the *shear modulus* and is a measure of the rigidity of the material. The in phase component  $G'$  is associated with energy storage and release during the deformation process and is called the *storage modulus*. The out of phase component  $G''$  is related to the energy loss and is called the *loss modulus*.  $\rho_f$  is the film density and  $\gamma = j\omega(\rho_f / G)^{1/2}$  ( $\omega$ =the angular frequency of the series resonance).

Although the impedance of an ideal mass layer is additive due to the displacement across the film being constant, the combination of the impedances associated with all the layers including the liquid and viscoelastic is, however, nonlinear due to the phase shift occurring across those layers. For a system consisting of a viscoelastic layer and a semi-infinite Newtonian fluid, the surface mechanical impedance is given by<sup>26</sup>:

$$Z_s = Z_0 \left[ \frac{Z_L \cosh(\gamma h_f) + Z_0 \sinh(\gamma h_f)}{Z_0 \cosh(\gamma h_f) + Z_L \sinh(\gamma h_f)} \right] \quad (2.40)$$

where  $Z_0$  is the characteristic mechanical impedance of the viscoelastic layer and  $Z_L$  is the mechanical impedance of the Newtonian semi-infinite fluid.

In the case of multiple viscoelastic layers, Equation 2.40 can be generalised<sup>26, 32</sup>:

$$Z_s^{(n)} = Z_0^{(n)} \left[ \frac{Z_0^{(n+1)} \cosh(\gamma^{(n)} h_f^{(n)}) + Z_0^{(n)} \sinh(\gamma^{(n)} h_f^{(n)})}{Z_0^{(n)} \cosh(\gamma^{(n)} h_f^{(n)}) + Z_0^{(n+1)} \sinh(\gamma^{(n)} h_f^{(n)})} \right] \quad (2.41)$$

where  $Z_0^{(n)}$  is the characteristic impedance of the  $n^{th}$  viscoelastic layer and  $Z_0^{(n)} = (G^{(n)}\rho_f^{(n)})^{1/2}$ .

When the attenuation in the acoustic wave is sufficiently large, it will decay before reaching the outer film/solution interface; this is called the 'semi-infinite' case. In these

conditions the shear wave cannot distinguish between film and ‘bulk’ material. This occurs when  $h_f > 2\delta$ , where the decay length  $\delta$  is given by<sup>33</sup>:

$$\delta = \frac{1}{\omega \sqrt{\rho_f}} \sqrt{\frac{2|G|}{1 - G'/|G|}} \quad (2.42)$$

Due to the fact that the acoustic wave does not sample all the film, the Sauerbrey approximation is inappropriate.

For viscoelastic films there is an additional phenomenon that may occur – film resonance. As mentioned previously, as the thickness of a viscoelastic loading increases a phase shift  $\phi$  develops across the film, given by<sup>22,33,34</sup>:

$$\phi = \omega h_f \sqrt{\rho_f} \sqrt{\frac{1 + G'/G}{2|G|}} \quad (2.43)$$

The acoustic wave is reflected at the film/solution interface with a phase shift  $\pi$ . When the phase shift of the launched wave is a quarter of the wavelength,  $\phi = \pi/2$ , the wave returns to the resonator with overall phase shift  $2\pi$ , *i. e.* one wavelength. This causes a constructive interference between the returning and next outgoing wave. If the film and solution impedances are very different, the reflectivity coefficient is close to unity and there will be a dramatic change in coupling of energy from the resonator into the film, resulting in *increase* of both resonant frequency and admittance. Further increase of the film thickness results in a decrease of both parameters, and the system response returns to the typical viscoelastic trend.

The general case is undoubtedly the most accurate as it considers the existence of spatial variation composition, namely the variation of solvent content as a function of depth  $z$  within a viscoelastic film (in fact multiple viscoelastic layers) and consequently  $\rho_f(z)$ . Several studies<sup>35,36</sup> have shown that  $\rho_f(z)$  is not constant, with outer layers of polymer more opened and prone to solvent entry, approaching to the properties of the solution. The determination of  $\rho_f(z)$  can be accomplished by using optical techniques such as ellipsometry, or neutron reflectivity. Nevertheless, for the vast majority of systems  $\rho_f(z)$  is unknown, and then a more simplistic approach is required.

### 2.3.1.2 Particular case: viscoelastic layer

Usually, the use of the crystal impedance technique is intended to convert experimental data ( $Re(Z_s)$  and  $Im(Z_s)$ ) to film properties  $\rho_f$ ,  $h_f$ ,  $G'$  and  $G''$ . Since there are

two input variables and four output parameters to be determined, some simplifications must be made. As mentioned before, for the majority of the systems under study the variation of the film density  $\rho_f(z)$  is unknown. At most, only an average value of the density is available. As a result, the viscoelastic multilayer assumption must be replaced by a simpler approximation: the film consists of one homogeneous, viscoelastic layer. In this section, a procedure published by Hillman and colleagues<sup>33</sup> showing a possible route for the extraction of film properties is described.

In a first stage, crystal impedance measurements are performed in an *acoustically thin film*. This means that the film is sufficiently thin to be considered as rigid, with no acoustic deformation occurring along its thickness (and the acoustic phase shift  $\varphi \rightarrow 0$ ). The film can be considered in this regime when there are no changes in the admittance peak (the resistive element in the LEM model  $R_2 \rightarrow 0$ ) and  $\Delta f$  is proportional to the surface coverage ( $\Gamma$ ). In these conditions the Sauerbrey equation can be applied to determine the product  $\rho_f h_f$ . For systems based on electroactive films, the charge  $Q$  may be used as an independent measure of thickness.

The next step is to measure the impedance of films in the *acoustically thick regime*, when the response is viscoelastically controlled. In this case,  $\rho_f$  is imported from the thin regime,  $h_f$  is calculated coulometrically and the two remaining parameters  $G'$  and  $G''$  are obtained by fitting two measurands from the experimental data,  $Re(Z_S)$  and  $Im(Z_S)$ .

The thickness of an unsolvated, electroactive film  $h_f^0$  can be directly determined using the polymer coverage ( $\Gamma_P$  /mol cm<sup>-2</sup>), obtained by electrochemical (or other *in situ*) techniques, in conjunction with the monomer molar volume ( $V_m$ /cm<sup>3</sup> mol<sup>-1</sup>):

$$h_f^0 = \Gamma_P V_m = \frac{Q}{nFA} \frac{M}{\rho_f^0} \quad (2.44)$$

As long as the stoichiometry of the redox processes is known ( $n$  electrons transferred per mole), the value of  $\Gamma_P$  can be calculated coulometrically from charge ( $Q$ ) data for electrodeposition or subsequent redox switching.

The film in contact with the solution contains some solvent, which affects the polymer viscoelastic properties; in the case of electroactive films this content is a function of charge states.

Considering the solvated film with the parameters  $\rho_f$  and  $h_f$ , the total areal mass density is given by a sum of areal mass densities of the unsolvated polymer and the solvent:

$$\Delta m = h_f \rho_f = h_f^0 \rho_f^0 + (h_f - h_f^0) \rho_s \quad (2.45)$$

Substituting  $h_f^0$  by Equation 2.44, and rearranging and normalizing with respect to the solvent Equation 2.45 becomes:

$$\frac{\rho_f}{\rho_s} = \left( \frac{\rho_f^0}{\rho_s} - 1 \right) \left( \frac{QM}{nFA\rho_f^0} \right) \frac{1}{h_f} + 1 \quad (2.46)$$

#### *Acoustically thin regime*

For a thin and rigid film,  $h_f$  in Equation 2.46 can be replaced by the Sauerbrey approximation (Equation 2.35):

$$\frac{\rho_f}{\rho_s} = \left( \frac{\rho_f^0}{\rho_s} - 1 \right) \left( \frac{QM}{nFA\rho_f^0} \right) \frac{c_1}{\Delta f} + 1 \quad (2.47)$$

where  $c_1$  is  $c_1 = \frac{-2f_0^2}{\sqrt{\mu_q \rho_q}}$ . Rearranging Equation 2.47:

$$\rho_f = \left[ \frac{1}{\rho_s} - \left( \frac{1}{\rho_s} - \frac{1}{\rho_f^0} \right) \left( \frac{QM}{nFA} \right) \frac{c_1}{\Delta f} \right]^{-1} \quad (2.48)$$

In Equation 2.48  $\rho_s$  and  $\rho_f^0$  are known,  $Q$  and  $\Delta f$  are determined by EQCM measurements and all the other parameters are known constants. Since one single value of  $\rho_f$  is obtained, combination with Equation 2.45 gives Equation 2.49, and the determination of  $h_f$  is possible. The parameters characterising the film in the thin film regime are then obtained.

$$h_f = \left[ \frac{\Delta f}{c_1} - (\rho_f^0 - \rho_s) \left( \frac{QM}{nFA} \right) \right] \rho_s^{-1} \quad (2.49)$$

#### *Acoustically thick regime*

Assuming that the film is uniform, the value of  $\rho_f$  is the same as in the acoustically thin regime. The values of  $h_f$  are obtained by extrapolation of the linear relationship between the thickness and the charge ( $Q=f(h_f)$ ) from the acoustically thin regime (Equation



2.46). Shear moduli values are given by Equation 2.40, and calculated using iterative procedures.

#### *Semi-infinite regime*

When the thickness of the film is larger than a few decay lengths ( $h_f > 2\delta$ ), the outer layers of the film in contact with solution are not detected by the acoustic wave, and the film is infinitely thick. The surface mechanical impedance in this case is given by:

$$Z_s = (G\rho_f)^{1/2} \quad (2.50)$$

$h_f$  is no longer a fitted parameter, and now three parameters have to be determined iteratively.

### **2.3.2 Rheological characteristics and the effect of frequency**

The dependence of the viscoelastic properties of polymeric systems on frequency can be assessed *a posteriori* (once  $G$  values were extracted) by using different combinations of springs and dashpots<sup>37,38</sup>. The simplest approximations that consider both energy storage and loss are parallel and series combinations of a spring and a dashpot – designated by *Voigt* and *Maxwell models*, respectively<sup>37</sup>.

According to the Voigt model, the strains  $S$  are equal across the two elements, whilst the stresses  $T$  are additive:

$$G = \frac{T}{S} = \mu_f (1 + j\omega\tau) \quad (2.51)$$

where  $\mu_f$  is the stiffness of the material,  $\tau = \eta_f / \mu_f$  the relaxation time and  $\eta_f$  the viscosity.

The Maxwell model considers the stress across the elements to be the same, and the strains additive:

$$G = \mu_f \left( \frac{(\omega\tau)^2}{1 + (\omega\tau)^2} + j \frac{\omega\tau}{1 + (\omega\tau)^2} \right) \quad (2.52)$$

These two models predict different frequency dependences of shear modulus  $G$  (Figure 2.9). According to the Voigt model, the storage modulus  $G'$  is independent of frequency, whereas the loss modulus  $G''$  is proportional to frequency. On the other hand, the Maxwell model predicts a monotonic increase of  $G'$  with the frequency until reaching a plateau at  $\mu_f$ , whereas  $G''$  goes through a peak at  $\omega\tau=1$  (corresponding to  $\mu_f/2$ ). At low

frequencies  $G'$  changes quadratically and  $G''$  changes linearly. In spite of being more complicated, the latter model is more realistic when considering the typical behaviour of polymeric systems.

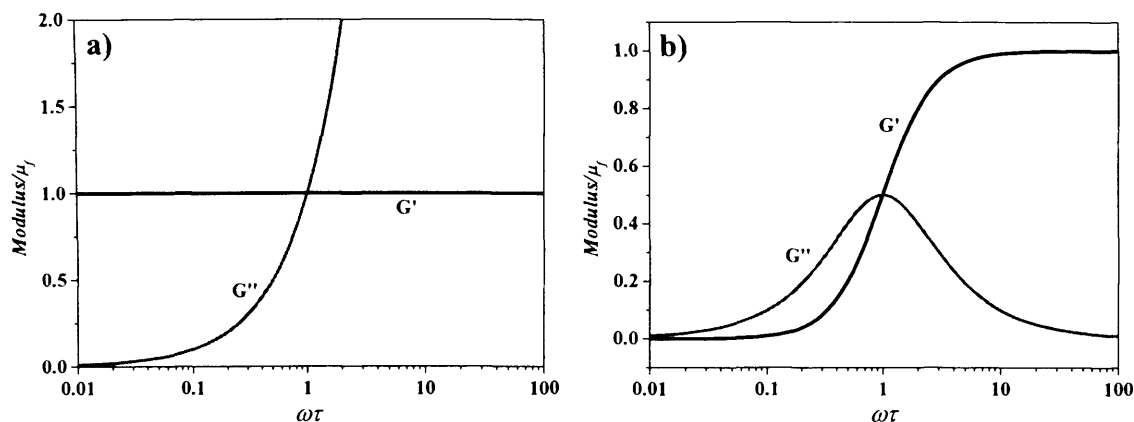


**Figure 2.9:** Frequency dependency of (—)  $G'$  and (—)  $G''$  predicted by **a)** the Voigt model and **b)** the Maxwell model.

### 2.3.3 Experimental

From the wide range of techniques and equipment available nowadays, acoustic wave (AW) devices assume a vital importance for the study of heterogeneous systems due to their extreme sensitivity for the characterisation of thin films<sup>39</sup>, low cost, no restriction in terms of environment (vacuum is not necessary) and real time sampling<sup>40</sup>. Perhaps the two most important features are (i) high sensitivity for a variety of film properties such as mass density ( $\text{ng}/\text{cm}^2$ ), conductivity and viscoelasticity, and (ii) real time monitoring which allows the study of polymer dynamics in the experimental timescale, including deposition processes and diffusion of species. Among the AW devices for chemical sensing purposes, thickness-shear mode (TSM) resonators are perhaps the most widely used.

In crystal impedance an impedance analyser measures the impedance/admittance of the TSM resonator in the vicinity of the frequency resonance. TSM resonators are one-port devices, with a single (coaxial) electrical connection<sup>41</sup>; the only output that can be measured is the reflected signal, which travels from the device along the same signal cable used to transmit the input signal ([Figure 2.10](#)). In typical EQCM/crystal impedance measurements, the quartz crystal must be characterised as: (i) bare crystal in air; (ii) immersed in solution (only one of the crystal faces is in contact with solution) and (iii)

loaded with the film/immersed in solution. The first will provide the electrical parameters associated with the crystal ( $R_l$ ,  $C_0$ ,  $C_l$  and  $L_l$  in the LEM); the second gives the parameters associated with the liquid, namely  $\eta_L$  and  $\rho_L$ ; the third provides the parameters associated with the film<sup>22</sup>.

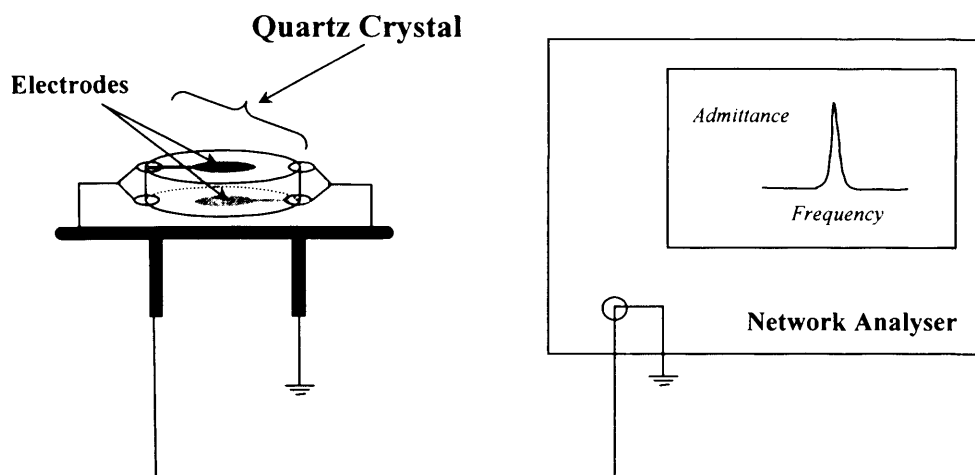


**Figure 2.10:** Schematic view of crystal impedance measurement set-up<sup>41</sup>.

## 2.4 X-RAY TECHNIQUES

The interaction of X-ray beams with matter can result in different processes: scattering, refraction and absorption. When absorption occurs, the X-ray photon is absorbed by an atom, and its energy is transferred to a core electron with a specific binding energy. When the photon energy  $E_v$  is equal to or higher than the electron binding energy  $E_0$ , the electron is ejected with energy given by the difference between  $E_v - E_0$ , leaving the atom in an excited state with a core hole, which later is filled through relaxation processes, fluorescence or emission of Auger electrons.

### 2.4.1 X-ray photoelectron spectroscopy (XPS)

In X-ray photoelectron spectroscopy a monochromatic beam of X-rays is focused onto the sample's surface. The radiation interacts with electrons of inner shells (1s, 2s, 2p, etc.) causing their ejection. The ejected electrons possess kinetic energy  $E_K$ , which is given by the difference between the X-ray quantum energy  $E_v = \hbar\omega$  and the electron binding energy  $E_0 = \Phi$ :

$$E_K = \hbar\omega - \Phi \quad (2.53)$$

Since the electronic levels are quantized, and the core orbitals of an atom are highly contracted, not overlapping significantly with neighbour atoms, the electron binding energy is characteristic of the element, and depends on the chemical environment surrounding the atom<sup>42</sup>. Generally the chemical shift varies in the range 0 up to 10 eV and arises due to the interaction between the core electrons with valence electrons and surrounding atoms<sup>43</sup>.

The photoelectron peak is proportional to the number of atoms present. XPS thus provides both qualitative and quantitative chemical information. When atoms of the same element are present in more than one oxidation state, the XPS peak may broaden and sometimes it shows a shoulder; in these cases, it is necessary to deconvolute the peaks to determine the oxidation states and the relative amount of each state within the compound. XPS data associated with carbon and oxygen must be handled carefully. These elements are omnipresent, thereby imposing difficulties to the deconvolution and quantification of related species within the sample.

Valence electrons can also be sampled by using radiation of lower energy. Nevertheless, analysis of these electrons is not as straightforward as for core electrons. They participate in chemical bonding and their binding energies (30 eV or less) are characteristic of the molecular orbitals, from which they arise, and depend upon the degree of orbital mixing. Consequently, the photoelectron peak cannot be associated directly to the number of atoms, and models or reliable databases are required to interpret the spectrum<sup>43</sup>. When XPS is used for chemical analysis it is sometimes designated as *ESCA*, *electron spectroscopy for chemical analysis*.

#### **2.4.1.1 Instrumentation**

In this technique a X-ray beam is incident on a sample placed in ultra-high vacuum (UHV) conditions and the kinetic energy of photoejected electrons is analysed using a hemispherical (or cylindrical mirror) analyser. The photoelectrons are detected by a channel electron multiplier. The X-ray source consists of an X-ray tube containing an appropriate target; the latter is usually in the form of a dual anode with aluminum and magnesium anodes, which give photons with energies 1486.6 eV and 1253.6 eV, respectively. Two-dimensional images of the surface at a chosen photoelectron kinetic

energy can be obtained by using the input lens system together with an additional exit lens between the analyser and the detector.

#### 2.4.1.2 Accuracy of electron binding energies

The binding energy in solids is usually reported with respect to the Fermi level, which is separated from the vacuum level by the sample work function  $\psi_{sample} = \Phi_{Fermi} - \Phi_{vacuum}$ . Additionally, there is a contact potential between the sample and the spectrometer given by the difference in the work function  $\psi_{sample} - \psi_{spectrometer}$ . The kinetic energy of the photoelectron is given by<sup>43</sup>:

$$E_K = \hbar\omega - \Phi_{Fermi} - \psi_{spectrometer} \quad (2.54)$$

In the case of conducting solid samples  $\psi_{spectrometer}$  can be calculated and  $\Phi_{Fermi}$  obtained. However, in insulators the charge that accumulates on the sample due to the loss of photoelectrons is not compensated by the flow of electrons into the sample. In fact, the charge is neutralised by secondary electrons produced by exposure of the sample chamber to X-rays and a constant charge  $S'$  is accumulated on the sample surface:

$$E_K = \hbar\omega - \Phi_{Fermi} - \psi_{spectrometer} - S' \quad (2.55)$$

In addition, charge may not be able to delocalise throughout the surface and different regions may experience different degrees of charge. The result is the appearance of multiple peaks in the XPS spectrum.

The value of  $S'$  can be reduced by exposing the sample surface to low-energy electrons by using a 'flood gun'; this is particularly important in instruments with monochromatized X-ray sources where the X-ray flux is low. However, the uncertainty associated with the determination of binding energy values is always present. Strategies to overcome this problem include the use of calibrants of known binding energy within the sample or the use of binding energy differences between elements within the same sample instead of using the absolute values.

#### 2.4.1.3 Surface sensitivity

In spite of X-rays being penetrating radiation ( $> 100$  nm), XPS is a surface technique because the photoejected electrons can only penetrate short distances, and only a few layers near the surface are analysed (usually 1 to 10 nm from the top into the material).

### 2.4.2 X-ray absorption spectroscopy (XAS)<sup>44-46</sup>

In practice, the absorption is described in terms of the linear absorption coefficient  $\mu$  ( $\text{cm}^{-1}$ ) or the mass absorption coefficient  $\mu/\rho$  ( $\text{cm}^2 \text{ g}^{-1}$ ). Consider a sample of total thickness  $t$  (cm) and  $N$  the number of atoms per  $\text{cm}^3$ . The incident X-ray beam intensity will change by  $-dI$  due to the absorption processes occurring in an infinitesimal thickness  $dz$  at depth  $z$  from the surface, with  $-dI$  given by:

$$-dI = IN\sigma_a dz \quad (2.56)$$

where  $\sigma_a$  is the absorption cross-section, the *area* of absorption as seen by the incident beam. Integration of Equation 2.56 gives:

$$I(t) = I_0 e^{-\mu t} \quad (2.57)$$

with  $\mu = N\sigma_a = \rho\sigma_a \frac{N_A}{A_w}$ ;  $N_A$  is the Avogadro's number,  $A_w$  the atomic weight and  $\rho$  the mass density. The X-ray absorption spectrum consists of a plot of the absorption-cross section of the relevant atom against the *photoelectron momentum vector*  $k = \frac{2\pi}{\lambda}$  (energy).

The X-ray range of interest, from a spectroscopic point of view, lies between 300 eV and 30 keV. Two different regions can be distinguished in X-ray absorption spectrum: (i) the X-ray absorption near edge structure (XANES) region and (ii) the extended X-ray absorption fine structure (EXAFS) region.

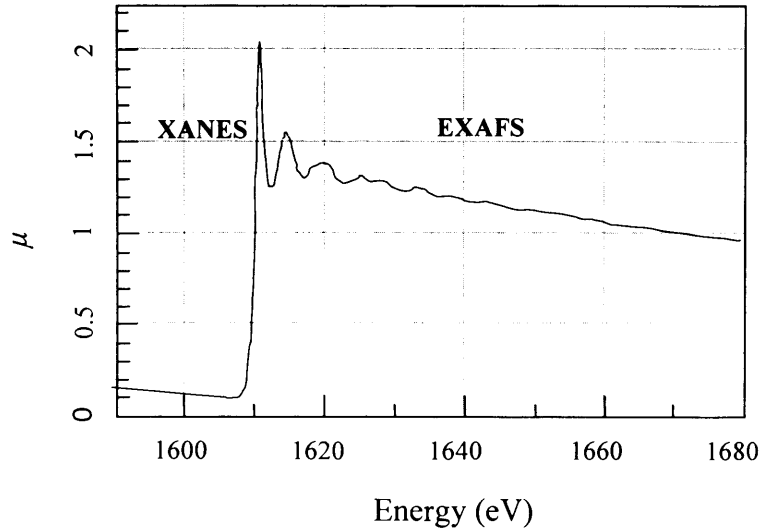


**Figure 2.11:** Example of XAS spectrum.

The XANES region includes the edge (emission of the photoelectron) and pre-edge features (the energy range is from 10 eV below to 50 eV above the edge). These are functions of the valence and local coordination of the relevant atom, as well as its concentration in the sample. The position of the edge depends on the combination of the valency of the system and the ligand distances: a longer distance and lower valency usually shifts the position of the edge towards lower energies. The influence of valency results from the core-hole interaction with the electrons localised or quasi-localised on the excited atom. For instance, when the oxidation state of the relevant atom is increased, this interaction occurs to a lesser extent and the edge shifts to higher energy. The sensitivity of the edge position also depends on the type of shell involved in the transition.

The EXAFS region extends from *ca.* 50 eV above the absorption edge up to 1000 eV, and results from interference effects causing oscillations in the absorption cross-section of the absorbing atom. The formalism used to explain EXAFS is based on the idea that the photoelectron is a low energy particle, which is scattered during propagation by any abrupt change of energy potential such as those associated with the atomic potentials of neighbouring atoms. In other words, the outgoing photoelectron wave interferes with the backscattered wavelets to generate the EXAFS oscillations.

#### 2.4.2.1 EXAFS theory

The EXAFS model presented above is based on the *plane wave theory*. The brief description of the plane wave theory presented here is based on the work of Lee and colleagues<sup>47</sup>, and is also presented on the website of CCRLC Daresbury Laboratory<sup>48</sup>.

According to this theory, EXAFS is defined as the normalised oscillatory part of  $\mu$  (Equation 2.57) and given by:

$$\chi = \frac{\mu - \mu_0}{\mu_0} \quad (2.58)$$

where  $\mu_0$  is the absorption coefficient of the free atom. The absorption spectra resulting from  $\mu_0$  and  $\mu$  are depicted in Figures 2.12a and 2.12b, respectively.

In the energy range of EXAFS the dominant photoelectronic process is absorption. Therefore, EXAFS can be described directly in terms of the photoelectron momentum, which in  $k$ -space is given by:

$$k = \left[ \left( \frac{2m_e}{\hbar^2} \right) (E_v - E_0) \right]^{1/2} \quad (2.59)$$

where  $m_e$  is the electron mass and  $E_0$  is approximated to the energy of the absorption edge.

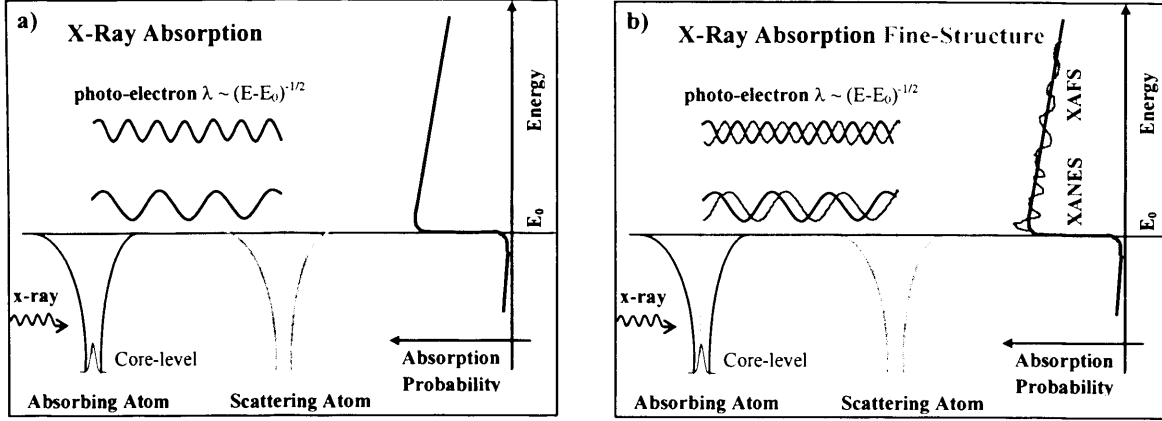


**Figure 2.12:** Absorption spectra for a) free atom ( $\mu_0$ ) and b) atom within a sample ( $\mu$ )<sup>49</sup>.

The excitation of the core electron is treated in a semi-classical way, with the photon represented by an electromagnetic field (classical description) and the photoelectron described quantum mechanically. It is assumed that the electromagnetic field is uniform. This is called *the dipole approximation* and is based on the assumption that the wavelength of the field is always large compared to the dimensions of the excited core state. Within this approximation, the absorption associated with the transition of the electron from the initial  $|i\rangle$  to the final  $\langle f|$  state, caused by the photon, is described by:

$$\mu \propto |\langle f | e \cdot r | i \rangle|^2 \quad (2.60)$$

where  $e$  is the polarization vector of the electric field and  $r$  is the electron coordinate. The EXAFS equation is then given by:

$$\chi(k) = - \sum_{m=1}^m S_i^2 \left( \frac{N_m}{k R_m^2} \right) |f_m(\pi, k)| \exp(-2\sigma_m^2 k^2) \exp \left[ \frac{-2R_m}{l_m(k)} \right] \sin[2kR_m + 2\delta_i(k) + \theta_m(k)] \quad (2.61)$$

where  $N_m$  is the number of neighbours in the  $m^{th}$  shell,  $R_m$  is the interatomic distance and  $|f_m(\pi, k)|$  is the element-specific and energy-dependent electron scattering amplitude (backscattering factor), which is used for determination of  $N_m$ .

There are several terms that account for damping in the amplitude of the EXAFS function. The term  $S_i^2(k)$  is an amplitude reduction factor for energy loss due to processes caused by multiple excitations at the central atom. Damping factors associated with inelastic scattering are: (i)  $\exp(-2R_m/l_m(k))$ , which depends on the ratio between the



distance travelled  $2R_m$  and the electron mean free path  $l_m(k)$ ; (ii)  $1/(kR_m^2)$ , a term that describes the loss of amplitude of a spherical wave with the increase of distance. The term  $\exp(-2\sigma_m^2 k^2)$  contains the Debye-Waller factor  $\sigma_m^2$ , which arises from thermal disorder and uncertainty in finding atoms at fixed positions; the interatomic distance is considered to have a Gaussian distribution. Notice that  $\sigma_m^2$  is the Debye-Waller factor, whilst  $\sigma_a$  (Equation 2.56) is the absorption cross-section.

EXAFS can be seen as a low energy electron diffraction experiment of spherical symmetry (the photoelectron is a spherical electronic wave) in which the source of the electron is created inside the sample itself. It provides information on: (i) *bond lengths*, through the *sin* term in Equation 2.61, where  $\delta_l$  is the phase shift with which the photoelectron wave leaves the absorbing atom,  $\theta_m$  the phase shift of the backscatter atom  $m$  and  $R_m$  the interatomic distance between the central atom and the backscatter  $m$ ; (ii) *chemical identification*, since the energy dependence of the amplitude and the phase shift of the signal are specific to each element (differentiation between two elements differing in the atomic number  $Z$  by more than a few units is possible); (iii) the *Debye-Waller factor*. The limited free path of the photoelectron restricts EXAFS to radial distances up to 0.5 nm. In this context, X-ray absorption spectroscopy (XAS) can provide structural information around the relevant atoms in soft and amorphous materials, irrespective of the physical state of the sample (crystal, amorphous solid, powder or solution).

The plane wave theory gives a physical picture of the EXAFS origin, showing that the structural information around the relevant atom is contained in the EXAFS function. In practice, computational methods use the more complex and advanced *rapid curved wave theory*<sup>50</sup> to fit the EXAFS, in order to extract the structural parameters mentioned above.

#### 2.4.2.2 Experimental

Different types of experimental configuration can be used to collect the data, depending on the sample characteristics.

##### *Transmission mode*

Transmission mode is the most widely used method and consists of analysing the intensity of a monochromatic beam that passes through the sample. The beam is tuned using a double reflection from silicon crystals and its intensity is measured before and after

the absorbing sample as a function of the photon energy, using two ion chambers. Application of [Equation 2.57](#) is straightforward and the cross-section  $\sigma_a$  is obtained. For each point of the spectrum, a dead time allows for mechanical movement and electronic stabilisation, and the time constant must also be long enough to increase the signal-to-noise ratio. In practice, the total time required for each point is about one second, half for the dead time and half for the effective data collection.

### *Energy dispersive mode*

In this configuration, a triangular-shaped crystal is bent to change the Bragg angle along the footprint of the beam on the crystal. The result is a polychromatic X-ray beam, with correlation between the energy and the direction of propagation, which is transformed in an energy-position correlation at the detector. When the average incident angle is tuned to the Bragg angle of the energy of the edge, the data is collected at once using a silicon-based detector. The advantage in using the dispersive mode is the absence of mechanical movement and simultaneous acquisition of the data in all the energy range. This is particularly important to give extreme stability to the energy scale and consequently extreme sensitivity to small changes in series of similar samples. Additionally, the sample can be very small (less than  $0.5 \text{ mm}^2$ ), and the speed and simultaneity of the data acquisition allows measurement of kinetics on the 100 ms - 1 s timescale. However, in this mode is not possible to detect the X-ray absorption signal via decay of intensity and therefore it cannot be used for ultra-dilute samples.

### *Decay modes – Auger and Fluorescence*

Auger and fluorescence processes are secondary processes resulting from the absorption of photons and consequent relaxation of the core states. Since they are proportional to the absorption process, their use is particularly useful when the EXAFS signal is only a small fraction of the total absorption. While in transmission mode isolating EXAFS from the background requires subtraction of two nearly equal signals, in decay modes a detector able to discriminate EXAFS from the background is used. In the fluorescence mode the detector is energy-selective but generally covers a limited solid angle, and cannot collect photons emitted over  $4\pi$ . The background consists of elastically

and Compton scattered radiation, both of which occur at higher energies than the fluorescence radiation.

The energy of fluorescence radiation is characteristic of the absorbing element and independent of the photon energy. This mode gives better data than simple transmission whether the absorption from the element of interest is less than a few percent of the total absorption in the sample. Furthermore, it is also useful for more concentrated samples which cannot be prepared thin enough in section to be measured in transmission mode, but in this case the fluorescent intensity is no longer directly proportional to the absorption coefficient. In fluorescence mode, the detector is placed at  $90^\circ$  to the incident radiation, in order to reduce the scattered signal (reflection of  $\pi$  polarization is 0).

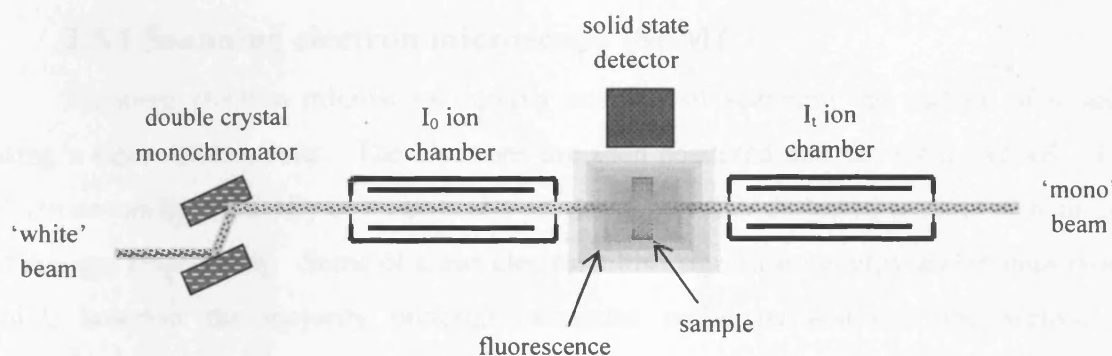


**Figure 2.13:** Experimental setup for EXAFS measurements in both transmission and fluorescent modes<sup>48</sup>.

In the case of Auger decay, the small mean free path of the electrons (0.5 to 50 nm) makes this process surface sensitive, which has been generally regarded as being possible only in UHV conditions. If the electron detector is tuned to the narrow energy window of the Auger electrons, the surface EXAFS (SEXAFS) signal comes from the upper part of the sample. In order to investigate deeper in the sample, the signal component from secondary electrons created by Auger electrons after collisions has to be considered.

There is also a mode called REFLEXAFS (reflection mode), which can be combined with fluorescence methods to study thin two dimensional samples, but its description is beyond the scope of this thesis.

## 2.5 IMAGING TECHNIQUES

In this section two techniques of surface characterisation at high resolution are described, *scanning electron microscopy* (SEM) and *atomic force microscopy* (AFM). These techniques provide surface images by moving a finely focused beam of electrons or a suitable probe onto the surface in a raster pattern: the beam (or probe) is swept across the surface in a straight line ( $x$  direction) after which it returns to the starting point; the beam is then shifted in the  $y$  direction and swept again in the  $x$  direction. The process repeats until all the chosen surface has been scanned. As the beam moves in the  $xy$  plane, information received in the  $z$  direction is stored and converted into an image<sup>51</sup>.

### 2.5.1 Scanning electron microscopy (SEM)

Scanning electron microscopy simply consists of scanning the surface of a solid using a beam of electrons. The electrons are then scattered and the solid excited. The electrons can be elastically or inelastically scattered, whether deflected without or with loss of energy, respectively. Some of these electrons lose significant energy and remain in the solid; however the majority undergo numerous collisions and exit the surface as backscattered electrons. The excited solid, in turn, may emit secondary electrons, which are produced as a result of the interaction between the energetic beam and weakly bound conduction electrons in the solid, leading to the ejection of the latter. Auger electrons and X-ray emission, as well as photons of varied energy, are other processes of decay that may occur in the solid. The mechanisms of formation are identical to those in XPS. All these signals are obtained from specific volumes within the samples enabling the study of different characteristics namely topography, morphology, crystallography and composition. For instance, secondary electrons have energies of a few eV, and escape from the outer layers of the solid, typically 1 or 2 nm depth; therefore, SEM images based on secondary electrons are surface sensitive<sup>52</sup>.

The signals most used in surface studies are backscattered and secondary electrons (scanning electron microscopy), since they vary primarily due to topographic differences arising in the surface, and X-ray emission (electron microprobe analysis), which allows both qualitative and quantitative elemental identification<sup>53</sup>. The latter is also called *energy dispersive analysis by X-rays* (EDAX) and routinely used in conjugation with SEM

imaging. However, due to the penetrating nature of the X-rays EDAX is not as surface sensitive as SEM, sampling *ca.* 10  $\mu\text{m}$  in depth.

The resolution depends upon several parameters: optical system, detectors, type of radiation used for observation and sample characteristics. The main limiting factor is the diameter of the incident electron beam. New SEM instruments use a field-emission gun to produce an electron beam of nanometer diameter, which gives a resolution of 1 nm or better.

#### **2.5.1.1 Instrumentation**

The basic components of a combined scanning electron microscope and scanning electron microprobe are electron gun, electron focusing system, the visual photorecording cathode ray tubes and detector (electron and X-ray), Figure 2.14. The modern SEMs store images digitally, which can be observed on a computer screen.

The incident electron beam energy may vary between 1 and 100 keV, but 20 to 30 keV is commonly used. For insulating systems lower voltages of 1 to 2 keV are often used, in order to overcome the charging-up of the sample<sup>54</sup>. In the electron focusing system, the magnetic condenser and objective lens system serves to reduce the image to a final spot size on the sample of 5 to 200 nm. The scanning of the electron beam is accomplished by using electromagnetic coils located within the objective lens system which deflects the beam in the  $x$  and  $y$  directions. Signals that are used to drive the electron beam in these directions also drive horizontal and vertical scans of a cathode-ray tube. The image is produced by using the output of a detector to control the intensity of the spot in the cathode-ray tube. The sample chamber has large-capacity vacuum pumps, which allows the rapid decrease in pressure from ambient down to  $10^{-4}$  torr or less, favouring the rapid changing of samples. The sample holder can be moved in  $x$ ,  $y$  and  $z$  directions and be rotated about each axis.

Samples must be stable under high vacuum conditions as well as physically and chemically stable when the electron beam is incident. Additionally, they should have superficial conductivity, since the flow of electrons to ground minimises artefacts associated with the build-up of charge. The latter may cause stability problems and loss of resolution. Frequently, when the sample is nonconducting a thin metallic coating is produced over it by sputtering or vacuum evaporation. This improves not only the

conductivity, but also the quality of the acquired image, since it contributes to an enhancement of secondary electron emission.

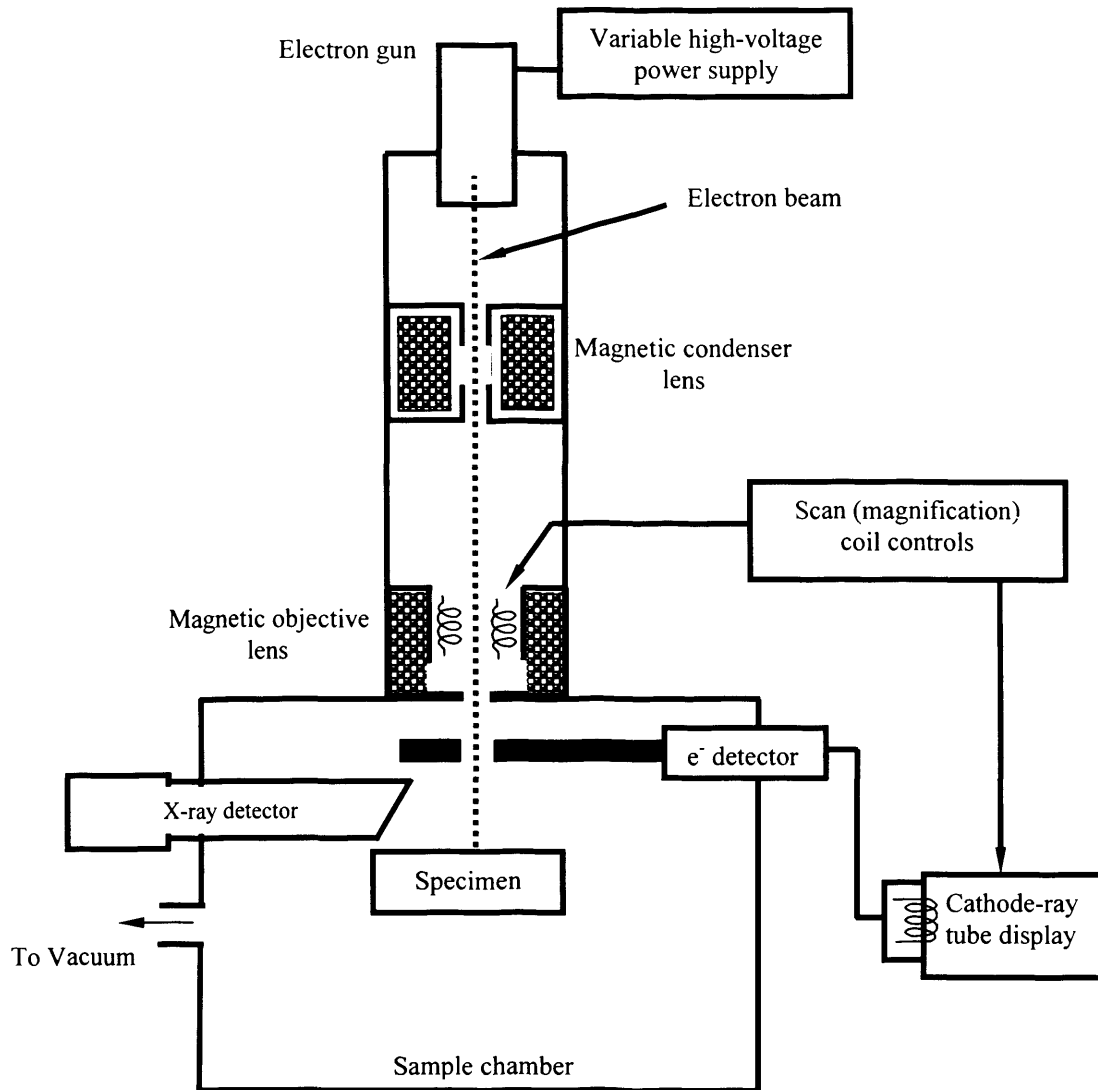


**Figure 2.14:** Schematic view of a SEM instrument<sup>51</sup>.

### 2.5.2 Atomic force microscopy (AFM)

In this technique the surface of a sample is scanned in an  $x/y$  raster pattern using a very sharp tip that moves up and down along the  $z$  axis as surface topology changes, revealing details also on the  $z$  axis. Its resolution is commonly about 2 nm in the  $xy$  plane, but for the best instruments and ideal samples it can reach down to 0.1 nm; resolution in the  $z$  direction is generally better than 0.1 nm. Therefore, atomic force microscopy is a technique able to image surfaces down to the atomic size scale<sup>51</sup>.

In the atomic force microscope, a very sharp tip attached to a flexible cantilever scans the surface (or the tip is scanned with respect to the sample). The force acting between the tip and the surface causes small deflections of the cantilever, which in turn is detected by optical means. The tip is moved using a piezoelectric tube; during the scan, the force exerted on the tip is held constant by the up-and-down movement of this probe, providing topographic information. One common way of detecting the deflection of the cantilever is shown in [Figure 2.15](#). A laser beam is reflected off a spot on the cantilever to a segmented photodiode which acts as a position sensitive detector. The output from the photodiode controls the force applied to the tip so that it remains constant<sup>51,55</sup>.

Since there is no flow of current and the type of force between the tip and the surface is quite general, atomic force microscopy has the advantage of being applicable to nonconducting samples. The force between tip and surface can arise from different type of interactions, including van der Waals, electrostatic and capillary forces<sup>56</sup>. Additionally, it can be operated in a variety of environments without limiting conditions such as UHV, including solid-liquid interface and biological materials; besides, the use of an ‘inert’ tip (e.g., silicon, silicon oxide, silicon nitride) enables the application of this technique to electrochemical systems.

The tip can be employed in contact, intermittent (tapping) or noncontact modes. In the contact mode, the tip is in direct contact with the sample and the interactions between them are repulsive. This interaction causes the tip to be displaced as it is rastered over individual atoms on the surface. In the noncontact mode the tip and sample are farther apart and do not contact, with attractive interactions prevailing. Measurements in this attractive mode are, though, substantially harder to make<sup>57</sup>.

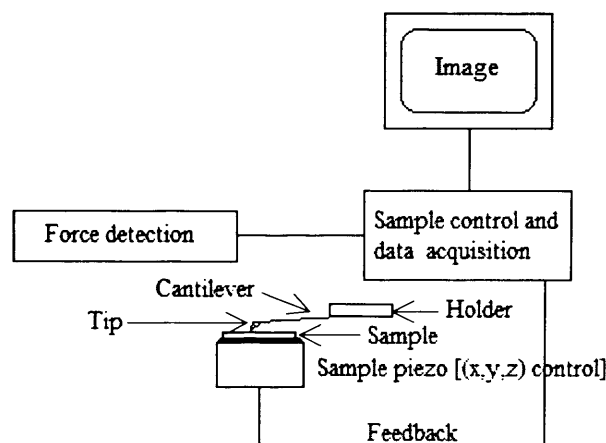


**Figure 2.15:** Typical setup of an AFM<sup>51</sup>.

In contact mode, the tip may damage the surface, which results in distortion of the image. This effect is particularly important in soft materials, such as polymers or biological samples. This problem can be overcome by employing the tip in tapping mode: it contacts with the surface only for small periods of time and then it is removed. In this operation the cantilever is oscillated at few hundred kHz, with the oscillation being driven by a constant driving force and the amplitude monitored continuously. The cantilever is positioned in such way that the tip only touches the surface at the bottom of each oscillation cycle<sup>51</sup>.

## REFERENCES:

1. Bard, A. J.; Faulkner, L. R., In *Electrochemical Methods: Fundamentals and Applications*, 2nd ed.; John Wiley & Sons, Inc.: New York, 2001; Chapter 6, p 226.
2. Speiser, B. In *Encyclopedia of Electrochemistry*; Bard, A. J., Stratmann, M., Eds.; Wiley-VCH: Weinheim, 2003; Vol. 3, Chapter 2.1, p 81.
3. Bard, A. J.; Faulkner, L. R., In *Electrochemical Methods: Fundamentals and Applications*, 2nd ed.; John Wiley & Sons, Inc.: New York, 2001; Chapter 1, p 1.
4. Nicholson, R. S.; Shain, I. *Anal. Chem.* **1964**, *36*, 706.
5. Sevcik, A. *Coll. Czech. Chem. Commun.*, **1948**, *13*, 349.
6. Reinmuth, W. H. *J. Am. Chem. Soc.* **1957**, *79*, 6358.
7. Matsuda, H.; Ayabe, Y. *Z. Electrochem.* **1955**, *59*, 494.
8. Gokhshtein, Y. P. *Dokl. Akad. Nauk SSSR* **1959**, *126*, 598.
9. Myland, J. C.; Oldham, K. B. *J. Electroanal. Chem.*, **1983**, *153*, 43.
10. Ramamurthy, A. C.; Rangarajan, S. K. *Electrochim. Acta* **1981**, *26*, 111.
11. Sevcik, A. *Czech Chem. Commun.* **1948**, *20*, 327.
12. Bard, A. J.; Faulkner, L. R., In *Electrochemical Methods: Fundamentals and Applications*, 2nd ed.; John Wiley & Sons, Inc.: New York, 2001; Chapter 14, p 580.
13. Vilas-Boas, M.; Freire, C.; de Castro, B.; Christensen, P. A.; Hillman, A. R. *Inorg. Chem.* **1997**, *36*, 4919.
14. Vilas-Boas, M.; Freire, C.; de Castro, B.; Hillman, A. R. *J. Phys. Chem. B* **1998**, *102*, 8533.
15. Vilas-Boas, M.; Henderson, M. J.; Freire, C.; Hillman, A. R.; Vieil, E. *Chem. -Eur. J.* **2000**, *6*, 1160.



16. Christensen, P. A.; Hamnett, A. In *Techniques and Mechanisms in Electrochemistry*; Blackie Academic & Professional: London, 1994; Chapter 2.1.2, p 55.
17. Bard, A. J.; Faulkner, L. R., In *Electrochemical Methods: Fundamentals and Applications*, 2nd ed.; John Wiley & Sons, Inc.: New York, 2001; Chapter 10, p 368.
18. Krause, S. In *Encyclopedia of Electrochemistry*; Bard, A. J., Stratmann, M., Eds.; Wiley-VCH: Weinheim, 2003; Vol. 3, Chapter 2.6, p 196.
19. Randles, J. E. B. *Disc. Farad. Soc.* **1947**, *1*, 11.
20. Warburg, E. *Ann. Phys. Chem.* **1899**, *67*, 493.
21. Christensen, P. A.; Hamnett, A. In *Techniques and Mechanisms in Electrochemistry*; Blackie Academic & Professional: London, 1994; Chapter 2.2.5, p 197.
22. Hillman, A. R. In *Encyclopedia of Electrochemistry*; Bard, A. J., Stratmann, M., Eds.; Wiley-VCH: Weinheim, 2003; Vol. 3, Chapter 2.7, p 230.
23. Sauerbrey, G. *Z. Phys.* **1959**, *155*, 206.
24. Nomura, T.; Iijima, M. *Anal. Chim. Acta* **1981**, *131*, 97.
25. Bruckenstein, S.; Shay, M. *Electrochim. Acta* **1985**, *30*, 1295.
26. Granstaff, V. E.; Martin, S. J. *J. Appl. Phys.* **1994**, *75*, 1319.
27. Rosenbaum, J. F. In *Bulk Acoustic Wave Theory and Devices*; Artech House: Boston, 1988.
28. Bandey, H. L.; Martin, S. J.; Cernosek, R. W. ; Hillman, A. R. *Anal. Chem.* **1999**, *71*, 2205.
29. Martin, S. J.; Bandey, H. L.; Cernosek, R. W.; Hillman, A. R.; Brown, M. J. *Anal. Chem.* **2000**, *72*, 141.
30. Bandey, H. L.; Hillman, A. R.; Brown, M. J.; Martin, S. J. *Farad. Discuss.* **1997**, *107*, 105.
31. Cernosek, R. W.; Martin, S. J.; Hillman, A. R.; Bandey, H. L. *IEEE Trans. Ultrason., Ferroelectr. Freq. Cont.* **1998**, *45*, 1399.
32. Lucklum, R.; Behling, C.; Cernosek, R. W.; Martin, S. J. *J. Appl. Phys. D: Appl. Phys.* **1997**, *30*, 346.
33. Hillman, A. R.; Jackson, A.; Martin, S. J. *Anal Chem.* **2001**, *73*, 540.
34. Ballantine, D. S.; White, R. M.; Martin, S. J.; Ricco, A. J.; Zellers, E. T.; Frye, G. C.; Wohltjen, H. In *Acoustic Wave Sensors - Theory, Design, and Physico-Chemical Applications*; Academic Press: San Diego; 1997.

35. Roser, S. J.; Richardson, R. M.; Swann, M. J.; Hillman, A. R. *J. Chem Soc. Faraday Trans.* **1991**, *87*, 2863.
36. Glidle, A. ; Cooper, J.; Hillman, A. R.; Bailey, L.; Jackson, A.; Webster, J. R. P. *Langmuir* **2003**, *19*, 7746.
37. Brown, M. J.; Hillman, A. R.; Martin, S. J.; Cernosek, R. W.; Bandey, H. L. *J. Mater. Chem.* **2000**, *10*, 115.
38. Aklonis, J. J.; MacKnight, W. J. In *Introduction to Polymer Viscoelasticity*; Wiley: New York, 1983.
39. Frye, G. C.; Martin, S. J. *Appl. Spec. Rev.* **1991**, *26*, 73.
40. Ballantine, D. S.; White, R. M.; Martin, S. J.; Ricco, A. J.; Zellers, E. T.; Frye, G. C.; Wohltjen, H. In *Acoustic Wave Sensors - Theory, Design, and Physico-Chemical Applications*; Academic Press: San Diego, 1997; Chapter 4, p 150.
41. Ballantine, D. S.; White, R. M.; Martin, S. J.; Ricco, A. J.; Zellers, E. T.; Frye, G. C.; Wohltjen, H. In *Acoustic Wave Sensors - Theory, Design, and Physico-Chemical Applications*; Academic Press: San Diego, 1997; Chapter 6, p 358.
42. Christensen, P. A.; Hamnett, A. In *Techniques and Mechanisms in Electrochemistry*; Blackie Academic & Professional: London, 1994; Chapter 2.1.9, p 131.
43. Sherwood, P. M. A. In *The Handbook of Surface Imaging and Visualization*; Hubbard, A. T., Ed.; CRC Press: Boca Raton, 1995; Chapter 63, p 875.
44. Koch, E.-E. In *Handbook of Synchrotron Radiation*; North-Holland Publishing Company: Amsterdam 1983; Vol. 1B.
45. Baruchel, J.; Hodeau, J.-L. ; Lehmann, M. S.; Regnard, J.-R.; Schlenker, C. In *HERCULES, Neutron and Synchrotron Radiation for Condensed Matter Studies*; Springer Verlag: Berlin, 1993; Vol. 1.
46. Farley, N. R. S. In *Structural Studies of Electroactive Transition Metal Oxide Films*, PhD Thesis, University of Leicester, Department of Physics and Astronomy, 2001.
47. Lee, P. A.; Pendry, J. B. *Phys. Rev. B* **1975**, *11*, 2795.
48. [srs.dl.ac.uk/xrs](http://srs.dl.ac.uk/xrs).
49. [http://cars9.uchicago.edu/~newville/Presentations/Denver\\_Xray.ppt](http://cars9.uchicago.edu/~newville/Presentations/Denver_Xray.ppt).
50. Gurman, S. J.; Binsted, N.; Ross, I. *J. Phys. C: Solid State Phys.* **1984**, *17*, 143.
51. Skoog, D. A.; Holler, F. J.; Nieman, T. A. In *Principles of Instrumental Analysis*, 5th ed.; Harcourt Brace College Publishers: Philadelphia, 1998; p 549.

52. Cowley, J. M. In *The Handbook of Surface Imaging and Visualization*; Hubbard, A. T., Ed.; CRC Press: Boca Raton, 1995; Chapter 11, p 131.
53. Goldstein, J.; Newbury, D. E.; Joy, D. C.; Lyman, C. E.; Echlin, P.; Lifshin, E.; Sawyer, L. C.; Michael, J. R. In *Scanning Electron Microscopy and X-Ray Microanalysis*; Springer: 2003.
54. Reimer, L. In *Scanning Electron Microscopy*; Springer-Verlag: Berlin, 1985.
55. Macpherson, J. V. In *Encyclopedia of Electrochemistry*; Bard, A. J., Stratmann, M., Eds.; Wiley-VCH: Weinheim, 2003; Vol. 3, Chapter 3.2, p 415.
56. Gewirth, A. A.; LaGraff, J. R. In *The Handbook of Surface Imaging and Visualization*; Hubbard, A. T., Ed.; CRC Press: Boca Raton, 1995; Chapter 2, p 23.
57. Ohnesorge, F.; Binning, G. *Science* **1993**, 260, 1451.

# Chapter 3

*EXPERIMENTAL*

### 3.1 CHEMICALS

The [M(*salen*)] complexes reported in this thesis were synthesised by colleagues in the Department of Chemistry, Faculty of Sciences from the University of Porto, Portugal. Complexes [Ni(3-Mesalophen)], [Ni(3-Mesalophen-b15-c5)], [Ni(3-MeOsaloophen-b15-c5)] and [Ni(3-Mesalophen-b18-c6)] were prepared as described in the literature<sup>1,2</sup> and [Ni(3-MeOsaltMe)] as described elsewhere<sup>2,3</sup>. The compounds were characterised by elemental analysis of carbon, nitrogen and hydrogen, low resolution mass spectrometry, nuclear magnetic resonance of proton (NMR <sup>1</sup>H) and spectroscopic techniques including FTIR and UV-Vis.

Multi-walled carbon nanotubes (MWCNTs) prepared by combustion chemical vapour deposition (CCVD) process were obtained from Nanocyl (reference NC3100). According to the supplier specifications, MWCNTs have average diameter of 9.5 nm, average length of 1.5  $\mu$ m and carbon purity >95%.

In electrochemical measurements, tetrabutylammonium perchlorate (TBAP) (Fluka, *puriss. Electrochemical grade*), dichloromethane (ROMIL, Ultra Purity Solvents-HPLC), and anhydrous acetonitrile (Aldrich, 99.8 %) were used as received. Anhydrous barium perchlorate and cesium perchlorate (Aldrich, 99.999 %), and magnesium perchlorate (Fluka, *puriss.  $\geq$  99.0 %*) were used as received in ion recognition studies.

### 3.2 PREPARATION AND CHARACTERISATION OF MODIFIED ELECTRODES BY CYCLIC VOLTAMMETRY

#### 3.2.1 Instrumentation

Electrochemical studies were performed using an Autolab PGSTAT 20 potentiostat/galvanostat, controlled by GPES software. A closed standard three-electrode cell was used with a Pt disc working electrode (0.0314 cm<sup>2</sup>), a Pt wire counter electrode, and a Ag/AgCl (1 mol dm<sup>-3</sup> NaCl) reference electrode (Metrohm ref. 60724140). Prior to use, the working electrode was polished with an aqueous suspension of 0.3  $\mu$ m alumina (Beuhler) on a Master-Tex (Beuhler) polishing pad, and then washed with deionised water and CH<sub>3</sub>CN. The reference and the auxiliary electrodes were washed with deionised water and solvent. All the solutions were deaerated by passing a flow of nitrogen gas through them.

### 3.2.2 Electropolymerisation

Poly[Ni(3-Mesalophen-b15-c5)] films were deposited by cycling the potential of the working electrode between  $-0.3$  and  $1.3$  V, in  $\text{CH}_3\text{CN}$  solution containing  $0.1 \text{ mmol dm}^{-3}$  of [Ni(3-Mesalophen-B15-C5)] and  $0.1 \text{ mol dm}^{-3}$  TBAP; the number of cycles was varied from 1 to 150, and the scan rate kept constant at  $0.1 \text{ V s}^{-1}$ .

### 3.2.3 Cyclic voltammetry of modified electrodes

Following electropolymerisation, the film was rinsed with dried  $\text{CH}_3\text{CN}$  and then immersed in  $0.1 \text{ mol dm}^{-3}$  TBAP/ $\text{CH}_3\text{CN}$ ; the modified electrode was cycled in the range  $-0.3$  V to  $1.3$  V, at different scan rates varying from  $0.01 \text{ V s}^{-1}$  up to  $0.5 \text{ V s}^{-1}$ . Five potential cycles was determined as optimum for a reproducible electrochemical response.

### 3.2.4 Determination of oxidation degree and surface coverage

The oxidation degree  $n$  associated with the electroactive films was determined by comparing the polymerisation charge  $Q_{pol}$  associated with films prepared with 1 deposition cycle, with the redox charge  $Q_{redox}$  of the resulting modified electrodes cycled in background electrolyte at  $0.01 \text{ V s}^{-1}$ . The coulometric assay used to calculate this parameter is published in the literature<sup>4</sup> and discussed in detail in Chapter 4 (Equation 4.1).

Surface coverage  $\Gamma$  was calculated for all the films by using  $Q_{redox}$  (from the voltammogram acquired in background electrolyte) and consequent application of Equation 2.23 (Chapter 2). To ensure complete redox conversion of the film on the voltammetric timescale, it was established that  $Q_{redox}$  was determined in a scan rate-independent regime;  $\nu = 0.01 \text{ V s}^{-1}$  was found to be optimum.

### 3.2.5 Ion recognition studies

After the electrochemical characterisation of poly[Ni(3-Mesalophen-b15-c5)] films in background electrolyte, solutions of perchlorate salts  $\text{X}(\text{ClO}_4)_y$  ( $\text{X}=\text{Cs}^+$ ,  $\text{Mg}^{2+}$  or  $\text{Ba}^{2+}$ ,  $y=1$  or  $2$ )/ $0.1 \text{ mol dm}^{-3}$  TBAP/  $\text{CH}_3\text{CN}$  were added to the system in different concentration ranges:

(i) *small additions*:  $10 \text{ }\mu\text{L}$  aliquots of  $2.5 \text{ mmol dm}^{-3}$   $\text{X}(\text{ClO}_4)_y$ /  $0.1 \text{ mol dm}^{-3}$  TBAP/  $\text{CH}_3\text{CN}$ , were added to films prepared with 1, 5, and 10 deposition cycles (final concentrations  $0.03$ ,  $0.08$  and  $0.1 \text{ mmol dm}^{-3}$ , respectively);

(ii) *intermediate additions*: 10  $\mu\text{L}$  and 50  $\mu\text{L}$  aliquots of  $0.05 \text{ mol dm}^{-3} \text{ X}(\text{ClO}_4)_2$  ( $\text{X} = \text{Mg}^{2+}$  and  $\text{Ba}^{2+}$ )/ $0.1 \text{ mol dm}^{-3}$  TBAP/  $\text{CH}_3\text{CN}$  were added to films prepared with deposition cycles ranging from 10 to 150; the low solubility of  $\text{CsClO}_4$  in  $\text{CH}_3\text{CN}$  limited this study, with only  $5 \text{ mmol dm}^{-3} \text{ CsClO}_4$  / $0.1 \text{ mol dm}^{-3}$  TBAP/  $\text{CH}_3\text{CN}$  being used (final concentrations  $3 \text{ mmol dm}^{-3}$  for  $\text{Mg}^{2+}$  and  $\text{Ba}^{2+}$  and  $0.05 \text{ mmol dm}^{-3}$  for  $\text{Cs}^+$ );

(iii) *large additions*: a single 500  $\mu\text{L}$  aliquot of  $1 \text{ mol dm}^{-3} \text{ X}(\text{ClO}_4)_2$  ( $\text{X} = \text{Mg}^{2+}$  and  $\text{Ba}^{2+}$ )/ $0.1 \text{ mol dm}^{-3}$  TBAP/  $\text{CH}_3\text{CN}$  was added to all the films (final concentrations  $0.1 \text{ mol dm}^{-3}$ ).

After each addition the system was left to equilibrate at 0.0 V for 15 minutes. The voltammetric response was then recorded at  $0.1 \text{ V s}^{-1}$ . At the end of the additions the films were then cycled at different scan rates ( $0.01 \text{ V s}^{-1}$  -  $1 \text{ V s}^{-1}$ ). The solution was replaced by fresh, metal cation-free supporting electrolyte and the potential cycled again at  $0.1 \text{ V s}^{-1}$ .

### 3.3 UV-VIS TRANSMISSION SPECTROSCOPY

#### 3.3.1 Instrumentation

The instrument used was a Hewlett Packard HP8451A spectrophotometer. The measurements were made *in situ* in transmission mode, with the electrode under potential control, using an Autolab PGSTAT 20 potentiostat/galvanostat. The electrochemical cell used was locally designed. Briefly, it consists of a main body made of Teflon, and two parallel optical windows which are placed in opposite positions within the cell. One of the windows is made of quartz and a Pt gauze is attached to it and used as counter electrode; the other is the working electrode which consists of indium tin oxide-coated conducting glass (ITO, Balzers) with its area (typically  $2.1 \text{ cm}^2$ ) defined by a silicone sealant (Dow Corning 3145TV). Both the electrodes are electrically connected to the potentiostat through copper wires using a conducting silver resin (R. S. Components). The reference electrode was Ag/AgCl ( $3 \text{ mol dm}^{-3} \text{ NaCl}$  – BAS ref. MF-2052). The spectrometer was programmed to acquire spectra at 0.5 s intervals in the range of 280-1100 nm.

### 3.3.2 Electropolymerisation

Prior to the polymerisation process, the spectra of  $0.1 \text{ mol dm}^{-3}$  TBAP/ $\text{CH}_3\text{CN}$  solution and  $0.1 \text{ mmol dm}^{-3}$  of  $[\text{Ni}(\text{3-Mesalophen-b15-c5})]/0.1 \text{ mol dm}^{-3}$  TBAP/ $\text{CH}_3\text{CN}$  solution were collected. Poly $[\text{Ni}(\text{3-Mesalophen-b15-c5})]$  film was then deposited by cycling the potential of the working electrode in the presence of monomer solution between  $-0.3 \text{ V}$  and  $1.3 \text{ V}$ , at  $0.02 \text{ V s}^{-1}$  during 5 cycles.

### 3.3.3 Characterisation of modified electrodes

Following the deposition process, the modified electrodes were washed with  $\text{CH}_3\text{CN}$  and immersed in  $0.1 \text{ mol dm}^{-3}$  TBAP/ $\text{CH}_3\text{CN}$ . The spectra were acquired and recorded during the process of oxidation/reduction (*redox switching*) of the films in similar conditions to those used in the polymerisation (potential interval, number of cycles, scan rate, wavelength range and acquisition time).

### 3.3.4 Ion recognition studies

After the characterisation in background electrolyte a  $200 \text{ }\mu\text{L}$  aliquot of  $0.05 \text{ mol dm}^{-3}$   $\text{X}(\text{ClO}_4)_2$  ( $\text{X} = \text{Mg}^{2+}, \text{Ba}^{2+}$ ) /  $0.1 \text{ mol dm}^{-3}$  TBAP/  $\text{CH}_3\text{CN}$  (or  $5 \text{ mmol dm}^{-3}$   $\text{CsClO}_4/0.1 \text{ mol dm}^{-3}$  TBAP/  $\text{CH}_3\text{CN}$ ) was added to the background electrolyte and the system was left to equilibrate at  $0.0 \text{ V}$  for 15 minutes. The potential was then cycled in the same conditions as in 3.3.2 and the spectra recorded, after which the film was rinsed with dried  $\text{CH}_3\text{CN}$  and the solution was replaced by fresh, metal cation-free supporting electrolyte. The films were then cycled as in 3.3.3 and the UV-Vis spectra recorded again.

## 3.4 COMPOSITIONAL CHARACTERISATION OF POLY[M(SALEN)] FILMS BY X-RAY PHOTOELECTRON SPECTROSCOPY (XPS)

### 3.4.1 Instrumentation

Some of the XPS measurements were performed using the Scienta ESCA300 photoelectron spectrometer at NCESS (Daresbury Laboratory). The instrument employs a high power rotating anode and monochromatised  $\text{Al K}\alpha$  /  $\text{Cr K}\beta$  ( $h\nu = 1486.7 / 5946.7 \text{ eV}$ ) X-ray source with selectable aluminium or chromium targets. The remainder were



performed at the 'Centro de Materiais da Universidade do Porto' (Portugal), in a VG Scientific Escalab 200A spectrometer using non-monochromated Mg K $\alpha$  radiation (1253.6 eV). Deconvolution of the peaks was effectuated using the software XPSPEAK41. Due to the experimental broadening effects, the peaks were adjusted using a combination of gaussian (50%) and lorentzian (50%) functions. The parameters used in the fitting procedures were binding energy and area (FWHM values were kept constant, typically 1 eV). Corrections for sample charge were made by referring all features to the C 1s line at a nominal 285.0 eV (or the N 1s line at 399.0 eV).

### **3.4.2 Preparation and characterisation of modified electrodes**

Poly[Ni(3-Mesalophen-b15-c5)] films were prepared by cycling the potential of the working electrode (ITO glass) in the range  $-0.3$  V to  $1.3$  V for 10 deposition cycles at scan rates of  $0.01$ ,  $0.05$  and  $0.1$  V s $^{-1}$ . After the electropolymerisation, the modified electrode was rinsed with dried CH $_3$ CN, immersed in  $0.1$  mol dm $^{-3}$  TBAP/CH $_3$ CN and cycled between  $-0.3$  V and  $1.3$  V, at  $0.1$  and  $0.01$  V s $^{-1}$ . For some samples,  $200$   $\mu$ L ( $500$   $\mu$ L) of  $0.1$  mol dm $^{-3}$  ( $1$  mol dm $^{-3}$ ) Ba(ClO $_4$ ) $_2$  was added to the electrolyte and the system left to rest for 15 minutes, after which the potential was cycled within the same range at  $0.1$  V s $^{-1}$ .

## **3.5 STRUCTURAL CHARACTERISATION OF POLY[M(SALEN)] FILMS BY X-RAY ABSORPTION SPECTROSCOPY (XAS)**

### **3.5.1 Instrumentation**

XAS measurements were carried out using stations 7.1 and 16.5 of the 2 GeV synchrotron radiation source at the CCLRC Daresbury Laboratory. Beam currents during data acquisition varied between  $145$  and  $200$  mA. Station 7.1 is a medium energy XAS station useable over the energy from  $4$  to  $10.5$  keV. The incident X-ray beam was monochromatised using a Si (111) double-crystal monochromator with harmonic rejection set at  $80\%$ . Before and after passing through the monochromator, the size of the beam was defined horizontally and vertically by two slits and both the monochromator and the slits were kept in evacuated chambers. Spectra were acquired near the Ni K-edge ( $8333$  eV) in both transmission and fluorescence modes. For transmission data, two gas-filled ion chambers were used to detect the beam intensities before and after the sample. A third

detector was placed behind a nickel foil to provide absolute energy calibration. The fluorescence detector was a compact nine-element solid-state detector with fast count rate electronics useable up to 150 kHz per channel. Station 16.5 provides XAS measurements on ultra-dilute systems in the energy range 7-40 keV. A pre-mirror provides collimation and the incident X-ray beam is monochromatized by a double crystal monochromator with sagittal focus. Spectra were acquired above the Ba K-edge (37441eV) in fluorescence mode. The detector used was a 30-element Ge solid-state detector with high count-rate electronics linear up to 200 kHz per channel.

### 3.5.2 Design of electrochemical cell for XAS applications

The electrochemical cell used in the first studies (XAS measurements of poly[Ni(3-MeOsaltMe)] near Ni K-edge) was designed by a previous researcher in the group<sup>5</sup>. This cell showed some experimental limitations for study of the specific systems under the scope of this thesis, primarily the small volume cell. The latter case limited the study of complexes with low solubility.

The *in situ* XAS electrochemical cell used for studies of poly[Ni(3-MeOsaltMe)] near the Ba K-edge as well as for poly[Ni(*salen*)(crown ether)] films is depicted in [Figure 3.1](#). It consists of a main body of Teflon cell with two mylar windows, whose position is adjustable by screw threads to define the cell volume and solution path lengths (typically 3 mm). The screws were designed in a manner to allow the use of the cell at 45° in fluorescence mode. An adjustable container of 60 mL volume enables the production of thick films from complexes with low solubility. The cell used in Ni K-edge was similar to this one, except that it had only one entrance/screw, and the counter and working electrodes were separated by a silicon disc. Leakages were prevented by using silicon glue.

The working electrodes were Pt discs (Goodfellow), with (i) thickness 1.0  $\mu\text{m}$  and area 1.77cm<sup>2</sup> for poly[Ni(3-MeOsaltMe)] in Ni K-edge experiments and (ii) thickness 50.0  $\mu\text{m}$  and area 0.72 cm<sup>2</sup> for the rest of experiments; there is no particular significance to the different cells and electrodes used. In both cases a Pt mesh electrode was used as the counter electrode while the reference electrode was Ag/AgCl (1.0 mol dm<sup>-3</sup> NaCl – BAS ref. MF-2052)).

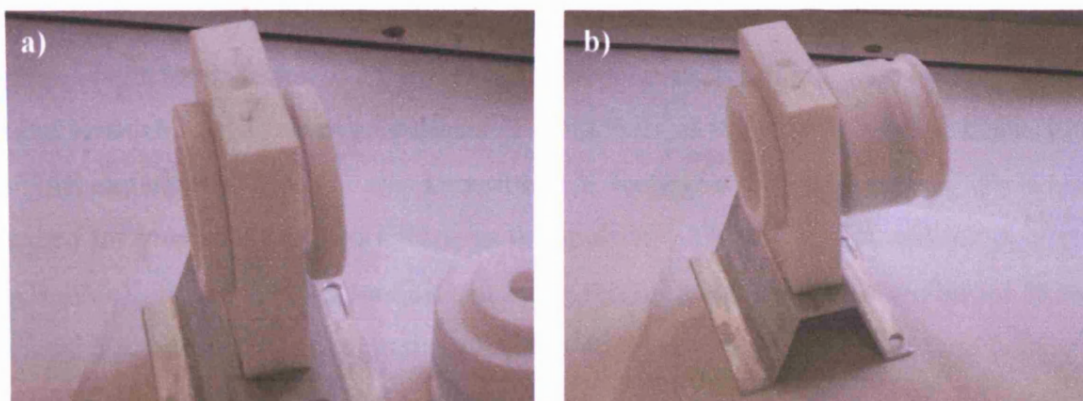


**Figure 3.1:** a) Electrochemical cell (machined from Teflon) for *in situ* XAS experiments and b) with the adjustable container for film polymerisation.

### 3.5.3 XAS measurements

At the Ni K-edge, the runs/spectra were collected and averaged as follows: 3 runs for the powders and solutions, and 8–10 for the films. In the case of Ba K-edge, 10 and 20 runs were respectively averaged for  $\text{Ba}(\text{ClO}_4)_2$  solution and film in background electrolyte. The film data were taken in clean electrolyte ( $\text{Ba}(\text{ClO}_4)_2$  absent), otherwise Ba in solution would have dominated the EXAFS signal completely. Each run took about 20 mins, with the run time per point increasing (as  $k^3$ ) from 2 to 10 seconds per point across the spectrum (standard procedure at the SRS Daresbury Laboratory facility).

#### 3.5.3.1 Poly[Ni(3-MeOsaltMe)]

Ni K-edge X-ray absorption spectra of monomer [Ni(3-MeOsaltMe)] were obtained in powder form,  $0.01\text{--}0.02 \text{ mol dm}^{-3}$  complex in  $0.1 \text{ mol dm}^{-3}$  TBAP/ $\text{CH}_3\text{CN}$  solution and  $0.01\text{--}0.02 \text{ mol dm}^{-3}$  complex in  $0.05 \text{ mol dm}^{-3}$   $\text{Ba}(\text{ClO}_4)_2$  /  $0.1 \text{ mol dm}^{-3}$  TBAP/ $\text{CH}_3\text{CN}$  solution. The films for Ni K-edge XAS measurements were obtained by electropolymerisation of the Ni complex solutions referred before (20 to 30 polymerisation cycles, potential interval 0.0 V to 1.3 V at scan rate  $0.02 \text{ Vs}^{-1}$ ). Upon polymerisation, films were thoroughly rinsed with dry  $\text{CH}_3\text{CN}$  and transferred to a  $0.1 \text{ mol dm}^{-3}$  TBAP/ $\text{CH}_3\text{CN}$  solution and cycled between 0.0 V and 1.3 V ( $\nu = 0.1 \text{ V s}^{-1}$ ). The X-ray absorption spectra of the films were obtained *in situ* under potentiostatic conditions, at 0.0 V and 1.3 V; before the beginning of each XAS experiment the films were kept at 0.0 V and 1.3 V, for approximately 900 s, to ensure that the films were fully reduced and oxidised, respectively. New films prepared in the same conditions were immersed in  $0.05 \text{ mol dm}^{-3}$   $\text{Ba}(\text{ClO}_4)_2/0.1$

mol dm<sup>-3</sup> TBAP/CH<sub>3</sub>CN solution for 15 minutes, and after being thoroughly rinsed with dry CH<sub>3</sub>CN and transferred to a 0.1 mol dm<sup>-3</sup> TBAP/CH<sub>3</sub>CN solution, the X-ray absorption spectra were collected under potentiostatic conditions at 0.0 V; prior to the beginning of the XAS experiment, the film was kept at 0.0 V for 900 s. The Ba K-edge spectra were obtained for 0.05 mol dm<sup>-3</sup> Ba(ClO<sub>4</sub>)<sub>2</sub> in 0.1 mol dm<sup>-3</sup> TBAP/CH<sub>3</sub>CN and for poly[Ni(3-MeOsaltMe)], deposited and conditioned using the same experimental conditions as those prepared for Ni K-edge measurements. The film spectra were obtained *in situ* under potentiostatic conditions, at 0.0 V; before the beginning of XAS experiment, the film was kept at 0.0 V for 900 s.

### 3.5.3.2 Poly[Ni(*salen*)(crown ether)]

The Ni K-edge XAS absorption spectra of the monomers and deposited films (absence and presence of barium solutions) were obtained, in powder and under potentiostatic conditions, respectively; the films were obtained by electropolymerisation (typically 20 to 30 polymerisation cycles) by cycling the potential between -0.3 V to 1.3 V, at a scan rate of 0.02 V s<sup>-1</sup>. Following the electropolymerisation, films were thoroughly rinsed with dried CH<sub>3</sub>CN and transferred to a 0.1 mol dm<sup>-3</sup> TBAP/CH<sub>3</sub>CN solution and cycled between -0.3 V and 1.3 V at 0.02 Vs<sup>-1</sup>. The X-ray absorption spectra of the films were then obtained *in situ* under potentiostatic conditions at 0.0 V. The films were then immersed in 0.05 mol dm<sup>-3</sup> Ba(ClO<sub>4</sub>)<sub>2</sub>/0.1 mol dm<sup>-3</sup> TBAP/CH<sub>3</sub>CN solution for 2 hours and after being thoroughly rinsed with dry CH<sub>3</sub>CN, they were transferred to a 0.1 mol dm<sup>-3</sup> TBAP/CH<sub>3</sub>CN solution and the X-ray absorption spectra collected at 0.0 V. At Ba K-edge, XAS spectra were obtained for a 0.05 mol dm<sup>-3</sup> Ba(ClO<sub>4</sub>)<sub>2</sub> in 0.1 mol dm<sup>-3</sup> TBAP/CH<sub>3</sub>CN and for the films deposited using the same experimental conditions as those prepared for Ni K-edge.

### 3.5.5 EXAFS data analysis

The background EXAFS signal was subtracted as follows. The pre-edge was fitted by a first-order polynomial and the post-edge data was fitted by third-order polynomials to give a smoothly varying background absorption  $\mu_0$ , which was then used to give the EXAFS function  $\chi(\text{Energy})$  in the usual manner<sup>6</sup>.

The data from EXBACK were processed by the program EXCURV98, which enabled extraction of the structural information from the data. This program is based on the fast curved wave theory<sup>7</sup>, and works with the EXAFS function in photoelectron momentum space,  $\chi(k)$ . Only single-scattering events were included in this analysis. Theoretical curves were fitted to the experimental data by means of non-linear least-squares fitting. In the process of fitting, several parameters were involved. The main fitting parameters are:  $R_m$  (the interatomic distances) and  $E_0$  (the energy offset which corresponds to the Fermi energy), correlated parameters which control the phase of the function  $\chi(k)$ ; and the pair  $N_m$  (the number of neighbours at a given distance) and  $\sigma_m$  (the root mean square deviation in distance, usually referred to as the Debye-Waller factor) which control the amplitude of  $\chi(k)$ . The type of neighbours  $T_m$  in the shells around the relevant atom was kept constant, being fixed by chemical considerations. The parameters were continuously refined by least-squares iteration until the best fit between the experimental and theoretical curves was obtained. The process of fitting was assisted by DFT calculations for the monomer and crystallographic data obtained for similar Nickel-*salen* complexes. The uncertainties in the parameters were obtained using EXCURV98: a 95% confidence limit was always used. The theory of this statistical test is fully described elsewhere<sup>8</sup>.

The fitting range used for both Ni and Ba K-edges ran from  $k=1$  to  $13 \text{ \AA}^{-1}$ . Throughout the fitting by EXCURV98, the amplitude factor AFAC was fixed at 0.78 for Ni K-edge measurements and at 1.0 for Ba K-edge measurements.

## 3.6 RHEOLOGICAL CHARACTERISATION OF POLY[M(SALEN)] FILMS BY ELECTROCHEMICAL QUARTZ CRYSTAL MICROBALANCE (EQCM)/CRYSTAL IMPEDANCE

### 3.6.1 Instrumentation

Crystal impedance spectra were recorded using a Hewlett-Packard HP8751A network analyser, connected via a 50 V coaxial cable to a HP87512A transmission/reflection unit. The crystals used were 10 MHz AT-cut quartz crystals, coated with Pt electrodes with piezoelectrically and electrochemically active areas, respectively, of  $0.21 \text{ cm}^2$  and  $0.23 \text{ cm}^2$ .

The cells used previously for this purpose required the use of large volumes of solution ( $> 5\text{ mL}$ ), which is an important issue when the compounds intended to be studied are expensive and/or difficult to synthesise. Additionally, the difficulty related to the handling of quartz crystals and their attachment to the cells was also a problem. The new cell (Figure 3.2) requires less than  $3\text{ mL}$  of solution; its design is similar to that of cells used in cyclic voltammetry, which means that comparisons between electrochemical data obtained with both cells are straightforward. The Pt coating in the quartz crystal was used as working electrode, a Pt wire was used as the counter electrode, and a Ag/AgCl ( $1\text{ mol dm}^{-3}\text{ NaCl}$ , Metrohm ref. 60724140) was used as reference electrode.

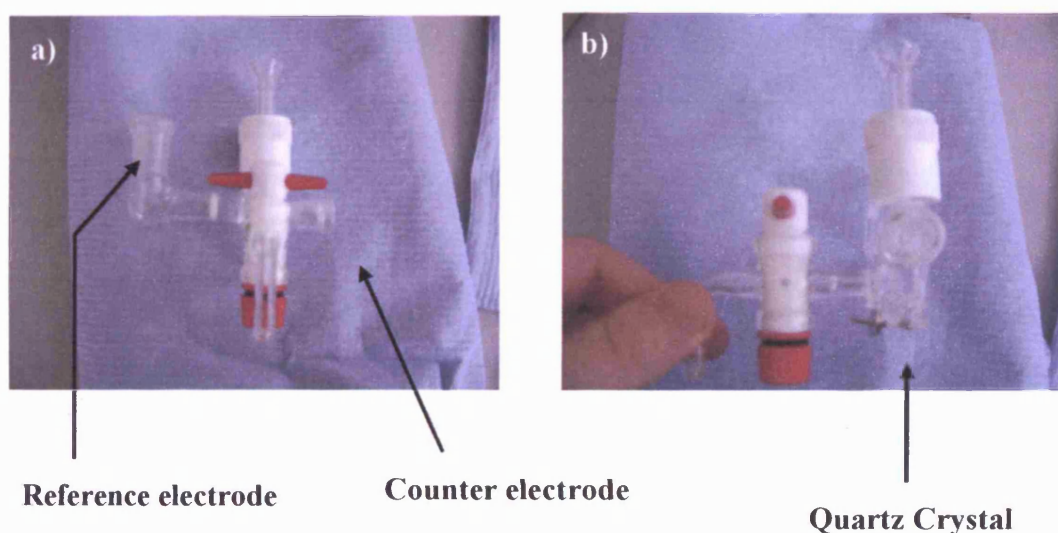


**Figure 3.2:** Electrochemical cell for crystal impedance measurements.

### 3.6.2 Electropolymerisation

Crystal impedance measurements were made in real time, monitoring the deposition process at the fundamental frequency (in the region of  $10\text{ MHz}$ ). Prior to the deposition process, the admittance spectra of the bare crystal were acquired in air and in solution at  $10\text{ MHz}$ , as well as at the harmonic frequencies ( $30$ ,  $50$ ,  $70$  and  $90\text{ MHz}$ ). A potentiodynamic program was used for the deposition, with the potential cycled between  $-0.3\text{ V}$  and  $1.3\text{ V}$  at scan rates of  $0.01$  and  $0.02\text{ V s}^{-1}$ . The films were prepared from  $\text{CH}_3\text{CN}$  solutions containing  $0.1\text{ mmol dm}^{-3}$   $[\text{Ni}(\text{3-Mesalophen-b15-c5})]$  and  $0.1\text{ mol dm}^{-3}$  TBAP.

### 3.6.3 Characterisation of modified electrodes

Following deposition, the modified electrode was transferred to background electrolyte solution ( $0.1 \text{ mol dm}^{-3}$  TBAP in  $\text{CH}_3\text{CN}$ ). Cyclic voltammetry (potential interval between  $-0.3 \text{ V}$  and  $1.3 \text{ V}$ , scan rate  $0.01/0.1 \text{ V s}^{-1}$ ) and monitoring of admittance were performed for all the films at  $10 \text{ MHz}$ . In the case of viscoelastic films the admittance was also recorded for  $30$ ,  $50$ ,  $70$  and  $90 \text{ MHz}$  harmonics. Following redox switching,  $500 \mu\text{L}$  of  $0.05 \text{ mol dm}^{-3} \text{ Ba}(\text{ClO}_4)_2 / 0.1 \text{ mol dm}^{-3} \text{ TBAP/CH}_3\text{CN}$  was added to background electrolyte and the system was left to rest for  $15 \text{ minutes}$ . Afterwards, the redox switching procedure was repeated and the admittance spectra recorded.

## 3.7 IMAGING AND MORPHOLOGY CHARACTERISATION OF POLY[M(SALEN)] FILMS BY ATOMIC FORCE MICROSCOPY (AFM) AND SCANNING ELECTRON MICROSCOPY (SEM)

### 3.7.1 Instrumentation

Film samples to be analysed by AFM and SEM were prepared using an Autolab PGSTAT 20 potentiostat/galvanostat, controlled by GPES software. A closed standard three-electrode cell was used with ITO glass as the working electrode, a Pt wire counter electrode, and a Ag/AgCl ( $1 \text{ mol dm}^{-3} \text{ NaCl}$ ) reference electrode (Metrohm ref. 60724140). AFM images were acquired using a Digital Instruments (DI) Nanoscope IV, Dimension 3100 instrument, in resonant/tapping mode (software version 6.12). SEM was performed in high-vacuum conditions, using a high resolution (Schottky) environmental scanning electron microscope (ESEM) with X-ray microanalysis and backscattered electron diffraction pattern analysis (FEI Quanta 400FEG / EDAX Genesis X4M).

### 3.7.2 Preparation of modified electrodes

Samples for SEM and AFM analysis were deposited on ITO conducting glass electrodes or Pt quartz crystals, and electrochemically characterised as follows. The potential was cycled between  $-0.3 \text{ V}$  and  $1.3 \text{ V}$  in the presence of a  $\text{CH}_3\text{CN}$  solution containing  $0.1 \text{ mmol dm}^{-3} [\text{Ni}(3\text{-Mesalophen-b15-c5})]$  and  $0.1 \text{ mol dm}^{-3} \text{ TBAP}$ . The potential scan rate ( $\nu$ ) was varied between  $0.005 \text{ V s}^{-1}$  and  $0.1 \text{ V s}^{-1}$ . The resulting



modified electrodes were then rinsed with dried CH<sub>3</sub>CN and the electrochemical response in background electrolyte (0.1 mol dm<sup>-3</sup> TBAP/CH<sub>3</sub>CN) recorded at 0.01 and 0.1 V s<sup>-1</sup>.

Before SEM measurements a thin (10 nm) Au layer was deposited on the top of the samples to prevent charging problems. AFM samples were cut with razor blades to provide an estimate of the film thickness.

### **3.8 PREPARATION AND CHARACTERISATION OF NANOCOMPOSITES BASED ON POLY[M(SALEN)] FILMS AND MULTI-WALLED CARBON NANOTUBES (MWCNTs)**

#### **3.8.1 Functionalisation of carbon nanotubes**

Functionalisation of MWCNTs was performed by colleagues at the Department of Chemical Engineering, Faculty of Engineering from the University of Porto, Portugal. It involved a range of oxidising treatments, as follows: (i) used as received with no treatment, *i.e.* the control sample, designated *T0*; (ii) oxidised under reflux with HNO<sub>3</sub> 7 M for 6 hours, washed with distilled water until a neutral pH was reached and dried overnight in an oven at 100 °C, designated *T1*; (iii) oxidised with 5% O<sub>2</sub> in N<sub>2</sub> at 500° C for 6 hours (burn off of 30 %), designated *T2*; (iv) sample *T1* heat treated under inert atmosphere (He) at 400 °C for 1 hour, designated *T3*.

Surface oxygen groups of MWCNT-TX (X = 0, 1, 2, 3, defined above) were characterised by temperature programmed desorption (TPD)<sup>9,10</sup>. The analyses were performed in an AMI-200 (Altamira Instruments) apparatus. In a typical experiment, a 100 mg sample was subjected to a 5°C° min<sup>-1</sup> linear temperature rise up to 1100°C under helium flow of 25 cm<sup>3</sup>° min<sup>-1</sup>. A mass spectrometer (Dymaxion 200 amu, Ametek) was used to monitor the desorbed CO (*m/z* = 28) and CO<sub>2</sub> (*m/z* = 44) signals.

BET surface areas (*S*<sub>BET</sub>) were calculated from the N<sub>2</sub> equilibrium adsorption isotherms, determined at -196 °C with a Coulter Omnisorp 100 CX apparatus.

#### **3.8.2 Instrumentation used in the preparation of composites**

Electrochemical studies were performed using an Autolab PGSTAT 20 potentiostat/galvanostat, controlled by GPES and FRA software. A closed standard three-electrode cell was used with a Pt disc working electrode (geometric area 0.0314 cm<sup>2</sup>), a Pt



wire counter electrode, and a Ag/AgCl (1 mol dm<sup>-3</sup> NaCl, Metrohm ref. 60724140) reference electrode.

### 3.8.3 Preparation of composites based on [M(*salen*)] and MWCNTs

The single component poly[Ni(3-Mesalophen-b15-c5)] film was deposited by immersing the working electrode in a CH<sub>3</sub>CN (or CH<sub>2</sub>Cl<sub>2</sub>) solution containing 0.1 mmol dm<sup>-3</sup> nickel(*salen*) monomer and 0.1 mol dm<sup>-3</sup> TBAP, then cycling the potential between -0.3 and 1.3 V at  $\nu = 0.005 \text{ V s}^{-1}$ . In the case of composites, the deposition solution contained also 0.02 % wt of MWCNTs-TX. Prior to use, the latter solutions were sonicated for 30 minutes to ensure complete suspension of the MWCNTs.

### 3.8.4 Electrochemical characterisation of composites

After film deposition, the polymer (or polymer composite) modified electrodes were thoroughly rinsed with dry solvent then immersed in 0.1 mol dm<sup>-3</sup> TBAP/solvent; the solvent (CH<sub>3</sub>CN or CH<sub>2</sub>Cl<sub>2</sub>) was the same used in deposition. The working electrode potential was then cycled between -0.3 V and 1.3 V at  $\nu = 0.1 \text{ V s}^{-1}$  and  $0.01 \text{ V s}^{-1}$  (the first for conditioning and the second for determination of *I*). The conditioning treatment is performed so the system response becomes reproducible: five cycles were used, although reproducibility was generally achieved after the second cycle.

Following the polymerisation and redox switching-based assay, impedance spectra were acquired with the films immersed in background electrolyte and held at DC potentials of -0.3, 0.2, 0.9 and 1.3 V. The frequency range explored was  $10^{-2} \leq f / \text{Hz} \leq 10^5$ , sampling 15 points per decade. The amplitude of the sinusoidal signal was 0.005 V. Between measurements the films were cycled in background electrolyte to check that there was no significant loss in surface-immobilised electroactive material.

### 3.8.5 Morphology characterisation of composites by SEM

The instrumentation used is the same as in 3.7.1. Nanocomposite samples for SEM analysis were deposited on ITO conducting glass electrodes as described in 3.8.3 and characterised electrochemically as described in 3.8.4.

## REFERENCES:

1. Pedersen, C. J. *J. Am. Chem. Soc.* **1967**, 89, 7017.
2. Holm, R. H.; Everett, G. W.; Chacravorty, A. *Prog. Inorg. Chem.* **1966**, 7, 183.
3. Vilas-Boas, M.; Santos, I. C.; Henderson, M. J.; Freire, C.; Hillman, A. R.; Vieil, E. *Langmuir* **2003**, 19, 7460.
4. Vilas-Boas, M.; Freire, C.; de Castro, B.; Christensen, P. A.; Hillman, A. R. *Inorg. Chem.* **1997**, 36, 4919.
5. Farley, N. R. S. In *Structural Studies of Electroactive Transition Metal Oxide Films*, PhD Thesis, University of Leicester, Department of Physics and Astronomy, 2001.
6. EXCALIB and EXBACK routines: [srs.dl.ac.uk/xrs](http://srs.dl.ac.uk/xrs).
7. Gurman, S. J.; Binsted, N.; Ross, I. *J. Phys. C: Solid State Phys.* **1984**, 17, 143.
8. Joyner, R. W.; Martin, K. J.; Meehan, P. *J. Phys. C: Solid State Phys.* **1987**, 20, 4005.
9. Figueiredo, J. L.; Pereira, M. F. R.; Freitas, M. M. A.; Orfao, J. J. M. *Carbon* **1999**, 37, 1379.
10. Figueiredo, J. L.; Pereira, M. F. R.; Freitas, M. M. A.; Orfao, J. J. M. *Ind. Eng. Chem. Res.* **2007**, 46, 4110.

## Chapter 4

***PREPARATION AND CHARACTERISATION OF  
POLY[Ni(3-MESALOPHEN-B15-C5)] BY CYCLIC  
VOLTAMMETRY AND UV-VIS SPECTROSCOPY***

## 4.1 INTRODUCTION

This chapter describes the preparation and characterisation of poly[Ni(3-Mesalophen-b15-c5)] films. Cyclic voltammetry is employed to prepare films by oxidative polymerisation of monomer, as well as to study the electrochemical properties of the resulting polymers (redox activity, charge transport). Additionally, UV-Vis spectroelectrochemistry is used to investigate the electronic structure of the films, with particular attention given to the type of charge carriers. The objective is to correlate the intrinsic electronic structure of poly[Ni(3-Mesalophen-b15-c5)] with its electrochemical properties. Similar studies were performed for poly[Ni(*salen*)] analogues<sup>1-4</sup> and will be mentioned here to contextualise the results obtained for this specific polymeric film.

In addition, film ion recognition properties were investigated using perchlorate salts of Cs<sup>+</sup>, Mg<sup>2+</sup> and Ba<sup>2+</sup>. These are of paramount importance to assess, from an electrochemical/electronic point of view, the effectiveness of macrocycle substituents towards ion binding.

## 4.2 PREPARATION AND CHARACTERISATION OF POLY[Ni(3-MESALOPHEN-B15-C5)] BY CYCLIC VOLTAMMETRY

### 4.2.1 Electropolymerisation

Figure 4.1 depicts the voltammetric response of 0.1 mmol dm<sup>-3</sup> [Ni(3-Mesalophen-b15-c5)] in 0.1 mol dm<sup>-3</sup> TBAP/CH<sub>3</sub>CN, as the potential was cycled between -0.3 V and 1.3 V. The current intensity increases in successive cycles, with the occurrence of new peaks corresponding to the irreversible formation of new species (insoluble, bound to the electrode).

In the first scan (panel a) the system shows two anodic waves at  $E_{pa}$  = 0.89 V and 1.03 V, and two cathodic waves at  $E_{pc}$  = 0.12 V and 0.75 V. In the second scan a new anodic wave appears at  $E_{pa}$  = 0.21 V, which is attributed to the oxidation of the film formed during the first cycle. The feature attributed to the monomer oxidation in the first cycle ( $E_{pa}$  = 0.89 V), is overlapped in subsequent scans with an anodic wave occurring at lower potentials ( $E_{pa}$  = 0.88 V); the latter corresponds to the oxidation of deposited film. The lower oxidation potential of oligomers with respect to monomeric species is a premise for the occurrence of electropolymerisation<sup>5,6</sup>.

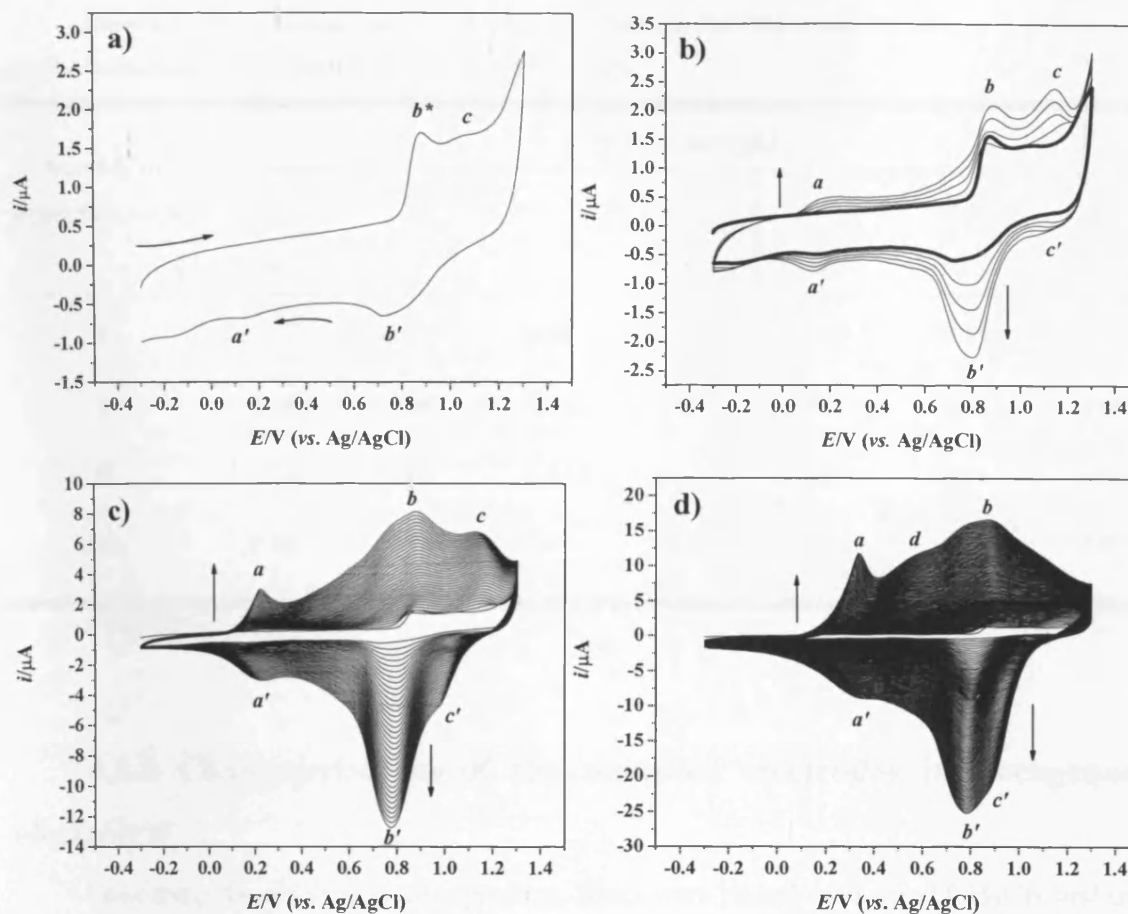


**Figure 4.1:** Voltammograms obtained during the oxidative polymerisation of [Ni(3-Mesalophen-b15-c5)] at  $0.1 \text{ V s}^{-1}$ , by cycling the potential between  $-0.3 \text{ V}$  and  $1.3 \text{ V}$ . Number of deposition cycles **a)** 1, **b)** 5, **c)** 35 and **d)** 100. Arrows in panel **a** indicate the direction of potential cycling; in panels **b**, **c** and **d** arrows indicate the increase of anodic/cathodic current intensity as a result of deposition of electroactive species. The peak potentials associated with the redox features  $a/a'$ ,  $b/b'$ ,  $c/c'$  and  $d$  are shown in [Table 4.1](#);  $b^*$  corresponds to the monomer oxidation.

The current intensity associated with the redox features increases with the number of scans ([panels b, c and d](#)) up to 150 cycles, the largest number of deposition cycles used. Broadening and coalescence of redox features may occur; this makes the assignment of peaks difficult. Additionally, positive displacement of peak potentials labelled as  $a/a'$  and negative displacement of peak potentials  $b/b'$  and  $c/c'$  are detected. For the thickest films ([Figure 4.1, panel d](#)) a new anodic wave is formed at  $E_{pa} = 0.58 \text{ V}$ .

**Table 4.1:** Peak potentials associated with redox features observed during oxidative polymerisation of [Ni(3-Mesalophen-b15-c5)] in 0.1 mol dm<sup>-3</sup> TBAP/CH<sub>3</sub>CN.

Number of deposition cycles	E/V vs. Ag/AgCl						
	E <sub>pa</sub>				E <sub>pc</sub>		
	a	b	c	d	a'	b'	c'
1	-	0.89*	1.03	-	0.12	0.75	-
5	0.19	0.88	1.15	-	0.12	0.80	1.08
35	0.22	0.88	1.14	-	0.22	0.78	0.98
100	0.34	0.86	-	0.58	0.34	0.78	0.87

(\*) monomer's oxidation

#### 4.2.2 Characterisation of the modified electrodes in background electrolyte

Following the polymerisation process, films were rinsed with dried CH<sub>3</sub>CN and then immersed in monomer-free, background electrolyte. [Figure 4.2](#) shows the voltammetric response of modified electrodes. For each film the *i*-*E* curve for the first anodic half-cycle differs from the subsequent ones. This effect, more pronounced for thinner films, was reported by Dahm for similar poly[Ni(*salen*)] films<sup>7</sup> and attributed to structural reorganisation. After the second scan, the electrochemical response becomes fairly reproducible. This initial stage, which includes the first few scans, is designated as *film conditioning*. Unless otherwise specified, all the data presented refer to conditioned films.

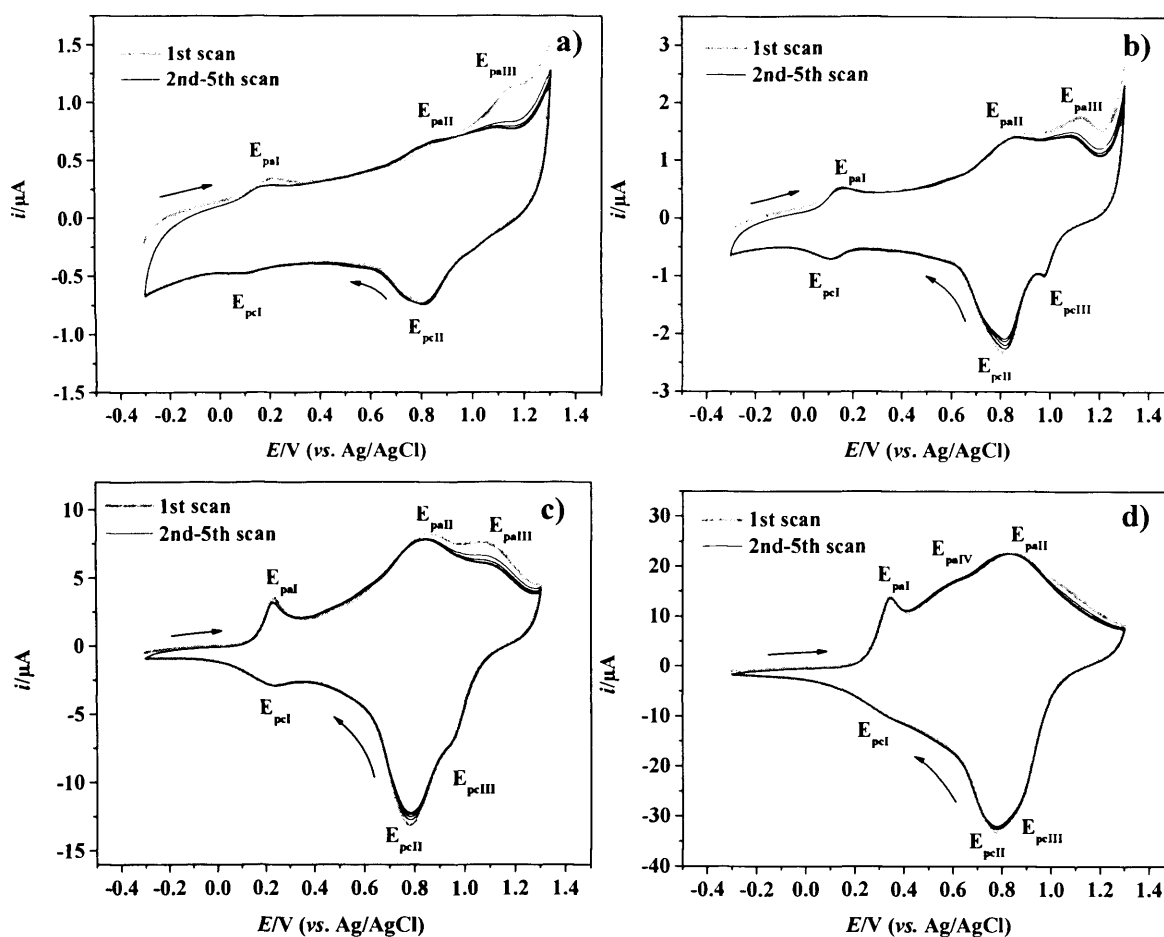


**Figure 4.2:** Voltammetric response of modified electrodes poly[Ni(3-Mesalophen-b15-c5)] prepared with a) 1, b) 5, c) 35 and d) 100 cycles, and acquired in 0.1 mol dm<sup>-3</sup> TBAP/CH<sub>3</sub>CN at 0.1 V s<sup>-1</sup> from -0.3 to 1.3 V. Arrows indicate the direction of potential cycling.

Table 4.2 shows the peak potentials of the redox features observed in Figure 4.2. For the film prepared with 5 deposition cycles (Figure 4.2b) three anodic processes occurring at  $E_{pal}=0.15$  V,  $E_{paiI}=0.86$  V and  $E_{paiII}=1.08$  V and three cathodic processes at  $E_{pcl}=0.11$  V,  $E_{pclI}=0.82$  V and  $E_{pclII}=0.98$  V are observed. Excluding the thickest films, all the others show three reversible processes. A fourth process occurring at  $E_{paiV}=0.55$  V, is evident for films prepared with 100 and 150 deposition cycles as  $E_{paiIII}$  virtually disappears. These films also show a less reproducible electrochemical response when compared to thinner films.

**Table 4.2:** Peak potentials associated with redox features of poly[Ni(3-Mesalophen-b15-c5)], by cycling  $E$  between  $-0.3$  and  $1.3$  V at  $0.1$  V s $^{-1}$ , in  $0.1$  mol dm $^{-3}$  TBAP/CH $_3$ CN (5 $^{th}$  scan).

Number of deposition cycles	E/V vs. (Ag/AgCl)						
	E <sub>paI</sub>	E <sub>paII</sub>	E <sub>paIII</sub>	E <sub>paIV</sub>	E <sub>pcI</sub>	E <sub>pcII</sub>	E <sub>pcIII</sub>
1	0.17	0.84	1.09	-	0.10	0.79	-
5	0.15	0.86	1.08	-	0.11	0.82	0.98
35	0.23	0.84	1.11	-	0.24	0.79	0.95
100	0.35	0.83	-	0.55	0.37	0.78	0.89

#### 4.2.2.1 Determination of oxidation degree and electroactive surface coverage

The number of deposition cycles is not a reliable parameter to estimate either the thickness or the number of electroactive sites present in the modified electrodes. Instead, surface coverage  $\Gamma$  (Equation 2.23, Chapter 2) is used as the measure of the electroactive sites and is obtained using coulometric data ( $Q$ ).

In order to estimate  $\Gamma$ , it is necessary to have knowledge about the extent of oxidation/reduction per monomer unit. This parameter is called oxidation degree,  $n$ , and can be calculated by using a double-coulometric assay<sup>1,2,4</sup>. In this assay the anodic charge passed during polymerisation ( $Q_{pol}$ ) and the anodic charge passed during redox switching ( $Q_{redox}$ ) are compared. It is assumed that polymerisation is 100% efficient and charge associated with film degradation is negligible. In the case of polymerisation, three processes involving charge consumption are considered: (i) polymerisation, (ii) redox processes associated with the metal centre and (iii) redox processes associated with the ligand. In the oxidation/reduction of the modified electrode in background electrolyte only processes (ii) and (iii) may occur. Polymerisation is assumed to occur by removal of 2 electrons of each monomeric unit and linkage between the phenyl rings. Assigning  $y$  as the number of electrons transferred per phenyl ring ( $2y$  per monomer) and  $x$  as the number of electrons transferred per metal centre,  $Q_{pol}:Q_{redox}$  ratio is given by:

$$\frac{Q_{pol}}{Q_{redox}} = \frac{2 + 2y + x}{2y + x} \quad (4.1)$$



For films prepared with 1 deposition cycle,  $Q_{pol}$  and  $Q_{redox}$  were found to be in the range of 4.93-5.77  $\mu\text{C}$  and 0.881-1.21  $\mu\text{C}$ , respectively, which gives an average  $Q_{pol}:Q_{redox}$  ratio of 5.29. The only meaningful solution is obtained when  $x$  is an integer (either 0 or 1) and  $y$  positive. In the present case  $x$  cannot be 1, otherwise  $y < 0$ ; therefore, the solution of Equation 4.1 is  $x=0$  and  $y=0.237$ , which corresponds to  $n=2y+x=0.47$  (one positive charge delocalised over *ca.* two monomeric units). This indicates that redox processes occurring in the polymeric film are ligand-based. Similar results were found for poly[Ni(*salen*)] homologues<sup>1,2,4</sup>.

$\Gamma$  quantifies the number of electroactive sites along the polymer. The deposition of electroactive species is dependent on several experimental factors, including the number of deposition cycles, potential interval, scan rate and monomer concentration.

All the experimental parameters except the number of deposition cycles were kept constant during polymerisation. Therefore,  $\Gamma$  can be depicted directly as a function of deposition cycles (Figure 4.3). In this case,  $\Gamma$  was calculated using the anodic charge  $Q_{redox}$  acquired in background electrolyte at 0.01  $\text{V s}^{-1}$ . The increase of polymeric material on the electrode surface may result in two distinct situations: all the deposited material remains electroactive or the film loses conductivity due to limitations in charge transport. In the present case  $\Gamma$  was found to increase linearly with the number of deposition cycles (0.78  $\text{nmol cm}^{-2} \text{ cycle}^{-1}$ ), so the first scenario is observed. The use of a relatively low scan rate guarantees that all the sites are oxidised/reduced. Similar results were obtained for other poly[Ni(*salen*)] films<sup>2,4</sup>.

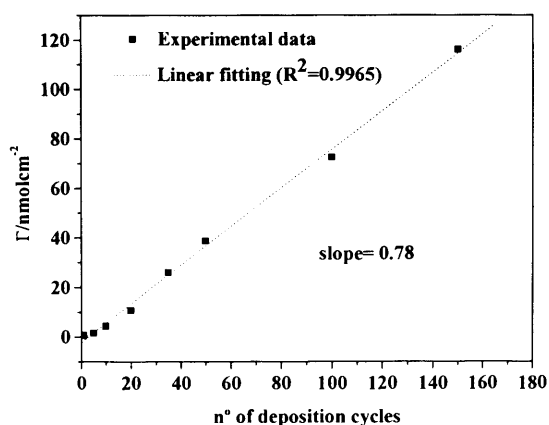


**Figure 4.3:** Dependence of electroactive surface coverage on the number of deposition cycles.

The modified electrodes prepared are classified according to the amount of material deposited:

- (i) *thin films*:  $\Gamma < 10 \text{ nmol cm}^{-2}$ ;
- (ii) *films of intermediate thickness*:  $10 \text{ nmol cm}^{-2} < \Gamma < 70 \text{ nmol cm}^{-2}$ ;
- (iii) *thick films*:  $\Gamma > 70 \text{ nmol cm}^{-2}$ ;

#### 4.2.2.2 Dynamics of charge transfer processes

To study the dependence of both  $i$  and  $E$  on the scan rate  $v$ , the modified electrodes were cycled in background electrolyte at different scan rates ( $0.01\text{-}0.5 \text{ V s}^{-1}$ ). Redox processes whose peak potentials are labelled as  $E_{pall}$  and  $E_{pcll}$  (see section 4.2.2, Table 4.2) were chosen for this purpose because the current intensity associated with them is the highest and can be detected at all scan rates. Figure 4.4 shows the electrochemical responses of two modified electrodes prepared with different surface coverage. Qualitatively, when the scan rate increases the redox features become less resolved and the positions of peak potentials change. For thin films, the degree of symmetry between the shapes of anodic and cathodic waves remains relatively constant (Figure 4.5 panel a), whereas for thick films the symmetry is lost (Figure 4.5 panel b) and some of the waves resolved at long timescales are not restored at shorter timescales.

The dependence of current intensity  $i_{pII}$  upon the scan rate gives evidence regarding the nature of the limiting step associated with charge transport. If the rate of charge transport is faster than the experimental timescale, current density changes linearly with the scan rate. However, when the process of diffusion through the film is slower than the experimental timescale, current density changes with  $v^{1/2}$ . In other words, when the slope of  $\log i_p$  vs.  $\log v$  plot is 1 the charge transport is said to be at equilibrium; when the slope is 0.5 the regime is said to be controlled by diffusion.

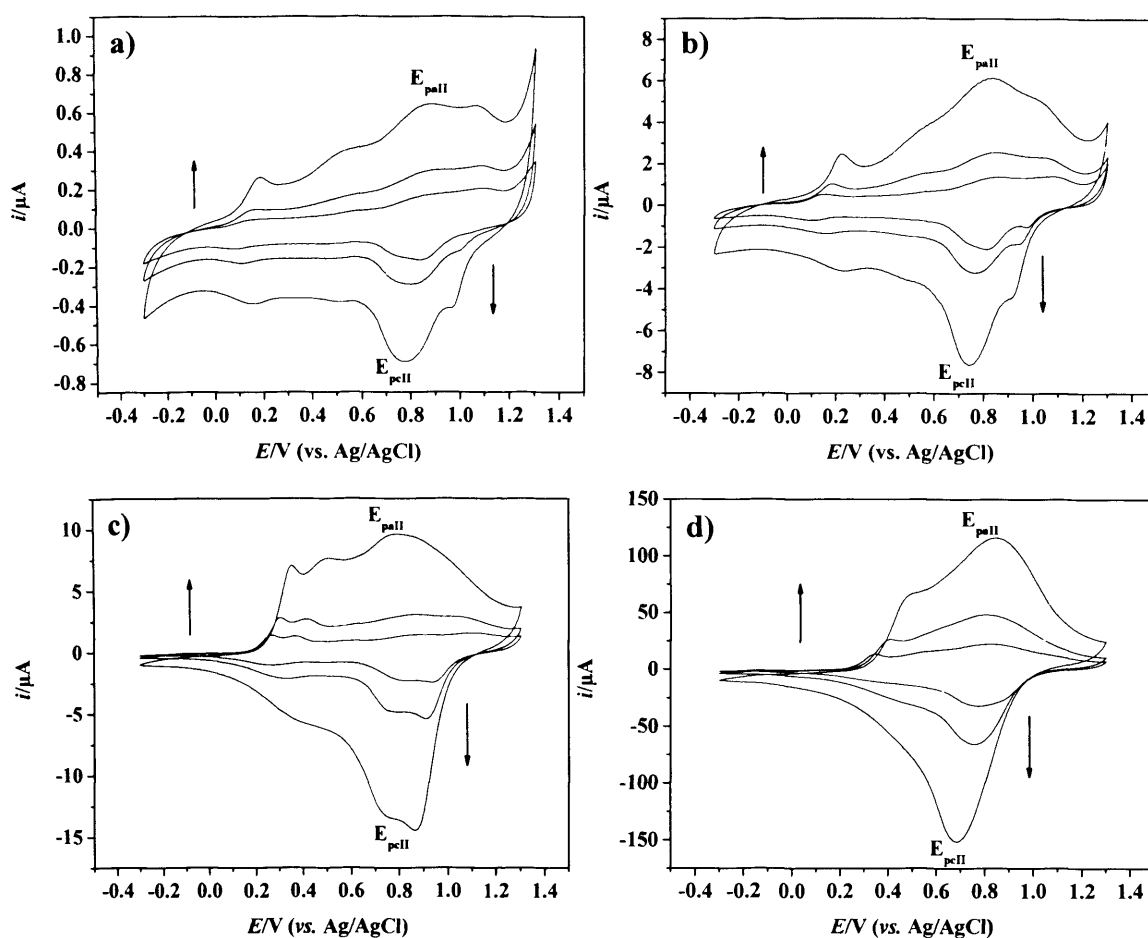


**Figure 4.4:** Voltammetric response of two poly[Ni(3-Mesalophen-b15-c5)] modified electrodes ( $\Gamma=1.7 \text{ nmol cm}^{-2}$  panels a and b;  $\Gamma=86 \text{ nmol cm}^{-2}$  panels c and d), acquired at different scan rates: 0.01, 0.02 and  $0.05 \text{ V s}^{-1}$  (panels a and c) and 0.1, 0.2 and  $0.5 \text{ V s}^{-1}$  (panels b and d). Arrows indicate the increase of current intensity as a result of the scan rate increase.

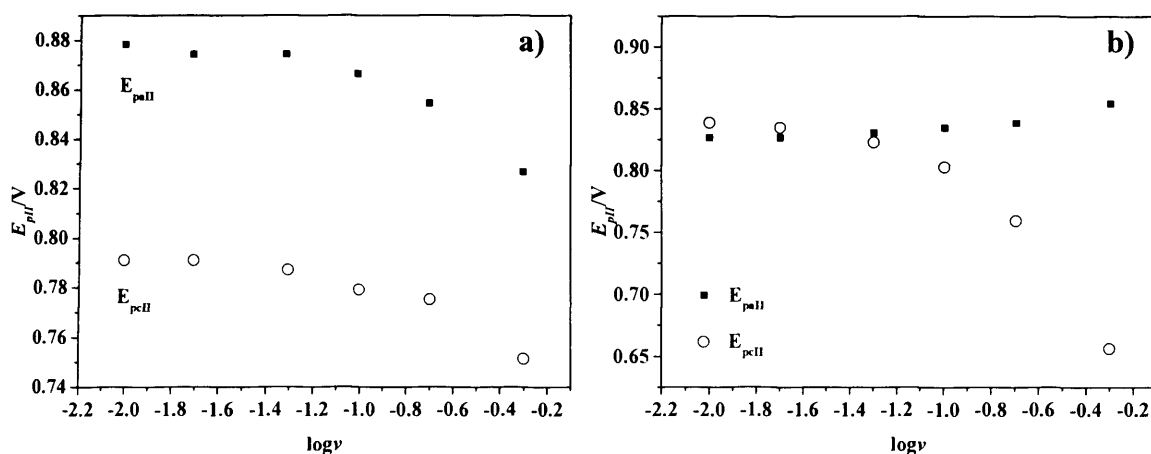


**Figure 4.5:** Dependence of peak potential  $E_{pII}$  on scan rate  $\nu$  of two poly[Ni(3-Mesalophen-b15-c5)] modified electrodes, a)  $\Gamma=1.7 \text{ nmol cm}^{-2}$  and b)  $\Gamma=86 \text{ nmol cm}^{-2}$ .

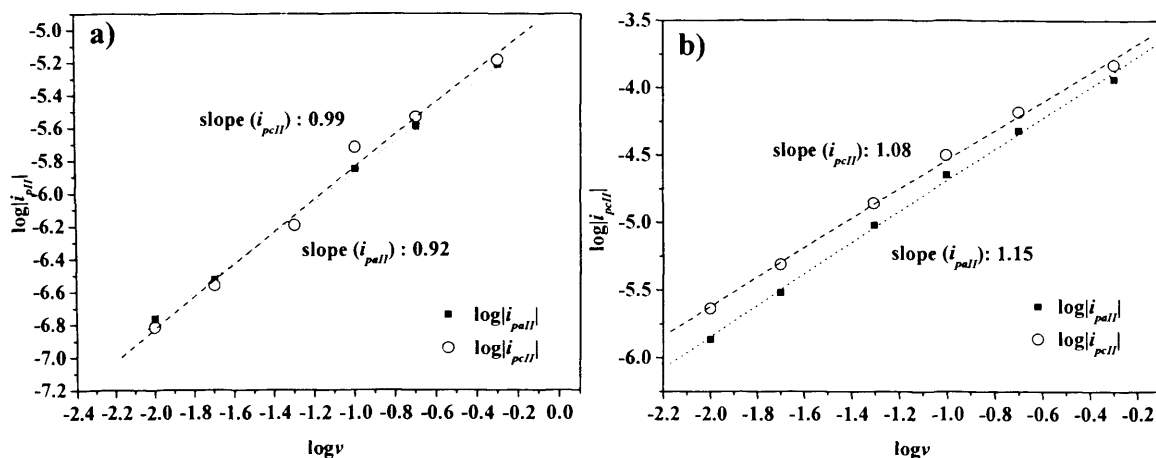


**Figure 4.6:** Dependence of  $\log|i_{p||}|$  on  $\log v$  for two poly[Ni(3-Mesalophen-b15-c5)] modified electrodes, a)  $\Gamma=1.7 \text{ nmol cm}^{-2}$  and b)  $\Gamma=86 \text{ nmol cm}^{-2}$ .

Figure 4.6 depicts the logarithmic dependence of current peak  $i_{p||}$  on the scan rate for the same films reported in Figure 4.4 and Figure 4.5. Both films show a linear dependence with slope values close to 1. Therefore, the charge transport rate is fast in the timescale studied. The same trend was found in all the range of prepared films (Table 4.3), with the system showing a diffusionless behaviour.

**Table 4.3:** Results obtained from dynamics studies of poly[Ni(3-Mesalophen-b15-c5)].

$\Gamma / \text{nmol cm}^{-2}$	Number of deposition cycles	Anodic slope	Cathodic slope	Regime of charge transport
0.71	1	0.86	0.88	Equilibrium
1.7	5	0.92	0.99	Equilibrium
4.3	10	0.99	1.07	Equilibrium
11	20	1.09	1.12	Equilibrium
26	35	1.15	1.12	Equilibrium
39	50	1.15	1.13	Equilibrium
86	100	1.15	1.08	Equilibrium
116	150	1.15	1.04	Equilibrium

### 4.3 ION RECOGNITION STUDIES OF POLY[Ni(3-MESALOPHEN-B15-C5)]

#### 4.3.1 Qualitative analysis of the voltammetric response of poly[Ni(3-Mesalophen-b15-c5)] in the presence of alkali and alkaline earth metal ions

Following the characterisation of poly[Ni(3-Mesalophen-b15-c5)] modified electrodes in background electrolyte, ion recognition studies were performed in order to investigate the influence of alkali and alkaline earth metal cations ( $\text{Cs}^+$ ,  $\text{Mg}^{2+}$  and  $\text{Ba}^{2+}$ ) on the voltammetric response of the system. The effects of metal charge ( $\text{Cs}^+$  vs.  $\text{Ba}^{2+} \sim \text{Mg}^{2+}$ ) and size ( $\text{Mg}^{2+}$  vs.  $\text{Ba}^{2+} \sim \text{Cs}^+$ ) were explored.

Figure 4.7 shows the evolution of the voltammetric response of poly[Ni(3-Mesalophen-b15-c5)] ( $\Gamma \approx 10 \text{ nmol cm}^{-2}$ ) as successive amounts of metal cations are added to the electrolyte. Considering the volume variation negligible after each addition (10  $\mu\text{L}$  and 50  $\mu\text{L}$  aliquots vs. 5 mL of solution), the metal concentration in background electrolyte increased by increments of 5  $\mu\text{mol dm}^{-3}$  for films of panels a, c, and e (24 additions were performed). These increments are here designated as *small additions*. Comparatively, in panels b, d, and f a smaller number of aliquots was added (10), but the concentration of metal cations was higher (*intermediate additions*). The concentration of  $\text{Cs}^+$  solution, limited by the low solubility in  $\text{CH}_3\text{CN}$ , was increased by a factor of 2 (final concentration per increment 10  $\mu\text{mol dm}^{-3}$ ). In the case of  $\text{Mg}^{2+}$  and  $\text{Ba}^{2+}$  additions, the concentration was increased by a factor of 20 (final concentration per increment 100-500  $\mu\text{mol dm}^{-3}$ ). After each single addition, the films were kept under potentiostatic control at 0.0 V for 15 minutes and then the potential cycled between -0.3 and 1.3 V.

Comparisons between the first and last recorded voltammograms show that the evolution of electrochemical response is similar regardless the type of cation added. More specifically, the process occurring at  $E_{\text{pal}}/E_{\text{pcl}}$  is displaced toward more positive potentials, whereas  $E_{\text{palII}}/E_{\text{pclII}}$  and  $E_{\text{palIII}}/E_{\text{pclIII}}$  are displaced in the opposite direction. The decrease in the charge under the voltammogram is an indication of a decrease in film electroactivity, mainly associated with processes at  $E_{\text{palII}}/E_{\text{pclII}}$  and  $E_{\text{palIII}}/E_{\text{pclIII}}$ . These findings suggest that in the presence of metal cations the oxidation of electroactive films becomes increasingly

difficult. Similar results were found for conducting polymers derived from thiophene<sup>8-14</sup> and pyrrole<sup>15-17</sup> repeat units bearing crown ether substituents.

Following small additions the film response shows some specificity (panels a, c, and e). Comparing the response before any addition and at the end of the last addition, the film whose response changed more dramatically is that exposed to  $\text{Cs}^+$  (panel a). Films exposed to  $\text{Mg}^{2+}$  and  $\text{Ba}^{2+}$  (panels c and e) show similar responses at the end of additions. However, there are small differences in the way the redox features evolve after the first few additions: in the case of  $\text{Mg}^{2+}$  additions,  $i_{\text{pall}}$  increases and then decreases, whilst for  $\text{Ba}^{2+}$  additions  $i_{\text{pall}}$  decreases during all the range. The increase of metal concentration per aliquot (panels b, d and f) does not change significantly the trends observed previously, except for  $\text{Ba}^{2+}$  whose  $i_{\text{pall}}$  feature increases after the first few additions (panel f).

In spite of the voltammetric response depending upon metal concentration, its evolution cannot be entirely attributed to the effect of concentration. The final response of modified electrodes after small additions (final cation concentration  $120 \mu\text{mol dm}^{-3}$ ) shows a greater loss in electroactivity and change of peak potentials than the response of modified electrodes at the end of intermediate additions (final cation concentration  $3 \text{ mmol dm}^{-3}$ ). Since in the former case the redox switching was performed on a higher number of occasions, the decrease of electroactivity is also dependent on doping/undoping processes.

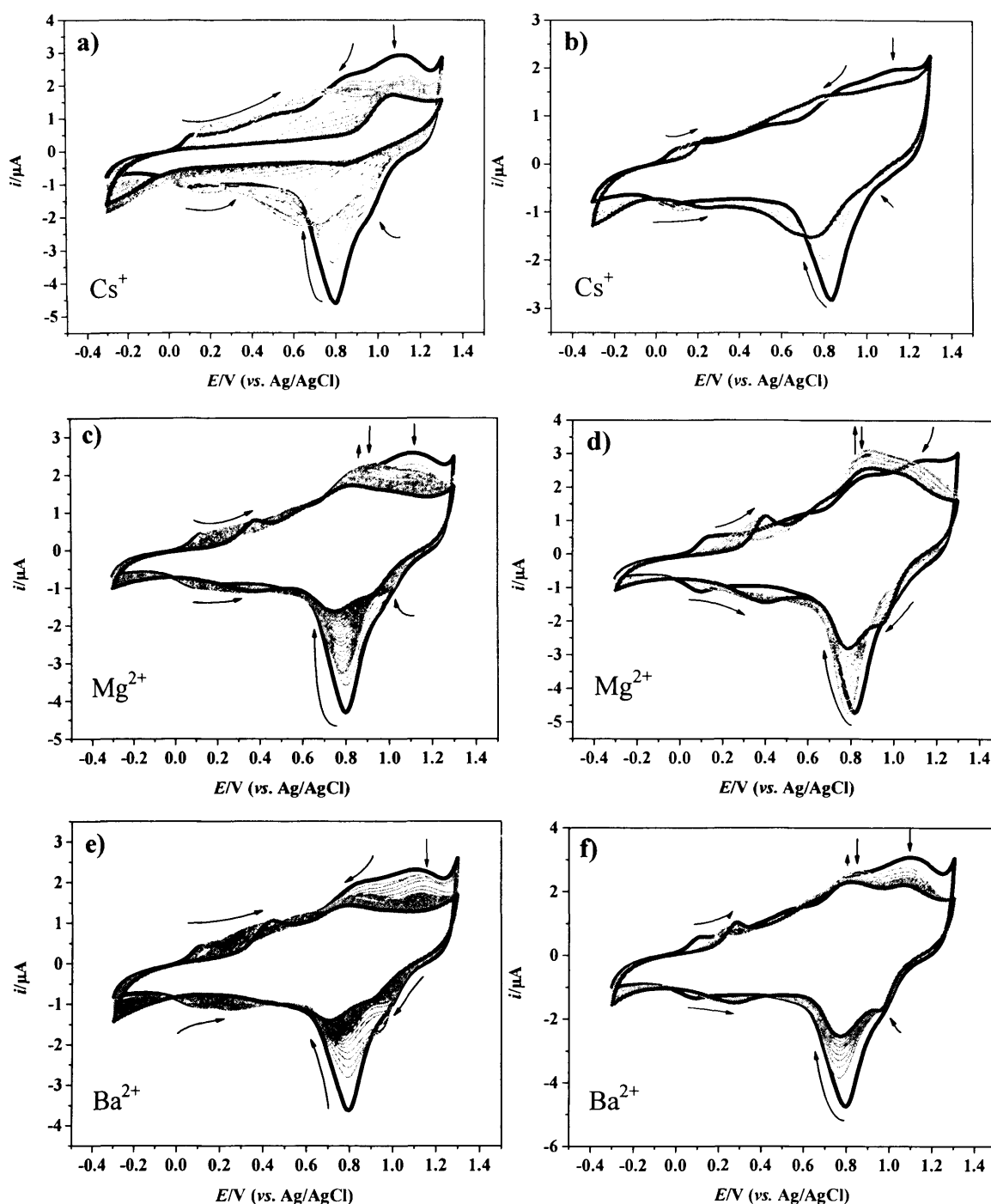


**Figure 4.7:** Voltammetric response of poly[Ni(3-Mesalophen-b15-c5)],  $\Gamma \approx 10 \text{ nmol cm}^{-2}$ , acquired in  $0.1 \text{ mol dm}^{-3}$  TBAP/ $\text{CH}_3\text{CN}$ : (—) before, (---) between successive metal cation additions and (—) after the last addition. Responses in panels a, c and e were obtained following the addition of  $5 \mu\text{mol dm}^{-3}$  aliquots of  $\text{X}(\text{ClO}_4)_y$  ( $\text{X} = \text{Cs}^+$ ,  $\text{Mg}^{2+}$  and  $\text{Ba}^{2+}$ ) to the electrolyte solution; response in panel b was obtained after the addition of  $10 \mu\text{mol dm}^{-3}$  of  $\text{CsClO}_4$  and in d and f after the addition of 100 and  $500 \mu\text{mol dm}^{-3}$  of  $\text{X}(\text{ClO}_4)_2$  ( $\text{X} = \text{Mg}^{2+}$  and  $\text{Ba}^{2+}$ ). Arrows indicate the evolution of the electrochemical features with metal addition and redox-switching.

The voltammetric response of thicker films was also assessed (Figure 4.8). As metal cation additions proceed, films prepared with  $\Gamma \approx 20\text{-}35 \text{ nmol cm}^{-2}$  (panels a, c and e) show the positive displacement of  $E_{pal}/E_{pcl}$  and negative displacement of  $E_{pall}/E_{pcII}$ . Nonetheless, peak potentials and current intensity associated with process II do not change significantly upon addition. This indicates that thicker films are more resilient and electrochemically more stable in the presence of metal cations than thin films.

The responses of poly[Ni(3-Mesalophen-b15-c5)] films prepared with electroactive surface coverage  $\Gamma \approx 80\text{-}100 \text{ nmol cm}^{-2}$  are depicted in Figure 4.8b, d, and f. In spite of being prepared under identical conditions, these films show different voltammetric responses in background electrolyte. This is an indication of the low reproducibility mentioned in section 4.2.2. The coalescence of peaks makes it possible only to assign peak potentials  $E_{pal}$ ,  $E_{pall}$  and  $E_{pcII}$ . Upon metal ion addition,  $E_{pal}$  is displaced to more positive potentials and for  $\text{Cs}^+$  and  $\text{Ba}^{2+}$  additions it fuses completely with  $E_{pall}$ . An increase of peak current at  $E \approx 0.80 \text{ V}$  is observed whilst the current associated with  $E_{pcII}$  decreases for all the cations.

Addition of a  $\text{X}(\text{ClO}_4)_2$  ( $\text{X} = \text{Mg}^{2+}$  and  $\text{Ba}^{2+}$ ) aliquot with final concentration of  $100 \text{ mmol dm}^{-3}$  was also performed, designated here as *large addition* (Figure 4.9). The outcome is an extensive variation of the voltammetric response when compared to intermediate additions (concentration effect). Furthermore, films respond differently to  $\text{Mg}^{2+}$  and  $\text{Ba}^{2+}$ : for  $\text{Mg}^{2+}$  large additions  $E_{pall}$  and  $E_{pcII}$  do not vary to a great extent, and  $i_{pall}$  and  $i_{pcII}$  increase with  $\Gamma$ ; in the case of  $\text{Ba}^{2+}$  addition  $i_{pall}$  increases regardless of  $\Gamma$  but  $i_{pcII}$  is more sensitive to the amount of deposited material, increasing only for intermediate films ( $\Gamma \approx 20\text{-}35 \text{ nmol cm}^{-2}$ ). Additionally, the effect of doping/undoping is more pronounced for films in the presence of  $\text{Ba}^{2+}$ .

In the next section a more detailed and quantitative analysis of the voltammetric response of poly[Ni(3-Mesalophen-b15-c5)] is presented, based on the study of the variation of  $E_{pal}$  and  $i_{pcII}$  features, which change significantly with metal cation addition.



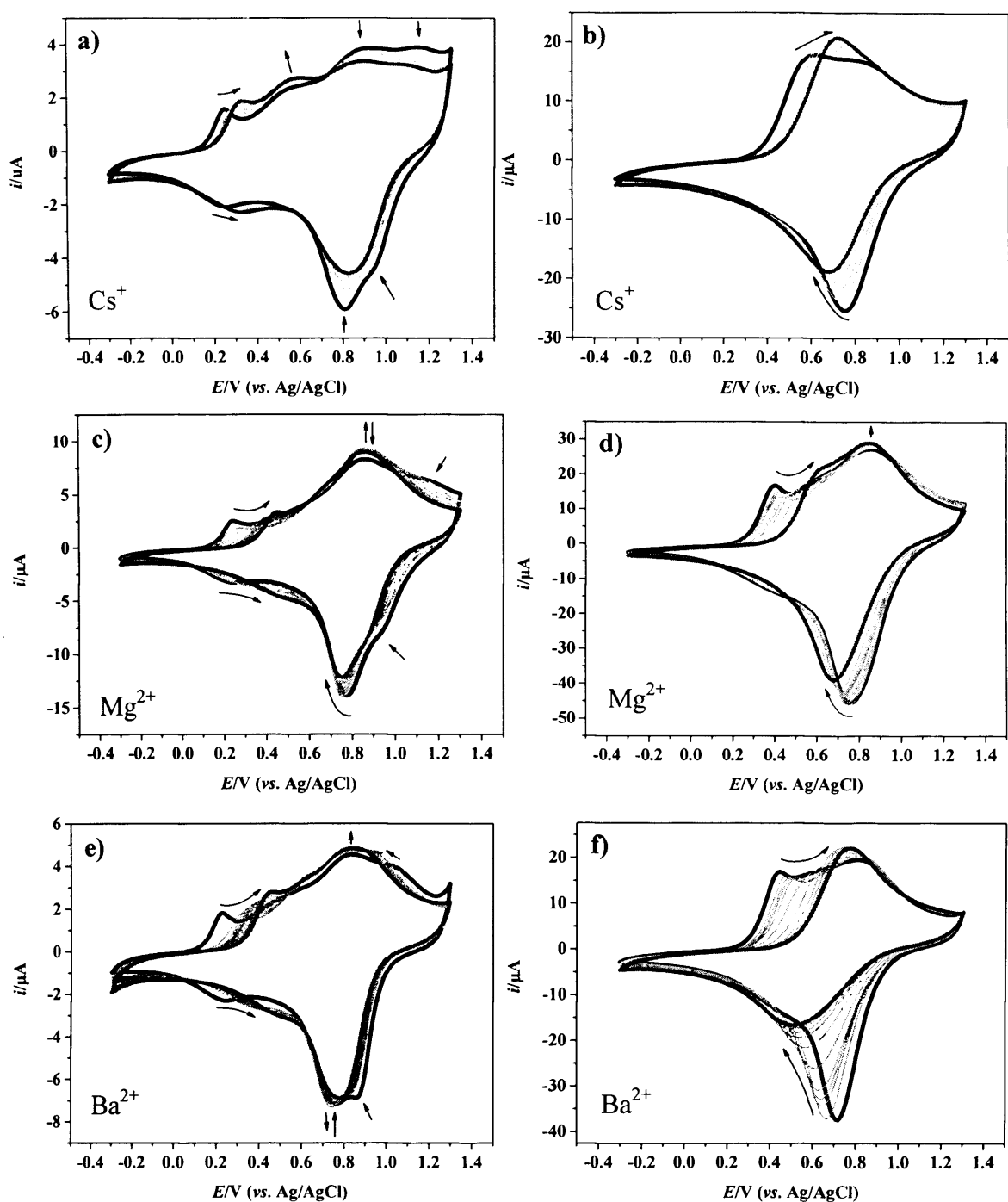


**Figure 4.8:** Voltammetric response of poly[Ni(3-Mesalophen-b15-c5)], acquired in 0.1 mol dm<sup>-3</sup> TBAP/CH<sub>3</sub>CN: (—) before, (---) between successive metal cation additions and (—) after the last addition. Additions consisted of 10 μmol dm<sup>-3</sup> aliquots of CsClO<sub>4</sub> (panels a and b) and 100 and 500 μmol dm<sup>-3</sup> aliquots of X(ClO<sub>4</sub>)<sub>2</sub> (X= Mg<sup>2+</sup> and Ba<sup>2+</sup>) (panels c to f). Films surface coverage: panels a, c, e  $\Gamma \approx 20\text{-}35 \text{ nmol cm}^{-2}$ ; panels b, d, f  $\Gamma \approx 80\text{-}100 \text{ nmol cm}^{-2}$ . Arrows indicate the evolution of the electrochemical features with metal addition and redox-switching.

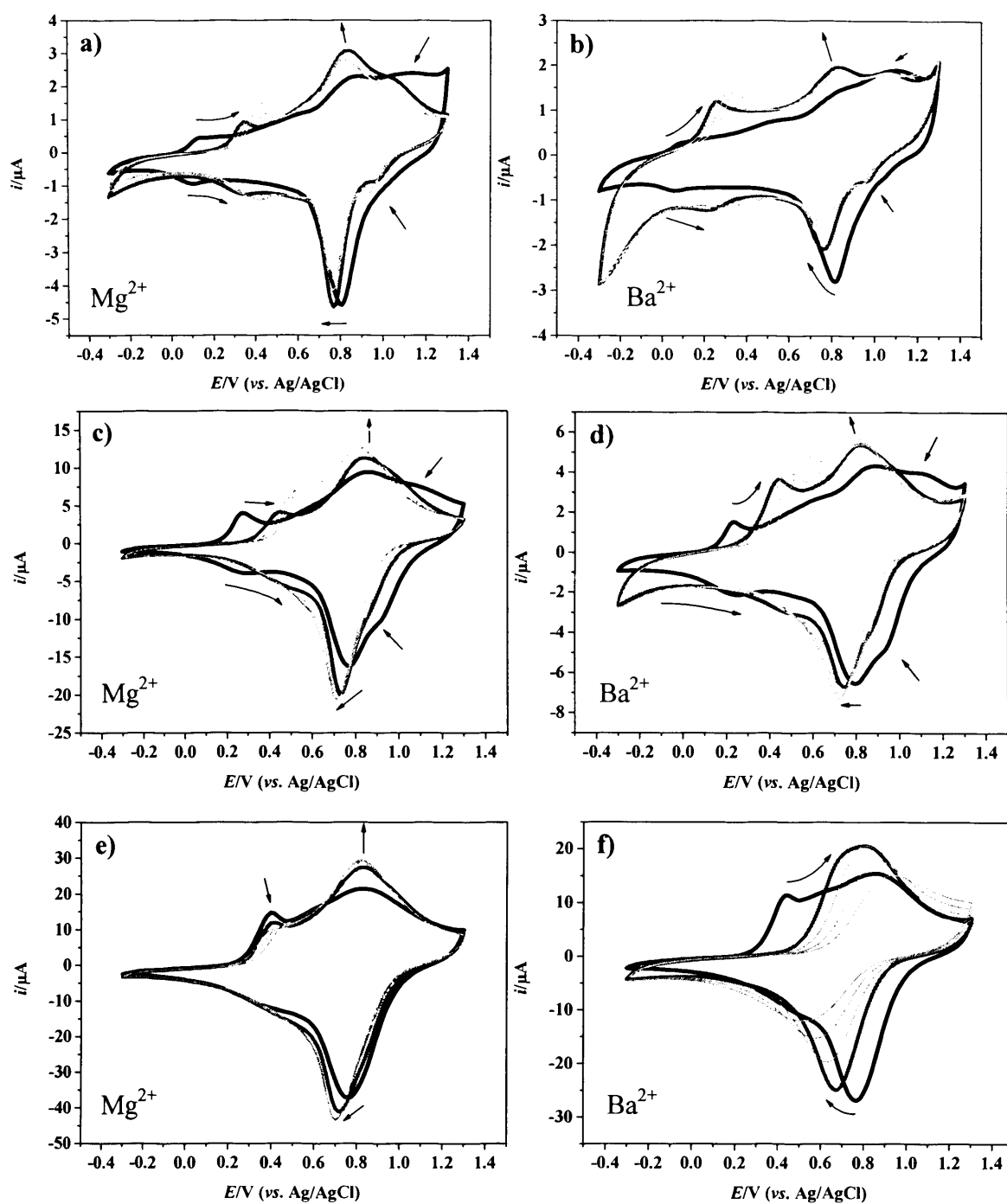


**Figure 4.9:** Voltammetric response of poly[Ni(3-Mesalophen-b15-c5)], acquired in  $0.1 \text{ mol dm}^{-3}$  TBAP/ $\text{CH}_3\text{CN}$ : (—) before and (---) after an addition of  $100 \text{ mmol dm}^{-3}$  of  $\text{X}(\text{ClO}_4)_2$  ( $\text{X} = \text{Mg}^{2+}$  and  $\text{Ba}^{2+}$ ); ( ) response acquired 15, 30 and 45 minutes after the addition. Films surface coverage: panels a, b  $\Gamma \approx 10 \text{ nmol cm}^{-2}$ ; panels c, d  $\Gamma \approx 20\text{-}35 \text{ nmol cm}^{-2}$ ; panels e, f  $\Gamma \approx 60\text{-}90 \text{ nmol cm}^{-2}$ . Arrows indicate the evolution of the electrochemical features with metal addition and redox-switching.

### 4.3.2 Quantitative analysis of the voltammetric response of poly[Ni(3-Mesalophen-b15-c5)] in the presence of alkali and alkaline earth metal ions

#### 4.3.2.1 Dynamic studies

In this section, the dependence of  $E_p$  and  $i_p$  on the scan rate  $\nu$  in the presence of metal cations is considered. Following the addition of the last metal cation aliquot, the potential was cycled at different scan rates (0.01 to 1 V s<sup>-1</sup>) and the voltammetric response of poly[Ni(3-Mesalophen-b15-c5)] recorded. It is assumed that films are electrochemically stable regardless of the potential sweep and the scan rate. This is verified for films which did not undergo many potential sweeps, such as films after intermediate and large additions. Nonetheless, the large number of redox switching procedures performed in small additions studies precluded the analysis of the resulting films in this section. Also, dynamic studies performed after Cs<sup>+</sup> addition studies (Figure 4.10) cannot be assessed due to the rapid loss of electroactivity. Hence, only dynamic studies following Mg<sup>2+</sup> and Ba<sup>2+</sup> additions are considered in detail.

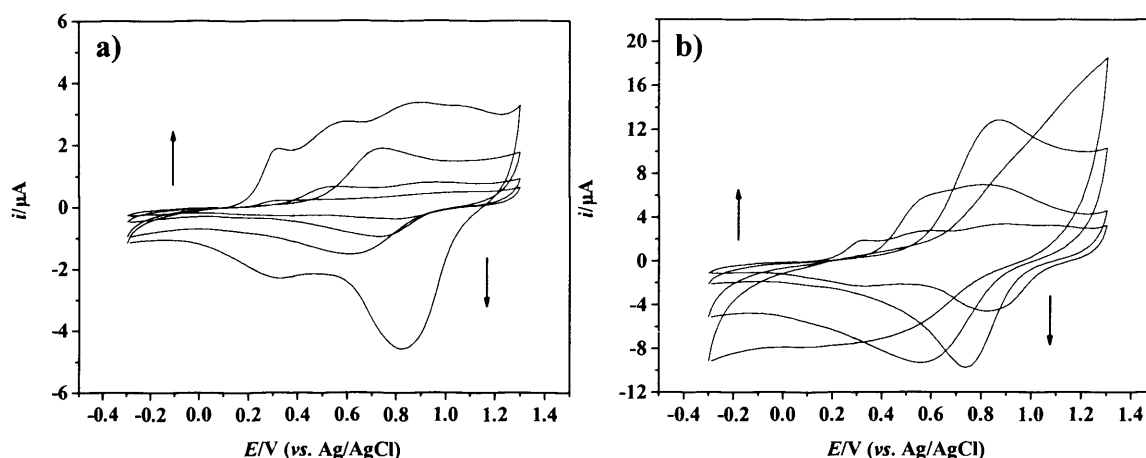


**Figure 4.10:** Voltammetric response of poly[Ni(3-Mesalophen-b15-c5)],  $\Gamma=19.3$  nmol cm<sup>-2</sup>, cycled at different scan rates following Cs<sup>+</sup> additions: **a)** 0.01, 0.02, 0.05, 0.1 V s<sup>-1</sup> and **b)** 0.1, 0.2, 0.5 and 1 V s<sup>-1</sup>. Arrows indicate the increase of current intensity as a result of the scan rate increase.

In the presence of 3 mmol dm<sup>-3</sup> of Mg<sup>2+</sup> (intermediate additions), poly[Ni(3-Mesalophen-b15-c5)] shows different responses depending on the amount of deposited, electroactive species  $\Gamma$ . For films prepared with  $\Gamma \leq 34$  nmol cm<sup>-2</sup> the response of the modified electrode is considered fast (Figure 4.11a,  $\log|i_{pII}|$  vs.  $\log \nu$  plots have slope of unity). However, for  $\Gamma \geq 65$  nmol cm<sup>-2</sup> the charge transport process is only at equilibrium

for  $v \leq 0.1 \text{ V s}^{-1}$  (Table 4.4). For higher scan rates the slope of  $\log|i_{pII}|$  vs.  $\log v$  decreases to values around 0.5, indicating that the response becomes diffusion controlled (Figure 4.11b). Similar trend was found for films in the presence of  $\text{Ba}^{2+}$  (Table 4.5).

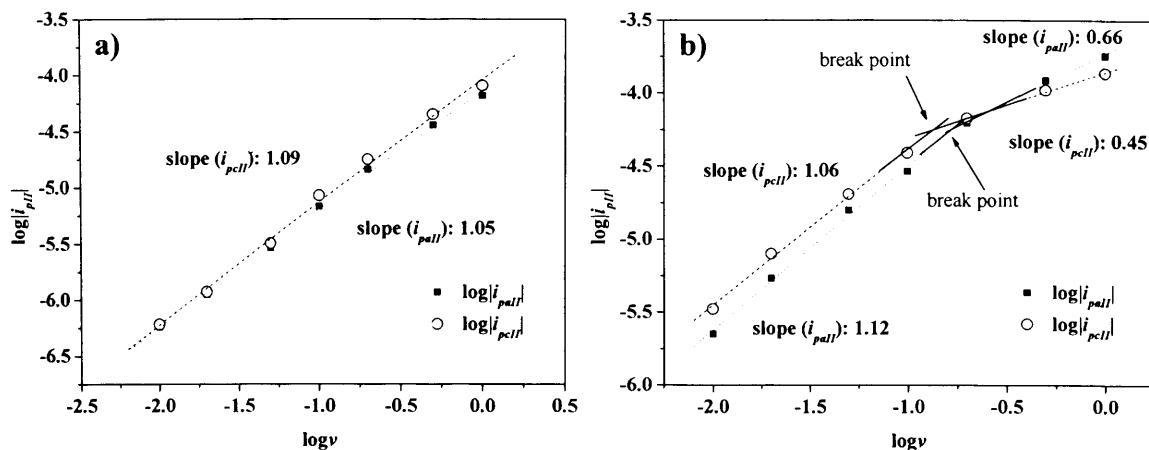


**Figure 4.11:** Dependence of  $\log|i_{pII}|$  on  $\log v$  for two poly[Ni(3-Mesalophen-b15-c5)] modified electrodes in the presence of  $\text{Mg}^{2+}$ , a)  $\Gamma = 26 \text{ nmol cm}^{-2}$  and b)  $\Gamma = 99 \text{ nmol cm}^{-2}$ .

In the same way, dynamic studies performed on films to which larger amounts of  $\text{Mg}^{2+}$  were added (large additions, Table 4.6) show that the charge transport is fast for small  $\Gamma$ . For thick films and low timescales the response becomes diffusion controlled. Intermediate films ( $\Gamma \approx 35\text{--}40 \text{ nmol cm}^{-2}$ ) show a different behaviour depending on the metal cation concentration: the response is diffusion controlled following large additions. In the case of  $\text{Ba}^{2+}$  large additions, thin films show a response typical of fast charge transfer processes (Table 4.7). It was not possible to study films with  $\Gamma \geq 10 \text{ nmol cm}^{-2}$  due to the considerable loss of electroactivity as the films were cycled at different scan rates.

In the diffusion controlled regime it is possible to make an estimate of the diffusion coefficient by using the Randles-Sevcik equation<sup>2,18</sup>. Table 4.8 depicts the estimates of  $CD^{1/2}$ , where  $C$  is the concentration of the electroactive species and  $D$  the diffusion coefficient. These values increase with the increase of surface coverage, and for similar  $\Gamma$  the diffusion coefficient is larger for  $\text{Mg}^{2+}$  than for  $\text{Ba}^{2+}$ . The values of  $CD^{1/2}$  obtained for poly[Ni(3-Mesalophen-b15-c5)] films are about one order of magnitude smaller than those found for similar poly[Ni(salen)] complexes in the presence of the same metal cations<sup>19</sup>.

**Table 4.4:** Dynamic studies of poly[Ni(3-Mesalophen-b15-c5)] in the presence of  $\text{Mg}(\text{ClO}_4)_2$  – intermediate additions.

$\Gamma / \text{nmol cm}^{-2}$	Anodic slope		Cathodic slope		Break point ( $\text{V s}^{-1}$ )	Regime of charge transport
	Low $\nu$	High $\nu$	Low $\nu$	High $\nu$		
12		1.01		1.09	-	Equilibrium
20		1.03		1.07	-	Equilibrium
26		1.05		1.09	-	Equilibrium
34		1.03		1.04	-	Equilibrium
67	1.06	0.55	1.00	0.36	Anodic: 0.16 Cathodic: 0.11	Equilibrium (low $\nu$ ) Diffusion controlled (high $\nu$ )
99	1.12	0.66	1.06	0.45	Anodic: 0.18 Cathodic: 0.14	Equilibrium (low $\nu$ ) Diffusion controlled (high $\nu$ )

**Table 4.5:** Dynamic studies of poly[Ni(3-Mesalophen-b15-c5)] in the presence of  $\text{Ba}(\text{ClO}_4)_2$  – intermediate additions.

$\Gamma / \text{nmol cm}^{-2}$	Anodic slope		Cathodic slope		Break point ( $\text{V s}^{-1}$ )	Regime of charge transport
	Low $\nu$	High $\nu$	Low $\nu$	High $\nu$		
11		1.02		1.08	-	Equilibrium
16		1.06		1.10	-	Equilibrium
17		1.04		1.06	-	Equilibrium
21		1.04		0.99	-	Equilibrium
63		1.01		0.94	-	Equilibrium
87	1.13	0.68	1.10	0.40	Anodic: 0.19 Cathodic: 0.15	Equilibrium (low $\nu$ ) Diffusion controlled (high $\nu$ )

**Table 4.6:** Dynamic studies of poly[Ni(3-Mesalophen-b15-c5)] in the presence of Mg(ClO<sub>4</sub>)<sub>2</sub> – large additions.

$\Gamma / \text{nmol cm}^{-2}$	Anodic slope		Cathodic slope		Breaking point (V s <sup>-1</sup> )	Regime of charge transport
	Low $\nu$	High $\nu$	Low $\nu$	High $\nu$		
1.4		0.92		1.07	-	Equilibrium
6.5		1.01		1.13	-	Equilibrium
12		1.07		1.17	-	Equilibrium
18		1.05		1.06	-	Equilibrium
31		1.00		0.94	-	Equilibrium
37	1.06	0.49	1.12	0.21	Anodic: 0.20 Cathodic: 0.14	Equilibrium (low $\nu$ ) Diffusion controlled (high $\nu$ )
68	1.06	0.51	1.07	0.28	Anodic: 0.19 Cathodic: 0.15	Equilibrium (low $\nu$ ) Diffusion controlled (high $\nu$ )
84	1.04	0.62	1.00	0.28	Anodic: 0.10 Cathodic: 0.12	Equilibrium (low $\nu$ ) Diffusion controlled (high $\nu$ )

**Table 4.7:** Dynamic studies of poly[Ni(3-Mesalophen-b15-c5)] in the presence of Ba(ClO<sub>4</sub>)<sub>2</sub> – large additions.

$\Gamma / \text{nmol cm}^{-2}$	Anodic slope		Cathodic slope		Breaking point (V s <sup>-1</sup> )	Regime of charge transport
	Low $\nu$	High $\nu$	Low $\nu$	High $\nu$		
2.3		0.80		0.80	-	Equilibrium
5.7		0.89		0.88	-	Equilibrium
10		0.93		0.95	-	Equilibrium

**Table 4.8:** Values of  $CD^{1/2}$  and  $D$  estimated using voltammetric data and the Randles-Sevcik equation.

	$\Gamma/\text{nmol cm}^{-2}$	$CD^{1/2} 10^{-8}/\text{mol s}^{-0.5} \text{cm}^{-2}$		$D 10^{-10}/\text{cm}^2 \text{s}^{-1}$	
		Anodic	Cathodic	Anodic	Cathodic
Film+Mg <sup>2+</sup>	37	2.12	-	1.1	-
	67	3.07	-	2.4	-
	81	4.86	-	5.9	-
	99	6.81	5.11	12	6.5
Film+Ba <sup>2+</sup>	87	3.64	2.66	3.3	1.8

Using the film density  $\rho_f$ , it is possible to estimate the concentration of electroactive species in the polymer. Assuming that the polymer molar volume is identical to that of the monomeric species<sup>20</sup>,  $C = \rho_f/M = 2.0 \text{ mmol cm}^{-3}$ , where  $\rho_f=1.2 \text{ g cm}^{-3}$  and  $M$  is the monomer molar mass ( $591.278 \text{ g mol}^{-1}$ ). The result is  $D \approx 10^{-10}$ - $10^{-9} \text{ cm}^2 \text{ s}^{-1}$ , which is within the range of reported (ionic) diffusion coefficients<sup>21</sup> and is similar to permeation rates found in conjugated polymers<sup>22,23</sup>.

#### 4.3.2.2 Analysis of $E_{pal}$

The variation of peak potential  $E_{pal}$  with concentration of added metal cation was studied in detail. [Figure 4.12](#) and [Table 4.9](#) show the dependence of  $E_{pal}$  on the logarithmic concentration of metal for both small and intermediate additions. This approach assumes that the system is characterised by fast charge transport in the experimental timescale. The cases in which the charge transport was found to be diffusion controlled occur for scan rates higher than  $0.1 \text{ V s}^{-1}$  ([Tables 4.4-4.7](#)). Since all the films were cycled at  $0.1 \text{ V s}^{-1}$ , this precludes the possibility of responses limited by diffusion. If the response of the system showed a Nernstian dependence on the concentration of added metal cation, the expected slopes would have been  $0.059 \text{ V}$  for  $\text{Cs}^+$  additions and  $0.030 \text{ V}$  for both  $\text{Mg}^{2+}$  and  $\text{Ba}^{2+}$  ( $T=298.15 \text{ K}$ ). For small additions ([Figure 4.12a, c, e](#)) there are clearly two ( $\text{Cs}^+$ ) or three ( $\text{Mg}^{2+}$  and  $\text{Ba}^{2+}$ ) regions defined by the slopes depicted in the plots. These vary according to the sequence region I < region II < region III. Region I is characterised by a slope typical of Nernstian dependence ([Table 4.9](#)). When the concentration of the aliquots increased (intermediate additions), a Nernstian relation was

observed for thin films in the presence of  $\text{Cs}^+$  and  $\text{Ba}^{2+}$ , whilst for  $\text{Mg}^{2+}$  the same dependence was observed only in the range  $35 < \Gamma < 70 \text{ nmol cm}^{-2}$ . This may imply that the morphology of the system changes with the variation of  $\Gamma$ .

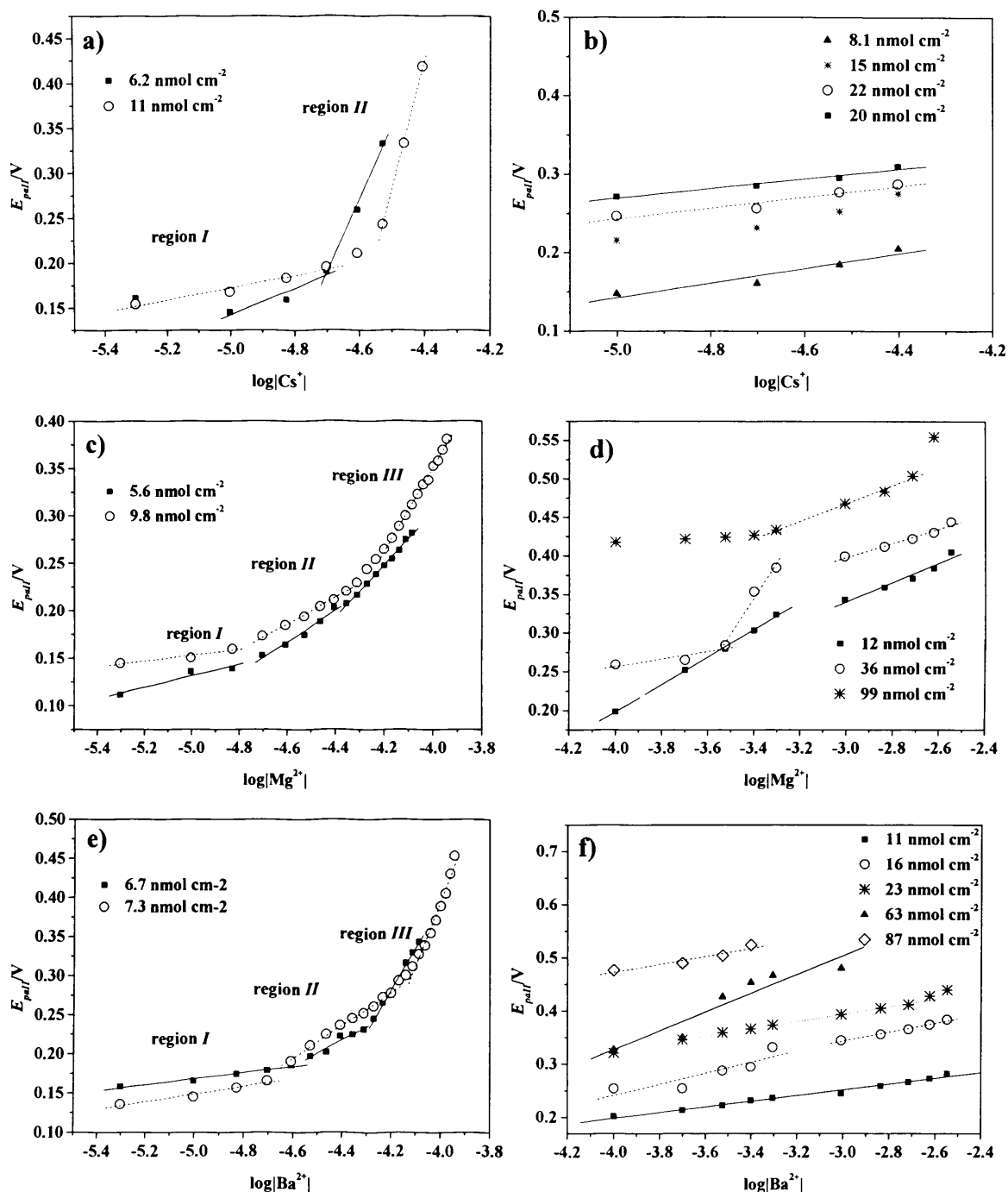


**Figure 4.12:** Graphic representation of  $E_{pol}$  vs.  $\log|cation|$  for small (panels a, c and e) and intermediate additions (panels b, d and f). Different symbols ( $\blacksquare$   $\circ$   $\blacktriangle$   $*$   $\diamond$ ) correspond to different films, prepared with different  $\Gamma$ .



**Table 4.9:** Slopes of  $E_{pal}$  vs.  $\log|\text{cation}|$  plots.

$\Gamma/\text{nmol cm}^{-2}$			Slope I		
			Region I	Region II	Region III
Film+Cs <sup>+</sup>	Small	6.2	-	0.147	0.809
	Additions	11	0.079	1.422	-
		8.1	0.094	-	-
	Intermediate	15	0.096	-	-
	additions	22	0.068	-	-
		20	0.062	-	-
Film+Mg <sup>2+</sup>	Small	5.6	0.060	0.165	0.276
	Additions	9.8	0.030	0.140	0.446
		12	0.178	0.086	-
		20	0.117	-	-
	Intermediate	26	-	0.264	0.057
	additions	36	0.049	0.462	0.093
		67	0.028	0.541	-
		99	0.015	0.116	-
Film+Ba <sup>2+</sup>	Small	6.7	0.039	0.168	0.540
	Additions	7.3	0.049	0.207	0.700
		11	0.053	-	-
	Intermediate	16	0.104	0.067	-
	additions	23	0.070	-	-
		63	0.176	-	-
		87	0.075	-	-

The variation of  $E_{pal}$  upon metal ion addition was also considered as a function of  $\Gamma$ . Figure 4.13 presents  $E_{pal}$  variation after a large addition ( $100 \text{ mmol dm}^{-3}$ ) of  $\text{X}(\text{ClO}_4)_2$  ( $\text{X}=\text{Mg}^{2+}$ ,  $\text{Ba}^{2+}$ ) being effectuated.  $\Delta E_{pal}$  varies in opposite ways with respect to the type of metal cation. In the case of  $\text{Mg}^{2+}$   $\Delta E_{pal}$  decreases with the increase of  $\Gamma$ ; this is expected if there are no limitations in terms of exchange of the metal cation at the film/solution interface, together with its movement across the film. Therefore, the system possesses more ability to sense larger amounts of metal cation with the increase of  $\Gamma$ . Contrastingly,

for  $\text{Ba}^{2+}$  additions  $\Delta E_{pal}$  increases in thin and intermediate films until reaching a plateau. This may be associated with limitations in  $\text{Ba}^{2+}$  movement across thicker films. In fact, if this large cation blocks the flow of species responsible for charge transport and restoration of electroneutrality, there will be a positive displacement of potential peaks (overpotential) to dope/undope the films.

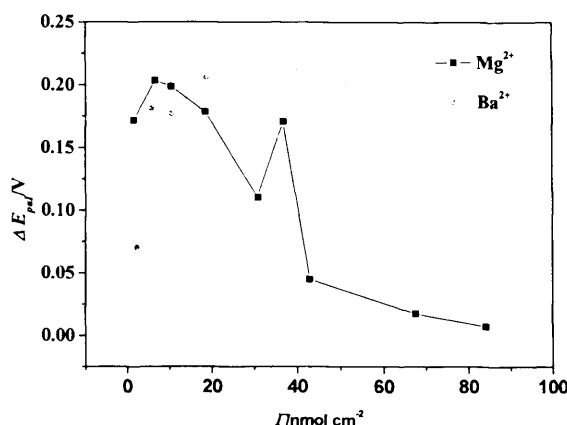


**Figure 4.13:** Graphic representation of  $\Delta E_{pal}$  vs.  $\Gamma$  following the addition of a 100 mmol dm<sup>-3</sup> aliquot of  $\text{X}(\text{ClO}_4)_2$  ( $\text{X}=\text{Mg}^{2+}$ ,  $\text{Ba}^{2+}$ ).

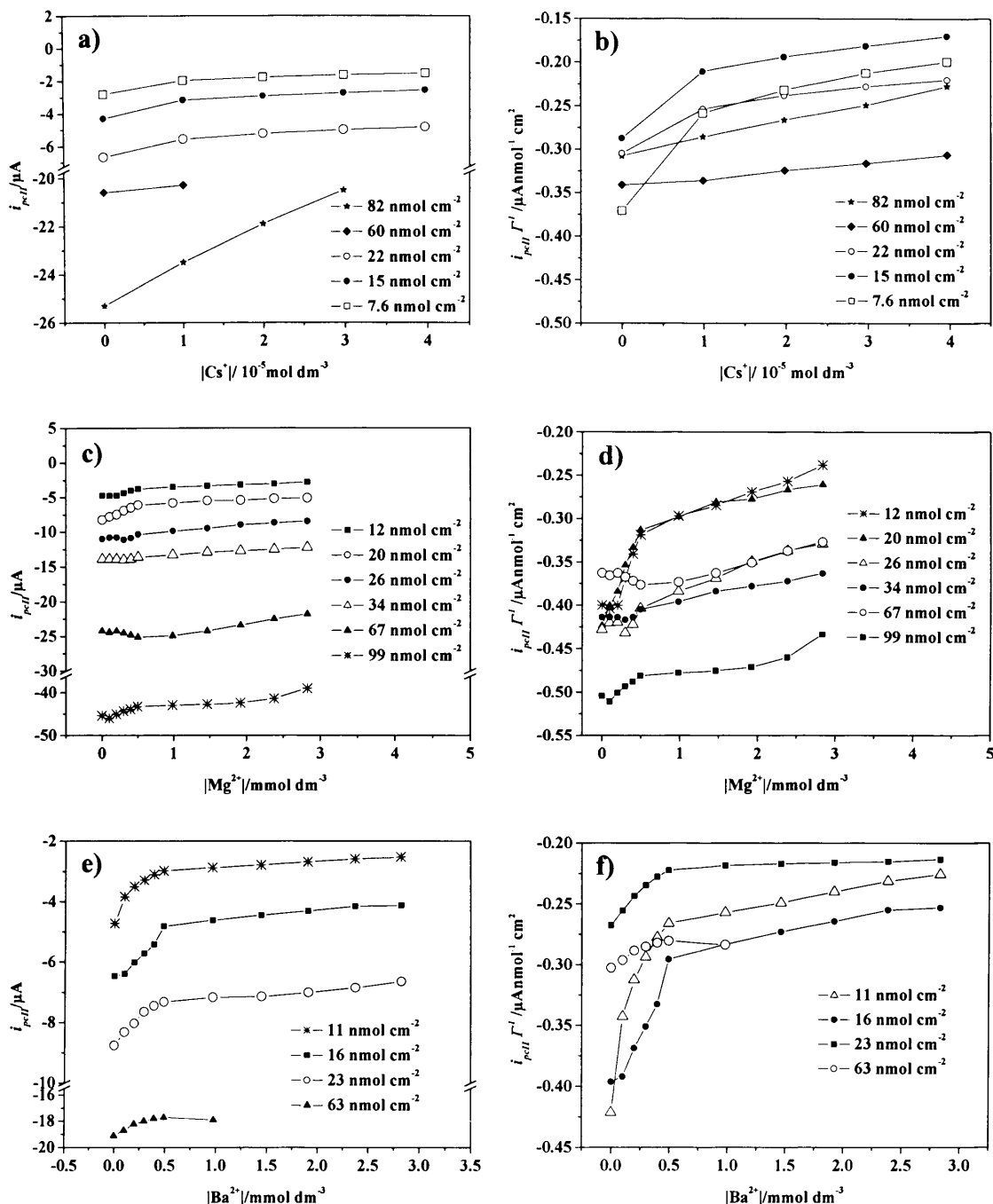
#### 4.3.2.3 Analysis of $i_{pcII}$

Figure 4.14 depicts the variation of  $i_{pcII}$  with additions of  $\text{Cs}^+$ ,  $\text{Mg}^{2+}$  and  $\text{Ba}^{2+}$ . The major differences observed in the values of  $i_{pcII}$  in panels a, c and e are removed, to a great extent, when the current peak is normalised with respect to the surface coverage  $\Gamma$  (panels b, d and f). This indicates that  $i_{pcII}$  is a function of the amount of electroactive material deposited.

The variation of  $i_{pcII}$  upon ion addition depends on the size of the metal cation. In the case of the large cations ( $\text{Cs}^+$  and  $\text{Ba}^{2+}$ )  $i_{pcII}$  decreases in magnitude. The rate of this variation is not constant over the concentration range: for the first additions  $i_{pcII}$  varies to a higher extent than for subsequent additions. Contrastingly, for  $\text{Mg}^{2+}$   $i_{pcII}$  increases in magnitude after the first few additions and then decreases at two different rates, as observed for the large cations.

The effect of surface coverage in  $\Delta i_{pcII}$ , following a large addition, was also considered (Figure 4.15).  $\Delta i_{pcII}$  was found to vary similarly for both  $\text{Mg}^{2+}$  and  $\text{Ba}^{2+}$ . For thin films it is roughly constant and positive, implying that after the addition  $i_{pcII}$  decreases in magnitude and possibly the system response is saturated in this range of  $\Gamma$ . Oppositely,

$i_{pcII}$  increases in magnitude (becomes negative) for intermediate films up to  $\Gamma \approx 40 \text{ nmol cm}^{-2}$ . For higher  $\Gamma$ ,  $\Delta i_{pcII}$  is still negative, but a different profile is observed. This may be associated with morphological changes that may occur with the increase of deposited species.



**Figure 4.14:** Graphic representation of  $i_{pcII}$  vs.  $[\text{cation}]$  (panels a, c and e) and  $i_{pcII} \Gamma^{-1}$  vs.  $[\text{cation}]$  (panels b, d and f). Different symbols ( $\blacksquare \bullet \circ \blacktriangle \triangle *$ ) correspond to different films (prepared with different  $\Gamma$ ).

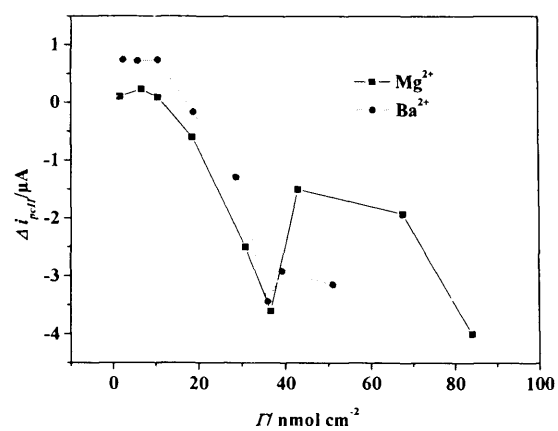


**Figure 4.15:** Graphic representation of  $\Delta i_{pcll}$  vs.  $\Gamma$  following the addition of a  $100 \text{ mmol dm}^{-3}$  aliquot of  $\text{X}(\text{ClO}_4)_2$  ( $\text{X}=\text{Mg}^{2+}, \text{Ba}^{2+}$ ).

#### 4.3.2.4 Reversibility

After ion recognition studies, the solution containing metal cations was substituted by fresh background electrolyte  $0.1 \text{ mol dm}^{-3}$  TBAP/ $\text{CH}_3\text{CN}$  and the voltammetric response recorded. In none of the cases was the electrochemical response found to be reversible (Figure 4.16), *i.e.* the ions were irreversibly trapped in the film.

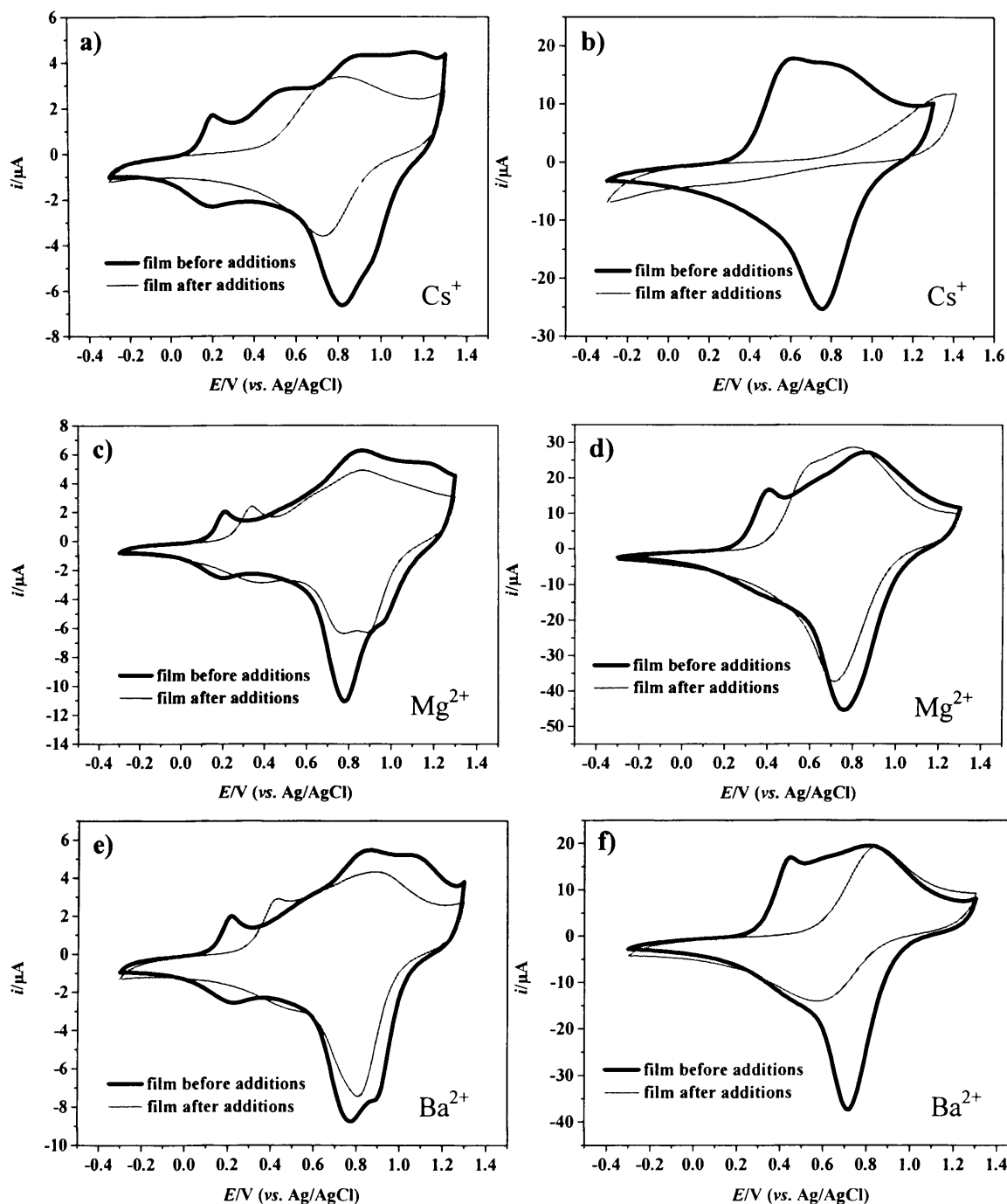


**Figure 4.16:** Voltammetric response of poly[Ni(3-Mesalophen-b15-c5)] recorded in metal cation-free  $0.1 \text{ mol dm}^{-3}$  TBAP/ $\text{CH}_3\text{CN}$ , before and after cation addition studies:  $\Gamma \approx 25 \text{ nmol cm}^{-2}$  (panels a, c and e) and  $\Gamma \approx 90 \text{ nmol cm}^{-2}$  (panels b, d and f).

## 4.4 CHARACTERISATION OF POLY[Ni(3-MESALOPHEN-B15-C5)] BY *IN SITU* UV-VIS SPECTROSCOPY

### 4.4.1 Electropolymerisation of [Ni(3-Mesalophen-b15-c5)]

At the end of the deposition processes, inspection of the working electrode surface revealed the presence of a reddish deposit, indicating the chromophoric nature of these films. UV-Vis spectra acquired during the polymerisation (Figure 4.17) shows not only that the deposited film absorbs in this region of the electromagnetic spectrum but also that the absorbance changes with the applied potential. However, these spectra were acquired in the presence of monomer [Ni(3-Mesalophen-b15-c5)], which impedes the correct assignment of film bands.

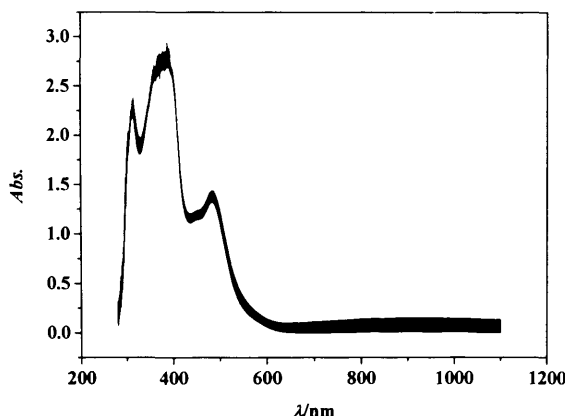


**Figure 4.17:** UV-Vis spectra collected and referenced to 0.1 mol dm<sup>-3</sup> TBAP/CH<sub>3</sub>CN solution during the 5<sup>th</sup> deposition cycle.

Figure 4.18 presents the UV-Vis spectra of both monomer ([Ni(3-Mesalophen-b15-c5)]) and film (poly[Ni(3-Mesalophen-b15-c5)]), obtained in background electrolyte. The spectrum of [Ni(3-Mesalophen-b15-c5)] is typical of square planar [Ni<sup>II</sup>(salen)] complexes. These usually show a broad band of medium intensity ( $100 < \epsilon < 1000 \text{ mol}^{-1} \text{ dm}^3 \text{ cm}^{-1}$ ) occurring at  $\lambda = 400\text{--}550 \text{ nm}$ , which corresponds to three (unresolved) allowed *d-d* transitions ( $d_{xy} \leftarrow \{d_{z^2}; (d_{xz}, d_{yz}) \text{ and } d_{x^2-y^2}\}$ ) of similar energies. For higher energies, several bands of high intensity ( $\epsilon > 1000 \text{ mol}^{-1} \text{ dm}^3 \text{ cm}^{-1}$ ) occur. The latter are associated with charge transfer and intra-ligand transitions<sup>24</sup>.

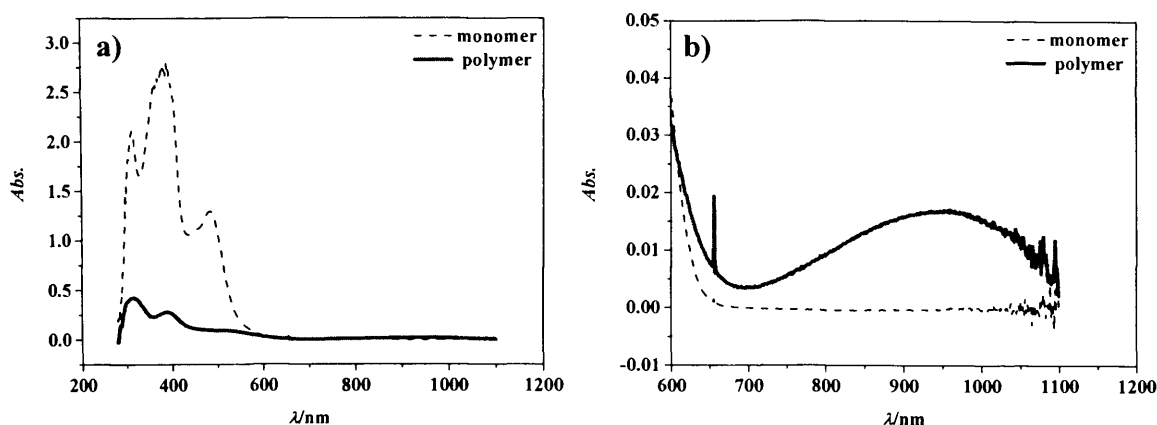


**Figure 4.18:** UV-Vis spectra of [Ni(3-Mesalophen-b15-c5)] and reduced poly[Ni(3-Mesalophen-b15-c5)] referenced to 0.1 mol dm<sup>-3</sup> TBAP/CH<sub>3</sub>CN solution. **a)** 280-1100 nm and **b)** 600-1100 nm.

In the present case, the monomeric species and the reduced film show similar bands for  $\lambda < 500$  nm ([panel a](#)). The differences in intensity are due to the different amounts of monomer (higher) and deposited polymer (lower) in the optical path. The most significant differences between the two spectra are observed for low energies ([panel b](#)), where a band occurs in the case of the polymer but not the monomer. The detailed analysis of the polymer electronic properties is presented in the following sections.

#### 4.4.2 Spectroscopic characterisation of poly[Ni(3-Mesalophen-b15-c5)]

The UV-Vis spectra of the modified electrode, acquired during redox switching in background electrolyte, are shown in [Figure 4.19](#). Different colours (grey scale) are used for spectra corresponding to different potential intervals. These intervals were defined based on the voltammetric response of the modified electrode ([Figure 4.20](#)): -0.3 to 0.3 V, 0.3 to 0.9 V and 0.9 to 1.3 V. The spectra show five bands at  $\lambda_{\text{max}} = 315$  nm, 382 nm, 435 nm, 508 nm and 945 nm, whose responses are reversible with potential.

Differential spectra representing changes for the spectra presented above are shown in [Figure 4.21](#). These highlight the variation of the absorbance with the applied potential. When the potential is cycled from -0.3 to 0.3 V ([panel a](#)), the absorbance of the band occurring at  $\lambda_{\text{max}} = 315$  nm decreases while for bands at  $\lambda_{\text{max}} = 382$ ,  $\lambda_{\text{max}} = 435$  and  $\lambda_{\text{max}} = 945$  nm it increases. During the oxidation, up to 0.9 V ([panel b](#)), similar variations are observed but occurring to a greater extent. For the most oxidising potentials (0.9 to 1.3 V,

panel c) the absorbance of bands occurring at  $\lambda_{\text{max}} = 315\text{nm}$  and  $\lambda_{\text{max}} = 382\text{ nm}$  decreases. In addition, a new band appears at  $\lambda_{\text{max}} = 508\text{ nm}$ , thereby masking the band at  $\lambda_{\text{max}} = 435\text{ nm}$ . The band at  $\lambda_{\text{max}} = 945\text{ nm}$  shows a mixed profile, first increasing and then decreasing.

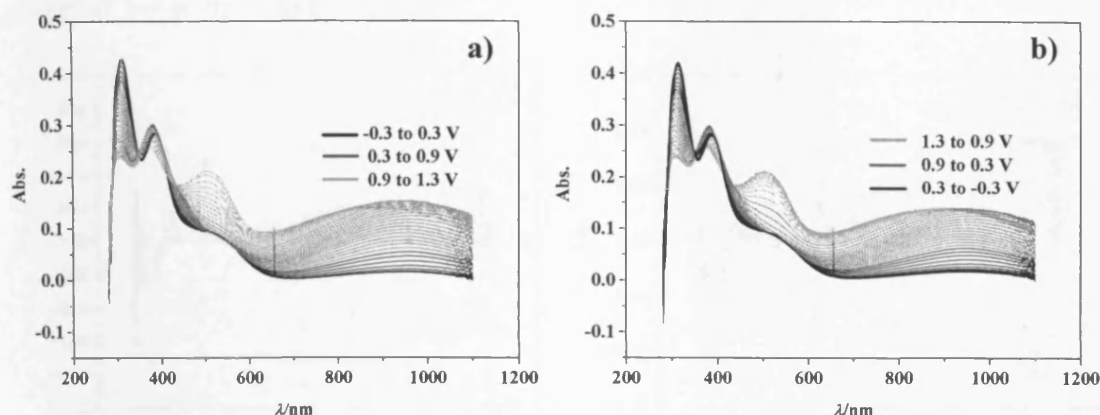


**Figure 4.19:** UV-Vis spectra of poly[Ni(3-Mesalophen-b15-c5)] acquired in  $0.1\text{ mol dm}^{-3}$  TBAP/ $\text{CH}_3\text{CN}$  from a)  $-0.3$  to  $1.3\text{ V}$  and b)  $1.3$  to  $-0.3\text{ V}$ . The spectra are referenced to  $0.1\text{ mol dm}^{-3}$  TBAP/ $\text{CH}_3\text{CN}$  and different colours (grey scale) correspond to different intervals of potential (Figure 4.20).

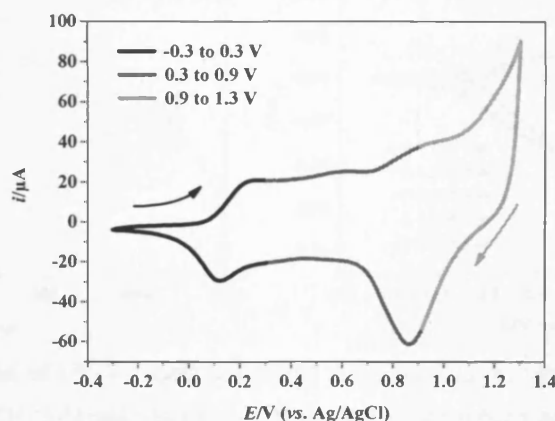


**Figure 4.20:** Voltammetric response of poly[Ni(3-Mesalophen-b15-c5)] acquired in  $0.1\text{ mol dm}^{-3}$  TBAP/ $\text{CH}_3\text{CN}$  by cycling the potential between  $-0.3$  and  $1.3\text{ V}$ . Arrows indicate the direction of potential sweep.

Panel d summarises the variation of absorbance during a complete voltammetric cycle. The absorbance of bands associated with the modified electrode only varies between  $0.2$  and  $1.3\text{ V}$ , which coincides with the electrochemical response of the electroactive film (Figure 4.20). In terms of absorbance variation there are three distinct profiles (anodic half-cycle): (i) decrease of absorbance between  $0.2$  and  $1.3\text{ V}$  (band at



$\lambda_{\max} = 315$  nm); (ii) increase of absorbance between 0.2 and 0.9 V and subsequent decrease between 0.9 and 1.3 V for bands at  $\lambda_{\max} = 382$  nm, 435 nm and 945 nm; (iii) negligible variation of absorbance between 0.2 and 0.9 V and increase of absorbance between 0.9 and 1.3 V for the band at  $\lambda_{\max} = 508$  nm. In the reverse (cathodic) half-cycle these profiles are reversed, but with some hysteresis.

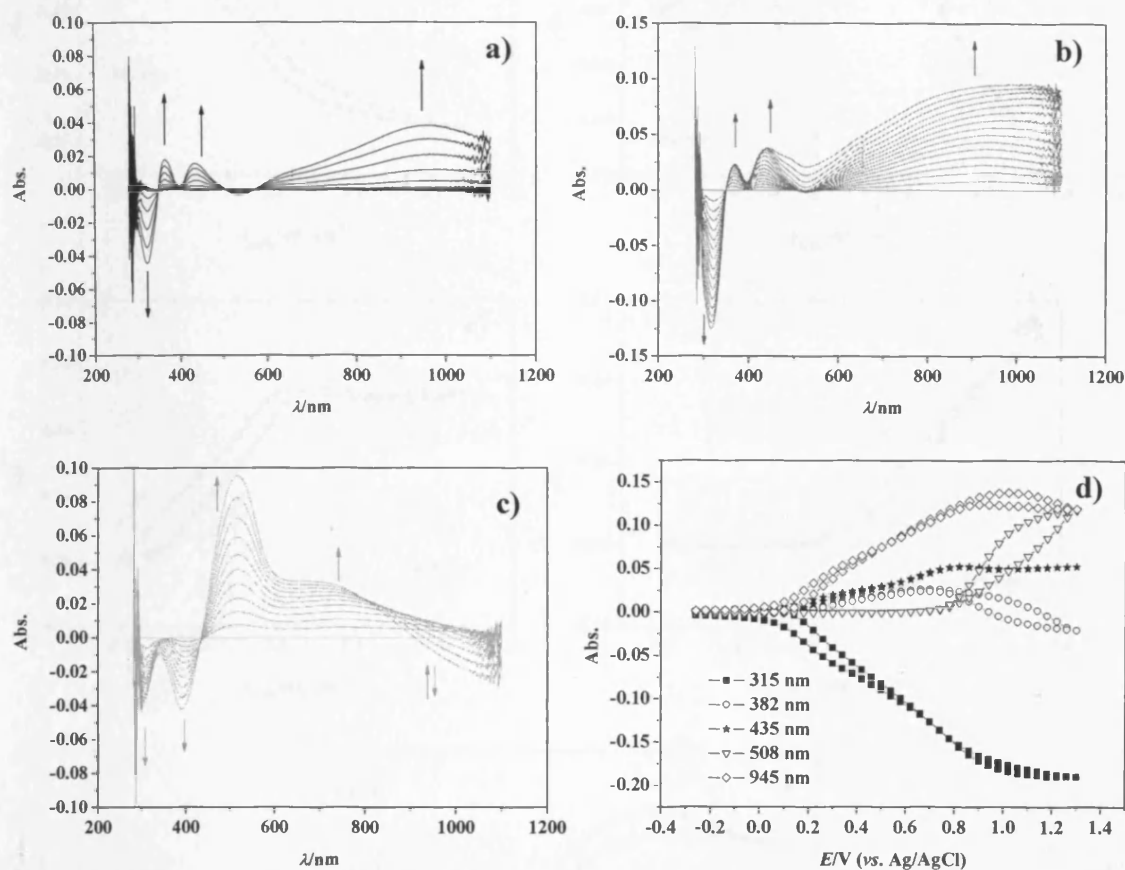


**Figure 4.21:** Differential of UV-Vis spectra depicted in Figure 4.19: **a)** spectra acquired from  $-0.3$  to  $0.3$  V and referenced to poly[Ni(3-Mesalophen-b15-c5)] at  $-0.3$  V; **b)** spectra acquired from  $0.3$  to  $0.9$  V referenced to poly[Ni(3-Mesalophen-b15-c5)] at  $0.3$  V and **c)** spectra acquired from  $0.9$  to  $1.3$  V referenced to poly[Ni(3-Mesalophen-b15-c5)] at  $0.9$  V; **d)** variation of absorbance with the applied potential for a complete voltammetric cycle (absorbance referenced to poly[Ni(3-Mesalophen-b15-c5)] at  $-0.3$  V).

#### 4.4.2.1 Determination of extinction coefficients associated with the UV-Vis bands

Figure 4.22 shows the  $Abs$  vs.  $q_{redox}$  plots at the wavelengths associated with electronic transitions. The relation between the charge consumed during redox switching ( $Q_{redox}$ ) and the absorbance enables the estimation of extinction coefficients  $\epsilon_{\lambda}$  (Equation

2.34, Chapter 2). The slopes of linear regions where the variation of absorbance is maximum were used for the determination of  $\epsilon_\lambda$  (Table 4.10).

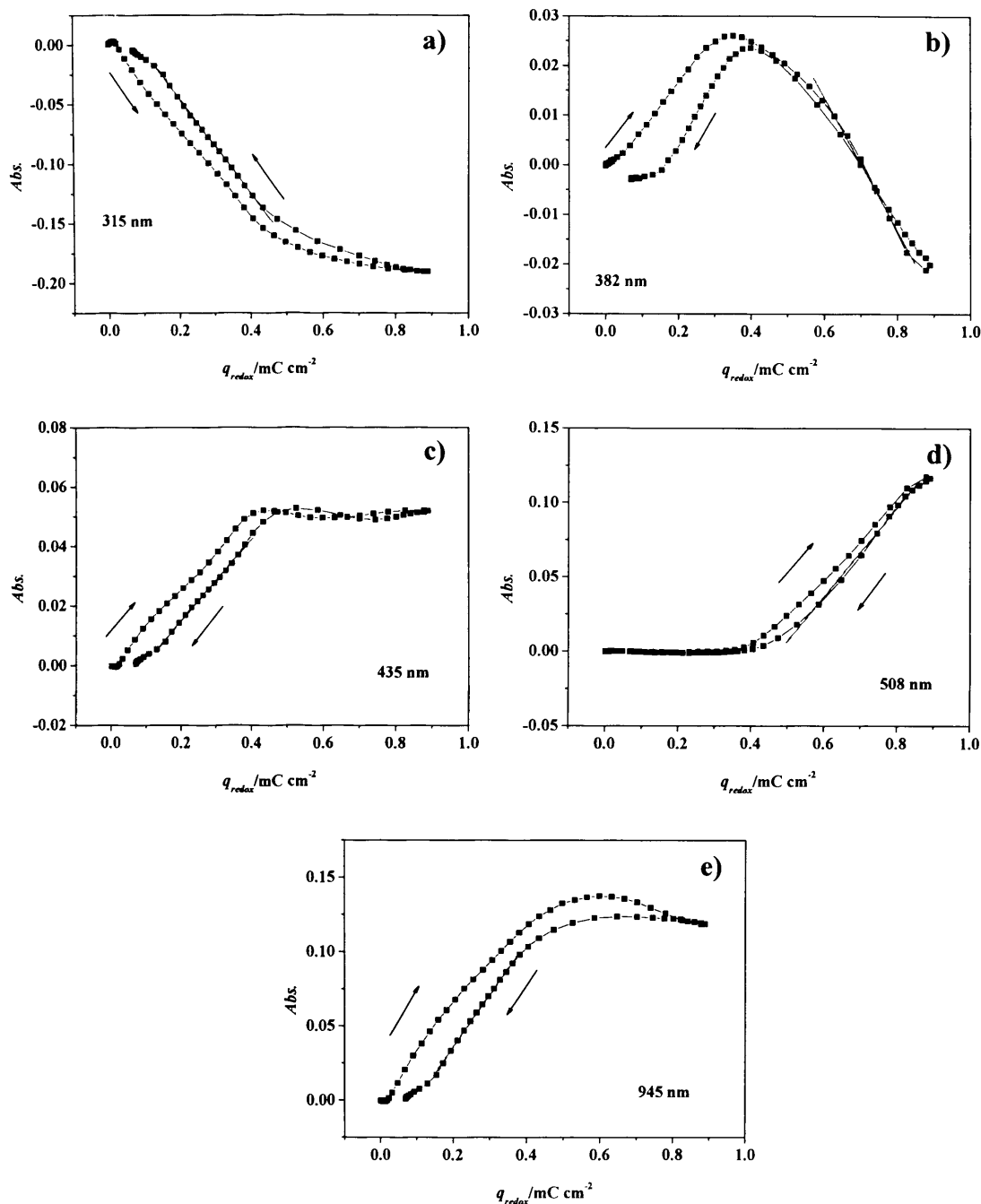


**Figure 4.22:** Dependence of absorbance (referenced to the polymer at  $-0.3$  V) on  $q_{redox} = Q_{redox}/A$  at a)  $\lambda_{max} = 315$  nm, b)  $\lambda_{max} = 382$  nm, c)  $\lambda_{max} = 435$  nm, d)  $\lambda_{max} = 508$  nm and e)  $\lambda_{max} = 945$  nm.

The values obtained for extinction coefficients show that the electronic transitions occurring during oxidation involve states with considerable contribution from ligand orbitals<sup>24</sup>. Since these bands are associated with the occurrence of oxidation/reduction

processes within the polymer, these findings support the assumption of the electrochemical response being ligand-based. Similar results were found for analogous poly[Ni(*salen*)] films<sup>1,25</sup>.

**Table 4.10:** Extinction coefficients  $\epsilon_\lambda$  associated with the electronic transitions.

Peak wavelength	$\lambda = 315$ nm	$\lambda = 382$ nm	$\lambda = 435$ nm	$\lambda = 508$ nm	$\lambda = 945$ nm
$\epsilon_\lambda/\text{mol}^{-1} \text{ dm}^3 \text{ cm}^{-1}$	18120	6200	6210	13540	16010

#### 4.4.2.2 Charge carriers and the polaron model

Spectroscopic studies carried out for similar poly[Ni(*salen*)] films by Vilas-Boas and co-workers<sup>1,25</sup> showed that the occurrence of vibrational bands whose intensity varies with the applied potential are associated with the movement of charge carriers along the polymeric chains. Additionally, EPR studies identified these charge carriers as being radicals (paramagnetic) and UV-Vis studies showed that some of the bands only appeared when the polymers were oxidised. Based on these results, the polaron model<sup>26-28</sup> was suggested to explain the conductive properties of these polymeric systems.

Similarly, poly[Ni(3-Mesalophen-b15-c5)] film shows electronic properties typical of conducting polymers and the assignment of the bands is then based on the polaron model (Figure 4.23). The band occurring at  $\lambda_{\text{max}} = 315$  nm ( $W_{\text{Total}}$ : 3.93 eV), which decreases throughout all the oxidation process, corresponds to the electronic transition between the valence band and the conduction band. The bands occurring at  $\lambda_{\text{max}} = 382$ ,  $\lambda_{\text{max}} = 435$  and  $\lambda_{\text{max}} = 945$  nm show similar behaviour with the potential and are assigned to polarons formed during the polymer oxidation:  $\lambda_{\text{max}} = 382$  nm ( $W_1$ : 3.24 eV) corresponds to a transition between valence band and the anti-bonding polaronic state,  $\lambda_{\text{max}} = 435$  nm ( $W_2$ : 2.85 eV) to the transition from the bonding polaronic state to the conduction band, and  $\lambda_{\text{max}} = 945$  nm ( $W_3$ : 1.31 eV) to the transition between the valence band and the bonding polaronic state.

Considering a symmetrical distribution of energies,  $W_{\text{Total}} = W_2 + W_3$ . The sum gives 4.16 eV, only 6% different to the observed  $W_{\text{Total}}$ . Using the same logic, the energy corresponding to the transition between the bonding and anti-bonding polaronic states is

given by  $W_1 - W_3 = W_4$ , which in this case is 1.93 eV ( $\lambda_{\max} = 642$  nm). This transition possibly corresponds to the inflexion observed in [Figure 4.21c](#) at  $\lambda_{\max} \approx 740$  nm. This band may be masked by the transition at  $\lambda_{\max} = 945$  nm during all the potential range except when the absorbance of the latter decreases.

The transition occurring at  $\lambda_{\max} = 508$  nm shows a distinct behaviour, increasing only after the polaronic bands attain their maximum values. This band may be attributed to a charge transfer between the metal centre and the new electronic levels formed during the oxidation.

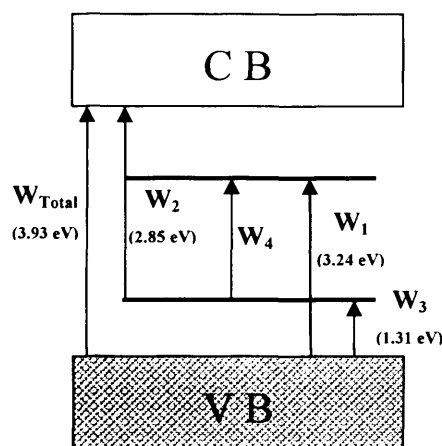


**Figure 4.23:** Assignment of electronic transitions for poly[Ni(3-Mesalophen-b15-c5)], based on the polaron model (VB = valence band; CB = conduction band).

#### 4.4.3 UV-Vis properties of poly[Ni(3-Mesalophen-b15-c5)] in the presence of metal cations - ion recognition studies

The UV-Vis spectra of poly[Ni(3-Mesalophen-b15-c5)] films were also studied in the presence of cations. After polymerisation and redox-switching in background electrolyte, a 200  $\mu\text{L}$  aliquot of 0.05  $\text{mol dm}^{-3}$   $\text{X}(\text{ClO}_4)_2$  ( $\text{X} = \text{Mg}^{2+}, \text{Ba}^{2+}$ ) (final concentration 2  $\text{mmol dm}^{-3}$ ) or 5  $\text{mmol dm}^{-3}$   $\text{CsClO}_4$  (final concentration 0.2  $\text{mmol dm}^{-3}$ ) was added to the background electrolyte solution. The system was then left to equilibrate for 15 minutes at 0.0 V and then the potential cycled and the UV-Vis spectra simultaneously acquired. The solution was then removed and the modified electrode washed with dried  $\text{CH}_3\text{CN}$ . The UV-Vis spectra of the film were again acquired in background electrolyte.

[Figure 4.24](#) shows the UV-Vis spectra of the modified electrode acquired at  $E = -0.3$  V. The response of the film in the reduced state is similar in the presence of  $\text{Cs}^+$

and  $\text{Ba}^{2+}$ , but different in the presence of  $\text{Mg}^{2+}$ . After the addition of  $\text{Cs}^+$  or  $\text{Ba}^{2+}$ , the absorbance of bands occurring at  $\lambda < 800$  nm decreases, while the absorbance of band at  $\lambda_{\text{max}}=945$  nm increases. In the presence of  $\text{Mg}^{2+}$ , the absorbance of all the bands increases, and the band at  $\lambda_{\text{max}}=508$  nm is displaced to lower wavelengths.

The UV-Vis spectra of the modified electrodes at 0.9 V are depicted in [Figure 4.25 \(panels a, c and e\)](#). At this oxidising potential the bands vary in a similar way, regardless of the nature of the cation: the absorbance of the band occurring at  $\lambda_{\text{max}}=315$  nm increases in the presence of metal cations, but the absorbance of bands at  $\lambda_{\text{max}}=382$  nm,  $\lambda_{\text{max}}=435$  nm and  $\lambda_{\text{max}}=508$  nm decreases. The band at  $\lambda_{\text{max}}=945$  nm shows an interesting profile: in the presence of metal cations the absorbance decreases and  $\lambda_{\text{max}}$  is displaced to shorter wavelengths; when the film is cycled again in background electrolyte, the band is displaced back to higher wavelengths, and in the case of  $\text{Mg}^{2+}$  and  $\text{Ba}^{2+}$  part of the absorbance is also restored. At 1.3 V ([panels b, d and f](#)) similar trends are observed, except for the absorbance of the band at  $\lambda_{\text{max}}=382$  nm, which increases in the presence of  $\text{Mg}^{2+}$ , and the absorbance at  $\lambda \approx 650$  nm, which also increases in the presence of  $\text{Mg}^{2+}$  and  $\text{Ba}^{2+}$ .

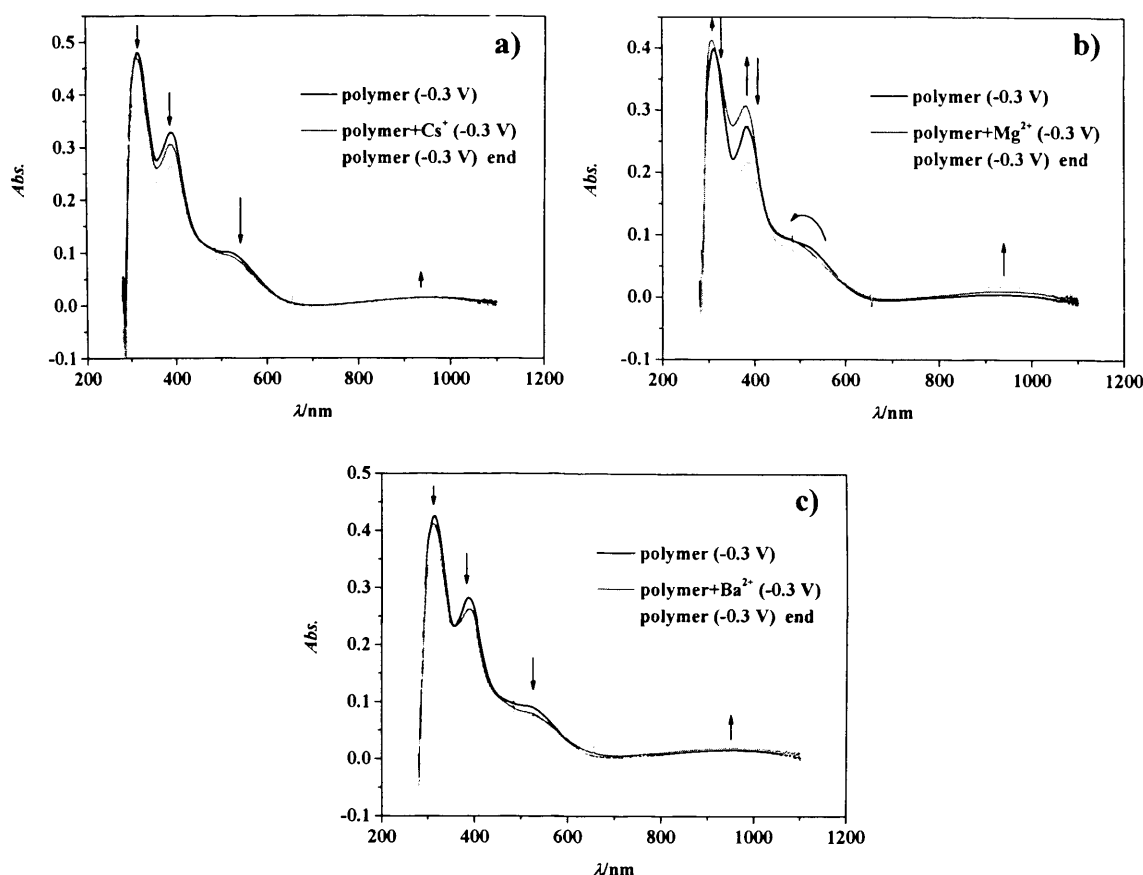


**Figure 4.24:** UV-Vis spectra of poly[Ni(3-Mesalophen-b15-c5)] acquired in  $0.1 \text{ mol dm}^{-3}$  TBAP/ $\text{CH}_3\text{CN}$  at  $-0.3 \text{ V}$  after the addition of  $200 \mu\text{L}$  of **a)**  $5 \text{ mmol dm}^{-3} \text{ CsClO}_4/0.1 \text{ mol dm}^{-3} \text{ TBAP/CH}_3\text{CN}$  and **b), c)**  $0.05 \text{ mol dm}^{-3} \text{ X(ClO}_4)_2$  ( $\text{X} = \text{Mg}^{2+}, \text{Ba}^{2+}$ ) /  $0.1 \text{ mol dm}^{-3} \text{ TBAP/CH}_3\text{CN}$ . The spectra are referenced to  $0.1 \text{ mol dm}^{-3} \text{ TBAP/CH}_3\text{CN}$ . Arrows indicate variation of absorbance (vertical) and wavelength (horizontal).

Table 4.11 depicts  $\lambda_{\text{max}}$  and  $\epsilon_{\lambda}$  for each type of cation added. Overall, both these parameters decrease upon cation addition, but when cycled again in background electrolyte they are partially restored, indicating some degree of reversibility.

The band at  $\lambda_{\text{max}}=945 \text{ nm}$  shows the highest displacement in the presence of metal cations. This band is associated with the transition between the valence band and the bonding polaronic state. Considering a symmetric distribution of energy, if the energy difference between these two electronic levels is increased, the electronic transition between bonding and antibonding polaronic states will occur at lower energies (recall Figure 4.23), which may explain the increase in absorbance observed in  $\lambda \approx 650 \text{ nm}$  at  $1.3 \text{ V}$ .

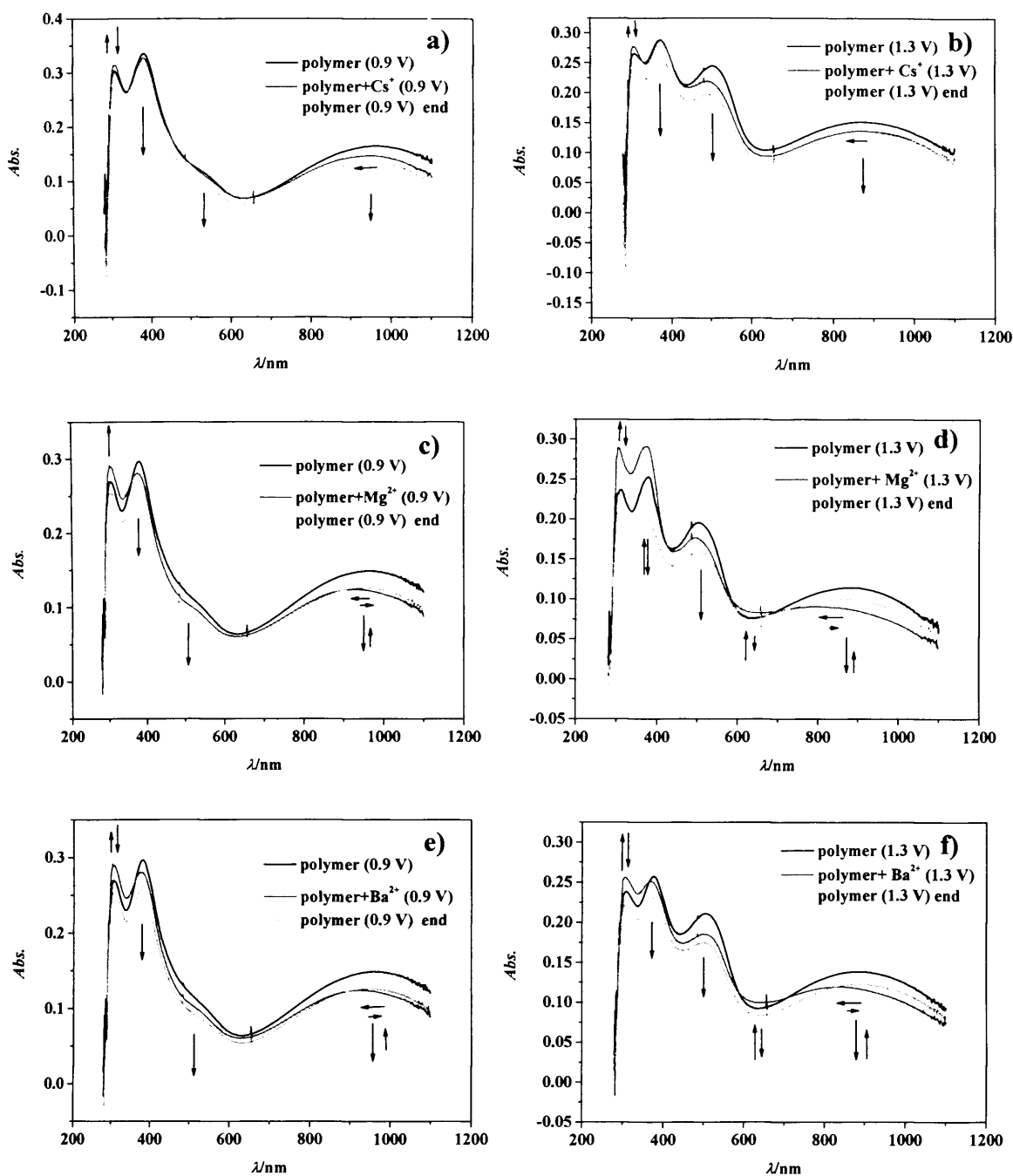


**Figure 4.25:** UV-Vis spectra of poly[Ni(3-Mesalophen-b15-c5)] acquired in 0.1 mol dm<sup>-3</sup> TBAP/CH<sub>3</sub>CN at 0.9 V (a, c and e) and at 1.3 V (b, d and f) after the addition of 200 μL of a) and b) 5 mmol dm<sup>-3</sup> CsClO<sub>4</sub>/0.1 mol dm<sup>-3</sup> TBAP/CH<sub>3</sub>CN and c) to f) 0.05 mol dm<sup>-3</sup> X(ClO<sub>4</sub>)<sub>2</sub> (X= Mg<sup>2+</sup>, Ba<sup>2+</sup>) / 0.1 mol dm<sup>-3</sup> TBAP/CH<sub>3</sub>CN. The spectra are referenced to 0.1 mol dm<sup>-3</sup> TBAP/CH<sub>3</sub>CN. Arrows indicate variation of absorbance (vertical) and wavelength (horizontal).

**Table 4.11:** Response of extinction coefficients  $\epsilon_\lambda$ , associated with the electronic transitions, to cation additions.

Before addition		After addition		Film+cation cycled in background electrolyte	
Cs <sup>+</sup> Additions					
$\lambda/\text{nm}$	$\epsilon / \text{mol}^{-1} \text{dm}^{-3} \text{cm}$	$\lambda/\text{nm}$	$\epsilon / \text{mol}^{-1} \text{dm}^{-3} \text{cm}$	$\lambda/\text{nm}$	$\epsilon / \text{mol}^{-1} \text{dm}^{-3} \text{cm}$
315	17560	313	11060	315	14410
384	5500	381	5490	382	5700
431	5980	427	4180	427	4720
508	15390	497	14430	500	13740
945	14750	932	11820	926	12880
Mg <sup>2+</sup> Additions					
$\lambda/\text{nm}$	$\epsilon / \text{mol}^{-1} \text{dm}^{-3} \text{cm}$	$\lambda/\text{nm}$	$\epsilon / \text{mol}^{-1} \text{dm}^{-3} \text{cm}$	$\lambda/\text{nm}$	$\epsilon / \text{mol}^{-1} \text{dm}^{-3} \text{cm}$
314	20900	308	12730	313	18310
381	6740	380	4990	380	5650
437	7430	429	4170	430	6540
504	15370	496	10720	506	14380
934	18960	887	11250	910	16570
Ba <sup>2+</sup> Additions					
$\lambda/\text{nm}$	$\epsilon / \text{mol}^{-1} \text{dm}^{-3} \text{cm}$	$\lambda/\text{nm}$	$\epsilon / \text{mol}^{-1} \text{dm}^{-3} \text{cm}$	$\lambda/\text{nm}$	$\epsilon / \text{mol}^{-1} \text{dm}^{-3} \text{cm}$
315	18120	312	15790	315	18700
382	6200	379	6240	380	6810
435	6210	429	5680	428	5910
508	13540	511	14500	506	15223
945	16010	906	15350	930	15540



## CONCLUDING REMARKS

The oxidation of [Ni(3-Mesalophen-b15-c5)] complex in acetonitrile leads to the formation of electroactive films on the surface of the working electrode. The oxidation degree  $n$  associated with poly[Ni(3-Mesalophen-b15-c5)] was found to be a fractional number (0.47), indicating that the electrochemical response is associated with the polymer backbone rather than the nickel metal centre. Moreover, surface coverage  $\Gamma$  was found to increase linearly with the number of deposition cycles in all the range of films prepared (1-150 deposition cycles) and the rate of charge transport considered fast in the experimental timescale investigated (0.01-0.5 V s<sup>-1</sup>).

Ion recognition studies were performed using perchlorate salts of Cs<sup>+</sup>, Mg<sup>2+</sup> and Ba<sup>2+</sup>. Cyclic voltammetry showed the displacement of redox features to positive potentials and decrease in the magnitude of current intensity, which was associated with the presence of metal cations within these conjugated polymers. Dynamic studies showed that in the presence of large amounts of metal cation, the rate of charge transport becomes diffusion controlled, particularly in thick films ( $\Gamma > 70 \text{ nmol cm}^{-2}$ ).

The electrochemical response of modified electrodes can be divided into two different stages: the first corresponds to the first few additions (1<sup>st</sup>-3<sup>rd</sup> addition), and the second to the subsequent additions (4<sup>th</sup>-  $n^{\text{th}}$  addition). In the first stage, Nernstian dependence of the peak potential  $E_{\text{pal}}$  on the metal cation concentration was observed when the following conditions were simultaneously fulfilled: (i) films prepared with low  $\Gamma$  and (ii) aliquots of low cation concentration (5-20  $\mu\text{mol dm}^{-3}$ ) were added. For thicker films and higher cation concentration the size of cation becomes important, and only for Mg<sup>2+</sup> additions could Nernstian relations be observed. The magnitude of the peak current  $i_{\text{pcll}}$  was also found to vary oppositely in the presence of Mg<sup>2+</sup> (increase) and Cs<sup>+</sup> or Ba<sup>2+</sup> (decrease). In the second stage the doping/undoping process, together with the presence of metal cation, seems to play a detrimental role in the stability of film.

The reproducibility of the voltammetric response decreases for films prepared with  $\Gamma > 70 \text{ nmol cm}^{-2}$ . Additionally, the variation of ion recognition properties was found to be non-monotonic with the increase of  $\Gamma$ . These findings suggest the occurrence of morphologic changes and increase of film heterogeneity with increase of  $\Gamma$ .

Analysis of UV-Vis spectra of the modified electrode showed that the deposited species are chromophores whose electronic structure varies reversibly with the doping state. In addition, the values of extinction coefficients suggest that the electronic transitions occurring during doping/undoping of these films involve states with considerable contribution from ligand orbitals. The UV-Vis bands were assigned to the formation of charge carriers, more specifically polarons, except for the band at  $\lambda_{max} = 508$  nm whose profile suggests it to be associated with charge transfer between the metal and fully oxidised polymer.

In the presence of metal cations there is a displacement of UV-Vis bands towards higher energies. The extinction coefficients are of the same order of magnitude as prior to the additions, indicating that the conduction mechanism is kept in the presence of metal cations. After the removal of metal cations from the electrolyte partial reversibility was observed. Although the optical changes observed in the presence of metal cations are useful in fundamental/mechanistic studies, they are not large enough to use analytically. The electrochemical response seems to be better suited for this purpose.

## REFERENCES:

1. Vilas-Boas, M.; Freire, C.; de Castro, B.; Christensen, P. A.; Hillman, A. R. *Inorg. Chem.* **1997**, *36*, 4919.
2. Vilas-Boas, M.; Freire, C.; de Castro, B.; Hillman, A. R. *J. Phys. Chem. B* **1998**, *102*, 8533.
3. Vilas-Boas, M.; Henderson, M. J.; Freire, C.; Hillman, A. R.; Vieil, E. *Chem. -Eur. J.* **2000**, *6*, 1160.
4. Vilas-Boas, M.; Santos, I. C.; Henderson, M. J.; Freire, C.; Hillman, A. R.; Vieil, E. *Langmuir* **2003**, *19*, 7460.
5. Genies, E. M.; Bidan, G.; Diaz, A. F. *J. Electroanal. Chem.* **1983**, *149*, 101.
6. Waltman, R. J.; Bargon, J.; Diaz, A. F. *J. Phys. Chem.* **1983**, *87*, 1459.
7. Dahm, C. E.; Peters, D. G.; Simonet, J. *J. Electroanal. Chem.* **1996**, *410*, 163.
8. Bauerle, P.; Gotz, G.; Hiller, M.; Scheib, S.; Fisher, T.; Segelbacher, U.; Bennati, M.; Grupp, A.; Mehring, M.; Stoldt, M.; Seidel, C.; Geiger, F.; Schweizer, H.; Umbach, E.; Schmelzer, M.; Roth, S.; Egelhaaf, H. J.; Oelkrug, D.; Emele, P.; Port, H. *Synth. Met.* **1993**, *61*, 71.
9. Bauerle, P.; Scheib, S. *Adv. Mater.* **1993**, *5*, 848.
10. Bauerle, P.; Scheib, S. *Acta Polym.* **1995**, *46*, 124.
11. Rimmel, G.; Bauerle, P. *Synth. Met.* **1999**, *102*, 1323.
12. Scheib, S.; Bauerle, P. *J. Mater. Chem.* **1999**, *9*, 2139.
13. Sanniccolo, F.; Brenna, E.; Benincori, T.; Zotti, G.; Secchin, Z.; Schiavon, G.; Pilati, T. *Chem. Mater.* **1998**, *10*, 2167.
14. Fabre, B.; Marrec, P.; Simonet, J. *J. Electroanal. Chem.* **2000**, *485*, 94.
15. Youssoufi, H. K.; Hmyene, M.; Garnier, F.; Delabouglise, D. *J. Chem. Soc., Chem. Commun.* **1993**, 1550.
16. Youssoufi, H. K.; Yassar, A.; Baiteche, S.; Hmyene, M.; Garnier, F. *Synth. Met.* **1994**, *67*, 251.
17. Garnier, F.; Youssoufi, H. K.; Hmyene, M.; Yassar, A. *Polym. Prepr.* **1994**, *35*, 205.
18. Sevcik, A. *Czech Chem. Commun.* **1948**, *20*, 327.
19. Carneiro, A. In *Filmes Polimericos do tipo [M(Salen)] Funcionalizados para o Reconhecimento de Catiões Representativos*, PhD Thesis, University of Porto, Department of Chemistry, 2005.

20. Tedim, J.; Freire, C.; Hillman, A. R. *submitted to PCCP*.
21. Penner, R. M.; Van Dyke L. S.; Martin, C. R. *Solid State Ionics* **1989**, 32-33, 553.
22. Olsen, C. L.; Sokoloski, T. D.; Pagay, S. N.; Michaels, D. *Anal. Chem.* **1969**, 41, 865.
23. Burgmayer, P.; Murray, R. W. In *Handbook of Conducting Polymers*, 1st ed.; Skotheim, T. A., Ed.; Marcel Dekker: New York, 1986; Vol. 1, p 507.
24. Lever, A. B. P. In *Inorganic Electronic Spectroscopy*, 2nd ed.; Elsevier: New York, 1984.
25. Vilas-Boas, M.; Freire, C.; de Castro, B.; Christensen, P. A.; Hillman, A. R. *Chem.-Eur. J.* **2001**, 7, 139.
26. Lyons, M. E. G. In *Electroactive Polymer Electrochemistry Part 1: Fundamentals*; Lyons, M. E. G., Ed.; Plenum: New York, 1994; Chapter 1.
27. Bredas, J. In *Handbook of Conducting Polymers*, 1st ed.; Skotheim, T. A., Ed.; Marcel Dekker: New York, 1986; Vol. 2, Chapter 25.
28. Bredas, J. L.; Scott, J. C.; Yakushi, K.; Street, G. B. *Phys. Rev. B* **1984**, 30, 1023.

## Chapter 5

***COMPOSITIONAL AND STRUCTURAL STUDIES OF  
POLY[M(SALEN)] FILMS BY X-RAY TECHNIQUES:  
XPS AND XAS***

## 5.1 INTRODUCTION

In the previous chapter poly[Ni(3-Mesalophen-b15-c5)] was shown to possess conducting properties typical of conjugated polymers. The coulometric assay suggested that the electrochemical response is ligand-based and the conducting properties were attributed to the formation of polarons; these are characteristics observed for all the range of poly[M(*salen*)] electroactive films studied so far<sup>1,4</sup>. In addition, spectroelectrochemical studies showed that the chemical and physical properties of these films are typical of polyphenylene compounds<sup>1,4</sup>. In spite of the extensive work involving the characterisation of these systems, little is known about their structure. There are crystallographic data reporting the structure of [Ni(*salen*)] complexes<sup>5</sup> but not of poly[Ni(*salen*)] films. The latter are soft, amorphous materials, with a low degree of long-range structural order, and therefore conventional X-ray diffraction techniques cannot be used.

Additionally, the electrochemical/spectroelectrochemical properties of poly[Ni(3-Mesalophen-b15-c5)] were investigated and found to change upon metal cation addition; these results suggest that this film fulfils two indispensable requirements for sensing applications: selectivity towards the target species and a suitable detection method<sup>6</sup>. The first is inherent to the characteristics of crown ethers, which are known to bind selectively to cations based on the macrocyclic effect<sup>7</sup>; the second results from the fact that this film possesses redox properties and the inclusion of guests at sites sensitive to changes in electronic environment offer the prospect of an electrochemical route for their detection<sup>6,8</sup>. Similar results were found by Carneiro<sup>9</sup> for films bearing pseudo-crown ethers, poly[M(3-MeOsaltMe)] (M=Ni, Cu). However, the location of the binding site and the mechanism by which the bound species perturbs the film electronic structure (and thus redox characteristics) are unknown; acquiring this information is critical to the optimisation of these systems for ion recognition purposes. Though not directly, electrogravimetric studies by Martins and co-workers<sup>10</sup> showed that poly[Ni(3-MeOsalophen-b15-c5)] films are able to detect electroinactive ions (such as Ba<sup>2+</sup>) at micromolar levels; furthermore, the shapes of the isotherms suggested two binding sites, the crown ether itself and a “pseudo-crown” involving the methoxy groups and the oxygens connected to the nickel metal centre.

In this chapter, compositional and structural studies of different poly[Ni(*salen*)] films by XPS and XAS are presented. The aims of this work are two-fold: (i) determination of the structure of poly[Ni(*salen*)] films; (ii) rationalisation of ion recognition properties in

terms of structural characteristics. The first objective is accomplished by the study of EXAFS near the Ni K-edge. The second is provided by using  $\text{Ba}^{2+}$  as the “probe” ion: analysis of EXAFS near Ba K-edge will unambiguously identify the structure around  $\text{Ba}^{2+}$  and therefore the receptor site<sup>11,12</sup>.

There are few works reporting XAS studies of  $[\text{M}(\text{salen})]$  complexes. The majority of them are associated with the application of  $[\text{M}(\text{salen})]$  for catalytic purposes, either in solution<sup>13,14</sup> or in heterogeneous systems<sup>15,16</sup>. There are two studies reporting  $[\text{M}(\text{salen})]$  complexes in polymeric systems, one by Nishide et al<sup>17</sup> and the other by Youm et al<sup>18</sup>; neither, however, reports the study of these complexes within *conducting* polymer systems. In the former, a  $[\text{Co}(\text{salen})]$  complex is supported in poly(octyl methacrylate) and the formation of a Co/dioxygen adduct results in the reversible stretching of the polymer. The work by Youm et al reports the preparation of a 1D heterometallic coordination polymer containing  $[\text{Mn}^{\text{III}}(\text{salen})]$  and a  $[\text{Fe}^{\text{II}}(\text{L})_2]$  moiety. XAS is used to confirm the reduction of the iron centres when the  $[\text{Fe}^{\text{III}}(\text{L})_2]^+$  moiety is incorporated into the polymer. Also, only a relatively small number of EXAFS studies involving polymers with crown ethers can be found in the literature<sup>19-21</sup>.

This chapter is divided into two sections: in the first, compositional studies by XPS are presented for one of the electroactive films also studied by XAS, poly[Ni(3-Mesalophenb15-c5)]; the second section presents the results of XAS studies performed in poly[Ni(*salen*)] films and is divided into two subsections. In the first subsection, a film bearing only a pseudo crown receptor (poly[Ni(3-MeOsaltMe)]) is studied in detail. The second subsection is devoted to XAS results obtained for poly[Ni(*salen*)] films bearing benzo-crown ether macrocycles.

## 5.2 COMPOSITIONAL STUDIES OF POLY[Ni(3-MESALOPHEN-B15-C5)] BY XPS

The results of XPS measurements for films cycled in background electrolyte, both in the absence and presence of  $\text{Ba}(\text{ClO}_4)_2$ , are depicted in [Figure 5.1](#). The spectra acquired show that there are no significant changes in the N, O, C, Ni and Cl spectral lines upon metal addition, although  $\text{Ba}^{2+}$  ingress into the film is evident.

[Table 5.1](#) presents the ratios of N:Ni, O:N, Cl:Ba and Ni:Ba in each sample analysed. Comparing the expected ratios of the monomer with those of the film, the amount of N in the film is higher than in the monomer structure. This may be due to the presence of solvent molecules ( $\text{CH}_3\text{CN}$ ), thereby indicating the film permeation by solvent. Furthermore, the presence of Cl within the polymeric film also shows the ingress of ionic species from the electrolyte. To some extent, this also explains the excess of O content in the film. Addition of  $\text{Ba}(\text{ClO}_4)_2$  to background electrolyte results in the increase of N (more solvent goes inside the polymer) probably because  $\text{Ba}^{2+}$  is solvated and the porosity of the film allows its ingress in this arrangement.

If  $\text{Ba}^{2+}$  and  $\text{ClO}_4^-$  contents in the film are influenced by its doping state, one would expect that, in the reducing state, the amount of  $\text{Ba}^{2+}$  would be half as much as that of  $\text{ClO}_4^-$  (in fact, the proportion of  $\text{ClO}_4^-$  could be higher than 2:1 with respect to  $\text{Ba}^{2+}$  if  $\text{TBA}^+$  is also entrapped). The Cl:Ba ratio was found to be considerably lower than expected, 0.6:1.

The Ni:Ba ratio is 3.6:1, *i.e.* there is about one  $\text{Ba}^{2+}$  for each 4 monomer units. Considering the classical cation diameter-hole size relationship,  $\text{Ba}^{2+}$  would not fit the crown pocket because its ionic radius is 1.35 Å<sup>22,23</sup> and the diameter of 15-crown-5 is 1.7-2.2 Å<sup>24</sup>. In this case, the formation of sandwich complexes (benzo-15-crown-5/ $\text{Ba}^{2+}$ /benzo-15-crown-5) would be expected<sup>25</sup>. However, if barium formed sandwich complexes with all these macrocycle rings, the Ni:Ba ratio would have been 2:1, which corresponds to twice as much  $\text{Ba}^{2+}$ .



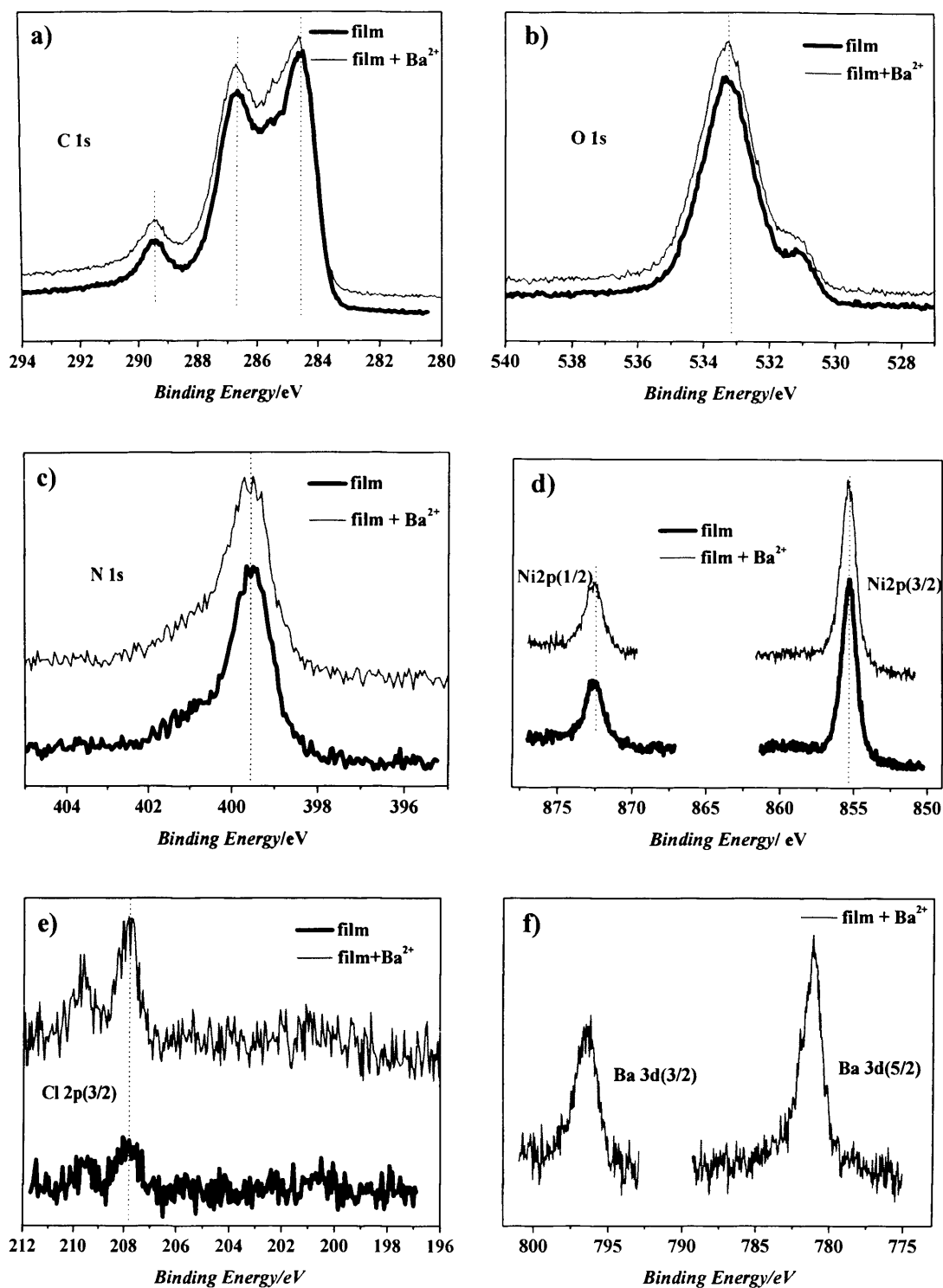


**Figure 5.1:** XPS spectra of poly[Ni(3-Mesalophen-b15-c5)] ( $\Gamma \approx 14 \text{ nmol cm}^{-2}$ , reduced state) with (—) and without (---)  $\text{Ba}(\text{ClO}_4)_2$ , in the regions of a) C 1s, b) O 1s, c) N 1s, d) Ni 2p, e) Cl 2p and f) Ba 3d.

**Table 5.1:** Atomic proportions of the elements present in films prepared with  $\Gamma \approx 14 \text{ nmol cm}^{-2}$  (scan rate of polymerisation  $\nu = 0.05 \text{ V s}^{-1}$ ), in the absence and presence of  $\text{Ba}(\text{ClO}_4)_2$  ( $0.002 \text{ mol dm}^{-3}$ ). The precision is generally 0.1 atomic %.

Sample	Atomic %						N/Ni	O/N	Cl/Ba	Ni/Ba
	C	N	O	Ni	Cl	Ba				
<b>Monomer*</b>	75.0	5.0	17.5	2.5	—	—	2.0	3.5	—	—
<b>Film</b>	71.7	3.3	23.5	1.1	0.4	—	2.9	7.2	—	—
<b>Film+Ba<sup>2+</sup></b>	70.1	3.9	24.4	1.1	0.2	0.3	3.6	6.3	0.6	3.6

(\*) estimated values based on the monomer structure

Table 5.2 summarises the XPS results obtained for films prepared in similar conditions to those presented in Table 5.1, except for the scan rate: the poly[Ni(3-Meslophen-b15-c5)] films shown in Table 5.1 were prepared by cycling the potential at  $0.05 \text{ V s}^{-1}$ , whereas the films presented in Table 5.2 were prepared at  $0.1 \text{ V s}^{-1}$ . Electrochemically, the former have twice as much electroactive deposited species as the latter, which is expected since at lower scan rates the system spends longer times at oxidising/polymerising potentials (higher amount of deposited species per cycle). Comparing the N:Ni and O:N ratios of films in Table 5.1 and Table 5.2, films prepared at lower scan rates show lower amounts of  $\text{CH}_3\text{CN}$ ; this may be explained by the fact that solvent molecules are uncharged species and therefore ‘respond’ slower to changes in doping states when compared to ionic species. This is particularly evident at shorter timescales.

The effect of  $\text{Ba}(\text{ClO}_4)_2$  concentration was also studied. When the concentration of  $\text{Ba}(\text{ClO}_4)_2$  in solution increased 25 times (from  $0.002 \text{ mol dm}^{-3}$  to  $0.05 \text{ mol dm}^{-3}$ ) the Cl:Ba proportion was found to remain the same, indicating that even when the concentration is increased,  $\text{Ba}^{2+}$  may be coordinated to donor atoms of the polymeric film (oxygen atoms from the crown ethers and/or oxygen atoms bonded to Ni). However, the Ni:Ba proportion changed dramatically from 3.6:1 for  $0.002 \text{ mol dm}^{-3}$  of  $\text{Ba}(\text{ClO}_4)_2$  in solution to 1:2.4 for  $\text{Ba}(\text{ClO}_4)_2$   $0.05 \text{ mol dm}^{-3}$ . It seems that for low concentrations  $\text{Ba}^{2+}$  occupies sites within the film which are more stable, whilst at more concentrated concentrations  $\text{Ba}^{2+}$  occupies all the sites potentially available. This behaviour unambiguously identifies change in terms of an ‘adsorption’ isotherm with the concentration of  $\text{Ba}^{2+}$  in solution. Nonetheless,

these changes cannot be considered to occur in all the film; XPS is a surface sensitive technique probing at most the first (outer) 10 nm of film, which excludes the inner layers. The films presented here have thickness ranging from 40 to 70 nm (estimated using  $\Gamma$  and film density), implying that, at most, only the outer 25 % of the film was probed.

In the next section, the deconvolution of XPS spectra and chemical identification of films in [Table 5.1](#) are presented.

**Table 5.2:** Atomic proportions of the elements present in films prepared with  $\Gamma \approx 8 \text{ nmol cm}^{-2}$  (scan rate of polymerisation  $\nu = 0.1 \text{ V s}^{-1}$ ), in the absence and presence of  $\text{Ba}(\text{ClO}_4)_2$  ( $0.05 \text{ mol dm}^{-3}$ ). The precision is generally 0.1 atomic %.

Sample	Atomic %						N/Ni	O/N	Cl/Ba	Ni/Ba
	C	N	O	Ni	Cl	Ba				
<b>Monomer*</b>	75.0	5.0	17.5	2.5	—	—	2.0	3.5	—	—
<b>Film</b>	71.7	4.7	20.5	0.6	2.6	—	8.5	4.4	—	—
<b>Film+Ba<sup>2+</sup></b>	66.0	4.3	26.1	0.7	1.2	1.7	6.1	6.0	0.7	0.4

(\*) estimated values based on the monomer structure

### 5.2.1 Deconvolution of XPS data

Deconvolution of the XPS spectra for C 1s, N 1s and O 1s allows one to obtain information related to the different chemical environments experienced by different atoms within the structure, which is depicted in [Figure 5.2](#) (the results are summarised in [Table 5.3](#)).

The peak energies of the raw XPS spectra are displaced to more negative values than the typical energies found in XPS databases. This may be due to the flood gun effect (section 2.4.1.2, Chapter 2). Usually, to correct this energy shift, the binding energy for aliphatic C 1s is considered to be at 285 eV. The difference between this value and the experimental peak energy is then adjusted to all the analysed elements (data used here as reference are reported elsewhere<sup>26</sup>). In the present case, the C 1s spectrum is rather complex to assign. Using the N 1s spectra and considering from reference data that the spectral line should appear at 399 eV, the chemical shift was calculated and found to be *ca.* 3 eV (see [Figure 5.1](#)).

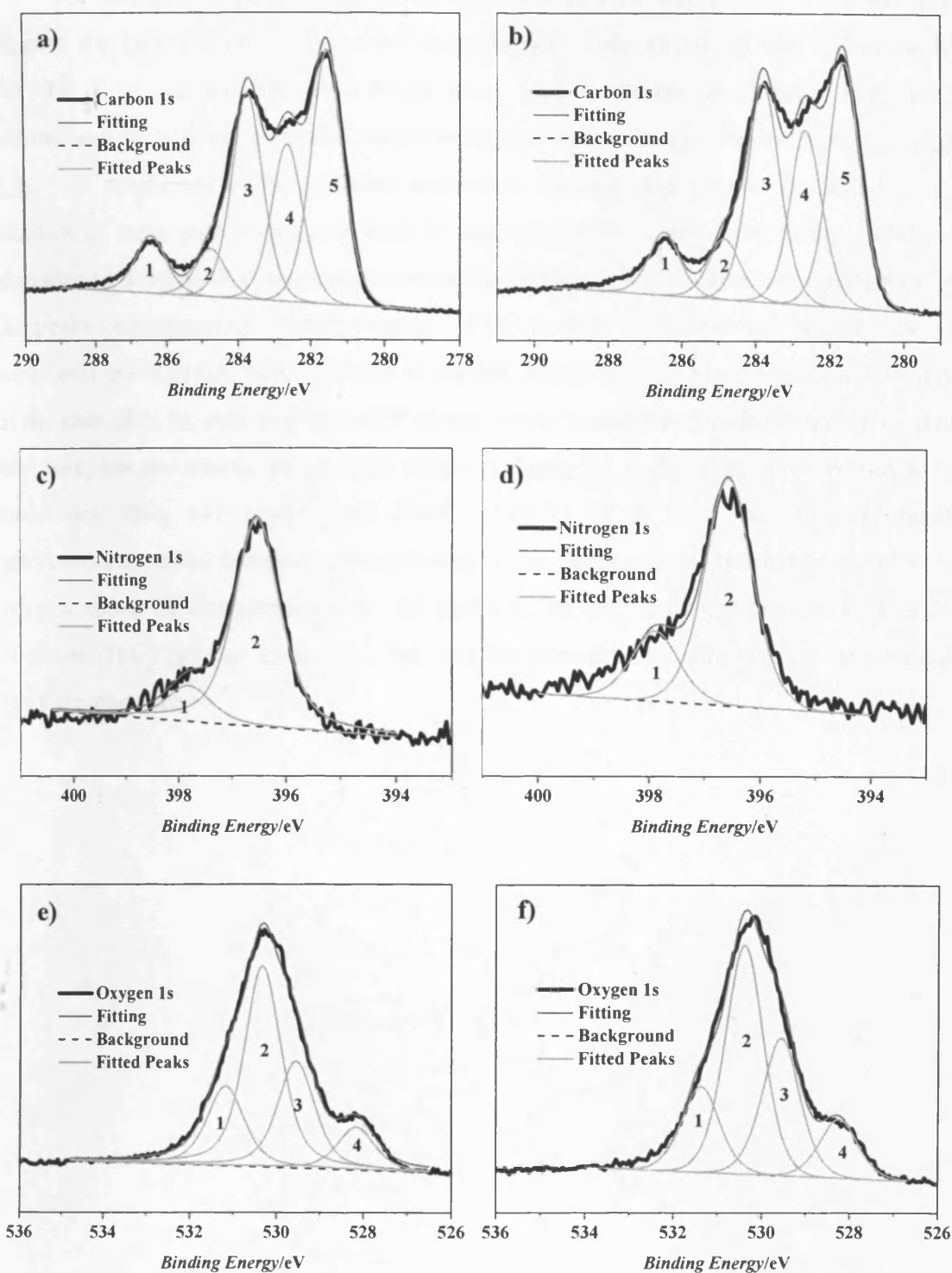


**Figure 5.2:** Deconvolution of raw XPS spectra for films in the absence (panels a, c and e) and presence (panels b, d and f) of  $\text{Ba}(\text{ClO}_4)_2$ . Numbers of the fitted peaks for the C 1s spectral line (panels a and b) are assigned to the carbon atoms as shown in Figure 5.3 (see next page).

The number of peaks used to fit the XPS spectra was chosen considering two aspects: the chemical environment and the presence of electrolyte species within the film. For the C 1s spectral line, five peaks were used to fit the spectrum. This number corresponds to different chemical environments present in the monomeric structure (Figure 5.3). As mentioned earlier, solvent molecules are also expected to be found, but the addition of extra peaks does not result in major improvements of the fitting. Then, it is plausible to assume that the peaks accounting for these extra sources are overlapped with the peaks corresponding to the polymer. If this is true, the proportion between the peak areas will not coincide with the ratio of carbon atoms in the monomer/polymer structure. In the case of N 1s, only one type of N atoms would be observed considering the monomer structure, but the atomic percentages listed in Table 5.1 indicate the presence of solvent molecules; thus, two peaks were fitted. For O 1s at least two distinct chemical environments can be detected, corresponding to the oxygen atoms bonded to nickel and the oxygen atoms in the crown ether. In addition, oxygen from perchlorate ions and the substrate (ITO) are also expected. The number of peaks found to give the best fitting in this case was four.

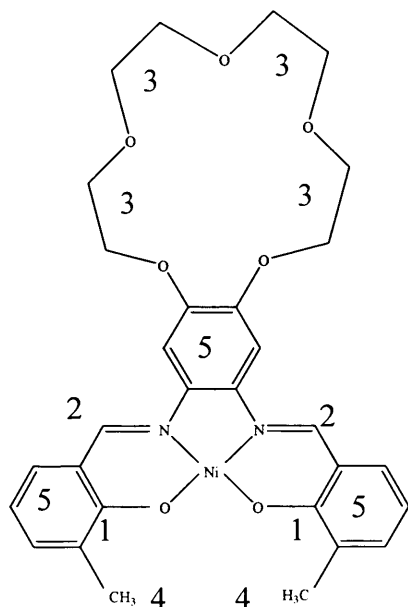


**Figure 5.3:** Different chemical environments of carbon in poly[Ni(3-Mesalophen-b15-c5)].

**Table 5.3:** Corrected binding energy values for XPS spectra presented in [Figure 5.2](#).

Poly[Ni(3-Mesalophen-b15-c5)]					
Spectral line	Binding Energy/eV				
C 1s	289.4	287.8	286.7	285.6	284.6
N 1s	399.5	400.9	_____	_____	_____
O 1s	534.3	533.4	532.5	531.1	_____
Cl 2p	207.7 <sub>[2p(3/2)]</sub>	_____	_____	_____	_____
Ni 2p	855.2 <sub>[2p(3/2)]</sub>	872.4 <sub>[2p(1/2)]</sub>	_____	_____	_____
Poly[Ni(3-Mesalophen-b15-c5)]+Ba(ClO <sub>4</sub> ) <sub>2</sub>					
Spectral line	Binding Energy/eV				
C 1s	289.5	287.8	286.8	285.6	284.6
N 1s	399.6	400.9	_____	_____	_____
O 1s	534.4	533.4	532.6	531.2	_____
Cl 2p	207.8 <sub>[2p(3/2)]</sub>	_____	_____	_____	_____
Ni 2p	855.3 <sub>[2p(3/2)]</sub>	872.5 <sub>[2p(1/2)]</sub>	_____	_____	_____
Ba 3d	797.3 <sub>[3d(3/2)]</sub>	781.1 <sub>[3d(5/2)]</sub>	_____	_____	_____

For the C 1s spectral line, the peak occurring at the highest energy ([Figure 5.2, panel a](#)) is attributed to the carbon atoms assigned with *1* in [Figure 5.3](#) because they are bonded to the O atom, whose electronegative character is accentuated due to the bond established with the nickel metal centre. The area of peak 2 is similar to that of peak 1 (*i.e.* the number of carbon atoms is identical) and is attributed to carbon atoms bonded to nitrogen atoms. Despite the binding energies being higher than expected for cyanides, it may be explained by the increase of nitrogen electronegativity arising from its interaction with Ni<sup>2+</sup>. Peak 3 corresponds to the carbon atoms bonded to the crown ether, since the relative area is one of the largest and the peak energy is similar to the reference data (C 1s for ethanol - 286.3 eV vs. 286.7 eV for peak 3). Peaks 4 and 5 are assigned to the electronically ‘shielded’ carbon atoms (occurring at lower energies). Comparison with the reference data allows the

assignment of peak 4 to C atoms of methyl substituents (C 1s for toluene is 284.7 eV vs. 285.6 eV obtained for peak 4), whilst peak 5 is assigned to the aromatic carbons 5 (C 1s for benzene is 284.4 eV vs. 284.6 eV observed).

Table 5.4 shows the areas of the C 1s fitted peaks and their normalisation with respect to the smallest peak (in this case peak 2). There is good agreement between this parameter (column 3) and the proportion of C atoms (column 5), except for peaks 4 and 5. The area of peak 4 is higher than the expected whereas for peak 5 the opposite is observed. This may be related to the presence of solvent molecules, an additional source of carbon atoms (CH<sub>3</sub>CN). In the presence of Ba<sup>2+</sup> (Figure 5.2, panel b) similar fittings were obtained for C 1s. Notwithstanding some differences in the absolute values, the normalised areas still match the number of C 1s atoms.

**Table 5.4:** Normalised areas and proportion of C atoms in poly[Ni(3-Mesalophen-b15-c5)].

Poly[Ni(3-Mesalophen-b15-c5)]				
Peak	Area	Normalised areas*	Number of C atoms	Proportion of C atoms
1	1837	1.2	2	1
2	1541	1.0	2	1
3	6622	4.3	8	4
4	5053	3.3	2	1
5	8202	5.3	16	8
Poly[Ni(3-Mesalophen-b15-c5)]+Ba(ClO <sub>4</sub> ) <sub>2</sub>				
Peak	Area	Normalised areas*	Number of C atoms	Proportion of C atoms
1	2015	1.0	2	1
2	1957	1.0	2	1
3	7048	3.6	8	4
4	5623	2.9	2	1
5	7898	4.0	16	8

(\*) Peak areas normalised with respect to the smallest area (Peak 2).

In the N 1s spectral line (Figure 5.2 panels c, d), the area of peak 2 is 4 to 5 times higher than peak 1; peak 2 is then assigned to nitrogen from the imine bridge, and peak 1 to nitrogen from solvent molecules. The area of peak 1 is about 20 % of the total, which gives a measure of solvent entrapment within this system. The reference data show a very small difference in terms of energy between these two different sources of nitrogen (for instance, the spectral line N 1s for (C<sub>6</sub>H<sub>5</sub>)CN lies in the range 397.7-399.7 eV <sup>26</sup>). In the presence of Ba<sup>2+</sup> (panel d) the area of peak 1 corresponds to 30 % of the overall area, which is higher than observed for the film with no Ba<sup>2+</sup>.

Four peaks were used to fit the O 1s spectrum (panels e, f). According to reference data, the spectral line associated with O 1s in ethers occurs at higher energies for aliphatic than for aromatic compounds (538.5 vs. 533.0 eV, respectively<sup>26</sup>). To a first approximation, the XPS region including peaks 1, 2 and 3 would be assigned to the oxygen atoms of the crown ether whilst peak 4 would be assigned to oxygen atoms bound to Ni<sup>2+</sup>. Nonetheless, the proportion between these two is much higher than expected considering the monomeric structure (9:1 vs. 2.5:1). On the other hand, the ratio of (Peak 1+ Peak 2):Peak 3 gives 2.4:1, closer to that expected. Hence, peaks 1 and 2 are assigned to the oxygen atoms of the crown ether, whilst peak 3 is attributed to the oxygen atoms bound to Ni<sup>2+</sup>. The area of peak 4 has to be assigned to another source of oxygen. In principle it could be assigned to perchlorate, whose O 1s spectral line may occur at lower energies than those of the ether functionalities (532.7 eV <sup>26</sup>). The area of peak 4 corresponds to about 10 % of the overall area in the O 1s region. The atomic percentage of O was found to be around 23 % (Table 5.1), so 2.3 % of oxygen may be attributed to the presence of ClO<sub>4</sub><sup>-</sup>. According to the atomic percentage of Cl (0.4 %) the percentage of oxygen associated with the perchlorate ion should be about 1.6 %, which is considered in reasonable agreement. On the other hand, for the film with Ba<sup>2+</sup> the area of peak 4 still represents 10 % of the total O 1s area (2.4 %). Since the atomic percentage of Cl in this case is only 0.2 % (and the oxygen atomic percentage in ClO<sub>4</sub><sup>-</sup> is 0.8 %), the assignment of peak 4 cannot correspond to ClO<sub>4</sub><sup>-</sup>; the other possibilities include residual atmospheric contaminants and/or oxygen from the substrate (ITO). The former possibility is discarded because the samples were analysed in UHV conditions. The latter is more likely and would result in a fairly constant source of oxygen, which may be the reason why peak 4 does not change from sample to sample. Oxygen from ClO<sub>4</sub><sup>-</sup> has to be included in the area



of the peaks at higher binding energies. A proof of this is the ratio (Peak 1+ Peak2):Peak 3, which decreases to 2.3:1 in the presence of  $\text{Ba}^{2+}$ .

For  $\text{Ni } 2p_{(3/2)}$  the position of the spectral line, both in the absence/presence of  $\text{Ba}^{2+}$ , is typical of Ni in oxidised states (+2) ( $\text{Ni } 2p_{(3/2)}$  in  $\text{Ni(OH)}_2$  occurs at 855.3-856.6 eV <sup>26</sup>). For  $\text{Ba } 3d_{(5/2)}$ , the value obtained is very similar to that obtained for  $\text{Ba(ClO)}_4$ , but changes in the oxidation state or chemical environment cannot be confirmed because the energy of this spectral line does not change significantly with barium oxidation state. However, the oxidation state of barium is considered to be +2 and to remain unchanged.

The deconvolution of XPS spectra was here used to provide insight into the different chemical environments experienced by atoms of the same element within the sample. Recognizing the uncertainties associated with the number and area of the fitted peaks, together with the characteristics of the fitting procedure, these insights are valid at the qualitative level.

## 5.3 STRUCTURAL STUDIES OF POLY[Ni(*SALEN*)] FILMS BY XAS

### 5.3.1 Poly[Ni(3-MeOsaltMe)]: polymeric films bearing pseudo crown receptors

The preparation and characterisation of poly[Ni(3-MeOsaltMe)] by cyclic voltammetry and analysis by XPS is beyond the scope of this thesis and was performed by other colleagues. Nonetheless, it is necessary to present here some information in order to interpret the data obtained by XAS (for further information see reference<sup>11</sup>).

#### 5.3.1.1 Electrochemical Characterisation

Similar to other poly[M(*salen*)] films (Chapter 4), poly[Ni(3-MeOsaltMe)] was prepared by oxidative polymerisation of [Ni(3-MeOsaltMe)] in CH<sub>3</sub>CN. Figure 5.4a shows the voltammetric response acquired during the polymerisation process. In the first scan the current is characterised by a sharp increase in current at 0.71 V, followed by two incompletely resolved anodic waves at  $E_{pa}$ =0.84 and 0.92 V. On the reverse scan, four peaks occurring at  $E_{pc}$ =0.80, 0.72, 0.43, and 0.26 V correspond to the reduction of prior deposited film. In the second anodic half-cycle two new anodic waves corresponding to the oxidation of the previously deposited film occur at  $E_{pa}$ =0.26 and 0.56 V. All the observed features increase continuously with potential cycling, except for the broad peak occurring around 1.0 V in the first cycle, which is attributed to the monomer oxidation.

The voltammetric response of the modified electrode was also analysed in background electrolyte (Figure 5.4b). The voltammetric response evolves during the first few scans but then it stabilises, typically after 5 scans - 'film conditioning'. At this stage four chemically reversible processes occur at potential mean values  $\langle E(I) \rangle = 0.19$  V,  $\langle E(II) \rangle = 0.40$  V,  $\langle E(III) \rangle = 0.80$  V and  $\langle E(IV) \rangle = 0.92$  V. Similar coulometric assay to that presented in section 4.2.2.1 was used to determine the oxidation degree of poly[Ni(3-MeOsaltMe)]. The value of  $n$  (per monomeric unit) was found to be 0.52, indicating that the redox processes are ligand-based<sup>3</sup>.

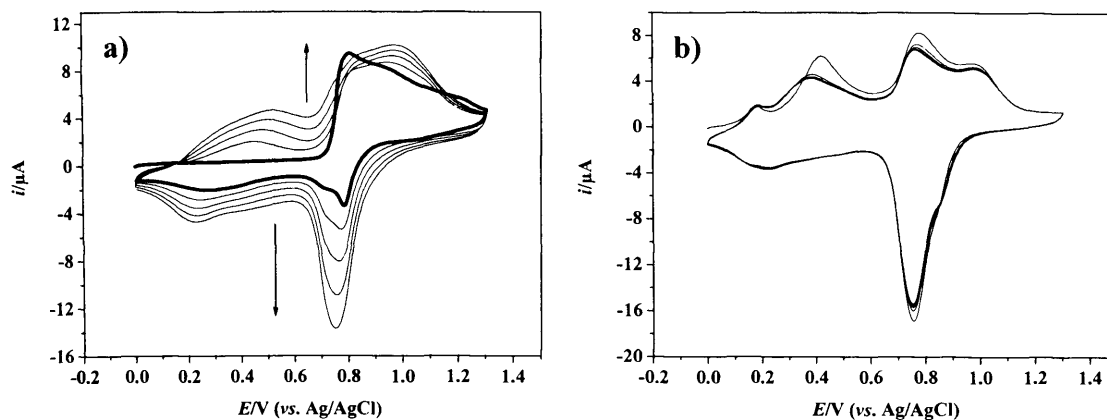


**Figure 5.4:** a) Oxidative polymerisation of 1 mmol dm<sup>-3</sup> [Ni(3-MeOsaltMe)] in 0.1 mol dm<sup>-3</sup> TBAP/CH<sub>3</sub>CN, between 0.0 and 1.3 V at 0.1 V s<sup>-1</sup> (10 deposition cycles) and b) redox switching of the modified electrode poly[Ni(3-MeOsaltMe)] ( $\Gamma=46$  nmol cm<sup>-2</sup>) in 0.1 mol dm<sup>-3</sup> TBAP/CH<sub>3</sub>CN between 0.0 and 1.3 V at 0.1 V s<sup>-1</sup>. Arrows indicate time sequence of cycles.

The voltammetric response of a poly[Ni(3-MeOsaltMe)] modified electrode ( $\Gamma = 5.0$  nmol cm<sup>-2</sup>) and its change upon successive additions of Ba(ClO<sub>4</sub>)<sub>2</sub> to the supporting electrolyte solution is shown in [Figure 5.5](#). Upon Ba(ClO<sub>4</sub>)<sub>2</sub> additions, a new anodic feature appears at  $E_{pa}=0.88$  V, whose peak intensity increases until reaching a plateau value. There is also a decrease in the current intensity associated with the anodic features previously observed in background electrolyte; the feature occurring at  $E_{pa} = 0.40$  V is positively shifted. In the reverse half-cycle changes are less significant: the peak at  $E_{pc} = 0.80$  V increases in magnitude whereas the features at  $E_{pc} = 0.13$  and 0.26 V decrease.

These observations suggest barium uptake by poly[Ni(3-MeOsaltMe)]; considering the monomer structure ([Table 1.1](#), Chapter 1) the most likely site for Ba<sup>2+</sup> allocation is the receptor site (pseudo-crown) formed by the two methoxy groups and the oxygen atoms bound to nickel. In solution, UV-Vis spectroscopy revealed the formation of two Ba<sup>2+</sup> adducts with [Ni(3-MeOsaltMe)]:Ba<sup>2+</sup> stoichiometries of 1:1 and 2:1 and association constants  $\log \beta_{11} = 6.20 \pm 0.17$  and  $\log \beta_{21} = 10.95 \pm 0.16$ , respectively<sup>27</sup>. The variation of the electrochemical response upon Ba<sup>2+</sup> addition is qualitatively similar for thicker films. Additionally, the saturation of  $E_{pa}=0.88$  V is a function of  $\Gamma$ , occurring at higher concentrations of added Ba<sup>2+</sup> for thicker films. Since the electrochemical data suggest Ba<sup>2+</sup> ion recognition is retained upon polymerisation, it is relevant to study this process with structural techniques.

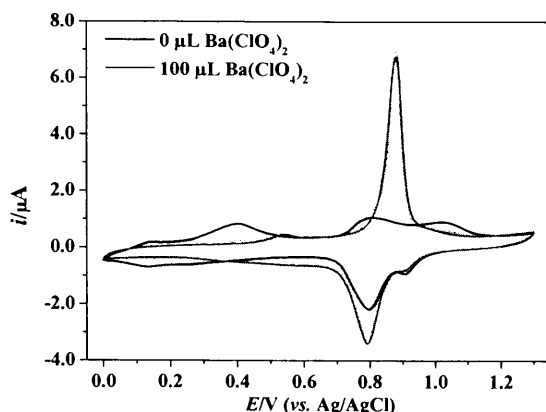


**Figure 5.5:** Voltammetric response of poly[Ni(3-MeOsaltMe)] ( $\Gamma=5.0 \text{ nmol cm}^{-2}$ ) acquired after successive additions of  $10 \text{ }\mu\text{L}$  aliquots of  $2.5 \text{ mmol dm}^{-3} \text{ Ba(ClO}_4)_2/0.1 \text{ mol dm}^{-3} \text{ TBAP/CH}_3\text{CN}$  to  $0.1 \text{ mol dm}^{-3} \text{ TBAP/CH}_3\text{CN}$ <sup>11</sup>.

### 5.3.1.2 Structural characterisation by XAS

#### *XANES*

In Figure 5.6 panel a Ni-K edge XANES spectra of  $\text{Ni(NO}_3)_2$  solution, Ni metal foil and [Ni(3-MeOsaltMe)] powder are presented. The strong ‘white line’ (the absorption peak just above the edge) in  $\text{Ni(NO}_3)_2$  is characteristic of ionic  $\text{Ni}^{2+}$ ; this implies that in aqueous solution the element is in its ionic form surrounded by solvent molecules, interacting in a purely electrostatic manner. The similarity between the edge shapes of Ni metal and [Ni(3-MeOsaltMe)] suggest that Ni in the *salen* monomer is covalently bonded to the *salen* ligand. Chemically this is expected, since the charge of the metal centre is delocalised among the ligands [Ni(3-MeOsaltMe)] and Ni is covalently bonded in the complex. Moreover, a pre-edge feature observed for [Ni(3-MeOsaltMe)] can be attributed to the transition  $1s \rightarrow 3d$  ( $8330 \text{ eV}$ ), which is typical of nickel complexes in a square-planar geometry<sup>28</sup>. These results support the assumption of Ni being covalently bonded with a square planar geometry in [Ni(3-MeOsaltMe)]. Moreover, the edge shift of *ca.*  $3 \text{ eV}$  between the metal and complex spectra may be attributed to the LUMO-HOMO gap, which is consistent with features observed in the electronic spectra at  $\lambda \approx 400 \text{ nm}$ <sup>9,29</sup>.

Figure 5.6 panel b depicts the raw spectra obtained for the complex [Ni(3-MeOsaltMe)] as a powder, dissolved in acetonitrile solution, in electroactive poly[Ni(3-MeOsaltMe)] films at different doping states in electrolyte solution, and in the presence of  $\text{Ba(ClO}_4)_2$ . When the powder is dissolved in acetonitrile, no changes in the geometry around nickel occur; this is because Ni is bonded to a tetra-coordinate strong-

field ligand, thereby preventing axial coordination by low-coordinating solvent such as  $\text{CH}_3\text{CN}$ . In another words, the backscattered waves at Ni K-edge ‘see’ the same atoms in the proximity of the relevant atom, independent of the physical state of the sample.

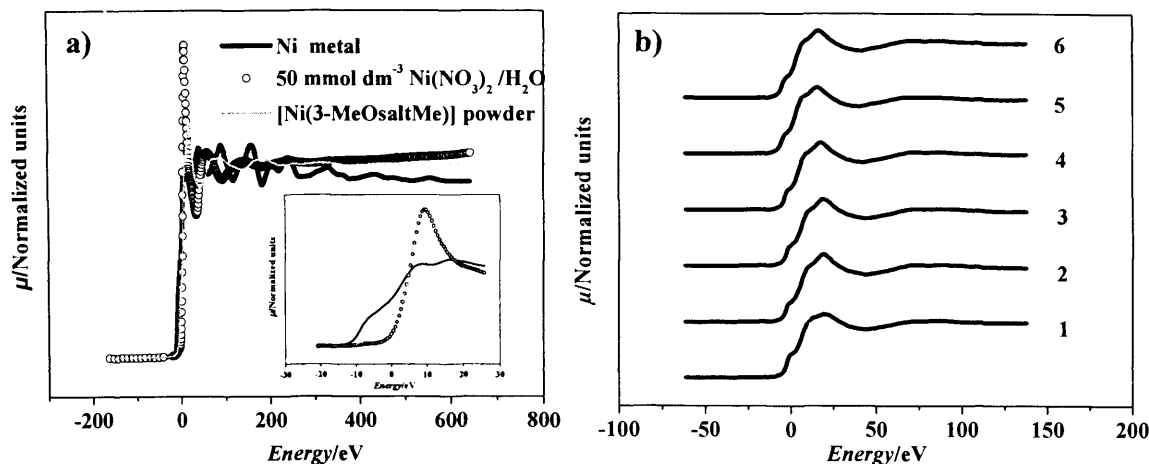


**Figure 5.6:** XANES spectra in the region near Ni K-edge: **a)** Ni metal, 50 mmol  $\text{dm}^{-3}$   $\text{Ni}(\text{NO}_3)_2/\text{H}_2\text{O}$ , and  $[\text{Ni}(3\text{-MeOsaltMe})]$  powder; **b)** 1  $[\text{Ni}(3\text{-MeOsaltMe})]$  powder; 2 20 mmol  $\text{dm}^{-3}$   $[\text{Ni}(3\text{-MeOsaltMe})]/\text{CH}_3\text{CN}$ ; 3 20 mmol  $\text{dm}^{-3}$   $[\text{Ni}(3\text{-MeOsaltMe})]/20$  mmol  $\text{dm}^{-3}$   $\text{Ba}(\text{ClO}_4)_2/\text{CH}_3\text{CN}$ ; 4 poly $[\text{Ni}(3\text{-MeOsaltMe})]$  in 0.1 mol  $\text{dm}^{-3}$  TBAP/ $\text{CH}_3\text{CN}$  at 0.0 V; 5 poly $[\text{Ni}(3\text{-MeOsaltMe})]$  in 0.1 mol  $\text{dm}^{-3}$  TBAP/ $\text{CH}_3\text{CN}$  at 1.3 V; 6 poly $[\text{Ni}(3\text{-MeOsaltMe})]+\text{Ba}^{2+}$  in 0.1 mol  $\text{dm}^{-3}$  TBAP/ $\text{CH}_3\text{CN}$  at 0.0 V.

Proceeding towards electropolymerisation, the XANES spectra of the electroactive films are almost identical to those of the monomers, regardless of the film doping state. These findings show that (i) no changes in the bonding nature and geometry around the nickel atom take place when polymerisation occurs and (ii) the film charge state does not affect the nickel XANES spectra, confirming that the redox processes are ligand-based, as expected from the electrochemical studies (section 5.3.1.1). With regard to ion recognition properties, the addition of barium perchlorate to both monomer and film also does not affect the XANES spectrum, and by inference, the local environment of nickel.

Further structural information may be inferred from data collected at the Ba K-edge. For ion recognition purposes, a modified electrode was prepared and placed in contact with a 50 mmol  $\text{dm}^{-3}$  barium solution for 15 minutes. After rinsing the deposited film with solvent and immersing it in a barium-free electrolyte solution X-ray absorption spectra were acquired near the Ba-K edge (Figure 5.7). The absorption signal *per se* proves the presence of  $\text{Ba}^{2+}$  within the polymer. Furthermore, when comparing  $\text{Ba}^{2+}$  in solution with that in the film, neither the pre-edge features nor the edge position (37441 eV) have changed (the metal oxidation state was unchanged). Although not shown in Figure 5.7 due

to the normalisation of the edge steps, the main difference occurs in the peak heights. The  $\text{Ba}^{2+}$  concentration in solution is much lower than in the film. Nonetheless, the larger volume of solution with respect to the film means that the  $\text{Ba}^{2+}$  population accounted for in solution is thus larger than that in the film (by a factor of 100, see the quantitative analysis in section 5.3.1.3).

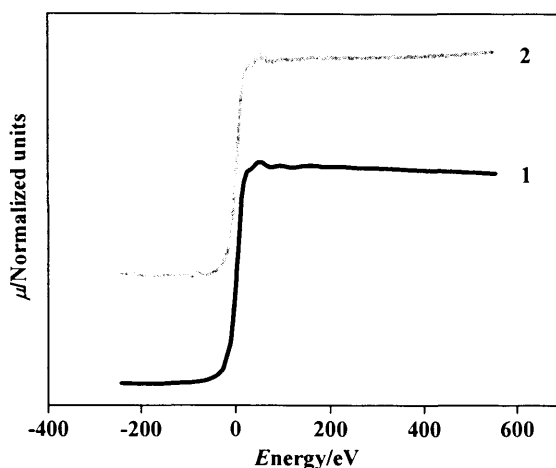


**Figure 5.7:** XANES spectra in the region of Ba K-edge for 1  $0.05 \text{ mol dm}^{-3} \text{ Ba}(\text{ClO}_4)_2/\text{CH}_3\text{CN}$  and 2  $\text{poly}[\text{Ni}(\text{3-MeOsaltMe})] + \text{Ba}^{2+}$  at 0.0 V.

#### *EXAFS at Ni K-edge*

Analysis of the EXAFS provides information on the Ni neighbourhood in greater detail in terms of coordination numbers, bond lengths and bonding nature. Due to the absence of crystallographic data for  $[\text{Ni}(\text{3-MeOsaltMe})]$  monomer, data obtained for similar compounds were used<sup>5</sup> to estimate coordination numbers and distances of neighbours around the relevant atom. The parameterisation is a fundamental step in order to get the best fit for the EXAFS data obtained.

Assuming in the first instance a nearly planar structure, the environment around nickel in the crystalline material (Figure 5.8) was approximated as a first shell around nickel composed of 4 atoms (2 nitrogen and 2 oxygen) all at 1.8 Å from the nickel atom, a second shell with 2 carbon atoms at 2.7 Å, a third shell with 1 carbon atom at 2.8 Å, a fourth shell composed of 3 carbon at 2.9 Å, and finally a fifth shell with 2 carbon atoms at 3.1 Å. Since oxygen and nitrogen scatter in a similar way and also the data range is short, these atoms were grouped as follows: the environment assumed to fit the raw data is three shells around nickel, with the first one composed of four oxygen/nitrogen atoms at about 1.8 Å, the second of 6 carbon atoms at 2.8 Å and a third with 2 carbon atoms at 3.1 Å. The

grouping of the second shell would give an extra static contribution to the Debye-Waller factor of about  $80 \times 10^{-4} \text{ \AA}^2$ .

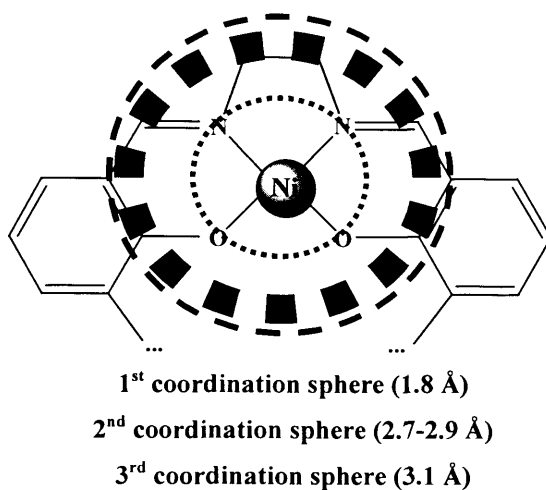


**Figure 5.8:** Structural environment around the Ni atom - initial parameters for the fitting of EXAFS function.

The EXAFS fittings vs. experimental data, as well as the corresponding Fourier transform, are shown in [Figure 5.9a and b](#), respectively. The first fitted peak is at 1.83 Å ([Figure 5.9b](#)), and corresponds to  $3.5 \pm 0.2$  N/O atoms; the second peak occurs at 2.82 Å and corresponds to  $4.2 \pm 1.0$  C atoms; the third peak, superposed with the previous, occurs at 3.20 Å and corresponds to  $2.2 \pm 1.6$  C atoms. These findings are in agreement with the crystal molecular structure of similar monomers as regards distances, but the coordination number for the grouped/second shell is low. The Debye-Waller factors are all reasonable, although the extra static contribution to the second shell appears to be only about  $35 \times 10^{-4} \text{ \AA}^2$ . This suggests that the given rounded distances rather overestimate the splitting.

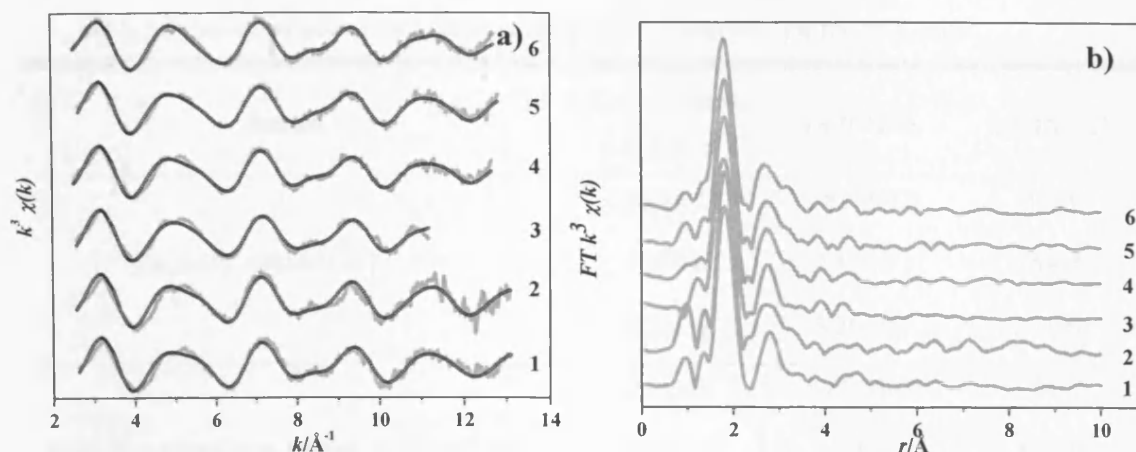


**Figure 5.9:** **a)** EXAFS functions (—) data and (○) fitting, and **b)** Fourier transforms for **1** [Ni(3-MeOsaltMe)] powder; **2** 20 mmol dm<sup>-3</sup> [Ni(3-MeOsaltMe)]/CH<sub>3</sub>CN; **3** 20 mmol dm<sup>-3</sup> [Ni(3-MeOsaltMe)] / 20 mmol dm<sup>-3</sup> Ba(ClO<sub>4</sub>)<sub>2</sub>/CH<sub>3</sub>CN; **4** poly[Ni(3-MeOsaltMe)] in 0.1 mol dm<sup>-3</sup> TBAP/CH<sub>3</sub>CN at 0.0 V; **5** poly[Ni(3-MeOsaltMe)] in 0.1 mol dm<sup>-3</sup> TBAP/CH<sub>3</sub>CN at 1.3 V; **6** poly[Ni(3-MeOsaltMe)]+Ba<sup>2+</sup> in 0.1 mol dm<sup>-3</sup> TBAP/CH<sub>3</sub>CN at 0.0 V.

The EXAFS fits for the rest of the samples are similar to those described above. The structural information is presented in detail in [Table 5.5](#). In the case of [Ni(3-MeOsaltMe)] monomer, no change in the EXAFS is observed when it is dissolved in acetonitrile solution. Then, not only the bonding state and geometry (inferred from XANES) but also the coordination spheres near the neighbourhood of the relevant atom ( $< 3.5 \text{ \AA}$ ) are maintained; this is a clear indication of conservation of both electronic and structural environment when dissolution occurs.

Moreover, the structural environment around the nickel atom is kept when polymerisation occurs. This is in agreement with the proposed model for polymerisation of [Ni(*salen*)] complexes: coupling of monomeric units without significant structural change. In addition, the structural environment around Ni was found to be invariant with respect to the film's doping state (reduced vs. oxidised state). This is striking evidence of a ligand-based redox process.

Effects arising from the insertion of a barium salt in the electrolyte solution and its incorporation into the electrochemical film are not detected in terms of structural features around nickel atoms. Therefore, barium is likely to interact with the polyphenylene backbone rather than the nickel atom. In order to understand the process of ion uptake and to get additional information regarding to Ba<sup>2+</sup> location inside the films, EXAFS analysis at the Ba K-edge data was performed.



**Table 5.5:** Structural information obtained from EXAFS analysis near the Ni K-edge.

Sample	Coordination number	$r \pm 0.02/\text{\AA}$	$\sigma^2/10^{-4}\text{\AA}^2$
[Ni(3-MeOsaltMe)] in powder	3.5 $\pm$ 0.2	1.83 (N/O)	15 $\pm$ 5
	4.2 $\pm$ 1.0	2.82 (C )	15 $\pm$ 15
	2.2 $\pm$ 1.6	3.20 (C )	30 $\pm$ 60
[Ni(3-MeOsaltMe)] in solution (20 mmol dm <sup>-3</sup> )	3.2 $\pm$ 0.3	1.83 (N/O)	5 $\pm$ 5
	4.7 $\pm$ 1.5	2.82 (C )	30 $\pm$ 30
	2.2 $\pm$ 1.6	3.20 (C )	-10 $\pm$ 45
[Ni(3-MeOsaltMe)] (20 mmol dm <sup>-3</sup> )/ Ba(ClO <sub>4</sub> ) <sub>2</sub> (20 moldm <sup>-3</sup> )	3.7 $\pm$ 0.2	1.83 (N/O)	30 $\pm$ 5
	4.0 $\pm$ 0.8	2.83 (C )	15 $\pm$ 20
	2.1 $\pm$ 1.2	3.17 (C )	45 $\pm$ 65
Poly[Ni(3-MeOsaltMe)] reduced state (0.0 V)	3.8 $\pm$ 0.2	1.84 (N/O)	30 $\pm$ 5
	4.5 $\pm$ 0.8	2.81 (C )	25 $\pm$ 15
	2.0 $\pm$ 1.0	3.19 (C )	0 $\pm$ 30
Poly[Ni(3-MeOsaltMe)] oxidized state (1.3 V)	3.8 $\pm$ 0.2	1.84 (N/O)	35 $\pm$ 5
	4.3 $\pm$ 1.0	2.82 (C )	25 $\pm$ 25
	1.5 $\pm$ 1.0	3.21 (C )	-30 $\pm$ 45
Poly[Ni(3-MeOsaltMe)]+Ba <sup>2+</sup> reduced state (0.0 V)	3.8 $\pm$ 0.2	1.84 (N/O)	25 $\pm$ 5
	4.5 $\pm$ 1.0	2.82 (C )	35 $\pm$ 20
	2.1 $\pm$ 1.0	3.20 (C )	-15 $\pm$ 35

*EXAFS at Ba K-edge*

Barium perchlorate solution (0.05 mol dm<sup>-3</sup>) was measured in the Ba K-edge region in order to determine both the electronic and chemical environment around the barium cation. For the initial parameterisation step, it was not obvious whether Ba<sup>2+</sup> is solvated by solvent molecules or instead if it forms ionic aggregates with ClO<sub>4</sub><sup>-</sup>. It was assumed that Ba<sup>2+</sup> would be surrounded by 4 N atoms (from the solvent) at 2.91  $\text{\AA}$ . The fitting of

EXAFS data showed that  $\text{Ba}^{2+}$  is surrounded by  $5 \pm 1$  N atoms at 2.91 Å with a Debye-Waller factor of  $130 \pm 30 \times 10^{-4} \text{ Å}^2$ . This suggests a coordination of either 6  $\text{CH}_3\text{CN}$  or  $\text{ClO}_4^-$  (the scattering factors of C, N and O are similar). The former is, however, more likely due to the low concentration of the perchlorate salt.

As suggested previously, the barium cation should be located in the receptor site with 4 oxygen atoms, 2 of them covalently coordinated to nickel and the other 2 from the methoxy substituents in the phenyl rings. Therefore, the EXAFS spectra were fitted by considering a shell of 4 oxygen atoms surrounding  $\text{Ba}^{2+}$  at 2.76 Å (Figure 5.10).

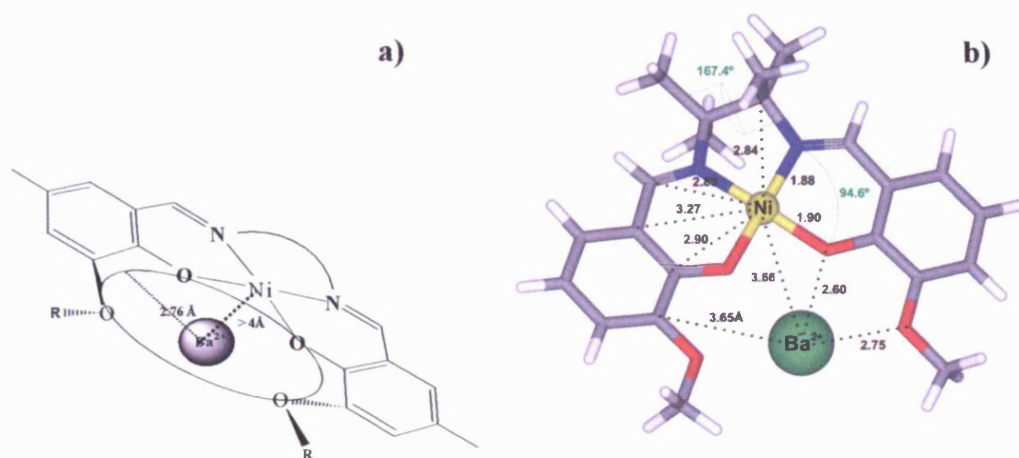


**Figure 5.10:** Structural environment around  $\text{Ba}^{2+}$  - initial parameters for the fitting of EXAFS function. a) Schematic view of  $\text{Ba}^{2+}$  coordinated to the pseudo-crown; b) result of DFT calculations for the complex  $[\text{Ni}(\text{3-MeOsaltMe})]^+ \text{Ba}^{2+}$  <sup>11</sup>.

The results obtained for  $\text{film} + \text{Ba}^{2+}$  indeed show a different environment around  $\text{Ba}^{2+}$  when compared to the salt in solution (Figure 5.11): fourfold Ba-O coordination at the usual Ba-O distance of about 2.75 Å (Table 5.6). Besides, the very large Debye-Waller factor of *ca.*  $200 \times 10^{-4} \text{ Å}^2$  shows that the environment is very distorted; comparing this value with that obtained for Ni-O near the Ni-K edge, it indicates that the nature of interactions between the sampled atom and its neighbourhood is quite different: while nickel is coordinated to oxygen/nitrogen atoms with some degree of covalence, the interactions between  $\text{Ba}^{2+}$  and the oxygen atoms in the pseudo-crown are purely electrostatic, which explains the higher thermal vibrations/disorder. If the barium cation is located in the pseudo-crown then it will be about 4 Å away from the nickel (from DFT calculations this is 3.66 Å). A weak contribution at this distance is possible according to EXAFS data, but cannot be fitted.

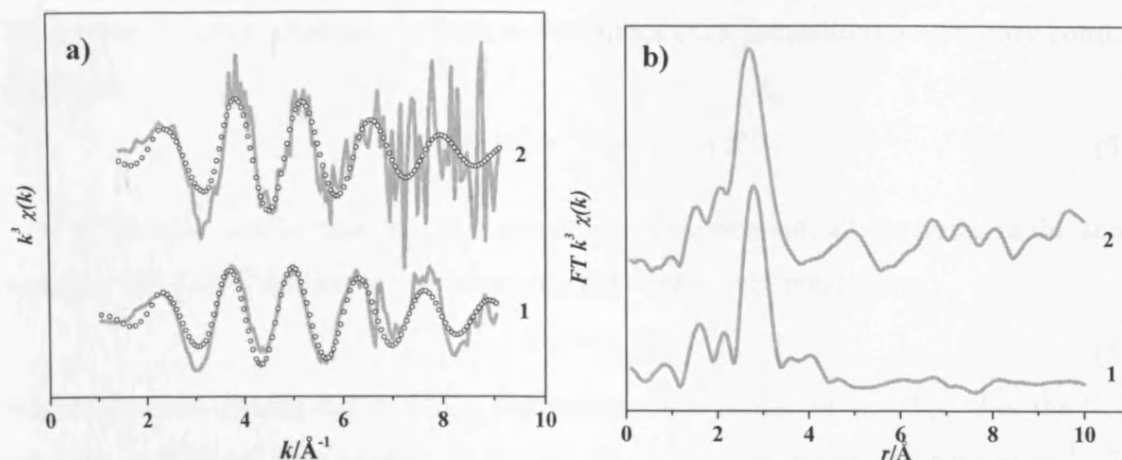


**Figure 5.11:** a) EXAFS functions (—) data and (o) fitting, and b) Fourier transforms for 1 50 mmol  $\text{dm}^{-3}$   $\text{Ba}(\text{ClO}_4)_2$ ; 2 poly[Ni(3-MeOsaltMe)]+ $\text{Ba}^{2+}$  in 0.1  $\text{mol dm}^{-3}$  TBAP/ $\text{CH}_3\text{CN}$  at 0.0 V.

**Table 5.6:** Structural information obtained from EXAFS analysis near the Ba K-edge.

Sample	Coordination number	$r \pm 0.02/\text{\AA}$	$\sigma^2/10^{-4} \text{\AA}^2$
$\text{Ba}(\text{ClO}_4)_2$ (0.05 $\text{mol dm}^{-3}$ ) solution	$5 \pm 1$	2.91 (C/N)	$130 \pm 30$
Polymer + $\text{Ba}^{2+}$ reduced state (0.0V)	$5.0 \pm 1.2$	2.75 (O)	$230 \pm 60$

### 5.3.1.3 XAS and XPS: bulk vs. surface probes

#### *Quantitative analysis of XANES*

The edge step in a transmission experiment can be used to measure the number of atoms per square metre in the beam and, if the density is known, the film thickness. It is also possible to determine the atom content from the fluorescence intensity by comparison with that from a known sample: in this case it is important that neither the sample nor the detector are moved. The absorption equation is given by:

$$I = I_0 \exp \left[ - \sum_i \sigma_{ai} n_{di} t_i \right] \quad (5.1)$$

where  $\sigma_a$  is the atomic absorption cross-section,  $n_d$  the atomic density,  $t$  the thickness and the sum is over all atomic types in the beam, including the sample, cell and substrates.  $I$  and  $I_0$  are in arbitrary units due to the variability of the gas filling in the ion chambers.

Thus, when  $\ln(I_0/I)$  is evaluated (which is the output from the station) an arbitrary constant is present:

$$\ln(I_0 / I) = \sum_i \sigma_{ai} n_{di} t_i + C \quad (5.2)$$

If the edge step is measured in a transmission experiment, all the terms in the above equation will cancel except for that involving the edge we are measuring:

$$step = n_d t \Delta \sigma_a \quad (5.3)$$

where  $\Delta \sigma_a$  is the change in the atomic absorption cross-section at the edge. For the Ni K-edge  $\Delta \sigma_a$  is  $2.9 \times 10^4$  barn atom<sup>-1</sup> and for the Ba K-edge  $\Delta \sigma_a$  is  $6 \times 10^3$  barn atom<sup>-1</sup>. The results for the Ni K-edge are presented in the [Table 5.7](#).

**Table 5.7:** Quantitative analysis of XANES for [Ni(3-MeOsaltMe)] systems (Ni K-edge).

Sample	Edge step	$n_d t /$ $10^{23} \text{ atom.m}^{-2}$
Ni(NO <sub>3</sub> ) <sub>2</sub> (50 mmol dm <sup>-3</sup> ) aqueous solution.	0.50	1.0
Monomer powder	0.15	0.5
Monomer (20 mmol dm <sup>-3</sup> ) solution	0.17	0.6
Monomer (20 mmol dm <sup>-3</sup> ) solution + Ba <sup>2+</sup>	0.20	0.7
Film reduced state (0.0 V)	0.09	0.3
Film+Ba <sup>2+</sup> reduced state (0.0 V)	0.10	0.4
Film oxidised state (1.3 V)	0.06	0.2
Film oxidised state (1.3 V)	0.03	0.1

The  $n_d t$  values are obtained using the complex molecular weight of 441 and the film density of about  $1200 \text{ kg m}^{-3}$ <sup>5, 30-35</sup>. The Ni concentration in the electrochemical films is therefore about  $n_d(\text{Ni}) = 1.8 \times 10^{27} \text{ atoms m}^{-3}$ . Thus the nickel atoms are separated by about 1 nm on average. Combining this data with the measured nickel edge steps, thicknesses of 10 to 20  $\mu\text{m}$  were derived for the various films studied. These films were deposited using between 20 and 30 electrochemical cycles, so the deposition rate is about 0.5  $\mu\text{m}$  per cycle.

The problems in using the fluorescence intensity are apparent: if the detector is moved, there is no proportionality with the absorption edge step. This is a particular problem on Station 7.1 at Daresbury where the fluorescence detector has a rather small angular acceptance. In the runs on Station 16.5 at Daresbury the detector was not moved significantly and has a larger angular acceptance. In all runs except the last,  $\text{Ba}^{2+}$  was present in both the film and the electrolyte. In these cases, the fluorescence intensity was always about 12. This corresponds to 5 or 6 mm of  $0.05 \text{ mol dm}^{-3}$  electrolyte solution and a  $n_{dt}$  value of  $0.5 \times 10^{23} \text{ atom m}^{-2}$ , as calculated above from the single edge step value. The last run was of  $\text{Ba}^{2+}$  in a film exposed to background electrolyte solution. The fluorescence was about 0.12, *i.e.* only about 1% of the  $\text{Ba}^{2+}$  measured previously was in the film. Thus the film contained about  $0.5 \times 10^{21} \text{ atom m}^{-2} \text{ Ba}^{2+}$ : an amount equivalent to  $100 \text{ nmol cm}^{-2}$ . This is in line with the electrochemical determinations on much thinner films. Assuming a Ni:Ba ratio of 1:1, so that  $n_d$  is  $1.8 \times 10^{27} \text{ Ba atoms m}^{-3}$ , then the  $\text{Ba}^{2+}$  film thickness (depth of  $\text{Ba}^{2+}$  into the film) is about  $0.5 \text{ }\mu\text{m}$ . If this assumption is right then  $\text{Ba}^{2+}$  only penetrates the surface layer of our electroactive films, which are  $10\text{-}20 \text{ }\mu\text{m}$  thick, as determined above. However, XAS does not distinguish between bulk and surface contents and therefore it is uncertain whether barium is instead homogeneously distributed in the film in a Ni:Ba ratio of 20:1. A surface sensitive technique such as XPS may give more information in this matter.

#### *XPS information for [Ni(3-MeOsaltMe)] system<sup>11</sup>*

XPS measurements were performed for poly[Ni(3-MeOsaltMe)] reduced films in the absence and presence of  $\text{Ba}(\text{ClO}_4)_2$ . The monomer and polymer show similar XPS spectra in the C 1s, O 1s, Ni  $2p_{(3/2)}$  and N 1s regions. Broad peaks in the C 1s region have binding energies of 284.7 and 286.6 eV (monomer), 284.1 and 286.6 eV (film), and 283.9 and 286.2 eV (film+ $\text{Ba}^{2+}$ ), associated with aromatic and aliphatic carbons in the *salen* ligand<sup>35-37</sup>. The intense N 1s peak at 399.8-399.2 eV is assigned to the imine nitrogen<sup>35-37</sup> and the broad low intensity feature at 403.5-402.0 eV to solvent. In the O 1s region there is a strong and intense peak at 533-532 eV, and a shoulder at lower energies that corresponds to the two unresolved types of oxygen atoms from the ligand and from the  $\text{ClO}_4^-$  in the case of the films. The Ni  $2p_{(3/2)}$  peak at 855.7-855.1 eV is typical of diamagnetic nickel ( $\text{Ni}^{2+}$ )<sup>35-37</sup>. Upon addition of  $\text{Ba}(\text{ClO}_4)_2$ , an additional peak at 780.5 eV

is observed. This Ba 3d peak is typical of  $\text{Ba}^{2+}$  <sup>36</sup> and confirms ion uptake. All the other peaks are similar to those of the film in the absence of barium, except the O 1s feature which becomes more symmetrical. This is caused by an increase of the binding energy of the shoulder (by 0.7 eV), attributed to the presence of  $\text{Ba}^{2+}$  in the pseudo-crown.

The ratios obtained for the atomic percentages for monomer, film and film+ $\text{Ba}^{2+}$  are highlighted in Table 5.8. The monomer and the polymer show similar C, N, O and Ni atomic % consistent with the proposed film composition, *i.e.* monomeric units linked at the phenyl moieties. The atomic ratios in the monomer are N:Ni = 2.2:1 and O:Ni = 4.7:1, which is in reasonable agreement with the monomer composition. In the polymeric system at reducing states,  $\text{Ba}^{2+}$  addition results in the increase of N:Ni and O:Ni ratios from 2.1:1 to 2.4:1 and from 6.3:1 to 9.2:1, respectively. These changes are attributed to the increase of solvent ( $\text{CH}_3\text{CN}$ ) and  $\text{ClO}_4^-$  populations inside the film, with the latter associated with the electroneutrality in the system.

**Table 5.8:** Atomic percentages and ratios of relevant elements for  $[\text{Ni}(\text{3-MeOsaltMe})]^\text{?}$ . The precision is generally 0.1 atomic %.

Sample	Atomic %						N/Ni	O/N	Cl/Ba	Ni/Ba
	C	N	O	Ni	Cl	Ba				
<b>Monomer</b>	77.3	6.3	13.6	2.9	-	-	2.2	2.2	-	-
<b>Film</b>	72.3	6.0	17.6	2.8	1.4	-	2.1	2.9	-	-
<b>Film+<math>\text{Ba}^{2+}</math></b>	65.2	5.7	22.0	2.4	3.3	1.4	2.4	3.9	2.3	1.7

Upon addition of  $\text{Ba}(\text{ClO}_4)_2$ , the XPS-derived Ni:Ba ratio is 1.7:1. This contrasts sharply with that obtained from the spatially integrated XAS data (Ni:Ba = 20:1). Since XPS is surface sensitive, this disparity excludes the possibility of  $\text{Ba}^{2+}$  being homogeneously dispersed throughout the film: the key conclusion here is that barium is concentrated in the outer region of the film.

### 5.3.2 Poly[Ni(*salen*)(crown ether)]: polymeric films bearing crown ether receptors

The results obtained by XAS for poly[Ni(3-MeOsaltMe)] showed that the structure of the monomer is retained upon polymerisation and that Ba<sup>2+</sup> uptake occurs by location of the cation in the pseudo-crown receptor. These results suggest that the design of electroactive films poly[M(*salen*)] for sensing purposes can be envisaged at the monomeric/molecular level, *i.e.* prior to polymerisation. In this section, the discussion is devoted to XAS studies of structurally related poly[Ni(*salen*)] films bearing benzo-crown ether macrocycles; these studies are supported by DFT calculations published elsewhere<sup>12</sup>.

The monomers presented in [Figure 5.12](#) and used to prepare electroactive films under the scope of this section, were chosen so Ba<sup>2+</sup>, the ‘probe’ ion used in these XAS studies, may be offered with different binding options.

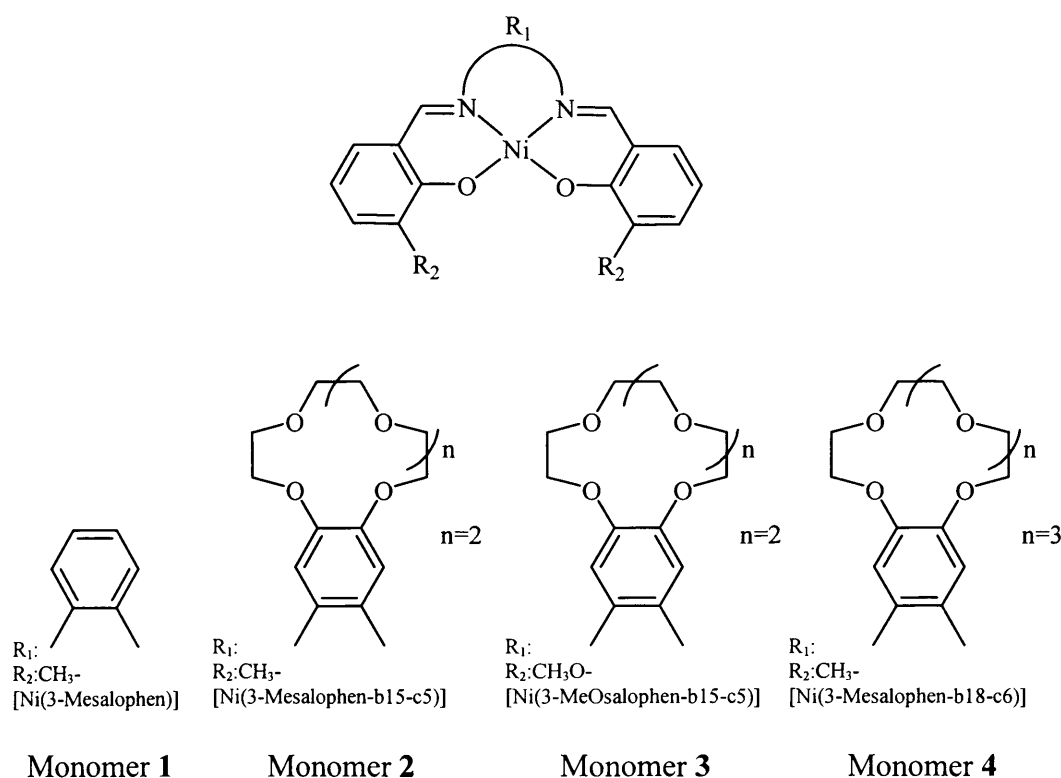


**Figure 5.12:** Structures of the [Ni(*salen*)] complexes studied by XAS.

[Ni(3-Mesalophen)], monomer (**1**), does not possess any specific binding sites, only the two oxygen atoms linked to the nickel centre may be considered as a binding site of non-specific nature; this can be regarded as the ‘control’ system since all the [Ni(*salen*)] complexes by definition present this binding site in their structure. It defines the baseline electrochemistry with the expectation that, at best, only low levels of Ba<sup>2+</sup> binding may occur. [Ni(3-Mesalophen-b15-c5)], monomer (**2**), shows an additional binding site, consisting of a benzo-crown with 5 oxygen atoms. The latter offers the prospect of specific binding (recognition). Application of crystallographic data<sup>38,39</sup> to the classical cation diameter – hole size relationship suggests that Ba<sup>2+</sup> (ionic radius 1.35 Å)<sup>22,23</sup> lies *above the plane* of 15-c5 (diameter 1.7-2.2 Å)<sup>24</sup>. The small size of the crown when compared to the cation size implies that formation of ‘sandwich-like’ complexes between the cation and two crowns on neighbouring chains is also a possibility<sup>39</sup>.

[Ni(3-MeOsaloophen-b15-c5)], monomer (**3**), is structurally related to monomer (**2**) and to [Ni(3-MeOsaltMe)] studied in section 5.3.1: in addition to the benzo-crown ether with 5 oxygen atoms in the diimine bridge, it also possesses a pseudo-crown site consisting of 4 oxygen atoms in the proximity of nickel centre, proved to be effective in Ba<sup>2+</sup> recognition. [Ni(3-Mesalophen-b18-c6)], monomer (**4**), offers the same option to Ba<sup>2+</sup> as does complex **2**, but with the more relaxed geometry and potentially greater donor availability of the larger six oxygen crown; in this case Ba<sup>2+</sup> will fit *into* the cavity of 18-c6 whose diameter is 2.6-3.2 Å<sup>24</sup>.

### 5.3.2.1 Electrochemical characterisation

The potentiodynamic responses during electrodeposition of all complexes are typical of those for electropolymerisation systems: irreversible anodic features (associated with monomer consumption) and progressive growth of pairs of anodic/cathodic features attributable to surface-bound electroactive polymer (Figure 5.13 panels a, c). Moreover, the voltammetric responses of the resulting modified electrodes (Figure 5.13 panels b, d) are qualitatively similar, except for some minor variations in the peak potentials (Table 5.9). Since the detailed description of the poly[Ni(3-Mesalophen-b15-c5)] (poly[**2**]) is presented in Chapter 4, further considerations in this matter would become repetitive.



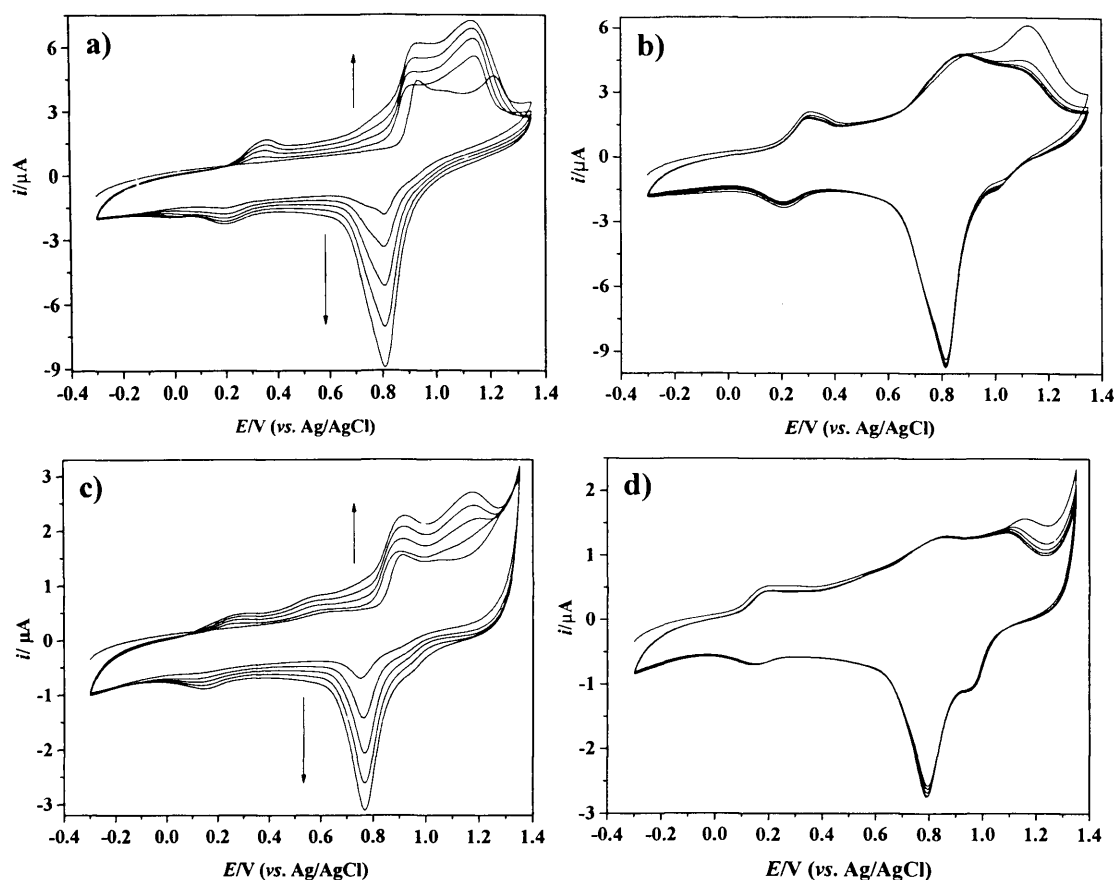


**Figure 5.13:** Voltammetric response acquired during a), c) polymerisation and b), d) redox-switching processes for a), b) [Ni(3-Mesalophen)] and c), d) [Ni(3-Mesalophen-b18-c6)] at  $0.1 \text{ V s}^{-1}$ <sup>12</sup>. Arrows indicate time sequence of cycles.

The addition of  $\text{Ba}(\text{ClO}_4)_2$  to the background electrolyte results in changes of the electrochemical response of the modified electrodes. The evolution of poly[2] response upon  $\text{Ba}^{2+}$  addition is also described in detail in Chapter 4. Succinctly, prior to any metal cation addition, a thin film ( $\Gamma=5.4 \text{ nmol cm}^{-2}$ ) shows anodic waves at  $E_{pal} = 0.15 \text{ V}$ ,  $E_{pall} = 0.86 \text{ V}$  and  $E_{palll} = 1.08 \text{ V}$ , and cathodic features at  $E_{pcl} = 0.11 \text{ V}$  and  $E_{pcII} = 0.82 \text{ V}$  (Figure 5.14). When  $\text{Ba}(\text{ClO}_4)_2$  is added to the background electrolyte, the features at  $E_{pl}$  are progressively displaced to more positive potentials whereas the  $E_{pII}$  features are displaced to more negative potentials; ultimately,  $E_{pl}$  and  $E_{pII}$  overlap. Also, there are shifts in peak amplitude (notably for the feature at  $E_{pcII}$ ), which result in a progressive decrease in total redox charge,  $Q_{redox}$ . All the other modified electrodes are characterised qualitatively by similar evolution of electrochemical response in the presence of  $\text{Ba}^{2+}$ . Nonetheless, for poly[1] these effects are less pronounced when compared to the rest of the films, an

indication that smaller amounts of  $\text{Ba}^{2+}$  are taken up by the film without specific binding sites.

**Table 5.9:** Peak potentials associated with the redox features of modified electrodes in  $0.1 \text{ mol dm}^{-3}$  TBAP/ $\text{CH}_3\text{CN}$ <sup>12</sup>.

Film	E/V vs. Ag/AgCl					
	$E_{\text{paI}}$	$E_{\text{paII}}$	$E_{\text{paIII}}$	$E_{\text{pcI}}$	$E_{\text{pcII}}$	$E_{\text{pcIII}}$
Poly[1]	0.31	0.89	1.06	0.21	0.81	-
Poly[2]	0.15	0.86	1.08	0.11	0.82	-
Poly[3]	0.45	0.77	0.95	0.20	0.73	1.04
Poly[4]	0.23	0.86	1.09	0.16	0.79	-

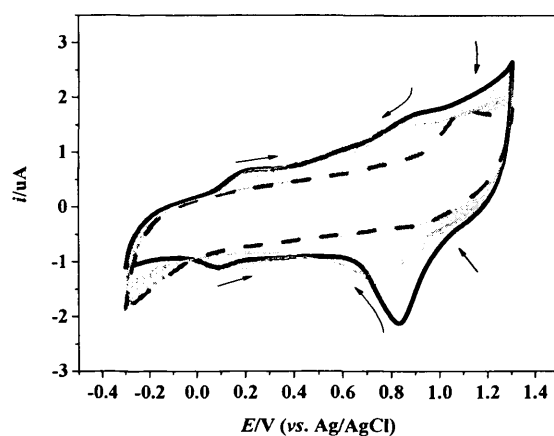


**Figure 5.14:** Voltammetric response of poly[Ni(3-Mesalophen-b15-c5)] ( $\Gamma = 5.4 \text{ nmol cm}^{-2}$ ) acquired in background electrolyte at  $0.1 \text{ V s}^{-1}$  (—) before  $\text{Ba}^{2+}$  additions, (–) following each  $\text{Ba}^{2+}$  addition and (– · –) at the end of  $\text{Ba}^{2+}$  additions.

### 5.3.2.2 Structural characterisation by XAS

#### *Ni K-edge*

The XANES data for Ni in the polymer films derived from complexes **1**, **2**, **3** and **4** (Figure 5.15) are relatively straightforward and basically the same as for [Ni(3-MeOsaltMe)] complex and the respective film studied previously<sup>11</sup> (section 5.3.1): Ni atoms are in a divalent state and covalently bonded with square planar geometry, regardless of the complex, its physical state and the presence or absence of barium. These findings suggest that (i) the polymerisation process does not alter either the geometry or the oxidation state of the metal centre - film electroactivity is associated with the polymer backbone (ligand-based response) and (ii) the distance between Ni<sup>2+</sup> and Ba<sup>2+</sup> is such that the latter does not affect the XANES spectrum, and by inference, the local environment of nickel.

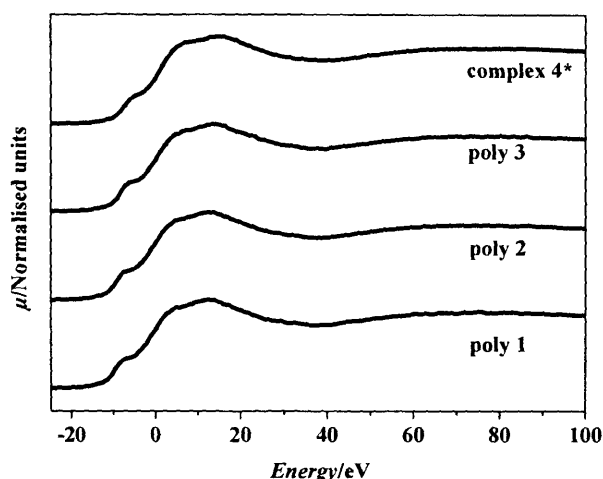


**Figure 5.15:** XANES spectra in the region of Ni K-edge for films poly[1], poly[2], poly[3] and complex [4]; (\*) XAS spectra were not obtained for poly[4] due to experimental problems.

The lack of crystallographic data for these complexes, structural information vital for parameterisation, would have impeded the EXAFS fitting. In order to overcome this problem, the fitting was based on a combination of DFT calculations and crystallographic data obtained for similar [Ni(*salen*)]<sup>5</sup> (recall section 5.3.1.2). The parameterisation based on crystallographic data is a reasonable starting point for the fitting of the EXAFS function, but DFT calculations made specifically for the complexes under study accounts for the specificity of the system enabling the improvement of the initial input data.

The outcome of DFT calculations performed for complexes **2** and **4** and respective barium adducts are summarised in Table 5.10, and in Figure 5.16 the optimised geometries

for  $[\text{Ni}(\text{3-Mesalophen-b15-c5})]+\text{Ba}^{2+}$  and  $[\text{Ni}(\text{3-Mesalophen-b18-c6})]+\text{Ba}^{2+}$  are shown (NOTE: DFT calculations were not performed by the author of this thesis and are published elsewhere<sup>12</sup>).

The predicted structures around the nickel atoms are identical for the two complexes: a first shell of O and N atoms (Ni nearest neighbours) covalently bonded at a distance of 1.86 Å, a second shell of C atoms at a distance of 2.80 Å, and a third shell of C atoms at 3.26 Å.

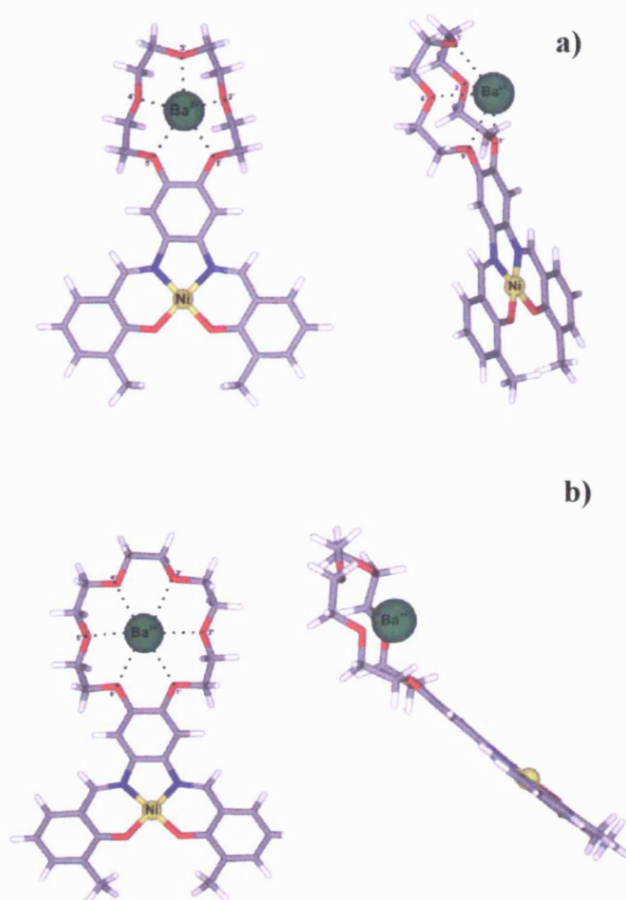


**Figure 5.16:** Optimised structures of  $[\text{Ni}(\text{3-Mesalophen-b15-c5})]+\text{Ba}^{2+}$  and  $[\text{Ni}(\text{3-Mesalophen-b18-c6})]+\text{Ba}^{2+}$  obtained by DFT calculations<sup>12</sup>.

**Table 5.10:** Interatomic distances determined by DFT for [Ni(*salen*)] complexes in the absence and presence of Ba<sup>2+</sup> <sup>12</sup>.

Complex	[Ni(3-Mesalophen-b15-c5)]		[Ni(3-Mesalophen-b18-c6)]	
Distance	Complex	Complex+Ba <sup>2+</sup>	Complex	Complex+Ba <sup>2+</sup>
<b>Element: Ni</b>				
	1 <sup>st</sup> coordination sphere		1 <sup>st</sup> coordination sphere	
Ni-N	1.89(3)	1.88(9)	1.89(3)	1.89(0)
Ni-O	1.85(2)	1.84(6)	1.85(2)	1.84(6)
<b>Average</b>	<b>1.87(2)</b>	<b>1.86(7)</b>	<b>1.87(2)</b>	<b>1.86(8)</b>
	2 <sup>nd</sup> coordination sphere		2 <sup>nd</sup> coordination sphere	
Ni-C(N)	2.85(4)	2.86(1)	2.85(4)	2.86(1)
Ni-C(O)	2.84(7)	2.84(2)	2.84(7)	2.84(2)
Ni-C(bridge)	2.76(1)	2.74(7)	2.76(1)	2.74(7)
Ni-C(bridge)	2.76(2)	2.74(8)	2.76(1)	2.74(8)
<b>Average</b>	<b>2.80(6)</b>	<b>2.79(9)</b>	<b>2.80(5)</b>	<b>2.79(9)</b>
	3 <sup>rd</sup> coordination sphere		3 <sup>rd</sup> coordination sphere	
Ni-C(aldehyde)	3.26(2)	3.26(2)	3.26(2)	3.26(2)
Ni-C(bridge)	4.13(8)	4.12(1)	4.13(7)	4.12(3)
Ni-Ba	-	8.48	-	8.44
<b>Element: Ba</b>				
<b>Ba-O1</b>		2.71(5)		2.75(1)
<b>Ba-O2</b>		2.80(0)		2.81(8)
<b>Ba-O3</b>		2.73(7)		2.79(9)
<b>Ba-O4</b>		2.81(2)		2.81(5)
<b>Ba-O5</b>		2.70(9)		2.79(8)
<b>Ba-O6</b>		-		2.78(6)
<b>Average</b>		<b>2.75(4)</b>		<b>2.79(4)</b>
<b>Ba-C(O)</b>		3.60(4)		3.61(3)
<b>Ba-C(bridge)</b>		4.88(3)		4.86(7)
<b>Ba-C(N)</b>		5.91(9)		5.89(5)

The EXAFS fitting and respective Fourier transforms for the monomer, film and film+Ba<sup>2+</sup> are depicted in [Figure 5.17](#) and the structural information extracted from EXAFS data summarised in [Table 5.11](#). For the powder of complex **1**, the first shell was found at 1.83 Å (3.6±0.3 O/N atoms), the second at 2.85 Å (5.5±3.2 C atoms) and the third at 3.23 Å (3.9±2.3 C atoms). The low and negative Debye-Waller factors found for the third shell signal the presence of additional atoms at greater distances from the nickel atom; nonetheless, any extra information is beyond the resolution of the data.

In spite of some minor variations in the distances of the second and third shell being observed, the results evidence no significant alterations in the structure around Ni with the physical state, polymerisation and absence/presence of Ba<sup>2+</sup>. Moreover, the obtained structural information by EXAFS represents only small refinements on the DFT calculations. Identical results were obtained for complexes **2**, **3** and **4**.

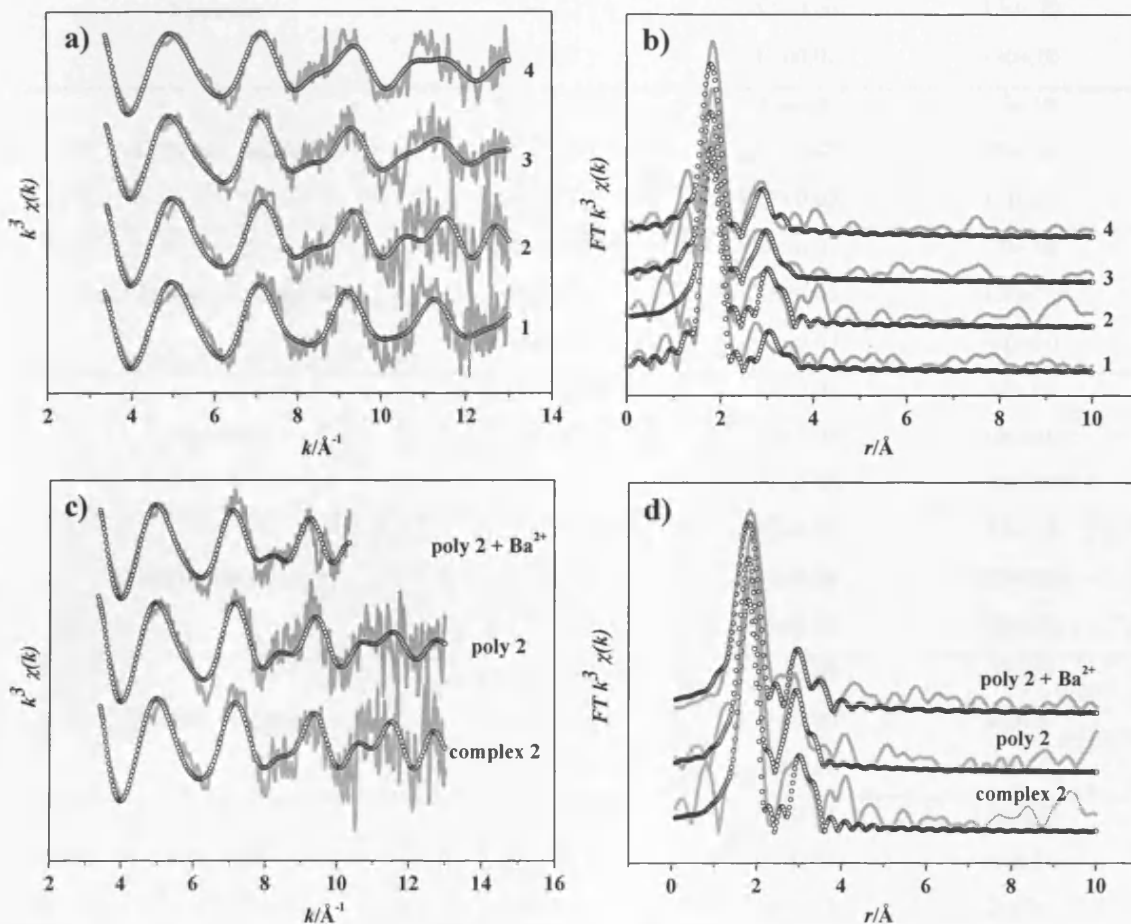


**Figure 5.17:** (—) Experimental data and (○) fitting of a), c) EXAFS functions, and b), d) Fourier transforms; a), b) monomers as powders and c), d) monomer **2** (powder), poly[**2**] and poly[**2**]+ Ba<sup>2+</sup>.

**Table 5.11:** Structural information obtained from EXAFS analysis near the Ni K-edge.

Sample	Coordination number	$r / \text{\AA}$	$\sigma^2 / 10^{-4} \text{\AA}^2$
1 powder	3.6±0.3 (O/N)	1.84±0.01	35±10
	5±3 (C )	2.87±0.06	140±80
	4±2 (C )	3.23±0.04	45±90
Poly[1]	4.1±0.4 (O/N)	1.83±0.02	90±15
	5±2 (C )	2.85±0.05	130±60
	2.1±0.6 (C )	3.23±0.02	-60±20
Poly[1]+Ba <sup>2+</sup>	4.2±0.4 (O/N)	1.83±0.02	110±20
	5±12 (C )	2.84±0.04	70±40
	3±2 (C )	3.18±0.04	20±90
2 powder	3.8±0.4 (O/N)	1.83±0.01	50±10
	5±3 (C )	2.81±0.06	110±70
	2±1 (C )	3.17±0.02	-30±20
Poly[2] reduced state	3.8±1.4 (O/N)	1.83±0.01	60±10
	5±2 (C )	2.81±0.03	70±30
	3±1 (C )	3.17±0.02	110±30
Poly[2]+Ba <sup>2+</sup> reduced state	3.8±0.3 (O/N)	1.84±0.01	70±10
	5±2 (C )	2.86±0.05	180±70
	2.0±0.6 (C )	3.22±0.02	-40±30
3 powder	3.5±0.3 (O/N)	1.84±0.01	50±10
	5±2 (C )	2.84±0.04	100±40
	3.1±1.3 (C )	3.21±0.03	30±50
Poly[3] reduced state	4.1±0.4 (O/N)	1.82±0.02	73±13
	9±6 (C )	2.88±0.08	300±240
	2.1±0.8 (C )	3.25±0.02	50±30
Poly[3]+Ba <sup>2+</sup> reduced state	3.6±0.3 (O/N)	1.83±0.01	60±10
	4.0±1.3 (C )	2.80±0.03	80±30
	2.5±1.4 (C )	3.18±0.03	10±40
4 powder*	3.4±0.3 (O/N)	1.84±0.01	50±10
	5±2 (C )	2.82±0.03	100±30
	2.5±1.1 (C )	3.15±0.03	20±40

(\*) Experimental problems occurred during the preparation of poly[4] did not allow the acquisition of XAS data near the Ni K-edge.

The chemical outcomes of these results are (i) electropolymerisation of [Ni(*salen*)(receptor)] complexes induces no significant structural changes around the nickel atom, and (ii) the absence of any effect in the Ni neighbourhood from Ba(ClO<sub>4</sub>)<sub>2</sub> insertion shows that Ba<sup>2+</sup> interaction with the electroactive film must occur in regions away from the Ni metal centre such as the crown receptors.

#### *Ba K-edge*

Predictions based on the DFT calculations (Table 5.10 and Figure 5.16)<sup>12</sup> indicate that Ba<sup>2+</sup> interacts with the crown, but it is not fully located inside the crown cavity. Moreover, this binding site is preferred when offered the choice between the crown and pseudo-crown sites. For all three crown systems, the variations in metal-oxygen distance are small, indicating equitable involvement of all oxygen donor atoms of the crown. Comparatively, DFT calculations suggest that the benzo-15-crown-5 shows a higher degree of bending towards the cation than does the benzo-18-crown-6. The average predicted distances between Ba<sup>2+</sup> and O are 2.75 Å for complex **2** and 2.79 Å for complex **4**, implying that the lower number of donor oxygen atoms in the former case is to some extent compensated by their greater proximity to the guest cation.

The results obtained from fitting the experimental EXAFS data for films exposed to Ba(ClO<sub>4</sub>)<sub>2</sub> solution are presented in Table 5.12. Based on the DFT predictions, it is perhaps unsurprising that outcomes are essentially identical for all three films. However, the striking outcome is that all the data could only be fitted to *a model with a very low coordination number*, namely a shell of 2 (at most 3) oxygen atoms at a distance of about 2.74 Å, contradicting the DFT calculations. Besides, any attempt to fit the data to models with more ‘typical’ coordination environments (5 or 6 oxygen atoms) resulted in physically unreasonable parameters.

The large Debye-Waller factor of *ca.* 130×10<sup>-4</sup> Å<sup>2</sup>, indicates a disordered environment around barium. Comparisons between these Debye-Waller factors and those obtained for Ni-O near the Ni K-edge indicates that the nature of interactions between the metal atoms and their neighbourhoods is different. Specifically, they suggest coordination with some degree of covalence between nickel and oxygen/nitrogen atoms and electrostatic interactions between Ba<sup>2+</sup> and the oxygen atoms.



**Table 5.12:** Structural information obtained from EXAFS analysis near the Ba K-edge.

Sample	Coordination number	$r/\text{\AA}$	$\sigma^2/10^{-4}\text{\AA}^2$
Poly[1]+Ba <sup>2+</sup> reduced state	1.9±1.5 (O)	2.84±0.12	120±50
Poly[2]+Ba <sup>2+</sup> reduced state	1.6±1.0 (O)	2.74±0.06	140±70
Poly[3]+Ba <sup>2+</sup> reduced state	1.5±0.7 (O)	2.72±0.05	110±60
Poly[4]+Ba <sup>2+</sup> reduced state	2.0±1.1 (O)	2.74±0.05	160±90

### 5.3.2.3 XAS quantitative analysis

The purpose of this section is to establish the Ba:receptor stoichiometry. Since XAS ‘sees’ the heavy elements in the system (here Ba and Ni), this goal is approached via the Ba:Ni ratio on the basis that the Ni:receptor ratio is known from the monomer structure.

The simplest route to determination of metal content is based on absorbance in a transmission XAS measurement, as shown in section 5.3.1.3. The Ba and Ni spectra were necessarily acquired on different synchrotron beamlines (16.5 and 7.1 at Daresbury, respectively) in different experiments, *i.e.* using different samples. For the Ba analysis, acquisition of transmission spectra is possible due to the high energy of beamline used. However, experimental constraints in station 7.1 (Pt electrode opacity at the lower energy of the beamline) meant that the Ni spectra could not be obtained in transmission mode, only acquired in the fluorescence mode.

The intensity data are not required to obtain structure, so fluorescence mode is an extremely convenient mode for determining local environment. Nevertheless, instrumental factors imply that absolute fluorescence intensities are not directly usable for quantitative analytical purposes. In principle, if all the instrumental factors are constant, one could determine atom content from fluorescence intensity by comparison with that from a known sample. In practice, this is far from trivial, since it requires perfect alignment and reproducibility of detector positioning; this is a particular problem on the instrument used, where the fluorescence detector has a rather small angular acceptance. In other words,

careful sample and detector positioning may allow a reasonable estimate of Ni population from fluorescence intensity, but this should not be regarded as quantitative.

An alternative way for determination of Ni content is using coulometric data, based on monomer structure and polymer electroactivity. This is also indirect since (i) for all poly[M(*salen*)] systems electroactivity is ligand-based and (ii) charge correlates differently to Ni content for each system, *i.e.* the doping level varies substantially. There is also the issue of incomplete film electroactivity for the deliberately thick samples used for XAS. Nonetheless, somewhat like the fluorescence intensity data, it provides an order of magnitude estimate of Ni population. Analysis of the coulometry of these electroactive films allows the estimate of the electroactive, surface coverage  $\Gamma$ . For the films under study,  $\Gamma$  was found to be in the range 90-400 nmol cm<sup>-2</sup>. Assuming a generic film density of  $\rho_f = 1.2 (\pm 0.1)$  g cm<sup>-3</sup>, this yields film thicknesses between 1-5  $\mu$ m.

The results obtained for the Ni K-edge data are presented in [Table 5.13](#). Although the data were acquired in the fluorescence mode, comparisons with the results from the electrochemical measurements (mentioned in the above paragraph and shown in the table) show a reasonable agreement, with *ca.* 30% of deviation. In the Ba K-edge the strategy consisted of using the electrochemical data ( $Q_{redox}$ ) for quantification of Ni atoms and the edge of Ba transmission spectra for determination of Ba atoms ([Table 5.14](#)). For all the polymers, both the fluorescence intensity and (indirect) coulometric estimates of Ni populations were approaching an order of magnitude *below* the XAS transmission estimates of Ba population. Both estimates of Ni population will be lower bounds: the fluorescence estimate because of incomplete capture of the emitted photons and the coulometric estimate because of incomplete redox conversion of the very thick films used for XAS. However, it is not expected that either of these estimates will be low by a factor of 10. Certainly, the Ba:Ni ratio is significantly *above* the 1:1 value predicted by the simplistic application of solution complexation chemistry concepts; a ratio in the range 2:1 to 3:1 appears to be more realistic.

The possibility that there are large amounts of non-complexed barium ions in the film is readily eliminated, since the spectral signature (notably barium-nearest neighbour distance) would be very different. The results show a Ba-O bond length that is entirely consistent with that expected – even though the coordination number is far from expectation.

**Table 5.13:** Quantitative analysis based on Ni K-edge steps (fluorescence spectra) and coulometry.

Sample	Edge Step	$nt/10^{22} \text{ atom m}^{-2}$	$n/10^{25} \text{ atom m}^{-3}$	Ni t(XAS) / $\mu\text{m}$	Ni t ( $Q_{\text{redox}}$ ) / $\mu\text{m}$
Ni(NO <sub>3</sub> ) <sub>2</sub> 0.02 mol dm <sup>-3</sup> aqueous solution	1.2	1.0	1.2	1.2x10 <sup>3</sup>	-
poly[1]	0.15	0.1	180	0.7	0.9
poly[1] + Ba <sup>2+</sup>	0.20	0.15	180	1	0.9
poly[2]	0.4	0.3	180	2	1.4
Poly[2] + Ba <sup>2+</sup>	0.4	0.3	180	2	1.4

Data in columns 2 and 3 were obtained directly from experiment; data in columns 4-6 involve postulation of a model for spatial distribution of sites.

**Table 5.14:** Quantitative analysis based on Ba K-edge steps (transmission spectra) and coulometry.

Sample	Edge Step	$nt/10^{22} \text{ atom m}^{-2}$	$n/10^{25} \text{ atom m}^{-3}$	Ba t(XAS) / $\mu\text{m}$	Ni t( $Q_{\text{redox}}$ ) / $\mu\text{m}$
Ba(ClO <sub>4</sub> ) <sub>2</sub> 0.050 mol dm <sup>-3</sup> solution (CH <sub>3</sub> CN)	0.19	30	3.0	1.0x10 <sup>4</sup>	-
poly[1]	0.012	2	180	11	1.3
poly[2]	0.018	3	180	17	1.2
poly[3]	0.018	3	180	17	0.5
poly[4]	0.017	2.7	180	15	0.6

Data in columns 2 and 3 were obtained directly from experiment; data in columns 4-6 involve postulation of a model for spatial distribution of sites.

There are two precedents for this high Ba uptake. XPS analysis of thinner poly[2] films shown in section 5.2 ( $I \approx 8 \text{ nmol cm}^{-2}$ ) gave greater than unity Ba:Ni ratios (2.4:1) when exposed to  $0.05 \text{ mol dm}^{-3} \text{ Ba}(\text{ClO}_4)_2$  solution for 15 minutes. Additionally, an EQCM gravimetric study for poly[3] by Martins and co-workers<sup>10</sup> showed a more complex Ba uptake isotherm than would be associated with a single binding site. Accepting this higher Ba population, the issue here is to address whether there are additional binding sites – and if so of what nature – or whether there is an excess of non-specifically incorporated  $\text{Ba}^{2+}$ .

#### 5.3.2.4 Rationalisation of $\text{Ba}^{2+}$ binding process

The unequivocal outcome of the EXAFS data is the low Ba-O coordination number, namely two rather than five or six, (or 10 to 12 for sandwich-like complexes). The assumption made here is that this low coordination in fact allows more barium to bind to the polymer: multiple binding to benzo-15-crown-5 (for complexes 2 and 3), and benzo-18-crown-6 (complex 4), one at each pseudo-crown associated with the methoxy groups (for complex 3) and one at the two oxygen atoms coordinated to the Ni (complexes 1, 2 and 4).

The twin criteria that any plausible model must satisfy are the facility to accommodate more Ba than Ni *and* accommodate the Ba ions in similar local environments. The latter feature suggests that binding to the pseudo-crowns formed by the methoxy groups in poly[3] is unlikely. In addition, the invariance of the Ni local environment to the presence/absence of  $\text{Ba}^{2+}$  also rules out binding to the oxygen atoms in the Ni coordination sphere. In the case of the oxygen also bound to the Ni, the question as to whether Ni should be ‘seen’ in the Ba coordination environment was addressed previously (see section 5.3.1.2): DFT calculations predict the Ni...Ba distance would be  $3.66 \text{ \AA}$ , which would be out of range of the EXAFS data. Although these notions provide an attractive explanation for the high  $\text{Ba}^{2+}$  population, they are inconsistent with the structural data.

The results point to multiple binding to the crown receptors; this is of course only relevant to the films derived from monomers 2, 3, and 4, for which the increased Ba population is observed (Table 5.14). Considering that steric factors play an important role in the multiple binding, Ba ions may bind on opposite sites of the crown (‘above’ and

‘below’); this might result in bridging between chains, although this would not necessarily be identified from EXAFS data.

It must be stressed that the above selection of binding site(s) is not absolute: the rejected sites (pseudo crowns) might come into play under other conditions, but the structural data simply show which ones are (not) involved under the practically relevant conditions used here. Again, the use of the full range of options would mean that the poly[1] would bind least  $\text{Ba}^{2+}$  and poly[3] the most. The relative capacity of the polymers derived from complexes **2** and **4** would depend on which sites were more active; the structural data show that these are the crowns, though in a rather unusual manner. Quantification of the Ba:Ni ratio is difficult, but the experimental observations suggest  $\text{Ba}^{2+}$  film populations for:  $\text{poly}[1] < \text{poly}[2] < \text{poly}[3] \approx \text{poly}[4]$  (Table 5.14), broadly consistent with this picture. The fact that poly[4] is comparable to poly[3] and more effective than poly[2] suggests that the 18-c6 group is more effective than the 15-c5 group in terms of cation binding.

A key outcome of this work is that solution phase complexation properties can only be used as a rather simplistic guide to properties of the same species immobilised in a surface-bound polymer film. In the specific cases studied here, the full power of the crown ether functionality does not seem to be realised (*i.e.* only some of the O-donors participate), but donor functionalities that might be considered ineffective in solution can play a significant role in the film. In this context, it seems then reasonable to suggest that the lack of freedom to participate of some crown O-donors is a consequence of geometrical constraints. One example of this might be compression of the crowns in the restricted free volume available in the film, when compared to monomers in solution.

In support of the above hypothesis, there are reported flaws in the cation diameter-hole size assumption. Gokel and colleagues<sup>40</sup> showed that this is the major factor ruling the ion/macrocyclic complexation process only when the ligands are ‘relatively inflexible’; the polymer film environment might well violate this requirement. More recently, a gas-phase study by More and co-workers<sup>41</sup> demonstrated that the extent of binding of alkali metal cations to crown ethers increases not only with the number of oxygen donors, but also higher flexibility of the crown. Thus, restriction of the degrees of freedom of the crown (as in the polymer films used here) would be expected to decrease crown flexibility and thereby the extent of binding.

The restricted flexibility of the crowns has an equalising effect on the complexing power of the different sites, which in turn has analytical implications. The decreased ability of the crowns to complex the metal ion represents a decrease in selectivity: if only a part of the crown is utilised, any selectivity based on cavity size is lost. In recompense for this, there may be two possible advantages: greater capacity available at higher concentrations and greater lability of the complexes. The former would result in a wider dynamic range. The latter would result in faster equilibration (faster response time), particularly when the ambient concentration is decreased, e.g., a metal-saturated film is exposed to a dilute metal ion solution. These possible practical implications would of course require direct testing. These structural changes may result in changes in free volume within the film, which in turn affect the film rheological properties, as has been noted via acoustic wave resonator impedance measurements (Chapter 6); although less well understood at this time, such changes offer an alternative response upon which a sensor might be based.

## CONCLUDING REMARKS

XPS measurements performed on poly[Ni(3-Mesalophen-b15-c5)] showed high amounts of C and N compared to the monomeric structure, and the presence of Cl. These results indicate the presence of electrolyte species within the film. Furthermore, the addition of Ba(ClO<sub>4</sub>)<sub>2</sub> to the electrolyte results in Ba<sup>2+</sup> uptake by the electroactive film. The Ba:Ni ratio was found to be dependent upon the concentration of Ba(ClO<sub>4</sub>)<sub>2</sub> added, which may indicate a change in the ‘adsorption’ isotherm. Moreover, the Ba:Cl ratio suggests that the Ba<sup>2+</sup> is stabilised in great extent by donor atoms of the film rather than its anionic counterpart ClO<sub>4</sub><sup>-</sup>. XPS peaks obtained by deconvolution of C, N and O spectral lines are in fair agreement with (i) the chemical environment in the monomer and (ii) the presence of electrolyte species. Specifically, the binding energies associated with the spectral lines of Ni and Ba confirm that these elements are in divalent states.

XAS measurements acquired near the Ni K-edge revealed that the local structure around nickel in [Ni(3-MeOsaltMe)] and [Ni(*salen*)(crown receptor)] is not influenced by polymerisation or by the ion uptake process. Analysis of XANES indicated that nickel has formal +2 oxidation state and exists in a square-planar environment defined by the two N and two O donors; this is kept upon polymerisation, surface immobilisation, and variation of film oxidation state or Ba<sup>2+</sup> binding. These findings underline the fact that the film redox processes are ligand-based. EXAFS data of [Ni(3-MeOsaltMe)] showed that the nickel environment comprises a first shell of O and N donors with coordination number 3.5±0.2 located at a distance of 1.83 Å, a second shell of (4.2±1.0) C atoms at 2.82 Å, and a third shell of (2.2±1.6) C atoms at 3.20 Å. In the case of [Ni(*salen*)(crown receptor)] systems similar results were obtained, except for the low and negative Debye-Waller factors found for the third shell, which indicates the presence of additional atoms at greater distances.

Ba K-edge EXAFS spectra show that the coordination sphere around Ba<sup>2+</sup> in solution is (5±1) N atoms at a distance of 2.91 Å. In poly[Ni(3-MeOsaltMe)], Ba<sup>2+</sup> was found to be surrounded by (5.0±1.2) O atoms at a distance of 2.75 Å, meaning that it occupies the pseudo-crown site formed by the four O donors, two from the methoxy groups and two shared with the Ni. For the thick films used in XAS experiments, the spatially integrated Ba:Ni ratio is typically 0.05:1; this contrasts with a Ba:Ni ratio 1:1 expected on the basis of the pseudo-crown:Ni stoichiometry and found for thin films used in electrochemical

studies; XPS showed that in the thick films Ba is located preferentially in the outer region of the film, with a local Ba:Ni ratio close to unity.

In the case of poly[Ni(*salen*)(crown receptor)] films XANES data acquired near the Ba K-edge provided the evidence of Ba<sup>2+</sup> uptake for all the films studied. Nevertheless, EXAFS data indicated that the Ba<sup>2+</sup> ions within the film are in an unusual coordination environment, which differs significantly from that for solution species: the barium nearest neighbour shell contains only two donor (oxygen) atoms, rather than the expected five or six. The low coordination number means that the predicted cavity size-based selectivity of the crown ether functionalities is not realised. Instead, there is a levelling of the coordinating ability of the crown ether and pseudo-crown functionalities present in the molecule.

For [Ni(3-MeOsaltMe)], the molecular design approach was found to be successful: the pseudo crown is effective for Ba<sup>2+</sup> binding and poly[Ni(3-MeOsaltMe)] electrochemical response changes in its presence. Conversely, for the poly[Ni(*salen*)(crown receptor)] films conventional concepts from macrocycle chemistry are not effective predictors of ion recognition capability. The predicted analytical consequences of this behaviour include greater capacity (via more receptor sites), wider dynamic range and faster response to concentration decreases, at the cost of lesser selectivity towards analyte size.

The characteristics and roles of the two metals in the system are very different. While Ni has a purely structural role, maintaining the structural motif intact, with strong directional covalent bonds within a square planar ligation shell, Ba<sup>2+</sup> interactions with poly[Ni(*salen*)] films are purely of electrostatic nature. The result of the latter is a larger Debye-Waller factor, which signals a much looser ‘fit’ of Ba<sup>2+</sup> into its location when compared to the Ni<sup>2+</sup> counterpart.



## REFERENCES:

1. Vilas-Boas, M.; Freire, C.; de Castro, B.; Christensen, P. A.; Hillman, A. R. *Inorg. Chem.* **1997**, *36*, 4919.
2. Vilas-Boas, M.; Freire, C.; de Castro, B.; Hillman, A. R. *J. Phys. Chem. B* **1998**, *102*, 8533.
3. Vilas-Boas, M.; Santos, I. C.; Henderson, M. J.; Freire, C.; Hillman, A. R.; Vieil, E. *Langmuir* **2003**, *19*, 7460.
4. Vilas-Boas, M.; Freire, C.; de Castro, B.; Christensen, P. A.; Hillman, A. R. *Chem.-Eur. J.* **2001**, *7*, 139.
5. Santos, I. C.; Vilas-Boas, M.; Piedade, M. F. M.; Freire, C.; Duarte, M. T.; de Castro, B. *Polyhedron* **2000**, *19*, 655.
6. McQuade, D. T.; Pullen, A. E.; Swager, T. M. *Chem. Rev.* **2000**, *100*, 2537.
7. Gokel, G. W.; Leevy, W. M.; Weber, M. E. *Chem. Rev.* **2004**, *104*, 2723.
8. Fabre, B.; Simonet, J. *Coord. Chem. Rev.* **1998**, *178-180*, 1211.
9. Carneiro, A. In *Filmes Polimericos do tipo [M(Salen)] Funcionalizados para o Reconhecimento de Catiões Representativos*, PhD Thesis, University of Porto, Department of Chemistry, 2005.
10. Martins, M.; Freire, C.; Hillman, A. R. *Chem. Commun.* **2003**, 434.
11. Tedim, J.; Carneiro, A.; Bessada, R.; Patricio, S.; Magalhaes, A. L.; Freire, C.; Gurman, S. J.; Hillman, A. R. *J. Electroanal. Chem.* **2007**, *610*, 46.
12. Tedim, J.; Bessada, R.; Patricio, S.; Magalhaes, A. L.; Freire, C.; Gurman, S. J.; Hillman, A. R. *Langmuir* **2008**, *24*, 8998.
13. Feth, M. P.; Bolm, C.; Hildebrand, J. P.; Kohler, M.; Beckmann, O.; Bauer, M.; Ramamonjisoa, R.; Bertagnolli, H., *Chem. -Eur. J.* **2003**, *9*, 1348.
14. Jain, S.; Zheng, X.; Jones, C. W.; Weck, M.; Davis, R. J. *Inorg. Chem.* **2007**, *46*, 8887.
15. Yano, H.; Ono, C.; Shiroishi, H.; Saito, M.; Uchimoto, Y.; Okada, T. *Chem. Mater.* **2006**, *18*, 4505.
16. Saito, M.; Shiroishi, H.; Ono, C.; Tsuzuki, S.; Okada, T.; Uchimoto, Y. *J. Mol. Catal. A: Chem.* **2006**, *248*, 99.
17. Nishide, H.; Mizuma, H.; Tsuchida, E.; McBreen, J. *Bull. Chem. Soc. Jpn.* **1999**, *72*, 1123.

18. Youm, K.-T.; Kim, M. G.; Ko, J.; Jun, M.-J. *Polyhedron* **2007**, *26*, 929.
19. Beniere, F.; Bertru, N.; Catlow, C. R. A.; Cole, M.; Simonet, J.; Angely, L. *J. Phys. Chem. Solids* **1992**, *53*, 449.
20. Bishop, D. B.; McCool, G. D.; Nelson, A. J.; Reynolds, J. G.; Baumann, T. F.; Fox, G. A.; DeWitt, J. G.; Andrews, J. C. *Microchem. J.* **2002**, *71*, 247.
21. Dietz, M. L.; Jensen, M. P. *Talanta* **2004**, *62*, 109.
22. Shannon, R. D. *Acta Crystallogr.* **1976**, *A32*, 751.
23. Henderson, P. In *Inorganic Geochemistry*; Pergamon: New York, 1982.
24. Mertes, K. B.; Lehn, J.-M. In *Comprehensive Coordination Chemistry*; Wilkinson, G., Gillard, R. D., McCleverty, J. A., Eds.; Pergamon: Oxford, 1987; Vol. 2, p 931.
25. Pedersen, C. J. *J. Am. Chem Soc.* **1970**, *92*, 386.
26. <http://srdata.nist.gov/xps/>
27. Bessada, R.; Biernacki, K.; Sousa, C.; Moura, C.; Gameiro, P.; Freire, C. *in preparation*.
28. Kwag, G.; Park, E.; Kim, S. *Bull. Korean Chem. Soc.* **2004**, *25*, 298.
29. Lever, A. B. P. In *Inorganic Electronic Spectroscopy*, 2nd ed.; Elsevier: New York, 1984.
30. Carronto, M. A. A. F. C. T.; de Castro, B.; Coelho, A. M.; Domingues, D.; Freire, C.; Morais, J. *Inorg. Chim. Acta* **1993**, *205*, 157.
31. Azevedo, F.; Carronto, M. A. A. F. C. T.; de Castro, B.; Convery, M.; Domingues, D.; Freire, C.; Duarte, M. T.; Nielsen, K.; Santos, I. C. *Inorg. Chim. Acta* **1994**, *219*, 43.
32. Freiburg, C.; Reichert, W.; Melchers, M.; Engelen, B. *Acta Crystallogr.* **1980**, *B36*, 1209.
33. Manfredotti, A. G.; Guastini, C. *Acta Crystallogr.* **1983**, *C39*, 863.
34. Radha, A.; Seshasayee, M.; Ramalingam, K.; Aravamudan, G. *Acta Crystallogr.* **1985**, *C41*, 1169.
35. Silva, A. R.; Freitas, M. M. A.; Freire, C.; de Castro, B.; Figueiredo, J. L. *Langmuir* **2002**, *18*, 8017.
36. Moulder, J. F.; Stickle, W. F.; Sobol, P. E.; Bomben, K. D. In *Handbook of X-ray Photoelectron Spectroscopy*; Perkin-Elmer: Eden Prairie, MN; 1992.

37. Silva, A. R.; Freire, C.; de Castro, B.; Freitas, M. M. A.; Figueiredo, J. L. *Microporous Mesoporous Mater.* **2001**, *46*, 211.
38. Christensen, J. J.; Hill, J. O.; Izzat, R. M. *Science* **1971**, *174*, 459.
39. Junk, P. C.; Steed, J. W. *J. Chem. Soc., Dalton Trans.* **1999**, 407.
40. Gokel, G. W.; Goli, D. M.; Minganti, C.; Echegoyen, L. *J. Am. Chem. Soc.* **1983**, *105*, 6786.
41. More, M. B.; Ray, D.; Armentrout, P. B. *J. Am. Chem. Soc.* **1999**, *121*, 417.

# Chapter 6

## *INTERFACIAL AND RHEOLOGICAL PROPERTIES OF POLY[Ni(3-MESALOPHEN-B15-C5)]*

## 6.1 INTRODUCTION

The studies presented in previous chapters consistently showed that poly[Ni(3-Mesalophen-b15-c5)] films are electroactive systems exhibiting properties typical of conducting polymers. There are, though, some points that remain unclear. In Chapter 4, the decrease in reproducibility of the voltammetric response and the non-monotonic variation of the ion recognition properties with the increase of  $\Gamma$  were attributed to morphological changes, which may occur during the deposition of electroactive material. Additionally, XAS results in Chapter 5 indicated that  $\text{Ba}^{2+}$  is not located *within* the monomer, instead surrounded by only a few oxygen (donor) atoms<sup>1</sup>. These findings open new possibilities for  $\text{Ba}^{2+}$  location within the polymer, namely interactions between atoms of different monomers or even different polymeric chains. Certainly, the presence of metal cation in those sites would change the mechanical properties of the system.

The characterisation methods presented so far were interpreted (i) without consideration of the role of the solvent, and (ii) on the basis of a homogeneous layer, *i.e.* assuming that all electroactive sites have identical solvation environments. In this chapter the results of TSM resonator measurements are presented in conjunction with AFM and SEM analysis. The acoustic wave method provides information on the system rheological properties, which is then interpreted in the context of film morphology via the microscopic techniques.

The chapter is divided into two main sections. The first comprises the determination of the shear moduli of poly[Ni(3-Mesalophen-b15-c5)] films during their potentiodynamic growth, and variation of film morphology with surface coverage<sup>2</sup>. The second presents the dependence of shear moduli values upon applied potential (doping state), absence/presence of  $\text{Ba}^{2+}$  (ion recognition) and frequency.

## 6.2 CHARACTERISATION OF THE POTENTIODYNAMIC DEPOSITION OF POLY[Ni(3-MESALOPHEN-B15-C5)]

Figure 6.1a shows the voltammetric response of [Ni(3-Mesalophen-b15-c5)] to a multi-cycle potentiodynamic procedure (film A); this was characterised in detail in Chapter 4. Basically, the electrochemical response is typical of an electropolymerisation system, with a chemically irreversible component at very anodic potentials and a complex set of chemically reversible waves at less anodic potentials. The former is associated with the electropolymerisation process, while the latter is attributed to the resulting polymer film. Figure 6.1b shows the admittance spectra recorded at the end of each deposition cycle. As the deposition of polymer film proceeds, there is a transition from an acoustically thin ('rigid') film regime to an acoustically thick film regime. According to the lumped-element model (Figure 2.8, Chapter 2), in the acoustically thin regime  $R_2 = 0$  and there is no change in the peak admittance with film thickness. Conversely, in the acoustically thick regime  $R_2 > 0$ ; the result is a progressive decrease of the peak admittance with film growth. In the present case, the spectra show peak admittances that decrease by 17% (after the 1<sup>st</sup> deposition cycle) and 39% (after the 10<sup>th</sup> deposition cycle).

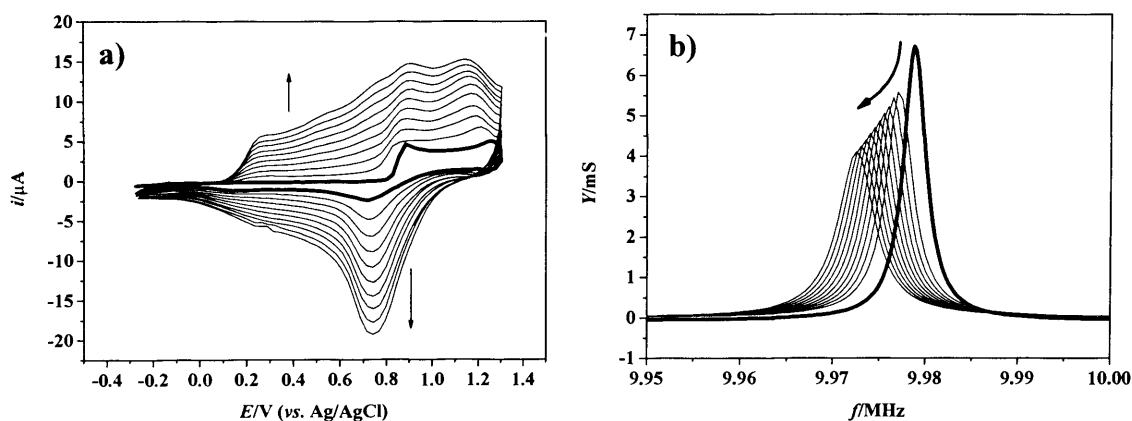


**Figure 6.1:** Polymerisation of [Ni(3-Mesalophen-b15-c5)] at  $0.01 \text{ V s}^{-1}$  (film A). **a)** Cyclic voltammogram (— first deposition cycle; — subsequent cycles); **b)** admittance spectra (— admittance spectrum of QCM in solution and — admittance spectra acquired at the end of each deposition cycle). Arrows indicate **a)** the increase of current intensity and **b)** the decrease of frequency and admittance with progressive cycling.

Figure 6.2a shows the admittance spectra acquired during the polymerisation process of another film (B), prepared in similar conditions to those of film A, except for

the higher scan rate ( $\nu=0.02 \text{ V s}^{-1}$ ). In this case, the admittance decreased by 5% to 10% over the same number of deposition cycles (Figure 6.2b).

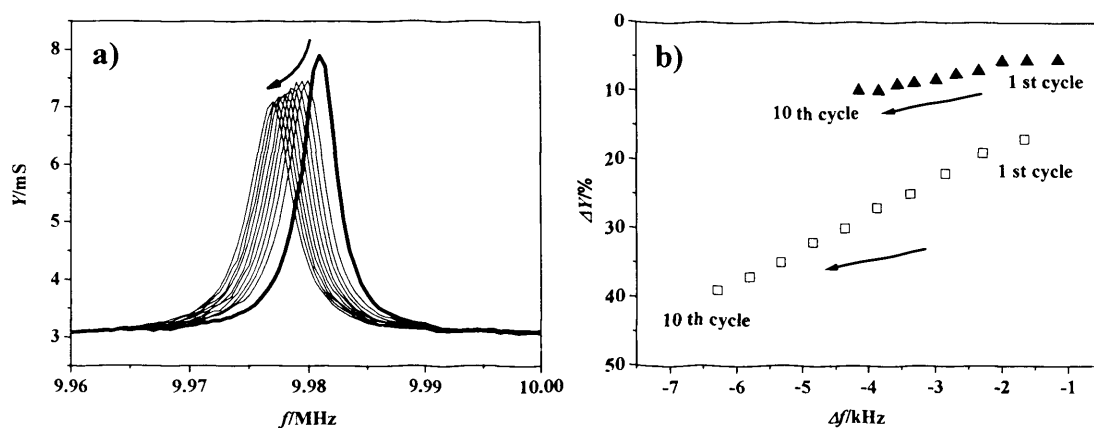


**Figure 6.2:** a) Admittance spectra acquired during the polymerisation of [Ni(3-Mesalophen-b15-c5)] at  $0.02 \text{ V s}^{-1}$  (film **B**) (— admittance spectrum of QCM in solution and — admittance spectra acquired at the end of each deposition cycle); b) variation of admittance vs. variation of resonant frequency for film A ( $\square$ ) and film B ( $\blacktriangle$ ). Arrows indicate the decrease of frequency and admittance.

For film **B**, the decreased time at very positive potentials results in less monomer oxidation, as judged by the total deposition charge of  $0.575 \text{ mC}$  at  $0.02 \text{ V s}^{-1}$  (film **B**) vs.  $1.18 \text{ mC}$  at  $0.01 \text{ V s}^{-1}$  (film **A**) (Figure 6.3). The outcome is less polymer deposition at the faster scan rate. Therefore, the relatively small energy losses observed for film **B** mean that a gravimetric interpretation (via the Sauerbrey equation) is appropriate. In the case of film **A** sufficient polymer is deposited that viscoelastic effects are dominant, allowing extraction of shear moduli as described in section 2.3.1, Chapter 2.

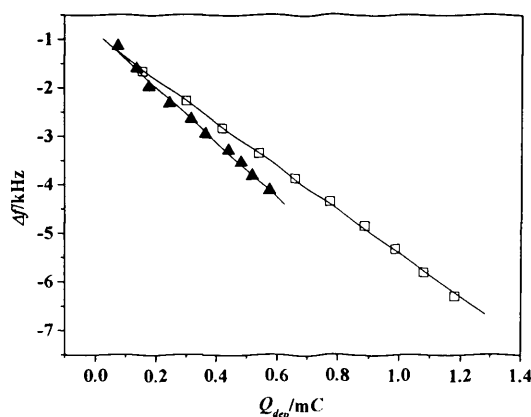


**Figure 6.3:** Variation of the resonant frequency with respect to the bare electrode, as a function of deposition charge  $Q_{dep}$  ( $\square$  film **A**:  $R^2=0.9994$ ; and  $\blacktriangle$  film **B**:  $R^2=0.9945$ ).

### 6.2.1 Acoustically thin film

According to the Sauerbrey approximation (Equation 2.35, Chapter 2), if the film density  $\rho_f$  is constant, variations in  $\Delta m$  are attributed solely to changes in  $h_f$ . In the case of thin films, the electrode surface roughness is also an aspect to be considered<sup>3</sup>. For the polished crystals used here, the scale of surface features is in the range 30-60 nm, which is similar to the (average) film thickness during the early stages of deposition. Nonetheless, the important physical feature is that surface entrapped polymer behaves as a rigid solid<sup>4</sup>, which is the assumption being made anyway.

The film density and thickness were determined using Equations 2.48 and 2.35, respectively. The solution density was approximated as that of the solvent,  $\rho_s \approx \rho(\text{CH}_3\text{CN}) = 0.786 \text{ g cm}^{-3}$ , and the polymer as that of the monomer. In the absence of crystallographic data for  $[\text{Ni}(\text{3-Mesalophen-b15-c5})]$ , the monomer molar volume was assumed to be the same as for similar  $[\text{Ni}(\text{salen})]$  complexes<sup>5-7</sup>, yielding  $\rho_f^0 = 1.4 \text{ g cm}^{-3}$ . XAS data presented in Chapter 5 provide structural support for this notion.  $Q_{\text{dep}}$  and  $\Delta f$  obtained at the end of the first deposition cycle (film **B**) were inserted into Equation 2.48, giving the solvated film density as  $\rho_f = 1.2 \pm 0.1 \text{ g cm}^{-3}$ . Ideally, the charge obtained in background electrolyte  $Q_{\text{redox}}$  would have been used to provide the quantification of deposited species; since the film was deposited in a potentiodynamic mode,  $Q_{\text{redox}}$  was not accessible and  $Q_{\text{dep}}$  had to be used for this purpose. Insertion of  $\rho_f$  in Equation 2.35 gives  $h_f$ .

Figure 6.4 shows the variation of  $h_f$  during the deposition process. The nucleation of polymer on the surface is clearly seen at *ca.* 0.85 V during the first anodic scan, which is consistent with the sharp rise of anodic current in Figure 6.1a. The film continues to grow until reaching 0.7 V in the reverse half-cycle. This potential coincides with appearance of the first cathodic peak (Figure 6.1a). Between 0.7 and -0.3 V there is no deposition of polymer, only reduction of that previously deposited. This process involves the ejection of counter anions and solvent, which explains the decrease in the film thickness (mass). In subsequent cycles a similar pattern is seen, but each time commencing from the higher baseline associated with the irreversible deposition of polymer during previous potential cycles. The decreasing amount of polymer deposited during each successive cycle is attributed to diffusional limitations associated with the depletion of monomer in the solution adjacent to the electrode.



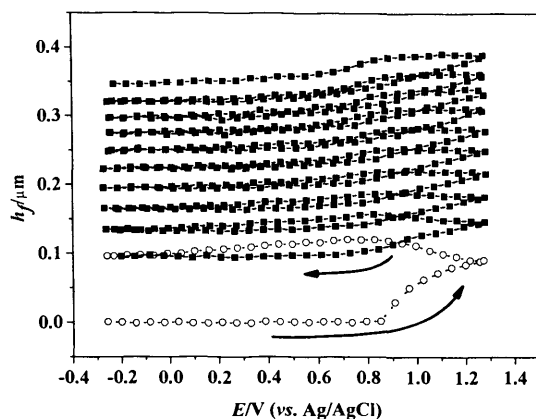


**Figure 6.4:** Polymerisation of [Ni(3-Mesalophen-b15-c5)] at  $0.02 \text{ V s}^{-1}$  (film **B**): variation of film thickness ( $h_f$ ) with the applied potential ( $\circ$  1st deposition cycle;  $\blacksquare$  subsequent cycles). Arrows indicate the direction of potential sweep.

### 6.2.2 Acoustically thick film

In order to extract  $G'$  and  $G''$  values from admittance spectra of film **A**, both  $\rho_f$  and  $h_f$  values are required. The film density was taken from the gravimetric interpretation of thin film data, whereas  $h_f$  values were estimated coulometrically by inserting  $Q_{dep}$  into [Equation 2.46](#). This is a minor variant on the previously used procedure<sup>3</sup>, in which the thin film data were taken from the early stages of deposition of the thick film. In the present study, the rapid deposition of polymer, evidenced by the sharp drop in peak admittance after a single deposition cycle (17% at  $0.01 \text{ V s}^{-1}$ ), prevents this ‘same film’ approach. The assumption associated with the extrapolation of  $\rho_f$  from film **B** to film **A** is that the film density is constant, regardless of the scan rate of deposition. Notice that the scan rates only differ by a factor of 2, so the solvation, and then the density, should not vary to a great extent. In this sense, the scan rate only determines the amount of electroactive material deposited.

The polymerisation process for film **A** was also performed in dynamic mode and  $Q_{redox}$  was not accessible for the 1<sup>st</sup>-9<sup>th</sup> deposition cycles;  $Q_{dep}$  was used in the determination of  $G$  values. At the end of the polymerisation (10<sup>th</sup> cycle) the film was cycled in background electrolyte and  $Q_{redox}$  was obtained, allowing an estimate of the error associated with the use of  $Q_{dep}$  instead of  $Q_{redox}$ . The area under the voltammogram gives a total deposition charge  $Q_{dep} = 1.18 \text{ mC}$ , and the redox switching of the film in background electrolyte gives  $Q_{redox} = 0.981 \text{ mC}$ . Hence,  $Q_{dep}$  overestimates the amount of deposited species by 20 %.

All the films were cycled in background electrolyte following the polymerisation. Therefore, except for the  $G$  values estimated *during* the polymerisation process, all the (coulometric) considerations involving films *after* polymerisation are based on  $Q_{redox}$ .

Notwithstanding the visible participation of viscoelastic phenomena during the first few deposition cycles as depicted in [Figure 6.1](#), the departure from thin film ('rigid') behaviour is sufficiently small that accurate shear moduli cannot be acquired. This is a consequence of a relatively small acoustic phase shift across the film<sup>8</sup>. When the phase shift becomes sufficiently large, the dominance of viscoelastic effects allows reliable shear moduli to be determined. [Figure 6.5](#) presents the obtained moduli values using coulometric  $h_f$  values and the best estimate of film density,  $\rho_f = 1.2 \text{ g cm}^{-3}$ . At the end of all deposition cycles the film can be considered a viscoelastic material, but there are some significant changes occurring during the polymerisation. In the early stages,  $G'$  is the dominant shear modulus component. As the polymerisation proceeds,  $G''$  increases while  $G'$  decreases, reversing the position. The increase in  $G''$  represents a shift from a solution-like layer to a more viscous medium, which may be associated with changes in chain packing.

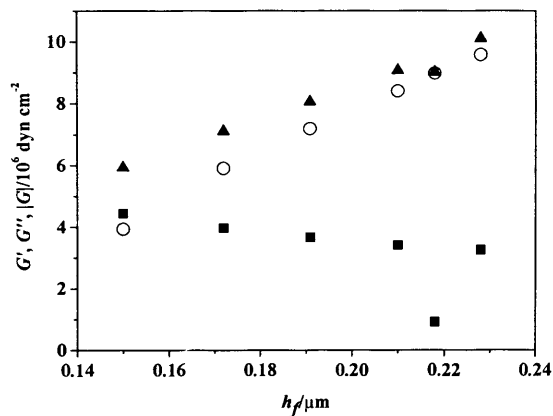


**Figure 6.5:** Shear moduli values vs.  $h_f$  fitted for the polymerisation process of film A ( $\rho_f = 1.2 \text{ g cm}^{-3}$ ); ■  $G'$ , ○  $G''$  and ▲  $|G|$  values.

The initial  $h_f$  values were estimated by using  $Q_{dep}$ . This yielded  $G'$  values that were negative, *i.e.* physically unreasonable. Knowing that  $Q_{dep}$  overestimates the amount of deposited electroactive species (see above), new  $h_f$  values were generated. This was accomplished by decreasing the initial  $h_f(Q_{dep})$  in 5% increments and recalculating the shear moduli; this procedure was repeated until positive moduli were obtained. Once the interval of  $h_f$  corresponding to positive shear moduli was found,  $h_f$  was varied by steps of 0.5 % within this same range, to obtain the highest shear moduli

values. The reason for this is the dependence of  $G$  values on the film thickness to have a maximum (turning point), which was here used as the criterion to get the acceptable  $G$  values.

The film thickness for which  $G$  values were fitted (Figure 6.5) is only 32.5 % of  $h_f(Q_{dep})$ . Although coulometric overestimation by using  $Q_{dep}$  introduces an error of 20 % in  $h_f$ , it alone does not explain this difference. Two different situations may have occurred: (i) the film may be in the semi-infinite regime or (ii) the outer regions of the film may be mechanically different (more ‘liquid-like’) to the inner layers and thus not ‘seen’ by the acoustic wave. The first hypothesis can be discarded by looking into the decay length values (Table 6.1) - the condition  $2h_f < \delta$  is always verified. In addition, the phase shift  $\varphi$  is smaller than  $\pi/2$ , so resonant effects are also not present. The second possibility seems more likely, especially if the system is highly heterogeneous.

**Table 6.1:** Film thickness ( $h_f$ ), decay length ( $\delta$ ) and phase shift ( $\varphi$ ) obtained from the fitting of the shear moduli, for a film density of  $\rho_f = 1.2 \text{ g cm}^{-3}$ .

Deposition cycle	$h_f / \mu\text{m}$	$\delta / \mu\text{m}$	$\varphi / \text{rad}$
6 <sup>th</sup>	0.15	1.00	0.40
7 <sup>th</sup>	0.17	0.83	0.39
8 <sup>th</sup>	0.19	0.79	0.39
9 <sup>th</sup>	0.21	0.79	0.40
10 <sup>th</sup>	0.23	0.80	0.40

### 6.2.3 Morphological Analysis

The film homogeneity is an important feature of the model used to interpret the acoustic admittance data. Consequently, and aside from differences in  $h_f$ , thin films provide a model for thicker films. This approximation is often made when interpreting other physical and chemical properties of electroactive films. In this section, the appropriateness of this assumption is considered.

Figure 6.6 shows SEM images of poly[Ni(3-Mesalophen-b15-5)] films prepared at different scan rates, which results in the generation of very different surface coverages. Based on the area under the voltammogram associated with chemically reversible redox switching ( $Q_{redox}$ ), the surface coverage of the film prepared at  $0.1 \text{ V s}^{-1}$

(film **C**) is  $\Gamma = 9.76 \text{ nmol cm}^{-2}$  (panels **a** and **c**), whereas for the film prepared at  $0.005 \text{ V s}^{-1}$  (film **D**)  $\Gamma = 162 \text{ nmol cm}^{-2}$  (panels **b** and **d**).

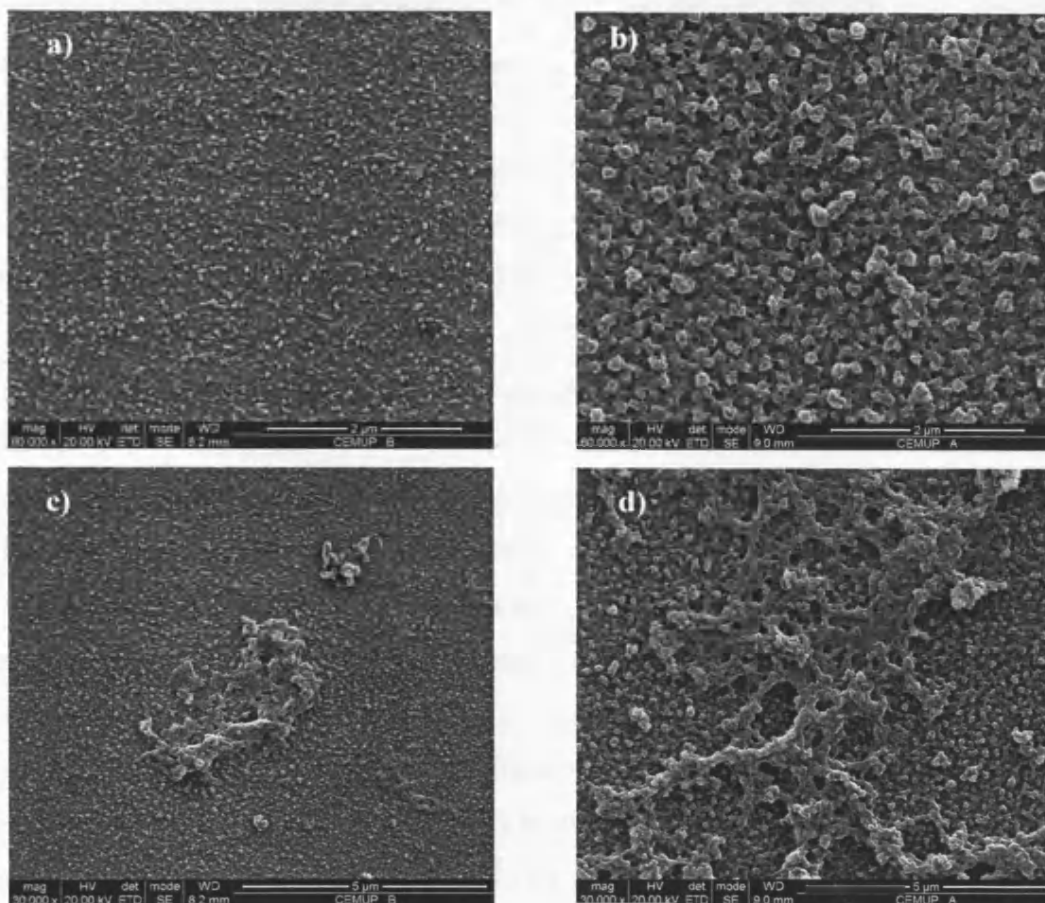


**Figure 6.6:** SEM images acquired for two films prepared on ITO electrodes at different scan rates: 5 cycles at  $0.1 \text{ V s}^{-1}$  (film **C**,  $\Gamma = 9.76 \text{ nmol cm}^{-2}$ , panels **a** and **c**), and 5 cycles at  $0.005 \text{ V s}^{-1}$  (film **D**,  $\Gamma = 162 \text{ nmol cm}^{-2}$ , panels **b** and **d**).

The morphologies of these two films are quite different. Both of them have an underlying layer that is smooth and dense, decorated by a layer of grains. However, for the thin film **C** these grains are small, of similar size and relatively closely packed, whilst for the thick film **D** they are larger and more heterogeneous, to the extent of forming large irregular interconnected domains ('islands'). Therefore, in the context of an acoustic model (see Equation 2.41) the films can be envisaged as bilayer, with an inner homogeneous layer and an outer heterogeneous layer. The inner layer is more dense (higher average polymer segment density) and the outer layer comprises islands of porous material that, when immersed, are perfused and surrounded by fluid.

Electrochemical and acoustic wave experiments are based upon entirely different phenomena. The coulometry accounts for those redox sites in good electrical contact

with the underlying electrode; the ‘sampling depth’ is dictated by the diffusional distance for coupled electron/ion transport, and may include all or only part of the film according to the experimental timescale. Most importantly, the effective sensitivity factor, the Faraday, is *insensitive to the local environment*, *i.e.* to both film morphology and solvation. Conversely, the acoustic wave data reflect material that is mechanically coupled to the electrode, with a ‘sampling depth’ determined by the decay length of the acoustic wave ([Equation 2.42](#)); this is *strongly sensitive to local environment* via the dependence of shear modulus on solvation. From these considerations two important conclusions result: (i) the use of qualitative terms ‘thin’ and ‘thick’ to describe the amount of polymer within a film is ambiguous unless the probe/technique is specified; (ii) films at the upper and lower ends of the acoustically thick (but not semi-infinite) regime may behave quite differently due to their diverse structures, compositions and dynamics. The latter issue has not been addressed previously in the context of correlating the outputs from different techniques. In this regard, AFM images *ex situ* were taken of films of varying ‘thickness’, *i.e.* with different polymer coverage, to provide additional insight.

[Figure 6.7](#) shows images for two films that are essentially replicates (aside from the use of ITO as substrate) of those films in the acoustically thin and thick regimes; the surface coverage are  $\Gamma=13.1 \text{ nmol cm}^{-2}$  (film **E**) and  $\Gamma=194 \text{ nmol cm}^{-2}$  (film **F**) for [panels a and b](#), respectively. Quantitative evaluation of film thickness was made by using a sharp blade to cut through the sample, thereby exposing the underlying ITO substrate. The physical thicknesses of the uniform inner layers ( $h_{f \text{ inner}}$ ) were found to be 90.3 nm and 483 nm, respectively ([Figure 6.8](#)). Inserting  $Q_{\text{redox}}$  for each one of these films in [Equation 2.46](#),  $h_f(Q_{\text{redox}}) = h_f^Q = 92.3 \text{ nm}$  for film **E** and  $h_f^Q = 1.37 \text{ }\mu\text{m}$  for film **F**. The results show that for *thin and uniform* films  $h_f^Q$  is a good estimate of film thickness, whilst for the more *heterogeneous and thicker* films the uniform region of the film is only one part of the overall deposited material. In order to demonstrate that the conflicts listed above are indeed a consequence of film heterogeneity, [Figure 6.9](#) shows the AFM image of a film that is ‘thin’ as judged by all the three probes (film **G**). From the coulometry  $\Gamma= 55.7 \text{ nmol cm}^{-2}$ , which leads to  $h_f^Q = 281 \text{ nm}$ . This value is in excellent agreement with thickness estimate using  $\Delta f$  and the Sauerbrey equation ( $h_f^{\text{grav}} = 261 \text{ nm}$ ), as well as AFM imaging  $h_{f \text{ inner}} = 258 \text{ nm}$  (from a linescan identical to those shown in [Figure 6.8](#)).

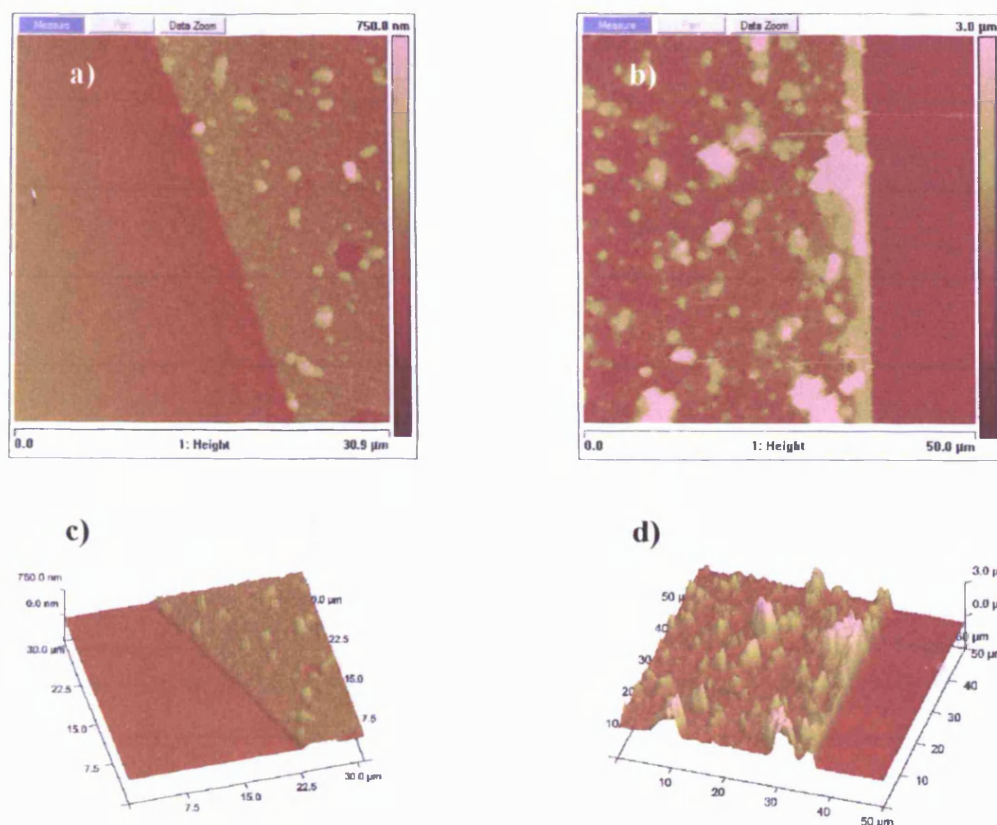


**Figure 6.7:** AFM images of films prepared on ITO electrodes at  $0.02 \text{ V s}^{-1}$  with 3 cycles (film **E**,  $\Gamma=13.1 \text{ nmol cm}^{-2}$ , panels **a** and **c**) and 35 deposition cycles (film **F**,  $\Gamma=194 \text{ nmol cm}^{-2}$ , panels **b** and **d**).

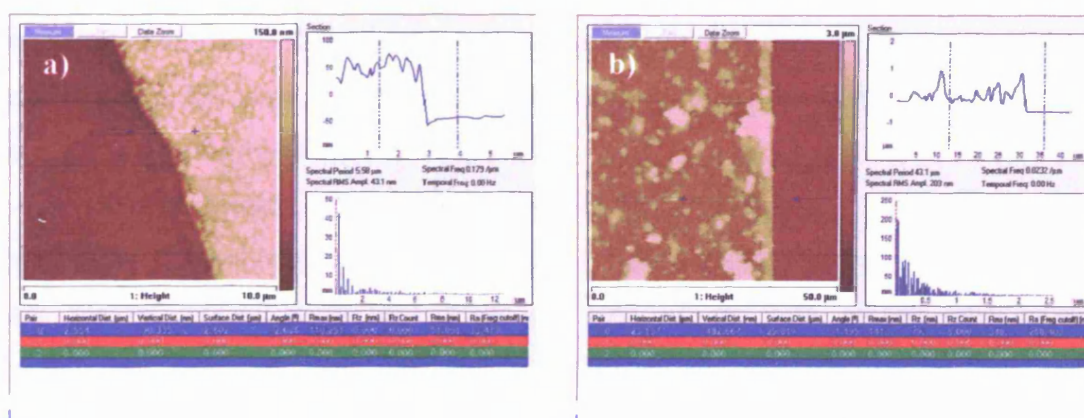


**Figure 6.8:** Estimate of  $h_f$  at the cut edge of a) film **E** and b) film **F** using AFM software.



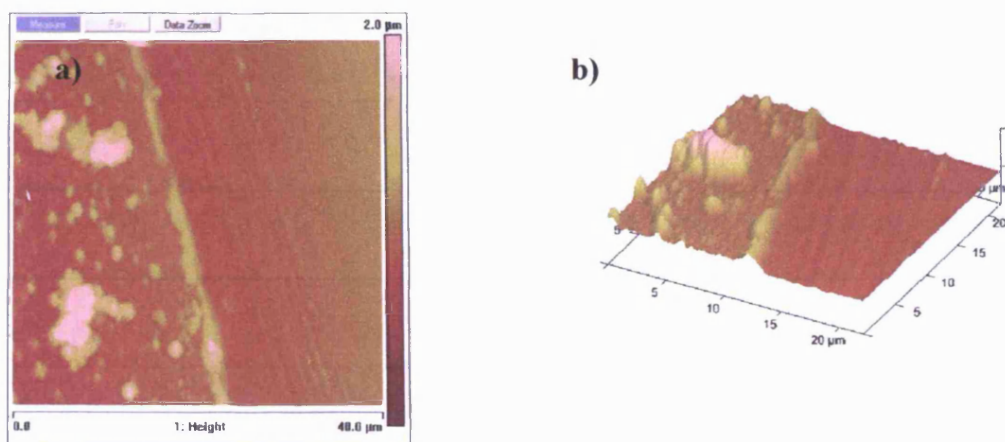


**Figure 6.9:** AFM images of an acoustically thin film prepared on QCM with 10 cycles at  $0.02 \text{ V s}^{-1}$  (film **G**),  $\Gamma = 55.7 \text{ nmol cm}^{-2}$ .

The AFM can also be used to estimate the thickness of films' outer regions ( $h_{f \text{ outer}}$ ). Together with coulometric data, it is possible to determine the concentration of electroactive material in the outer regions (Table 6.2). For the dense (relatively unsolvated) inner region, the molar mass and density data give a volume concentration of redox sites of  $1.4 \times 10^{-3} \text{ mol cm}^{-3}$ . The *surface concentration* of redox sites within the inner layer ( $\Gamma_{\text{inner}}$ ), is the product of this volume concentration (which is here considered constant for all the films) and the film thickness determined by AFM ( $h_{f \text{ inner}}$ ). The difference between  $\Gamma(Q_{\text{redox}})$  and  $\Gamma_{\text{inner}}$  gives the surface concentration of redox sites in the outer diffuse region,  $\Gamma_{\text{outer}}$ . The outcome is that thin films are dominated by the dense region and thick films by the diffuse region. In this sense, as the total amount of immobilised redox sites is increased, one expects a progressive shift in properties from those of a dense film to those of a diffuse film.

Going backwards, the quotient between  $\Gamma_{\text{outer}}$  and  $h_{f \text{ outer}}$  yields the volume concentration of redox sites in the outer region. As column 8 of Table 6.2 shows, the outer region concentration rises from *ca.* 10% to *ca.* 93% of the inner region concentration. The latter value represents the actual concentration of sites in the outer polymer regime, when the islands are overlapped. However these are not the effective concentrations, since the islands do not cover the entire film dense layer. For instance, in the extreme case of film **E**, the islands (Figure 6.7, panels a, c) occupy only *ca.* 1% of the surface, so estimating outer film thickness by joining their peaks overestimate the average thickness by a factor of 100. Similarly, for film **G**, the island coverage is *ca.* 30%, so the effective concentration is only *ca.* 30% of  $0.38 \times 10^{-3} \text{ mol cm}^{-3}$ , *i.e.*  $0.11$

$\times 10^{-3} \text{ mol cm}^{-3}$ . In the case of film **F**, the islands occupy around 20% of the surface, which gives  $0.26 \times 10^{-3} \text{ mol cm}^{-3}$ .

**Table 6.2:** Estimate of film thickness and effective concentrations in the outer film region ( $C_{\text{outer}}$ ).

Sample	$\Gamma(Q_{\text{redox}})$ / $\text{nmol cm}^{-2}$	$h_{\text{f inner}}$ / nm	$h_{\text{f outer}}$ / nm	$\Gamma_{\text{inner}}^a$ / $\text{nmol cm}^{-2}$	$\Gamma_{\text{outer}}$ / $\text{nmol cm}^{-2}$	Islands areal occupation	$C_{\text{outer}} \times 10^{-3}$ / $\text{mol cm}^{-3}$	Effective $C_{\text{outer}} \times 10^{-3}$ / $\text{mol cm}^{-3}$
<b>E</b>	13.1	90.3	39.2	12.6	0.5	1%	0.13	0.0013
<b>G</b>	55.7	281	434	39.3	16.4	30%	0.38	0.11
<b>F</b>	194	483	965	67.6	126.4	20%	1.30	0.26

<sup>a</sup>Obtained as the product of film thickness and unsolvated volume concentration,  $C = 1.4 \times 10^{-3} \text{ mol cm}^{-3}$ ;

While there are clearly some approximations in this spatially variant model, it is relatively simple, physically reasonable, and able to rationalise the observed electrochemical, acoustic and imaging data.

## 6.3 VARIATION OF RHEOLOGICAL PROPERTIES IN BACKGROUND ELECTROLYTE

### 6.3.1 Effect of doping state

Figure 6.10 depicts the voltammetric response of film **A** in background electrolyte. The electrochemical response of poly[Ni(3-Mesalophen-b15-c5)] films was described in detail in Chapter 4. Briefly, the film shows three anodic ( $E_{\text{paI}} = 0.29 \text{ V}$ ,  $E_{\text{paII}} = 0.80 \text{ V}$  and  $E_{\text{paIII}} = 1.12 \text{ V}$ ) and three cathodic features (two waves at  $E_{\text{pcI}} = 0.27 \text{ V}$  and  $E_{\text{pcII}} = 0.77 \text{ V}$  and one inflexion at  $E_{\text{pcIII}} = 0.94 \text{ V}$ ). This is rather similar for all the films, except for the increase of the current intensity and displacement of the peak potentials towards oxidising potentials with the increase of  $\Gamma$ .



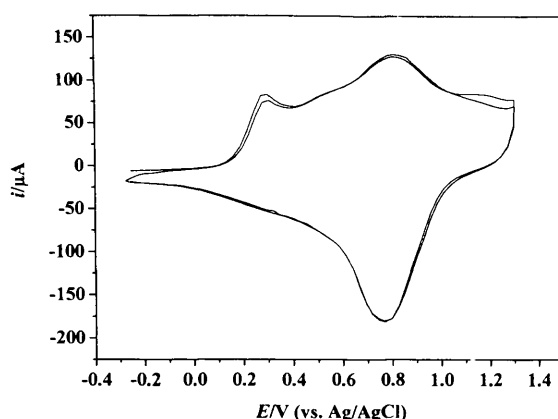


**Figure 6.10:** Voltammetric response of poly[Ni(3-Mesalophen-b15-c5)] (film A) acquired in 0.1 mol dm<sup>-3</sup> TBAP/CH<sub>3</sub>CN between -0.3 and 1.3 V.

### 6.3.1.1 EQCM studies – acoustically thin films

The admittance spectra of a film prepared with 3 deposition cycles at 0.02 V s<sup>-1</sup> (film H,  $\Gamma=17.0$  nmol cm<sup>-2</sup>) is shown in Figure 6.11a. The peak admittance decreases by 6 % during the process of polymerisation. Then, the film is considered to be within the acoustically thin regime. Figure 6.11b shows the variation of peak admittance as a function of the applied potential in background electrolyte. The admittance decreases when the potential is scanned in the positive (oxidation) direction. Sweeping the potential negatively results in the restoration of the initial admittance. This minor variation in the admittance (*ca.* 2%) indicates that the film loses some ‘rigidity’ at oxidising potentials, probably due to the ingress of electrolyte species.

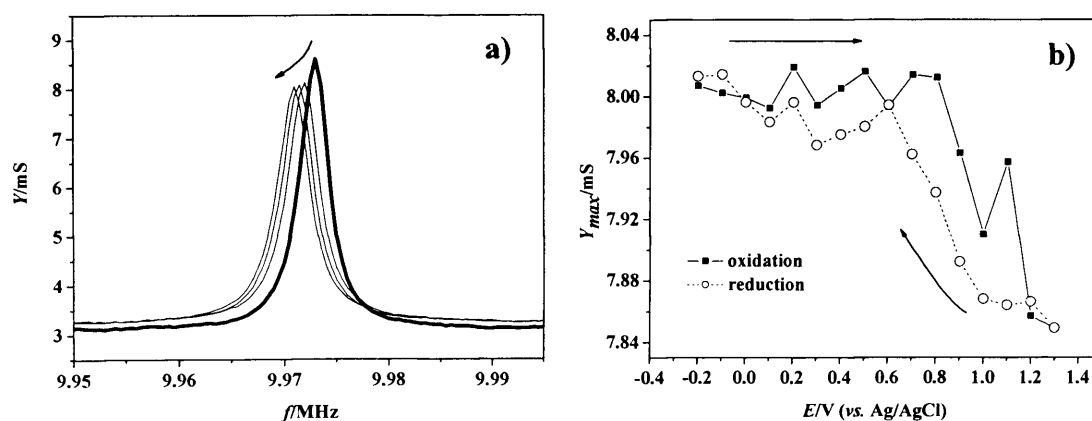


**Figure 6.11:** a) Admittance spectra acquired during the polymerisation of [Ni(3-Mesalophen-b15-c5)] at 0.02 V s<sup>-1</sup> (film H) (— admittance spectrum of QCM in solution and — admittance spectra acquired at the end of each deposition cycle); b) variation of the peak admittance (film H) with the applied potential in background electrolyte (arrows indicate the direction of potential sweep).

Insertion of the film density  $\rho_f = 1.2 \text{ g cm}^{-3}$  and the experimental  $\Delta f$  in the Sauerbrey equation lead to the determination of  $h_f$  as a function of the applied potential (Figure 6.12). The charge  $Q_{redox}$  starts to increase at 0.2 V reaching a maximum at 1.3 V (panel a). The cycling of potential in the opposite direction reverses this profile, but hysteresis is detected. When the electroactive film is oxidised, the charge developed must be compensated via electrolyte species in order to restore the system electroneutrality. This can be accomplished in different ways: (i) ingress of anions in the film to compensate the positive charge resulting from the oxidation (film swelling, increase of  $h_f$ ), (ii) egress of cations from the film to the solution (film shrinking, decrease of  $h_f$ ) (iii) movement of cations/anions in opposite directions (small net variation in  $h_f$ ). Since the  $h_f$  profile shows that the film swells upon oxidation, the net movement of species at the film/solution interface must favour the ingress of species.

Additionally, information can be obtained by plotting the mass  $\Delta M'$  against  $Q_{redox}$  (panel b). The slope of this plot gives the molar mass of species involved in the charge compensation process. According to Faraday's law<sup>9</sup>:

$$m' = \frac{zF\Delta M'}{Q} \quad (6.1)$$

where  $m'$  is the molar mass,  $z$  is the charge associated with the species, and  $F$  is the Faraday constant. Table 6.3 presents the molar mass estimated using the slopes from Figure 6.12b.

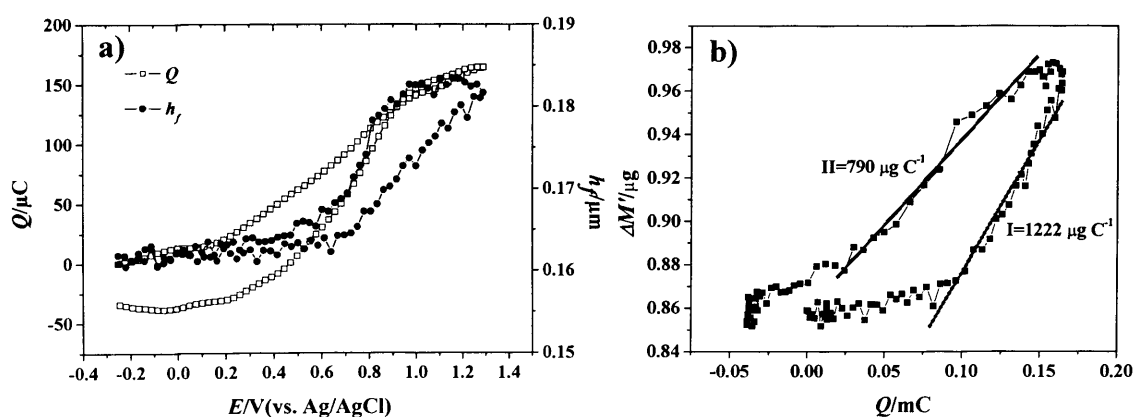


**Figure 6.12:** Plot of a)  $Q_{redox}$  and  $h_f$  vs. the applied potential and b)  $\Delta M'$  vs.  $Q_{redox}$  for film H, in  $0.1 \text{ mol dm}^{-3}$  TBAP/ $\text{CH}_3\text{CN}$ . 'I' is the slope in the anodic half-cycle and 'II' for the cathodic counterpart (—).

**Table 6.3:** Determination of molar mass associated with the slopes of Figure 6.12b.

Slope/ $\mu\text{g C}^{-1}$	$m' / \text{g mol}^{-1}$
1222 (anodic)	117.9
790 (cathodic)	76.2

There are three species present in the electrolyte solution:  $\text{TBA}^+$  ( $242.00 \text{ g mol}^{-1}$ ),  $\text{ClO}_4^-$  ( $99.45 \text{ g mol}^{-1}$ ) and  $\text{CH}_3\text{CN}$  ( $41.05 \text{ g mol}^{-1}$ ). Comparing the molar mass of these species with the values depicted in Table 6.2,  $\text{ClO}_4^-$  seems to play the main role in the charge compensation processes. These findings can be rationalised in terms of the relative dimensions of electrolyte species: the ionic radius of  $\text{TBA}^+$  is  $0.413 \text{ nm}$ , considerable larger than that of  $\text{ClO}_4^-$  ( $0.240 \text{ nm}$ )<sup>10</sup>. Therefore, it is expected that the movement of the cation at the film/solution interface will be considerably hindered with respect to the counterion.

The molar mass obtained from the slope in the anodic half-cycle is higher than the molar mass of  $\text{ClO}_4^-$ . Conversely, the molar mass obtained from the cathodic counterpart is lower than that of  $\text{ClO}_4^-$ . This may be explained in terms of the electrostatic nature of the driving force. The species prone to respond firstly to changes in the film doping state are those charged (in this case  $\text{ClO}_4^-$ ), whilst solvent molecules are dragged. As a result, the timescale associated to the movement of  $\text{ClO}_4^-$  is smaller than that of  $\text{CH}_3\text{CN}$ . Accordingly, the movement of electrolyte species can be envisaged in the following way: when the potential is cycled towards oxidising regions,  $\text{ClO}_4^-$  moves firstly into the film, which is then followed by solvent molecules (the movement of  $\text{ClO}_4^-$  and  $\text{CH}_3\text{CN}$  in the same direction results in a steeper slope than expected for  $\text{ClO}_4^-$  only); when the potential is reversed, there are still solvent molecules entering into the film while the anions are already leaving (this cross movement results in a decrease of the cathodic slope).

### 6.3.1.2 Acoustically thick films and the ‘thin film’ approach

In section 6.2.3 it was shown that the model of an uniform film used to describe the viscoelastic properties of poly[Ni(3-Mesalophen-b15-c5)] films can only be used to probe the thin and uniform underlayer of the film. In these conditions neither  $Q_{redox}$  nor  $\Delta f$  provide a good estimate of  $h_f$ . In order to obtain the  $h_f$  vs.  $E$  profile, it is assumed that the underlayer of an acoustically thick film behaves similarly to the acoustically thin

film. The strategy consists of normalisation of  $h_f(E)_{thin}$  depicted in [Figure 6.12a](#) and adjustment of it to the viscoelastic film:

$$h_f(E)_{thick} = \frac{h_f(E)_{thin}}{\langle h_f \rangle} \times h_f(pol) \quad (6.2)$$

where  $h_f(E)_{thick}$  is the variation of thickness with potential of the thick film (**A**),  $\langle h_f \rangle$  is the average thickness of film **H** in the reduced state (where  $h_f$  variation is considered to be negligible), and  $h_f(pol)$  is the thickness of the viscoelastic film at the end of the polymerisation process, which for film **A** was found to be 228 nm. Using  $\rho_f = 1.2 \text{ g cm}^{-3}$  and  $h_f(E)_{thick}$ , the determination of shear moduli values is then straightforward. The  $h_f$  values for which  $G$  values were fitted corresponds to 95% of  $h_f(pol)$  ([Figure 6.13, panel a](#)). This small difference may be due to (i) monomeric/oligomeric species trapped in the polymer that were removed at the end of deposition by rinsing of the modified electrode, or (ii) egress of electrolyte species from the film after the experiment was finished (*i.e.* solvent molecules). Moreover,  $G$  values could only be fitted for  $h_f$  within a 5% span, which shows the precision of this model.

The  $G$  values obtained are depicted in [Figure 6.13 b](#). The main outcome is that the loss component  $G''$  dominates the mechanical response of the film, regardless of the doping state. The film mechanical response is here divided into three potential intervals, according to the variations found in the  $G$  values: (i)  $-0.3$  to  $0.3$  V, (ii)  $0.3$  to  $0.7$  V and (iii)  $0.7$  to  $1.3$  V. In the first interval  $G$  values are roughly constant, with  $G''$  higher than  $G'$ . At this stage the film electroactivity is reduced, so it is expected that the sweep of potential within this interval will not provoke significant changes in terms of film local environment/electrolyte content. In the second interval  $G''$  decreases whereas  $G'$  increases; at this point the shear components become comparable. For these intermediate potentials the film becomes increasingly doped; the increase in the storage component indicates an increase in the intrachain rigidity, which structurally is associated with the formation of a quinoid-like structure ([Figure 1.5](#), Chapter 1). In this structure the establishment of double bonds between monomeric units stiffens the polymeric chain. Similar poly[M(*salen*)] films were found to assume a polyphenylene-like structure for reducing states and a quinoid-like structure for oxidising states<sup>11</sup>. In the third interval (extreme oxidising potentials) both components increase, with  $G''$  varying to a greater extent than  $G'$ . At this stage, the positively charged film swells with the ingress of  $\text{ClO}_4^-/\text{CH}_3\text{CN}$ . The small variation of  $G'$  indicates the gradual oxidation of the film, whereas the dramatic changes of  $G''$  show that the increase of

electrolyte content within the film results in a rise of polymer viscosity, making it more resilient to the egress of additional electrolyte species.

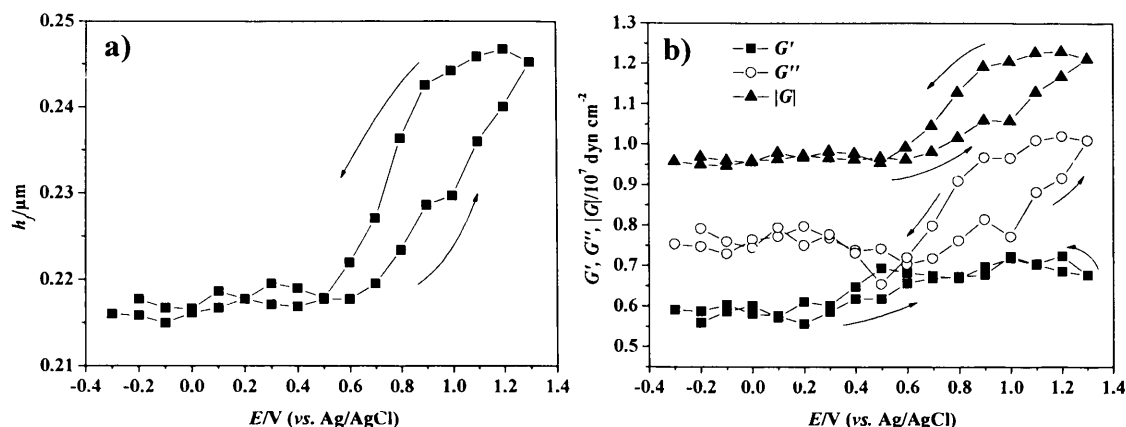


**Figure 6.13:** a) Film thickness profile  $h_f(E)_{thick}$  used in the fitting process and b) variation of shear moduli values with the applied potential (film A). Arrows indicate the direction of potential sweep.

The hysteresis observed in  $G$  values as a function of  $E$  indicates that a global equilibrium was not attained on the timescales used in these experiments ( $0.01 \text{ V s}^{-1}$ ). This may be associated with either (i) slow charge or (ii) slow solvent transport. In order to determine which one is the limiting factor, Figure 6.14 depicts the plot of  $Q$  vs.  $E$  (panel a) and the plot of  $G$  vs.  $Q$  (panel b), respectively. The hysteresis associated with  $Q$  profile (panel a) shows that the redox equilibrium is not fully established. However, this is not the only limiting factor, since the plot of  $G$  vs.  $Q$  also reveals hysteresis (indication of slow solvation process). Therefore, the  $G$  values obtained at different doping states are not only dependent upon the charge injected in the film, but also they reflect the prior history of the film.

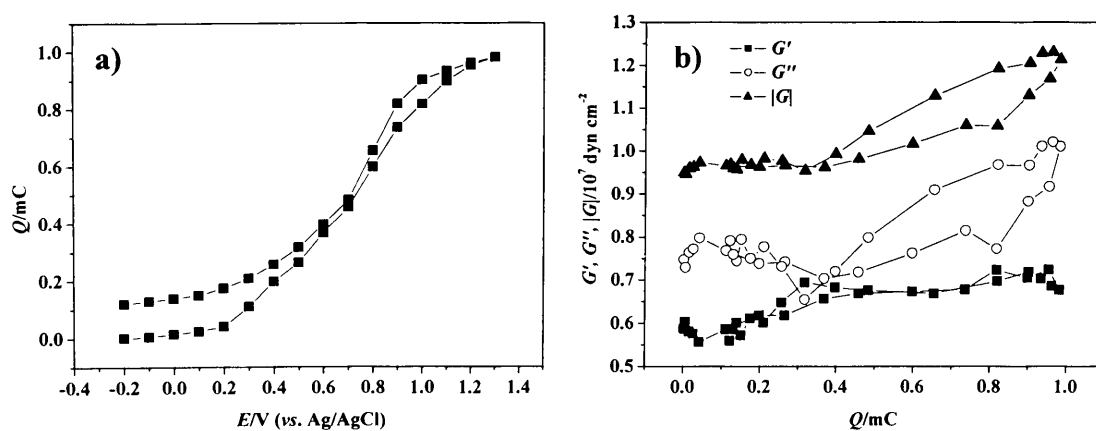


**Figure 6.14:** Plots of a)  $Q$  vs.  $E$  and b) shear moduli vs.  $Q$ , for film A.

### 6.3.2 Effect of Ba<sup>2+</sup> addition

Ba<sup>2+</sup> was used to study the ion recognition properties of poly[Ni(3-Mesalophen-b15-c5)] films in the context of acoustic wave sensors. The changes observed in the voltammetric response upon metal cation addition were already discussed in Chapter 4. Here, particular attention is given to the associated mechanical properties of the film.

#### 6.3.2.1 Acoustically thin films

The dependence of  $h_f$  upon the applied potential was recorded for film **H** after the addition of 200  $\mu\text{L}$  of a solution of 0.05  $\text{mol dm}^{-3}$  Ba(ClO<sub>4</sub>)<sub>2</sub> (final concentration 2  $\text{mmol dm}^{-3}$ ). Figure 6.15 shows the variation of  $h_f$  before and after the addition. There are two major differences in the  $h_f$  profile with the metal cation addition. First, the ‘baseline’ was positively displaced by *ca.* 30 nm following the addition, implying that in the presence of Ba<sup>2+</sup> the film swelled by 18 %. This is evidence of uptake of species from the solution, most likely Ba<sup>2+</sup> or barium derived species (Ba<sup>2+</sup>+ClO<sub>4</sub><sup>-</sup>+CH<sub>3</sub>CN). XPS and XAS results confirm this assumption (Chapter 5). Second, the extent to which the film swells upon oxidation is smaller after the cation addition. Possibly, the ingress of electrolyte+barium species prior to the potential sweep restricts the increase of  $h_f$ . In this sense, the charge compensation process becomes limited and may explain the decrease in the  $Q_{\text{redox}}$  upon metal cation addition (Chapter 4).

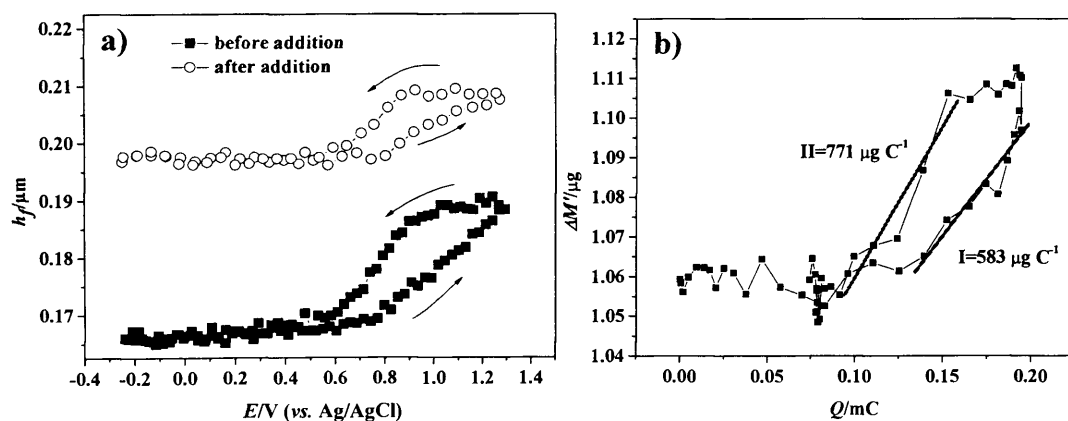


**Figure 6.15:** a) Variation of  $h_f$  (film **H**) before and after addition of Ba(ClO<sub>4</sub>)<sub>2</sub> (final concentration 2  $\text{mmol dm}^{-3}$ ) to the background electrolyte; b)  $\Delta M'$  vs.  $Q_{\text{redox}}$  for film **H** after Ba<sup>2+</sup> addition. ‘I’ is the slope in the anodic half-cycle and ‘II’ for the cathodic counterpart (—). Arrows indicate the direction of potential sweep.

Table 6.4 presents the molar mass obtained from the  $\Delta M'$  vs.  $Q$  plot shown in Figure 6.15b. The first inspection of the plot indicates that the mechanism of charge compensation does not change to any extent in the presence of  $\text{Ba}^{2+}$ . Then, barium derived species must be located in regions of the film where the effects of applied potential are small. There is, though, a ‘space limitation’. The slope of the anodic half-cycle is smaller than that found before the addition (Figure 6.12b). Since the film has already swelled with  $\text{Ba}^{2+}$  addition, restrictions in additional swelling may impose some degree of exchange at the film/solution interface in order to allow  $\text{ClO}_4^-$  ingress.

**Table 6.4:** Determination of molar mass associated with the slopes of Figure 6.15b.

Slope/ $\mu\text{g C}^{-1}$	$m' / \text{gmol}^{-1}$
583 (anodic)	56.2
771 (cathodic)	74.4

### 6.3.2.2 Acoustically thick films

The strategy followed for extraction of  $G$  values prior to  $\text{Ba}^{2+}$  addition (thin film extrapolation) was used again for determination of those parameters in the presence of the metal cation. Equation to 6.3, which is similar to Equation 6.2, was used for this purpose:

$$h_f(E)_{\text{thickBa}} = \frac{h_f(E)_{\text{thinBa}}}{\langle h_f \rangle_{\text{Ba}}} \times 95\% h_f(\text{pol}) \times \frac{\langle h_f \rangle_{\text{Ba}}}{\langle h_f \rangle} \quad (6.3)$$

According to this equation, the  $h_f$  profile of the thin film **H** after  $\text{Ba}^{2+}$  addition ( $h_f(E)_{\text{thinBa}}$ ) is normalised with respect to its average thickness in the reduced state ( $\langle h_f \rangle_{\text{Ba}}$ ), and multiplied by both the film thickness of film **A** ( $95\% h_f(\text{pol})$ ) and the swelling ratio of film **H**. Using this equation it is assumed (i) the variation of  $h_f$  in the presence of  $\text{Ba}^{2+}$  for the thick film is the same as that of the thin film, and (ii) the thick film swells to the same (relative) extent as the thin film. The shear moduli values obtained using the calculated  $h_f$  values are depicted in Figure 6.16a.  $G$  values could only be fitted for  $h_f$  within a 5% span, which show *per se* the validity of the approximations used. Additionally, when a different profile of  $h_f(E)$  is used for the extraction of  $G$  values *after*  $\text{Ba}^{2+}$  addition (for instance, the profile before the addition,  $h_f(E)_{\text{thin}}$ ), the extracted  $G$  values are in some cases negative. This shows that the interval in which  $G$  values are physically reasonable is small.

$G'$  values are roughly comparable to those obtained before the addition, which indicates that there are no major changes in terms of *intrachain* rigidity upon metal cation addition (panel b). Nevertheless,  $G''$  values are larger after the addition, indicating that the presence of  $Ba^{2+}$  plays an important role in the film viscosity, namely influencing *interchain* interactions (panel c). The dependence of shear moduli values on the doping state seems to be similar before and after  $Ba^{2+}$  addition.

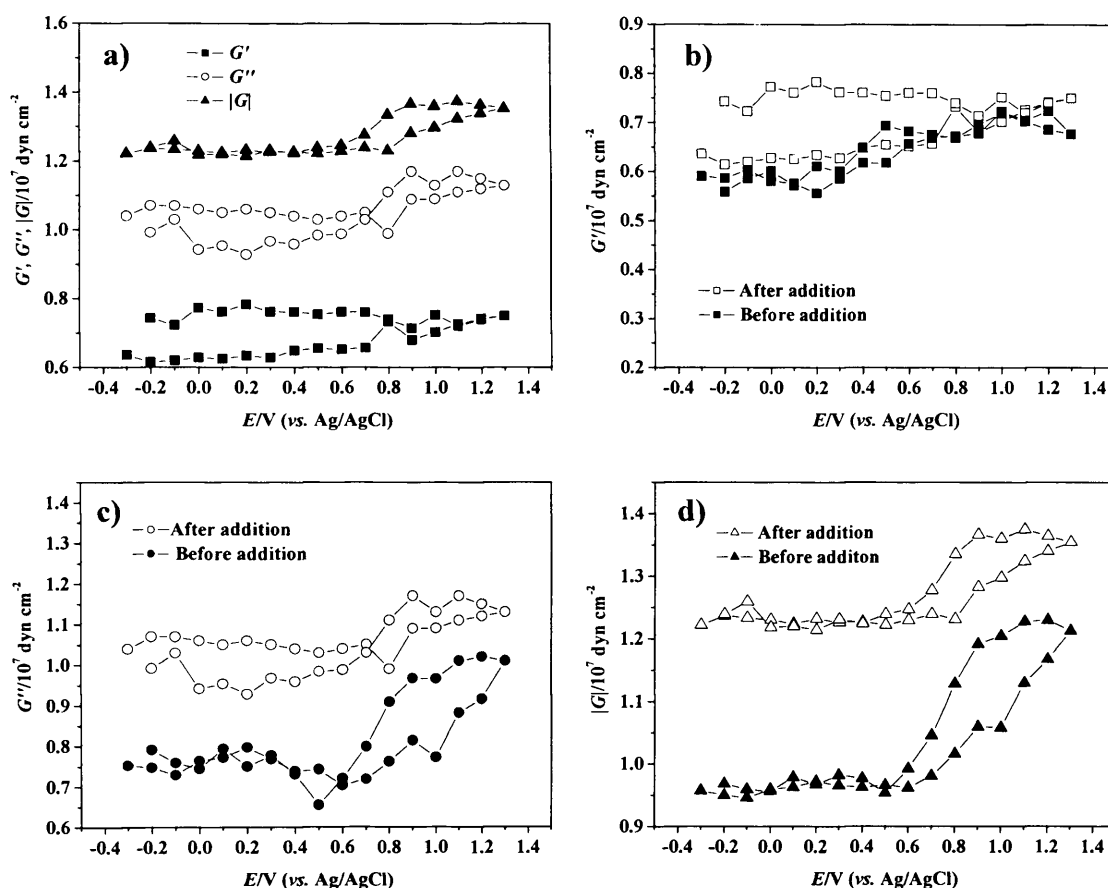


**Figure 6.16:** a) Variation of shear moduli values with the applied potential (film A). Comparisons between b) storage, c) loss and d) modulus moduli, before and after  $Ba^{2+}$  addition (final concentration  $2 \text{ mmol dm}^{-3}$ ).

These findings suggest that, following the addition of  $Ba(ClO_4)_2$  to the electrolyte,  $Ba^{2+}$  and/or derived species diffuse throughout the film. The cation occupies sites within the film that are little sensitive to changes in the film doping states, and the result is its reduced migration upon variation of the film doping state (irreversibility). Furthermore, the increase in viscosity indicates that  $Ba^{2+}$  occupies sites somewhere in between different polymeric chains, probably establishing interactions with oxygen atoms from different crown ethers. This assumption is consistent with XAS findings (Chapter 5).



### 6.3.3 Effect of the resonating frequency

$G$  values were also fitted for harmonics of the fundamental frequency (30 MHz, 50 MHz, 70 MHz and 90 MHz). [Figure 6.17](#) presents  $G'$  and  $G''$  values, before and after  $\text{Ba}(\text{ClO}_4)_2$  addition.

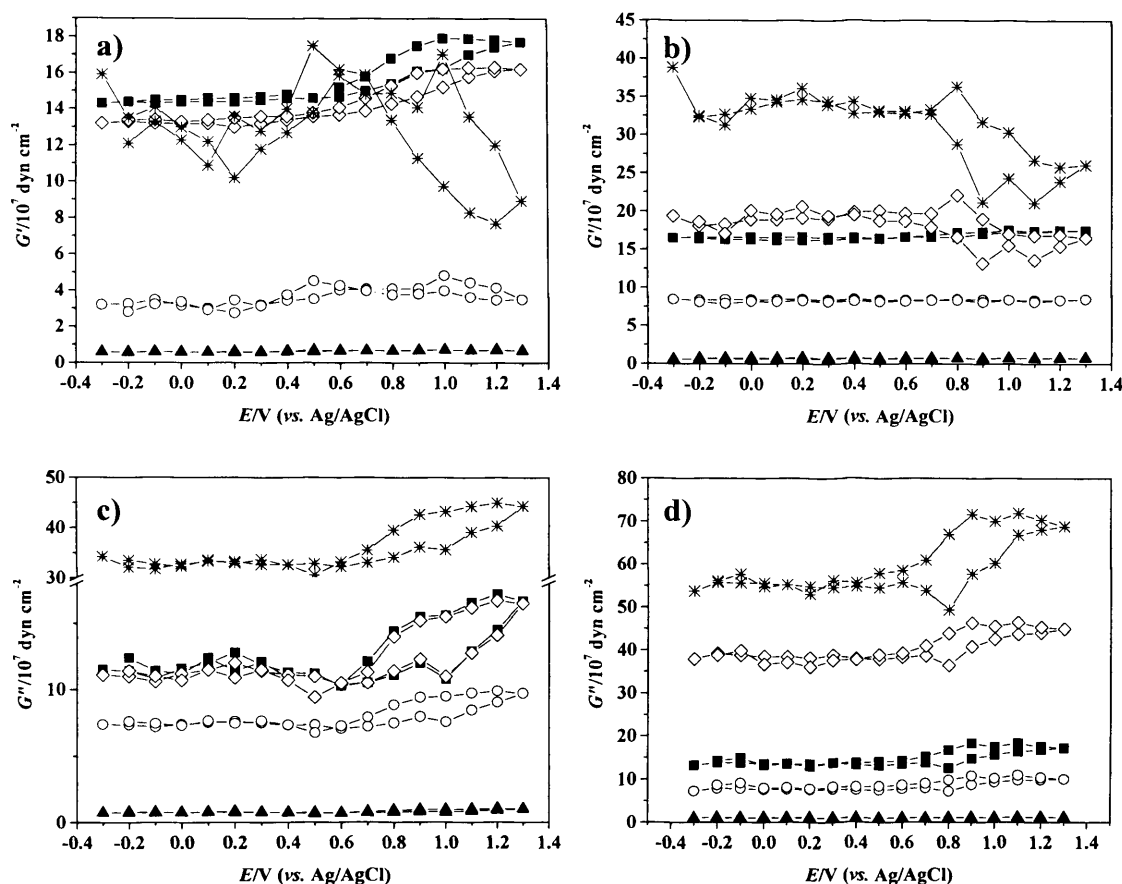


**Figure 6.17:** Storage (panels a, b) and loss (panels c, d) moduli before (panel a, c) and after (b, d)  $\text{Ba}^{2+}$  addition (final concentration  $2 \text{ mmol dm}^{-3}$ ). Resonant frequency: 10 MHz (▲), 30 MHz (○), 50 MHz (■), 70 MHz (◇) and 90 MHz (✱).

There are similarities in the trends of  $G$  vs.  $E$  with those observed for the fundamental frequency:  $G''$  values are always higher than  $G'$ , and the addition of barium leads to a considerable increase of  $G$  values. The hysteresis observed in the shear moduli values is due to the film spatial variations (in terms of oxidation state and solvation), which reflect the direction in which a given potential is approached (prior history). In addition, the rise in hysteresis with the frequency is associated with decrease of the decay length ([Equation 2.42](#), Chapter 2).

Although both  $G$  values increase with the frequency, the variation of  $G''$  values is more significant, which indicates that the material is in the transition region<sup>12</sup>.

Qualitatively, the variation of  $G'$  excludes the Voigt model. Instead, the increase of both  $G'$  and  $G''$  with the frequency are consistent with the Maxwell model in the rubbery regime ( $\omega\tau < 1$ , [Figure 2.9](#), Chapter 2). [Figure 6.18](#) depicts the logarithmic dependence of  $G$  on the resonant frequency, at extreme doping states: fully reduced (-0.3 V) and fully oxidised (1.3 V). Prior to addition  $G'$  and  $G'' \propto \omega^{3/2}$ , but in the presence of  $\text{Ba}^{2+}$  the dependence of  $G$  on the frequency seems to change ( $G'$  and  $G'' \propto \omega^2$ ). The Maxwell model, which predicts quadratic and linear dependencies of  $G'$  and  $G''$  for  $\omega\tau \ll 1$ , is rather too simplistic to explain the frequency dependencies found for this system; more complex (multi-element) spring and dashpot models are required.

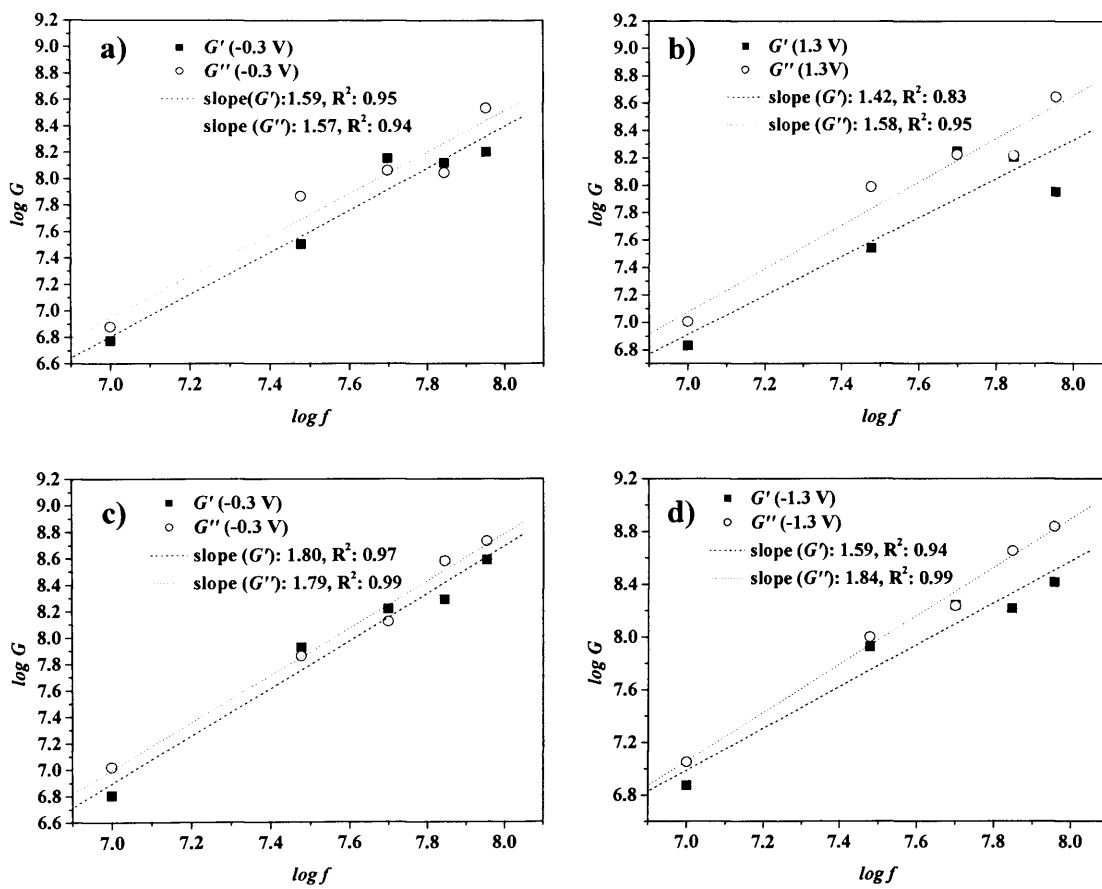


**Figure 6.18:** Logarithmic dependence of  $G'$  and  $G''$  on frequency, before (panels a and b) and after (panels c and d)  $\text{Ba}^{2+}$  addition.

At all the frequencies observed the ratio of film thickness prior to and following the barium addition is similar ( $1.23 \pm 0.05$ ), which not only confirms the validity of the fitting but also allows one to estimate the content of barium inside the film. Considering the film thickness  $h_f = 216$  nm,  $h_f(\text{Ba}^{2+}) = 256$  nm and electrode area  $0.23$  cm<sup>2</sup>, for the simplest case in which only  $\text{Ba}^{2+}$  diffuses into the film, the volume variation  $\Delta V$  corresponds to  $0.23 \times (0.256 - 0.216) \times 10^{-4} = 9.2 \times 10^{-7}$  cm<sup>3</sup>. Using the  $\text{Ba}^{2+}$  ionic radius  $0.137$  nm and a spherical volume of  $1.08 \times 10^{-23}$  cm<sup>3</sup>, the volume increase corresponds to  $8.5 \times 10^{16}$  atoms or  $1.4 \times 10^{-7}$  mol. The amount of electroactive sites corresponding to 32.5 % of  $Q_{\text{dep}}$  ( $0.325 \times 1.18$  mC) is  $3.65 \times 10^{-8}$  mol cm<sup>-2</sup>. Assuming the amount of Ni atoms within the same range of the electroactive sites, this gives a Ni:Ba ratio of 0.06:1 or 1:17. A more realistic approximation is to consider the ingress of  $\text{Ba}^{2+}$  accompanied by  $\text{ClO}_4^-$ . According to XPS data (Chapter 5), the Ba:Cl ratio is about 1. Using the  $\text{ClO}_4^-$  ionic radius  $0.240$  nm and considering the volume of  $[\text{Ba}(\text{ClO}_4)]^+$  as the sum of the individual species ( $6.87 \times 10^{-23}$  cm<sup>3</sup>), it gives  $2.2 \times 10^{-8}$  mol. Consequently, the result is a Ni:Ba ratio of 1:3, which is more consistent with XAS studies (Chapter 5).

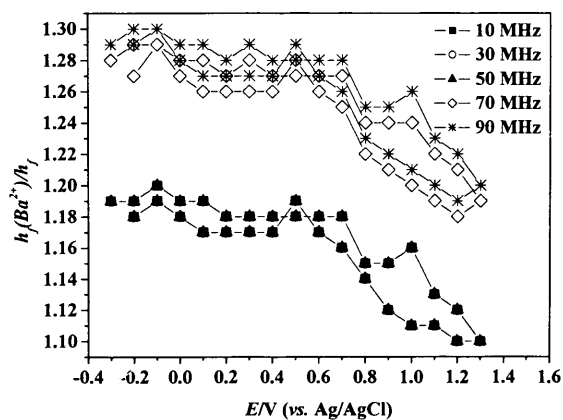


**Figure 6.19:** Ratio of  $h_f(\text{Ba}^{2+})/h_f$  at different resonant frequencies (film A).

## CONCLUDING REMARKS

The way in which film thickness and compositional/morphological changes are ‘seen’ by different techniques is dependent upon the physical nature of the interaction of the relevant probe with the interface. Here, electrochemical, acoustic wave and AFM images were used to determine film thickness, based on coulometric, mechanical and surface force interactions, respectively. The first two of these are spatially integrated, *i.e.* ‘averaged’, while the third is sensitive to spatial variations. The electrochemical assay reflects the population of redox sites in good electronic communication with the electrode on the observational timescale. The demarcation between ‘thin’ and ‘thick’ films – representing complete or partial assay - is diffusionally limited, according to the potential scan rate. The acoustic wave assay reflects the amount of material that is mechanically coupled to the underlying oscillator. In this case, the demarcation between ‘thin’ and ‘thick’ films – representing complete or partial assay - is determined by film viscoelastic properties. Low solvation levels result in low loss films that propagate the acoustic wave over long distances such that all the film may be observed, while high solvation levels plasticise the film and cause rapid decay of the acoustic wave such that only a fraction of the film may be observed.

Poly[Ni(3-Mesalophen-b15-c5)] films have structures that depend on the amount of surface-immobilised material. For sufficiently ‘electrochemical’ thin films ( $\Gamma < 15 \text{ nmol cm}^{-2}$ ), they are ‘thin’ by all measures and comprise a uniform layer of polymer with monodisperse, small polymer islands on the top. Acoustic, coulometric and AFM estimates of  $h_f$  are consistent. Films prepared with  $15 < \Gamma / \text{nmol cm}^{-2} < 60$  are rougher and can be considered as an underlying uniform layer decorated with islands of polymer. In this regime,  $h_f^Q$  overestimates the thickness of the uniform layer since the coulometric assay responds to all the electroactive species (in the uniform layer and the islands), but  $h_f^{grav}$  is still a good approximation to the thickness of the uniform layer. This corresponds to a transitional situation in which the uniform layer is the dominant component and can be considered acoustically thin, but the polymer islands are in a much more liquid-like environment that is not rigidly mechanically coupled to the underlying electrode. Films prepared with  $\Gamma > 100 \text{ nmol cm}^{-2}$  show a behaviour that is dominated by the large heterogeneous islands of polymer. As for the intermediate case,  $h_f^Q$  overestimates the thickness of the uniform layer (now to a greater extent) and, since the film is no longer in the acoustically thick regime,  $h_f^{grav}$  also overestimates the

thickness of the uniform layer. Although the amount of polymer in the diffuse region increases with  $\Gamma$ , the effective concentration of polymer is considerable less than in the dense, inner region.

EQCM studies performed in acoustically thin films showed that  $\text{ClO}_4^-$  plays the main role in the charge restoration process. Upon  $\text{Ba}^{2+}$  addition the film swells irreversibly, indicating the permanent ingress of solution species into the film. As a result, the film capacity to accept additionally electrolyte species in the oxidised state decreases. This may explain the loss of electroactivity upon metal cation addition, discussed in Chapter 4.

Knowing that the acoustic methods only ‘see’ the inner/dense region of poly[Ni(3-Mesalophen-b15-c5)] viscoelastic films, the study of the rheological properties in background electrolyte was performed assuming that the thickness profile of acoustically thick films mimics that of thin films. This model was found to be not only successful for the extraction of  $G$  values, but also quite precise. At reducing potentials  $G$  values are roughly constant, with  $G''$  higher than  $G'$ , consistent with the low film electroactivity; at intermediate potentials  $G''$  decreases whereas  $G'$  increases, which may be interpreted as an increase of *intrachain* rigidity, associated with the formation of a quinoid-like structure. At oxidising potentials,  $G''$  values increase to a greater extent than their  $G'$  counterparts, which may be associated with increase in the polymer viscosity due to the ingress of  $\text{ClO}_4^-/\text{CH}_3\text{CN}$ . The addition of  $\text{Ba}^{2+}$  increases the  $G''$  values, implying that the presence of the metal cation plays an important role in the film viscosity, namely influencing *interchain* interactions. This is consistent with EXAFS findings (Chapter 5).

Finally, the increase of  $G$  values with the resonant frequency is qualitatively consistent with the Maxwell model in the rubbery regime. Moreover, the hysteresis observed in the shear moduli indicates that these are dependent not only upon the applied potential but also in the way that potential is attained (prior history).

## REFERENCES:

1. Tedim, J.; Bessada, R.; Patricio, S.; Magalhaes, A. L.; Freire, C.; Gurman, S. J.; Hillman, A. R. *Langmuir* **2008**, *24*, 8998.
2. Tedim, J.; Freire, C.; Hillman, A. R. *submitted to PCCP*.
3. Hillman, A. R.; Jackson, A.; Martin, S. J. *Anal Chem.* **2001**, *73*, 540.
4. Bandey, H. L.; Hillman, A. R.; Brown, M. J.; Martin, S. J. *Farad. Discuss.* **1997**, *107*, 105.
5. Santos, I. C.; Vilas-Boas, M.; Piedade, M. F. M.; Freire, C.; Duarte, M. T.; de Castro, B. *Polyhedron* **2000**, *19*, 655.
6. Azevedo, F.; Carronto, M. A. A. F. C. T.; de Castro, B.; Convery, M.; Domingues, D.; Freire, C.; Duarte, M. T.; Nielsen, K.; Santos, I. C. *Inorg. Chim. Acta* **1994**, *219*, 43.
7. Carronto, M. A. A. F. C. T.; de Castro, B.; Coelho, A. M.; Domingues, D.; Freire, C.; Morais, J. *Inorg. Chim. Acta* **1993**, *205*, 157.
8. Bandey, H. L.; Martin, S. J.; Cernosek, R. W. ; Hillman, A. R. *Anal. Chem.* **1999**, *71*, 2205.
9. Skoog, D. A.; West, D. M.; Holler, F. J. In *Fundamentals of Analytical Chemistry*; Saunders College Publishing: Orlando, 1991.
10. Marcus, Y. *J. Chem Soc., Faraday Trans.*, **1993**, *89*, 713.
11. Vilas-Boas, M.; Freire, C.; de Castro, B.; Christensen, P. A.; Hillman, A. R. *Inorg. Chem.* **1997**, *36*, 4919.
12. Graessley, W. W. *Faraday Symp. Chem. Soc.* **1983**, *18*, 7.

## Chapter 7

***INTRODUCTORY STUDIES OF COMPOSITES BASED  
ON POLY[Ni(3-MESALOPHEN-B15-C5)] AND  
MULTI-WALLED CARBON NANOTUBES***

## 7.1 COMPOSITES BASED ON CONDUCTING POLYMERS AND CARBON NANOTUBES

As mentioned in earlier chapters, the application of modified electrodes extends over a wide range of areas including (bio)chemical sensing, electronic devices, optical displays, surface protection, (electro)catalysis, energy storage and energy conversion<sup>1-4</sup>. The growing demand for better performances prompts not only the preparation of new materials but also the improvement of existing ones. The latter can be accomplished in several ways, namely by exercising greater control over interfacial architecture via a range of templating methods<sup>5-8</sup>, or through assembly of the desired group of materials properties (electronic, mechanical, chemical, etc) by formation of a composite material.

The discovery of carbon nanotubes (CNTs) in 1991<sup>9</sup> has revolutionised the field of materials science as a consequence of their remarkable combination of electrical, chemical and mechanical properties. They present the opportunity to exploit metallic and/or semi-metallic structures, facile adsorption, doping and charge transfer processes, and mechanical strength (Young's modulus and tensile strength of over 100 GPa<sup>10</sup>). More specifically within the field of electrochemistry, CNTs have been employed in the fabrication of electrodes for detection of biological molecules<sup>11-13</sup> and of trace metals in water<sup>14</sup>, and for double-layer capacitors<sup>15-17</sup>.

Recently, there has been a growing interest in their combination with conducting polymers in nanocomposite materials. The general aspiration is to exploit synergistic interactions when the two components are combined: for example, the CNTs may introduce mechanical stability or enhance the electrical properties of the polymer<sup>18,19</sup>. Among the most promising combinations are CNT/polypyrrole<sup>16,19-22</sup> and CNT/polyaniline<sup>18,23</sup> nanocomposites. These materials were found to have improved conducting properties with respect to those of the polymer – notably in potential regimes in which the polymer is poorly conducting – and to considerably increase the specific capacitance.

A potentially convenient route to preparing composite films is the electropolymerisation of a suitable monomer and simultaneous entrapment of the CNTs within the depositing film. The main difficulty associated with the preparation of such composites is the insolubility of carbon nanotubes in typical solvents<sup>24</sup>. There are several reports of functionalisation or chemical derivatization of carbon nanotubes<sup>25-27</sup> as a way to



increase their dispersion/solubility. One such approach is treatment of the carbon nanotubes with oxidising acids prior to the polymerisation process<sup>16,17</sup>, in order to functionalise their walls with oxygenated groups, making them more readily dispersed in aqueous media. This method has the additional advantage of excluding the need for additional electrolyte, since the negatively charged CNTs are able to compensate the development of positive charge within the growing film during electropolymerisation.

When chemical constraints require the use of an organic solvent, the above strategy cannot be applied because the concentration of CNTs in the dispersion is considerably lower than in water. Consequently, for systems including a polymer such as poly(3-methylthiophene), the polymerisation cannot proceed without the presence of an additional supporting electrolyte<sup>28</sup>. Although there are several reports of CNT/conducting polymer composites being used for detection of biomolecules in aqueous systems<sup>29-33</sup>, similar performance in organic solvents is still elusive. In this context, crown ether macrocycles<sup>34</sup> are interesting in that they are at the boundary of these two distinct types of system: their ability to bind to alkali and alkaline earth metal cations has some similarity with biological systems but they can also function in organic media.

In this chapter the preparation of composites by the entrapment within crown ether-functionalised poly[Ni(*salen*)] films of multi-walled carbon nanotubes (MWCNTs) is reported. The aim of this study is to enhance the intrinsic characteristics of the single component poly[Ni(*salen*)] films by the insertion of MWCNTs into the polymeric matrix.

The strategy for accomplishing this (Figure 7.1) is the prior dispersion of the carbon nanotubes in the electropolymerisation solution, with the expectation that they will become physically entrapped within the depositing polymeric matrix. Since adequate dispersion of the carbon nanotubes is critical, two variables are explored: (i) functionalisation of the MWCNTs with different surface groups and (ii) variation of the organic solvent.

In previous chapters the correlation of performance with structure for single component poly[Ni(3-Mesalophen-b15-c5)] films was accomplished; here, the electrochemical performance of the composite film is assessed via cyclic voltammetry and electrochemical impedance, and rationalised in terms of structure (SEM analysis).

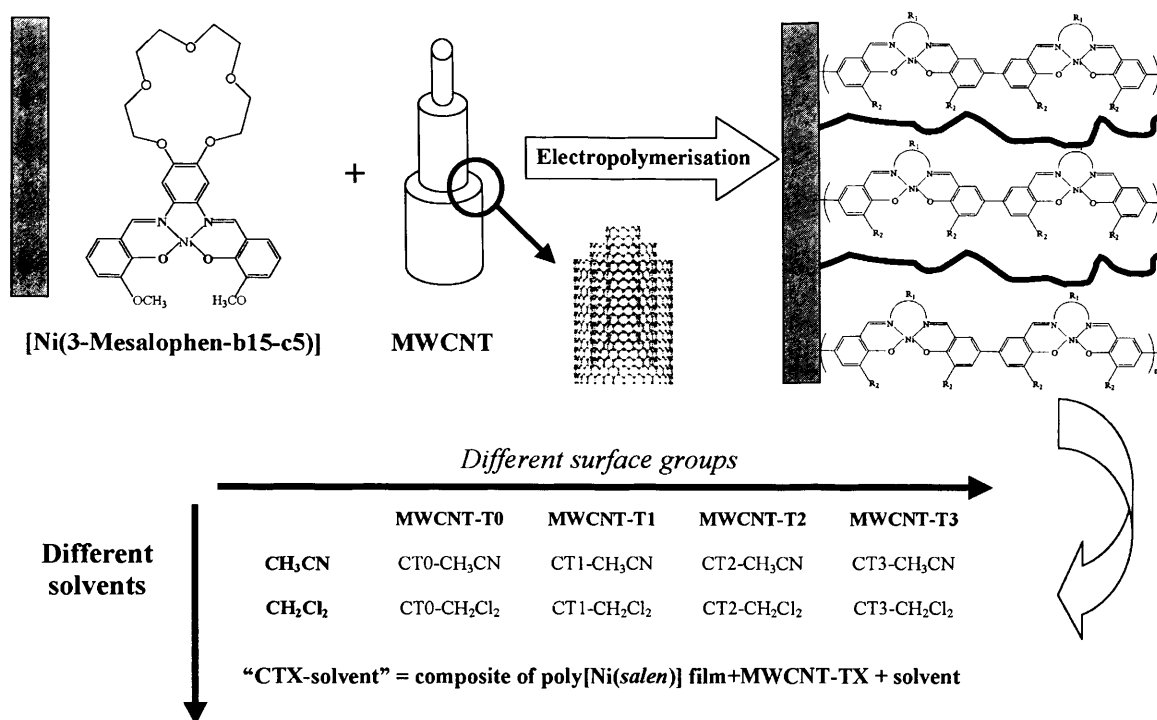


**Figure 7.1:** Schematic view of entrapment of MWCNTs<sup>35</sup> within the poly[Ni(3-Mesalophen-b15-c5)] matrix during the polymerisation step and nomenclature used to describe composite/solvent systems. The detailed description of MWCNTs functionalisation is presented in Chapter 3.

## 7.2 PREPARATION AND CHARACTERISATION OF COMPOSITES BASED ON POLY[Ni(3-MESALOPHEN-B15-C5)] AND MULTI-WALLED CARBON NANOTUBES

### 7.2.1 Functionalisation of carbon nanotubes

The functionalisation of nanotubes was performed by colleagues at the Department of Chemical Engineering, Faculty of Engineering, University of Porto, Portugal<sup>36</sup>.

The characterisation results of the MWCNTs are shown in [Table 7.1](#). The MWCNTs tested present BET surface areas between 196 and 260 m<sup>2</sup> g<sup>-1</sup>. The HNO<sub>3</sub> oxidation treatment (T1) has a small effect on the surface area of MWCNTs (an increase of 9%), while O<sub>2</sub> oxidation (T2) results in an increase of about 33%. The increase in the surface area of MWCNT-T2 can be explained by the opening of MWCNT tips by gasification with oxygen, which makes the internal surface accessible<sup>37</sup>. The BET surface area of sample MWCNT-T3 was not determined, but it is expected to be similar to the original sample MWCNT-T1.

**Table 7.1:** Textural properties of MWCNTs.

Sample	CO <sub>2</sub> <sup>a</sup> (μmol g <sup>-1</sup> )	CO <sup>a</sup> (μmol g <sup>-1</sup> )	CO/CO <sub>2</sub>	S <sub>BET</sub> <sup>b</sup> (m <sup>2</sup> g <sup>-1</sup> )
MWCNT-T0	25	113	4.5	196
MWCNT-T1	693	1106	1.6	215
MWCNT-T2	80	928	11.6	260
MWCNT-T3	150	892	6.0	n.d.

<sup>a</sup> Determined by TPD-MS. <sup>b</sup> From N<sub>2</sub> adsorption at 77 K

The different surface oxygenated groups created on carbon materials upon oxidising treatments decompose through heating, releasing CO and/or CO<sub>2</sub> at characteristic temperatures<sup>38</sup>; in CNTs the oxygenated groups are formed at the edges/ends and defects of graphitic sheets<sup>39</sup>. The total amounts of CO and CO<sub>2</sub> evolved from the MWCNTs were

obtained by integration of the TPD spectra and are also presented in [Table 7.1](#). Comparing the TPD spectra (not shown here) and the amounts of CO and CO<sub>2</sub> released by samples MWCNT-T0 and MWCNT-T1, it is clear that the treatment with HNO<sub>3</sub> (T1) produces a large amount of acidic oxygen groups (carboxylic acids, anhydrides and lactones), which decompose to release CO<sub>2</sub>. The thermally treated sample MWCNT-T3 shows a different spectrum compared to the starting MWCNT-T1. The CO<sub>2</sub> releasing groups at low temperatures (carboxylic acid groups) were almost completely eliminated while only a small amount of the more stable CO releasing groups (phenol and carbonyl groups) were removed. The treatment with oxygen (MWCNT-T2) mainly increases the CO releasing groups. The ratio CO/CO<sub>2</sub> increases significantly after the gas-phase treatments (MWCNT-T2 and MWCNT-T3), and decreases after the liquid-phase treatment (MWCNT-T1) indicating the higher acidity of this sample.

The presence of surface oxygenated groups in CNTs alters the hydrophobic/hydrophilic properties of the materials, allowing for a more facile solubilisation or dispersion in more hydrophilic media, at the cost of partial destruction of the intrinsic nanotube structure and  $\pi$ -conjugation<sup>39</sup>. In this context, it is expected that untreated MWCNTs will be more easily dispersed in the more hydrophobic solvent, CH<sub>2</sub>Cl<sub>2</sub>, and will retain to a greater extent their intrinsic electronic structure. This is a significant feature, since an increase in the population of oxygenated groups (whose formation is associated with local disruption of the  $\pi$ -conjugation) will lead to lower MWCNT conductivity.

### **7.2.2 Preparation and characterisation of composites by cyclic voltammetry**

The single component poly[Ni(3-Mesalophen-b15-c5)] films were prepared using the conditions described in Chapter 4, except in these studies films were prepared using either CH<sub>3</sub>CN or CH<sub>2</sub>Cl<sub>2</sub> as solvent and the scan rate was 0.005 V s<sup>-1</sup>. In the preparation of composites, the deposition solution also contained 0.02 % wt of MWCNTs-TX.

The polymerisation process of [Ni(3-Mesalophen-b15-c5)] in 0.1 mol dm<sup>-3</sup> TBAP/CH<sub>3</sub>CN, at a scan rate of 0.1 V s<sup>-1</sup>, was described in detail in Chapter 4. For a scan rate of 0.005 V s<sup>-1</sup>, there are some minor variations ([Table 7.2](#)): the first deposition anodic half-cycle shows two anodic waves (at 0.89 V and 1.08 V) and the reverse half-cycle two

well-resolved cathodic waves (at 0.81 V and 0.10 V), of which the latter is attributed to the reduction of polymer deposited in the anodic half-cycle. Continued deposition generates two additional broad, anodic waves (at 0.19 V and 0.42 V) corresponding to the oxidation of polymer deposited in the previous anodic half-scan. Subsequent cycles result in continued growth of the features assigned to deposited film and a positive displacement of the monomer oxidation peak. In dichloromethane solution (Table 7.3), the general picture is very similar, although the most positive current peak occurs at less positive potentials than in acetonitrile. Additionally, the increase with potential cycling in the heights of the peaks in the regions of 0.2 V and 0.4 V (relative to those in the regions of 0.9 V and 1.1 V) takes place faster in dichloromethane than in acetonitrile.

The voltammetric responses acquired during the polymerisation process of the composites (involving variously treated MWCNTs) are qualitatively very similar to that of the single component polymer film in the same solvent (Figures 7.2 and Figure 7.3). The primary difference in  $i$ - $E$  response resulting from the inclusion of carbon nanotubes (for otherwise identical deposition conditions) is a decrease in film redox charge,  $Q_{pol}$ . This could in principle be a consequence of (i) decreased deposition rate or (ii) incomplete electrochemical addressing of the same population of surface-immobilised sites, *i.e.* a film charge transport limitation. It is unlikely that the conducting nanotubes inhibit film electron transport in any way. The implication is that they have a minor inhibitory effect on film deposition; it is not possible to distinguish between a solution mass transport effect and a surface packing / adhesion effect, but the latter seems quite likely.

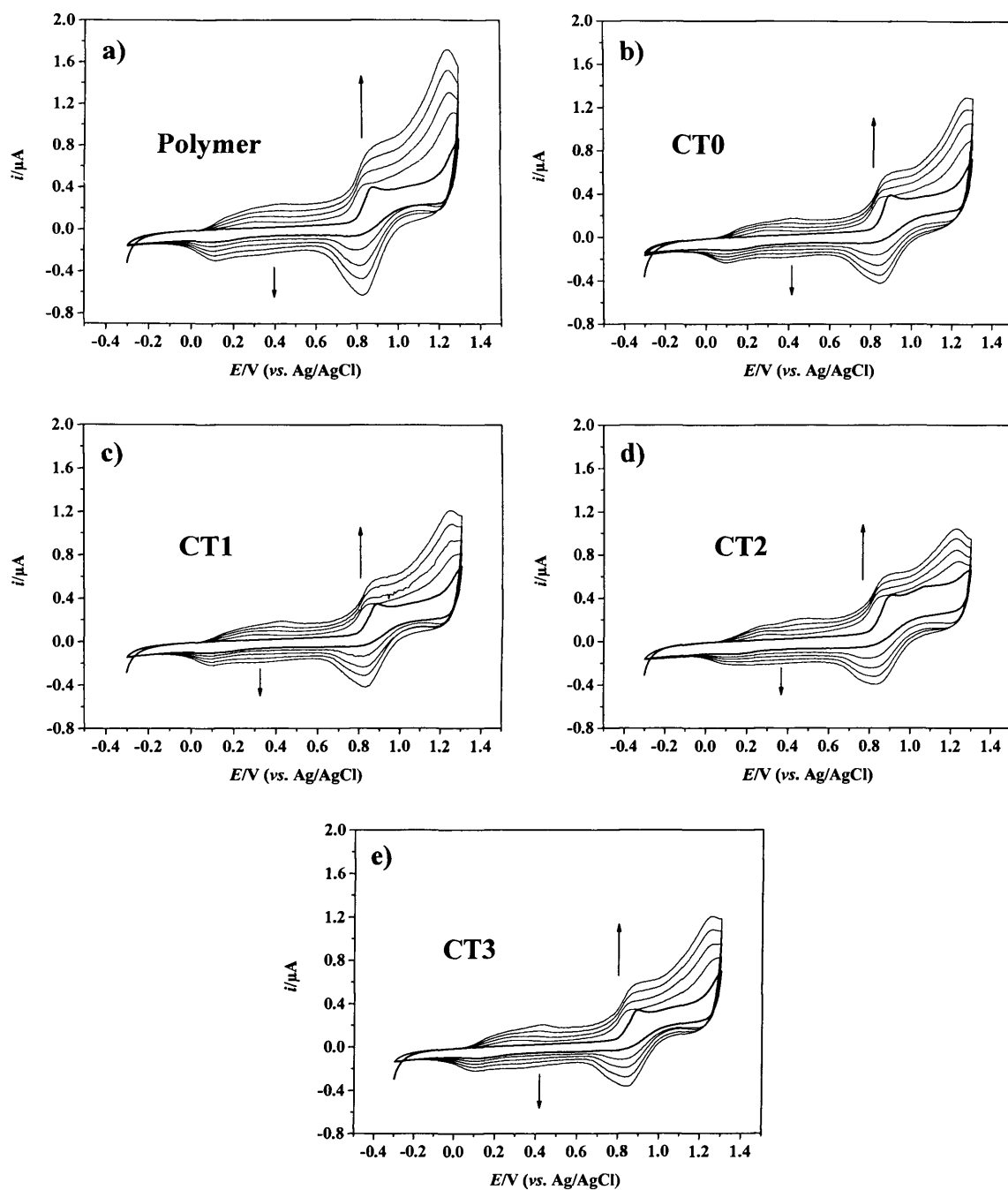


**Figure 7.2:** Cyclic voltammograms acquired during polymerisation of  $[\text{Ni}(\text{3-Mesalophen-b15-c5})]$  in  $0.1 \text{ mol dm}^{-3} \text{ TBAP/CH}_3\text{CN}$  at  $0.005 \text{ V s}^{-1}$ . Arrows indicate the increase of current intensity with progressive cycling.

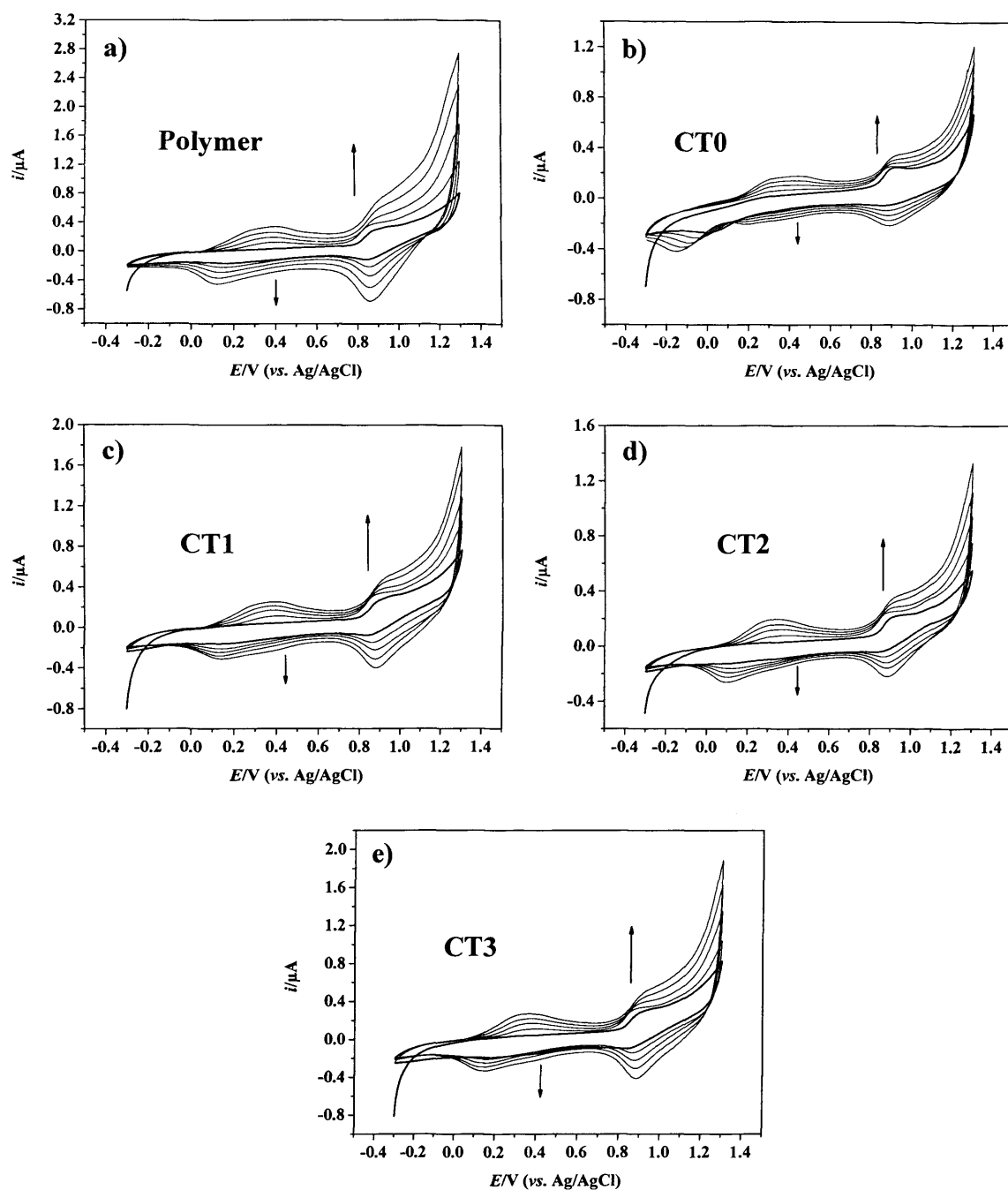


**Figure 7.3:** Cyclic voltammograms of polymerisation of  $[\text{Ni}(\text{3-Mesalophen-b15-c5})]$  in  $0.1 \text{ mol dm}^{-3}$  TBAP/ $\text{CH}_2\text{Cl}_2$  at  $0.005 \text{ V s}^{-1}$ . Arrows indicate the increase of current intensity with progressive cycling.

**Table 7.2:** Summary of voltammetric responses (peak potentials) in CH<sub>3</sub>CN during polymer / composite electrodeposition as a function of MWCNT pre-treatment.

E/V vs. Ag/AgCl (0.1 mmol dm <sup>-3</sup> monomer/0.1 mol dm <sup>-3</sup> TBAP/CH <sub>3</sub> CN)					
		E <sub>pa</sub> /E <sub>pc</sub>			
Film	1 <sup>st</sup> cycle	-/0.10	-/-	0.89/0.81	1.08/-
	5 <sup>th</sup> cycle	0.19/0.12	0.42/0.32	0.90/0.83	1.25/-
CT0	1 <sup>st</sup> cycle	-/0.11	-/-	0.90/0.81	1.07/-
	5 <sup>th</sup> cycle	0.20/0.10	0.42/0.34	0.88/0.85	1.26/-
CT1	1 <sup>st</sup> cycle	-/0.09	-/-	0.89/0.79	1.06/-
	5 <sup>th</sup> cycle	0.19/0.10	0.43/0.33	0.88/0.83	1.25/-
CT2	1 <sup>st</sup> cycle	-/0.10	-/-	0.91/0.79	1.08/-
	5 <sup>th</sup> cycle	0.26/0.20	0.50/-	0.88/0.82	1.23/-
CT3	1 <sup>st</sup> cycle	-/0.12	-/-	0.89/0.81	1.06/-
	5 <sup>th</sup> cycle	0.18/0.10	0.42/0.32	0.89/0.84	1.25/-

**Table 7.3:** Summary of voltammetric responses (peak potentials) in CH<sub>2</sub>Cl<sub>2</sub> during polymer / composite electrodeposition as a function of MWCNT pre-treatment.

E/V vs. Ag/AgCl (0.1 mmol dm <sup>-3</sup> monomer/0.1 mol dm <sup>-3</sup> TBAP/CH <sub>2</sub> Cl <sub>2</sub> )					
		E <sub>pa</sub> /E <sub>pc</sub>			
Film	1 <sup>st</sup> cycle	-/0.17	-/-	0.89/0.85	0.97/-
	5 <sup>th</sup> cycle	0.27/0.12	0.41/-	0.92/0.86	-/-
CT0	1 <sup>st</sup> cycle	-/0.01	-/-	0.91/0.87	-/-
	5 <sup>th</sup> cycle	0.30/-0.15	0.47/0.19	0.92/0.88	-/-
CT1	1 <sup>st</sup> cycle	-/0.12	-/-	0.91/0.84	-/-
	5 <sup>th</sup> cycle	0.39/0.15	-/-	0.93/0.88	-/-
CT2	1 <sup>st</sup> cycle	-/0.09	-/-	0.93/0.89	-/-
	5 <sup>th</sup> cycle	0.34/0.11	-/-	0.92/0.89	-/-
CT3	1 <sup>st</sup> cycle	-/0.14	-/-	0.94/0.84	-/-
	5 <sup>th</sup> cycle	0.36/0.14	-/-	0.94/0.89	-/-



Following deposition, the composite-coated electrodes were transferred to monomer- and MWCNT-free background electrolyte for the study of the electrochemical response (Figure 7.4, Figure 7.5). The general pattern was of four chemically reversible redox processes (summarised in Tables 7.4, 7.5), although the most positive feature was not always resolved in  $\text{CH}_2\text{Cl}_2$  solution.

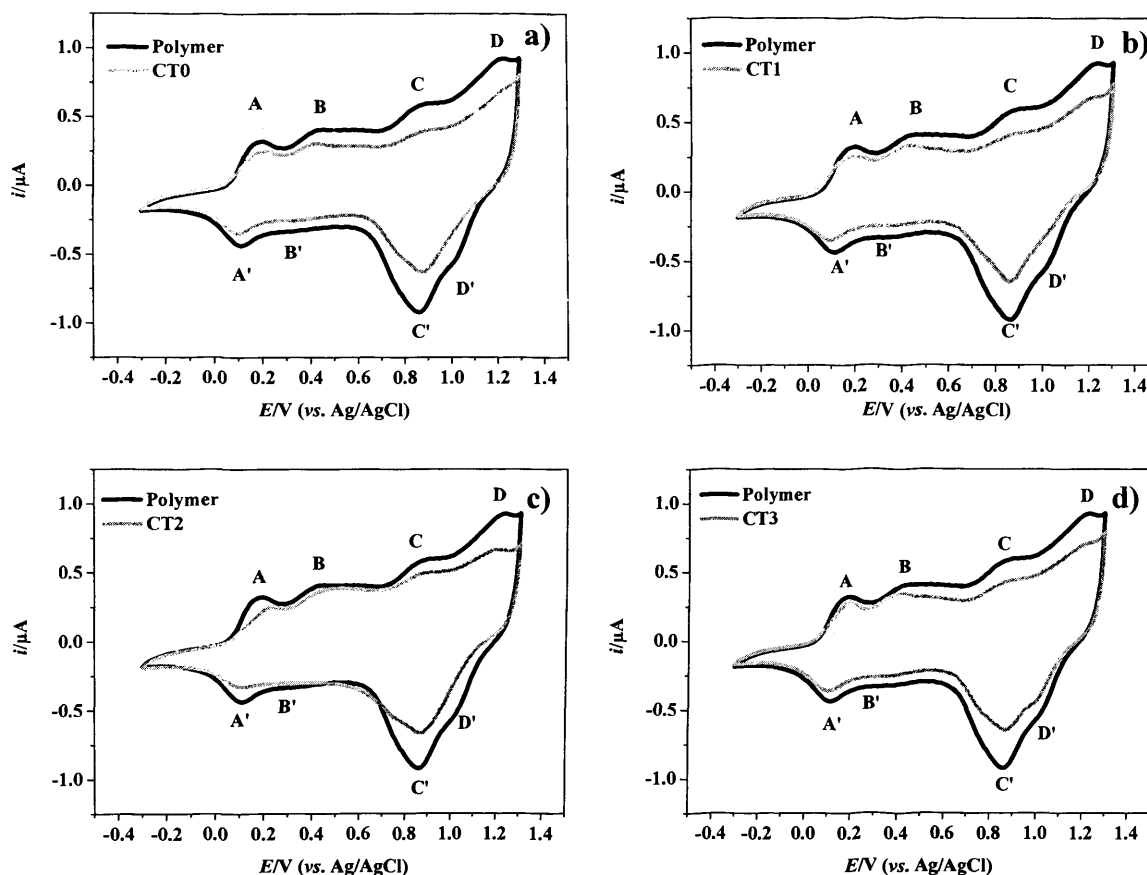


**Figure 7.4:** Redox switching of the composite-modified electrodes of Figure 7.2 in  $0.1 \text{ mol dm}^{-3}$  TBAP/ $\text{CH}_3\text{CN}$  at  $0.01 \text{ V s}^{-1}$ .

Turning to the effect of MWCNT pre-treatment (comparing composites prepared in the same solvent), this has generally very little effect on the polymer redox processes. The exceptions to this were MWCNT-T0 and MWCNT-T2 composites in  $\text{CH}_2\text{Cl}_2$ , for which the polymer redox peaks were more symmetrical and displaced to less positive potentials. This is attributed to the fact that composites containing MWCNTs with lower oxygen content will have greater  $\pi$ -conjugation. These MWCNTs can act synergistically with the polymer via  $\pi$ - $\pi$  interactions, thereby facilitating oxidation, *i.e.* lowering the redox potential. This type of effect in polypyrrole/nanotube composites exposed to aqueous

medium has been attributed to the decrease in resistance (and then of ohmic potential) within the film caused by the carbon nanotubes, with the result that oxidation of the reduced (insulating) polypyrrole is facilitated<sup>16,20</sup>. Data presented in the following sections suggest that the amounts of carbon nanotubes within the composites prepared here are likely to be considerably lower than in the polypyrrole case.

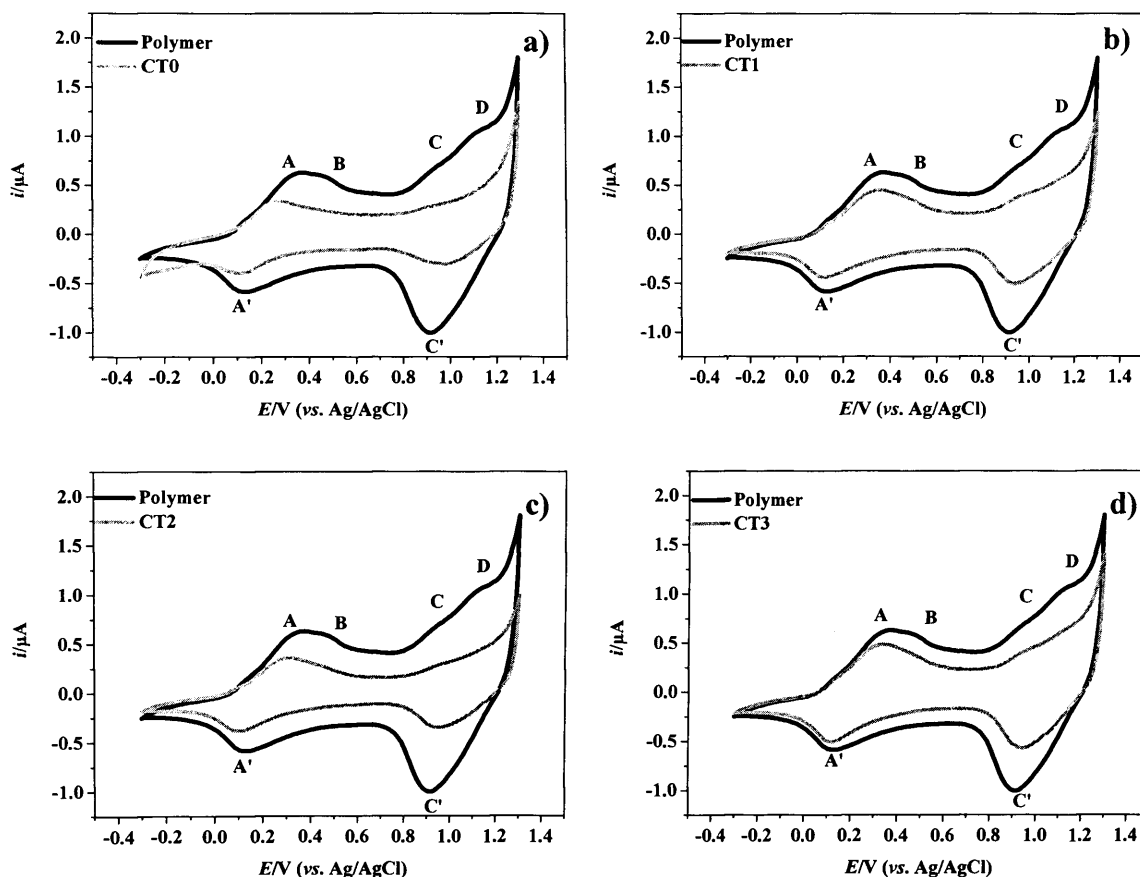


**Figure 7.5:** Redox switching of the composite-modified electrodes of [Figure 7.3](#) in 0.1 mol dm<sup>-3</sup> TBAP/CH<sub>2</sub>Cl<sub>2</sub> at 0.01 V s<sup>-1</sup>.

Inclusion of carbon nanotubes in the deposition medium decreases the amount of poly[Ni(*salen*)] deposited on the working electrode: coulometric assay of the films in background electrolyte shows the surface coverage of electroactive sites ( $\Gamma$ ) decreases by a factor of 1.5 in CH<sub>3</sub>CN and of 2.2 in CH<sub>2</sub>Cl<sub>2</sub> ([Table 7.6](#)).

**Table 7.4:** Summary of voltammetric responses (peak potentials) of modified electrodes in background electrolyte shown in Figure 7.4; solvent system as for deposition ( $\text{CH}_3\text{CN}$ , Figure 7.2).

<b>E/V vs. Ag/AgCl (<math>0.1 \text{ mol dm}^{-3} \text{ TBAP/CH}_3\text{CN}</math>)</b>				
<b>Redox processes</b>	<b><math>E_{\text{paI}}/E_{\text{pcI}}</math></b>	<b><math>E_{\text{paII}}/E_{\text{pcII}}</math></b>	<b><math>E_{\text{paIII}}/E_{\text{pcIII}}</math></b>	<b><math>E_{\text{paIV}}/E_{\text{pcIV}}</math></b>
Polymer	0.19/0.11	0.44/0.32	0.89/0.86	1.23/1.03
MWCNT-T0	0.20/0.09	0.42/0.31	0.89/0.88	1.23 /-
MWCNT-T1	0.19/0.09	0.42/0.30	0.88/0.86	1.22/-
MWCNT-T2	0.23/0.11	0.48/0.33	0.89/0.87	1.21/-
MWCNT-T3	0.20/0.10	0.42/0.32	0.89/0.87	1.22/1.00

**Table 7.5:** Summary of voltammetric responses (peak potentials) of modified electrodes in background electrolyte shown in Figure 7.5; solvent system as for deposition ( $\text{CH}_2\text{Cl}_2$ , Figure 7.3).

<b>E/V vs. Ag/AgCl (<math>0.1 \text{ mol dm}^{-3} \text{ TBAP/CH}_2\text{Cl}_2</math>)</b>				
<b>Redox processes</b>	<b><math>E_{\text{paI}}/E_{\text{pcI}}</math></b>	<b><math>E_{\text{paII}}/E_{\text{pcII}}</math></b>	<b><math>E_{\text{paIII}}/E_{\text{pcIII}}</math></b>	<b><math>E_{\text{paIV}}/E_{\text{pcIV}}</math></b>
Polymer	0.35/0.13	0.47/-	0.94/0.92	1.14/-
MWCNT-T0	0.27/0.12	-	0.91/0.94	-
MWCNT-T1	0.35/0.12	0.46/-	0.97/0.95	-
MWCNT-T2	0.31/0.10	0.44/-	0.95/0.96	-
MWCNT-T3	0.34/0.12	0.46/-	0.96/0.94	1.14/-

**Table 7.6:** Electroactive coverage of the composite-modified electrodes, expressed in terms of Ni-complex monomer units. Data in columns 3 and 4 refer to different films prepared and characterised in a single solvent.

Material	Sample	$\Gamma(\text{CH}_3\text{CN})/\text{nmol cm}^{-2}$	$\Gamma(\text{CH}_2\text{Cl}_2)/\text{nmol cm}^{-2}$
Film	A	45.9	51.6
	B	44.5	51.6
CT0	A	28.0	15.5
	B	27.5	25.1
CT1	A	31.5	28.9
	B	28.9	26.7
CT2	A	26.9	19.5
	B	31.1	19.4
CT3	A	28.9	30.2
	B	29.8	30.6

### 7.2.3 Characterisation of the composites by electrochemical impedance spectroscopy

To evaluate the variations in electrical response with the presence and pre-treatment of carbon nanotubes and with solvent medium, impedance spectra were recorded for all composites immersed in both solvents. These measurements were replicated with the polymer component in different oxidation states (doping levels): fully reduced ( $E = -0.3$  V), fully oxidised ( $E = 1.3$  V) and at two partially oxidised states ( $E = 0.2$  V and  $E = 0.9$  V). [Figure 7.6](#) and [Figure 7.7](#) show Nyquist diagrams for the single component film and composites, MWCNT-TX, in each case immersed in  $0.1 \text{ mol dm}^{-3}$  TBAP/ $\text{CH}_3\text{CN}$  and in  $0.1 \text{ mol dm}^{-3}$  TBAP/ $\text{CH}_2\text{Cl}_2$ , respectively. As these figures show, there are qualitative differences in impedance spectra according to the applied potential but qualitative similarities as the solvent and composite constituents are varied. In the latter instances, the differences are at a quantitative level, the details of which are now pursued. The qualitative shapes seen in the  $Z'-Z''$  plane are semi-circles, linear regimes of slope close to unity, and linear regimes of slope much greater than unity; where all three are seen, this progression represents increasing timescale (decreasing AC frequency).

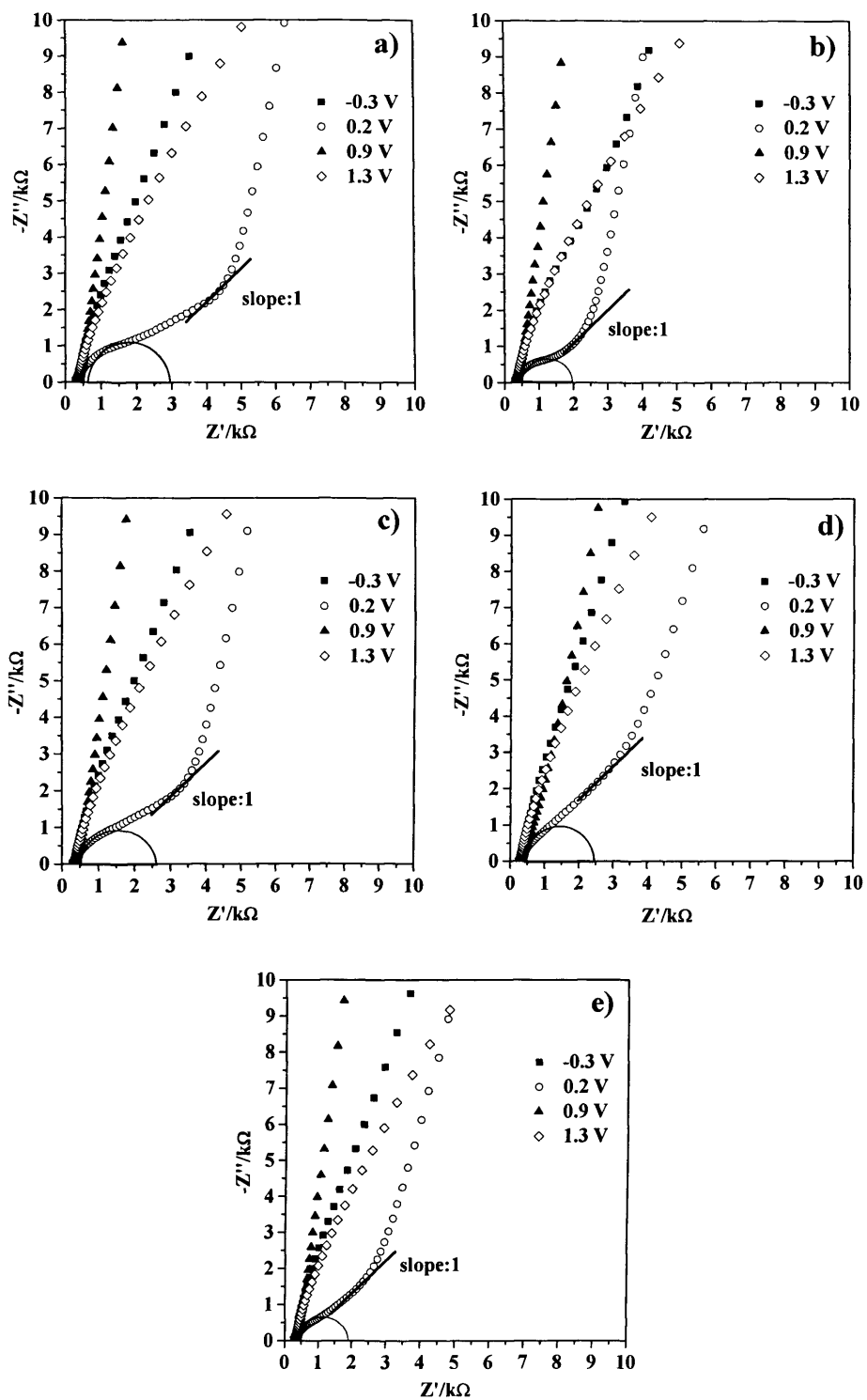


**Figure 7.6:** Nyquist representations obtained for a) polymer, b) MWCNT-T0, c) MWCNT-T1, d) MWCNT-T2 and e) MWCNT-T3 in  $0.1 \text{ mol dm}^{-3}$  TBAP/ $\text{CH}_3\text{CN}$ . Lines of unit slope are provided as a guide to the eye.

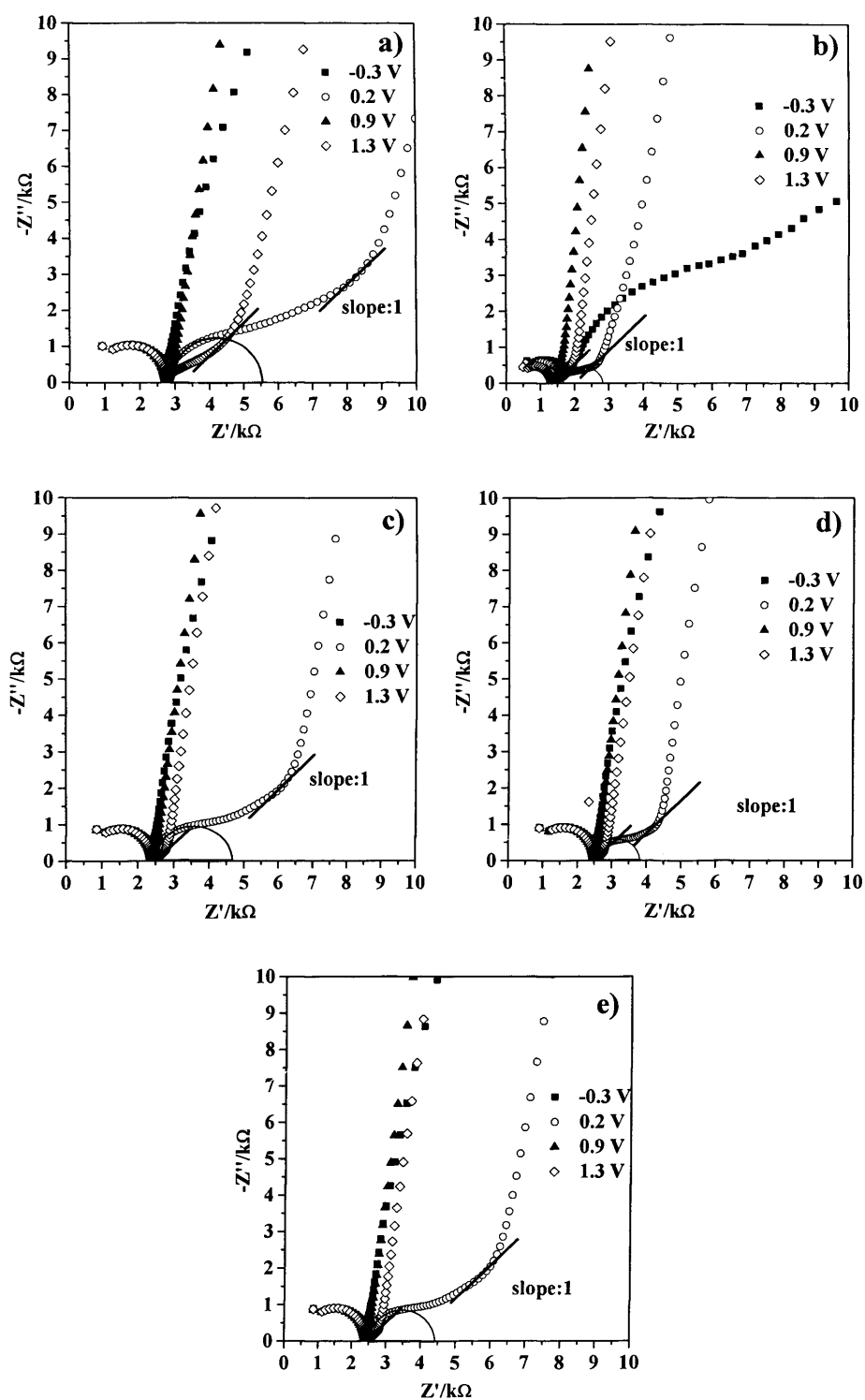


**Figure 7.7:** Nyquist representations obtained for a) polymer, b) MWCNT-T0, c) MWCNT-T1, d) MWCNT-T2 and e) MWCNT-T3 in  $0.1 \text{ mol dm}^{-3}$  TBAP/ $\text{CH}_2\text{Cl}_2$ . Lines of unit slope are provided as a guide to the eye.

The impedance data were interpreted using a similar procedure to that developed by Ferloni and colleagues<sup>40</sup> for polypyrrole and poly(3-methylthiophene) films. The electrical equivalent circuit model employed and the physical significance of the components are shown in Figure 7.8. As the imposed conditions (solvent, frequency, applied DC potential) are systematically varied, different processes control the response, which is here modelled by the dominance of different components in the electrical equivalent circuit. This approach is diagnostically implemented by visual inspection of the characteristics of the Nyquist plot, rationalised in terms of known changes in physical characteristics of the system.

### General Model

### Limiting Cases

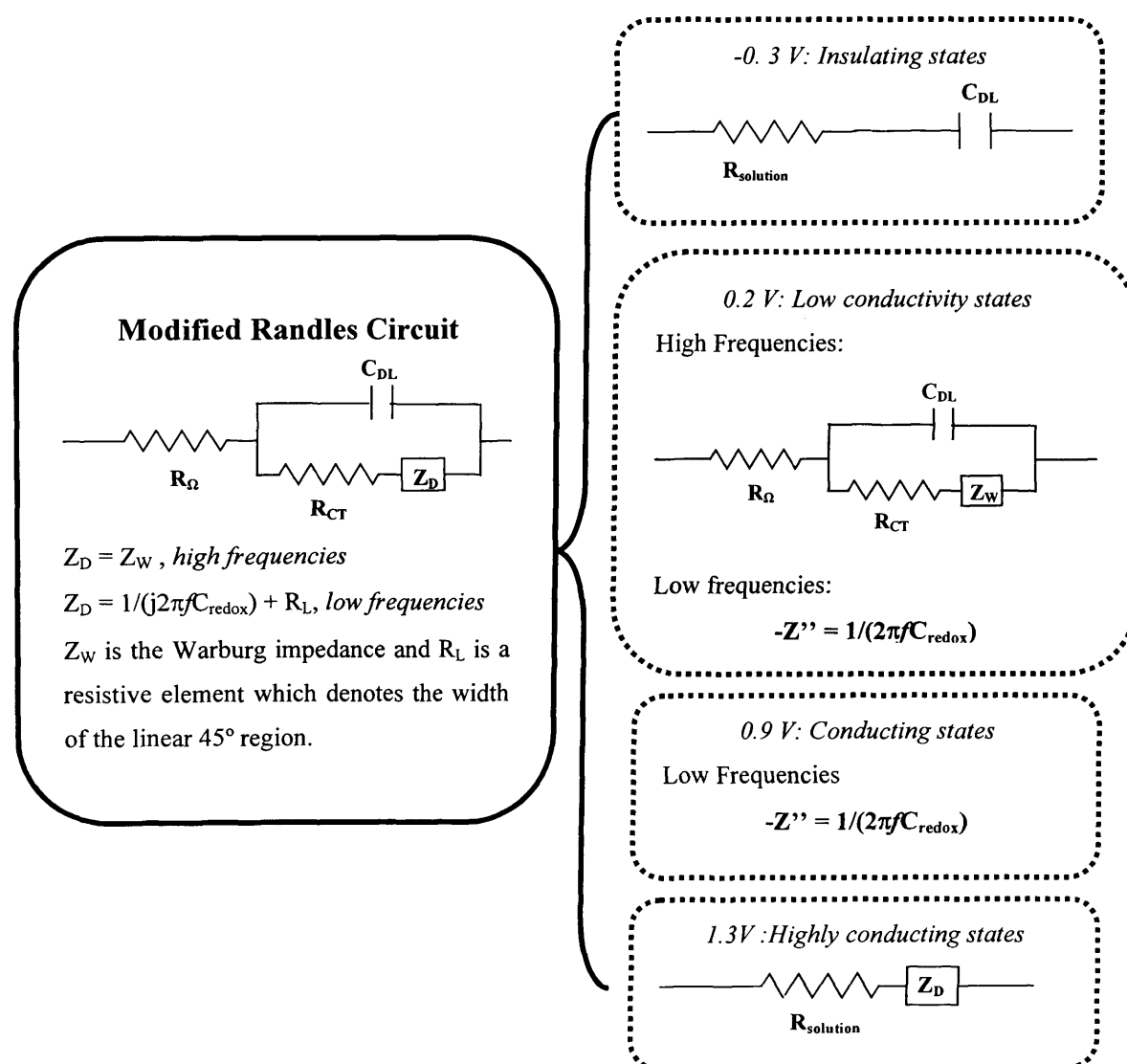


**Figure 7.8:** Modified Randles circuit and limiting cases.

At  $-0.3$  V the film/composite is fully reduced, behaving like an insulator. In this case, the system is represented by a resistance ( $R_{solution}$ ) in series with a parallel combination of a capacitor ( $C_{DL}$ ) and the film resistance ( $R_{film}$ ).  $R_{solution}$  is the ohmic resistance of the solution and  $C_{DL}$  is associated with the composite/solution interface. Since, at these potentials, the polymer is insulating,  $R_{film}$  is relatively large and this branch of the network is not active.

At  $0.2$  V, redox processes start to occur and charge flows through the film. The equivalent circuit for this doping state is the modified Randles circuit<sup>41</sup>. In this case,  $R_{film}$  is attributed primarily to the charge transfer resistance ( $R_{CT}$ ). An extra element  $Z_D$  based on the Warburg element<sup>42</sup> represents film mass transport, and is recognisable via a corresponding  $45^\circ$  slope in the Nyquist plot (Figures 7.6, 7.7). Additionally, at low frequencies it is possible to estimate the faradaic (redox) pseudocapacitance,  $C_{redox}$ , which is associated with the capacitive behaviour of a (dis)charging film. The physical origin of  $C_{redox}$  means that its magnitude increases with the quantity of electroactive material deposited,  $\Gamma / \text{nmol cm}^{-2}$ .

At more positive potentials, the polymer component is in a conducting state with negligible charge transfer resistance. Here, current flows primarily through the film branch of the network. Thus, at  $0.9$  V, only  $C_{redox}$  can be determined. The major difference between the composites in  $\text{CH}_3\text{CN}$  and  $\text{CH}_2\text{Cl}_2$  occurs at  $1.3$  V. The electrical response in  $\text{CH}_2\text{Cl}_2$  is controlled by mass transport ( $45^\circ$  slope in the Nyquist plot in Figure 7.7), whereas in  $\text{CH}_3\text{CN}$  the conducting properties are controlled by charge carrier concentration inside the film (only a near-vertical line is observed in the Nyquist plot in Figure 7.6 panel a). In  $\text{CH}_3\text{CN}$ , the mass transport is faster than in  $\text{CH}_2\text{Cl}_2$  and the impedance becomes purely capacitive in the low frequency range.

Following the assignment of dominant element circuits at different potentials, quantification of equivalent circuit element values is presented. Three parameters were chosen for this purpose: the charge-transfer resistance  $R_{CT}$  (a significant element at  $E = 0.2$  V), the double-layer capacitance  $C_{DL}$  (a significant element at  $E = -0.3$  V and  $E = 0.2$  V) and the faradaic capacitance  $C_{redox}$  (a significant element at  $E = 0.2$  V and  $E = 0.9$  V).

Figure 7.9 summarises the  $R_{CT}$  values (at  $E = 0.2$  V). For all composites prepared in  $\text{CH}_3\text{CN}$ , the charge transfer resistance values are decreased by the inclusion of nanotubes, although the effect is really only significant for MWCNT-T3. In  $\text{CH}_2\text{Cl}_2$ , the charge



transfer resistance varies significantly; although there is no obvious pattern with MWCNTs pre-treatment, the decrease by 50% on inclusion of untreated CNTs (MWCNT-T0) is quite dramatic. Viewed as a whole, the data show that, with the single exception of MWCNT-T3 in  $\text{CH}_2\text{Cl}_2$ , the incorporation of carbon nanotubes within the polymeric matrix improves performance by decreasing  $R_{\text{CT}}$ . A similar conclusion was reached for the somewhat different case of polypyrrole / MWCNT composites in water<sup>16</sup>.

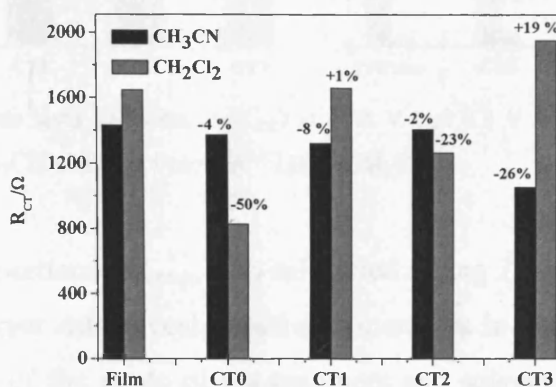


**Figure 7.9:** Estimate of charge transfer resistance ( $R_{\text{CT}}$ ) at 0.2 V (average of duplicate determinations). Annotated percentage figures indicate variation of value for composite from corresponding pure polymer value.

The double layer capacitance  $C_{\text{DL}}$ , was calculated from the responses at -0.3 V and 0.2 V, where most of the electroactive polymer sites are reduced (Figure 7.10). Since  $C_{\text{DL}}$  depends on the area of the polymer/solution interface, which is in turn the consequence of composite morphology, the idea is to explore the validity of this concept by direct SEM observation of morphology (next sections). In  $\text{CH}_3\text{CN}$  (panel a), the inclusion of MWCNTs (with or without pre-treatment) increases  $C_{\text{DL}}$  marginally at both potentials. However, this effect is secondary to the difference in  $C_{\text{DL}}$  with potential. In  $\text{CH}_2\text{Cl}_2$  (panel b) the picture is essentially the same as at  $E = 0.2$  V. The striking result in  $\text{CH}_2\text{Cl}_2$  is that at  $E = -0.3$  V, where  $C_{\text{DL}}$  for CT0 is *ca.* 4 times higher than for the other composites in  $\text{CH}_2\text{Cl}_2$  and all composites (including MWCNT-T0) in  $\text{CH}_3\text{CN}$ ; the extent of increase was variable, but at least a factor of 2. It is also worth noting that the high value cannot be the result of a redox-based contribution, since the latter would be larger at 0.2 V than at -0.3 V, which is not the observed fact.

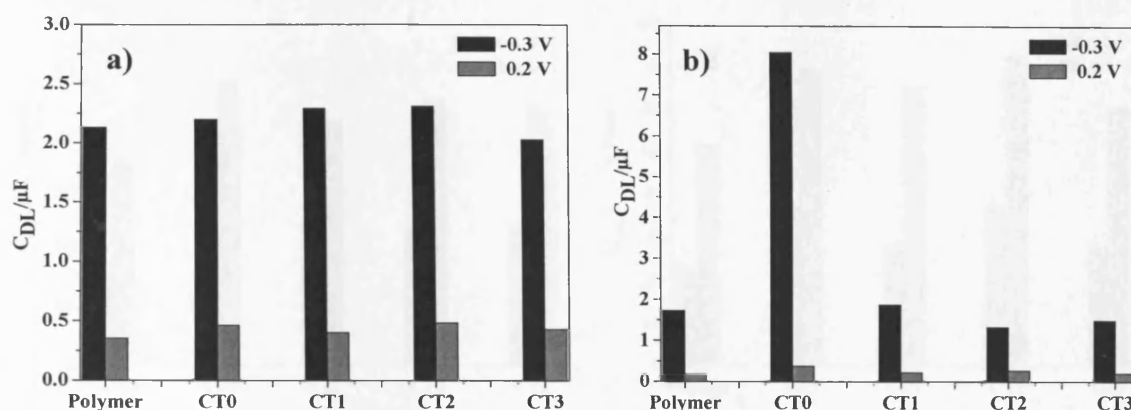


**Figure 7.10:** Double layer capacitance ( $C_{DL}$ ) at  $-0.3$  V and  $0.2$  V for polymers and composites in a)  $0.1 \text{ mol dm}^{-3}$  TBAP/ $\text{CH}_3\text{CN}$  and b)  $0.1 \text{ mol dm}^{-3}$  TBAP/ $\text{CH}_2\text{Cl}_2$ .

The faradaic capacitance  $C_{redox}$ , was calculated (using  $Z'' \rightarrow 1/\omega C_{redox}$ , as  $\omega \rightarrow 0$ ) at  $0.2$  and  $0.9$  V. The raw data reveal significant increases in  $C_{redox}$  upon the inclusion of nanotubes, regardless of the mode of pre-treatment and solvent. Nonetheless, since this parameter reflects the ability of the polymer redox sites to store charge, it is only meaningful to compare values that are normalised for the amount of polymer deposited on the working electrode, as represented by the electroactive surface coverage,  $\Gamma$ . The outcomes of this normalisation,  $C_{redox}/\Gamma$ , are presented in [Figure 7.11](#).

As an order of magnitude check, the data of [Figure 7.11](#) (which result from fitting a set of frequency-dependent responses) are compared with the single-point estimate resulting from a voltammetric  $i$ - $E$  curve ([Figure 7.4](#)). Functionally, the time derivative of the definition  $Q = CE$  is  $i = C_{redox}v$  (where  $v = dE/dt$ ). For a representative voltammogram ([Figure 7.4](#)),  $i \approx 0.4 \text{ } \mu\text{A}$  at  $v = 0.01 \text{ V s}^{-1}$ , so  $C_{redox} \approx 40 \text{ } \mu\text{F}$  (*i.e.*  $1.3 \text{ mF cm}^{-2}$  for an electrode area of  $0.0314 \text{ cm}^2$ ). Given that  $\Gamma = 30 \text{ nmol cm}^{-2}$ ,  $C_{redox}/\Gamma \approx 42 \text{ kF mol}^{-1}$ , which is broadly consistent with [Figure 7.11](#), giving confidence in the interpretational model. The enhanced capacitance observed for the composites may be a consequence of the increased interfacial area, rather than the intrinsic capacitance of the nanotubes<sup>19,40</sup>.

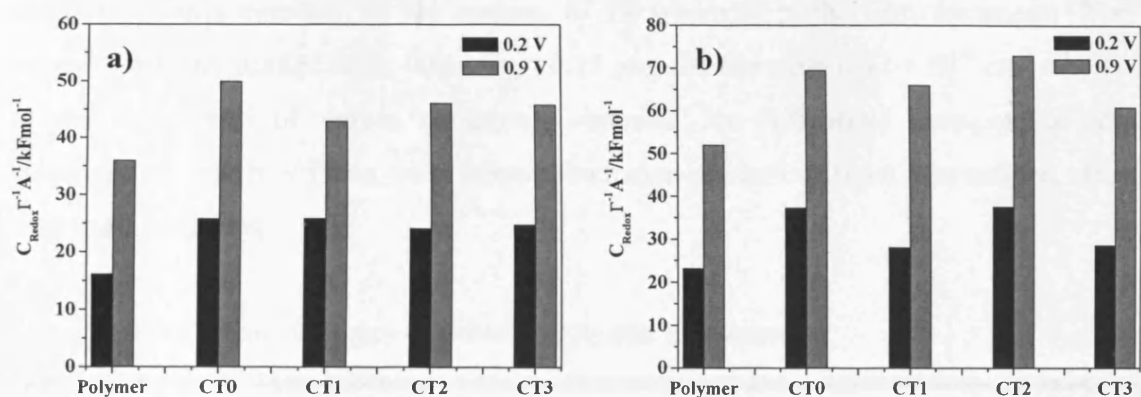


**Figure 7.11:** Faradaic capacitance ( $C_{redox}$ ) estimated at 0.2 V and 0.9 V for polymers and composites in **a)** 0.1 mol dm<sup>-3</sup> TBAP/CH<sub>3</sub>CN and **b)** 0.1 mol dm<sup>-3</sup> TBAP/CH<sub>2</sub>Cl<sub>2</sub>. Values are normalised by the polymer coverage,  $\Gamma$ , and geometric area of the electrode.

As the frequency is progressively decreased, the response of the system will ultimately switch from one characteristic of a diffusionally controlled response to one characteristic of complete charging/discharging of the film charge sites. The former is represented as a 45° line in the Nyquist plot ( $Z_D$ ) and the latter as a vertical line ( $C_{redox}$ ). The transition point between these two regions is referred to by some authors as a ‘knee’ in the Nyquist plot. The frequency associated with this transition is a measure of the electrical and ionic conductivities<sup>19</sup> and can thus be used to assess changes in these parameters, here as a consequence of the inclusion of nanotubes into the system. Specifically, a higher value of the ‘knee’ frequency is a consequence of the system being able to accomplish complete (dis)charge of the redox sites on a shorter timescale, *i.e.* charge transport is faster.

Inspection of the responses of [Figure 7.6, 7.7](#) shows that the inclusion of the carbon nanotubes – irrespective of pre-treatment - increases the ‘knee’ frequency, signalling an increase in the overall charge transport rate ([Table 7.7](#)). In CH<sub>3</sub>CN at an applied potential of 0.2 V, the increase is *ca.* 60%, with relatively little variation with nanotube pre-treatment. In CH<sub>2</sub>Cl<sub>2</sub> at an applied potential of 0.2 V, the increase varies significantly with MWCNT pre-treatment, from a rather modest 25% (CT3) to a factor of *ca.* 5 (CT0); the latter case is the one identified above as the best performance in terms of composite resistance. The data obtained in CH<sub>2</sub>Cl<sub>2</sub> at  $E = 1.3$  V, and in particular the ‘knee’, are also interpreted using a Warburg element to describe slow ion migration. At a semi-quantitative level, we can equate the reciprocal of the knee frequency,  $1/\omega^*$ , with the

diffusional time constant of the system,  $h_f^2/D$ , where  $h_f$  is the film thickness. For the composite films studied here, where  $h_f \approx 0.15 \mu\text{m}$ , the outcome is  $D \approx 10^{-9} \text{ cm}^2 \text{ s}^{-1}$ . This is at the upper end of values commonly reported for diffusional transport of ions in electroactive polymer films, so nanotube inclusion appears to have a beneficial effect on film mass transport.

**Table 7.7.** ‘Knee’ frequency estimated from Nyquist representations.

Material	CH <sub>3</sub> CN	CH <sub>2</sub> Cl <sub>2</sub>	
	E=0.2 V	E=0.2 V	E=1.3 V
Polymer	5.8 Hz	4.6 Hz	7.8 Hz
CT0	9.6 Hz	23 Hz	27 Hz
CT1	7.8 Hz	6.8 Hz	22 Hz
CT2	9.3 Hz	15 Hz	43 Hz
CT3	9.9 Hz	5.8 Hz	22 Hz

#### 7.2.4 Structural/morphologic characterisation of composites by scanning electron microscopy

In pursuit of a rational explanation for the diverse electronic and electrochemical properties of these systems, SEM images were acquired to establish differences in film structure and morphology. As the starting point (Figure 7.12), films of the single component poly[Ni(3-Mesalophen-b15-c5)] were prepared in CH<sub>3</sub>CN and analysed. They are clearly heterogeneous, with mesoscopically ‘uniform’ regions (annotated with *I*) of fine grains interspersed by distinctly rougher islands (annotated with *II* in panel a and magnified in panel b).

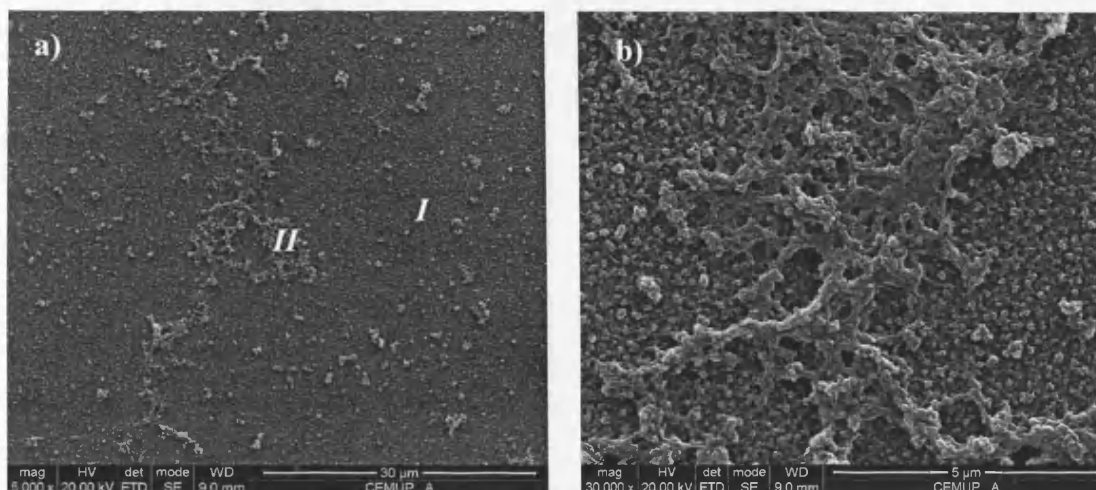


**Figure 7.12:** SEM images of poly[Ni(3-Mesalophen-b15-c5)] (pure polymer) prepared in CH<sub>3</sub>CN. **a)** The film shows distinctive uniform vs. heterogeneous regions (*I* and *II*, respectively); **b)** is a magnification of a heterogeneous region.

SEM images of composite MWCNT-T0, prepared and characterised in the two different solvents, are shown in [Figure 7.13](#). Even in these low-resolution images it is quite clear that the MWCNT-T0 morphology is different when produced using different solvents. The implication of the more complex and heterogeneous structures in CH<sub>2</sub>Cl<sub>2</sub> ([Figure 7.13b](#)) is the presence of a larger amount of entrapped MWCNTs than in MWCNT-T0 composite produced from CH<sub>3</sub>CN solution. Support for this is found in higher resolution images ([Figure 7.14](#)), where the presence of CNTs is revealed above the primary surface ([panel a](#)) and strongly indicated below the surface by large mounds of composite ([panel b](#)). Moreover, the CNTs ‘seen’ in these images are not bare MWCNTs (which are much smaller than the observed features), but polymer-wrapped MWCNTs. This is not surprising: if their interactions with the polymer component were so unfavourable that they were not coated, then they would be unlikely to be incorporated into a stable composite. In other words, formation of a composite has polymer-wrapping of the carbon nanotubes as a pre-requisite, so they will not be observed ‘bare’. This polymer ‘wrapping’ is a recognised phenomenon in CNT chemistry and its origins can be  $\pi$ - $\pi$  or hydrophobic type interactions.

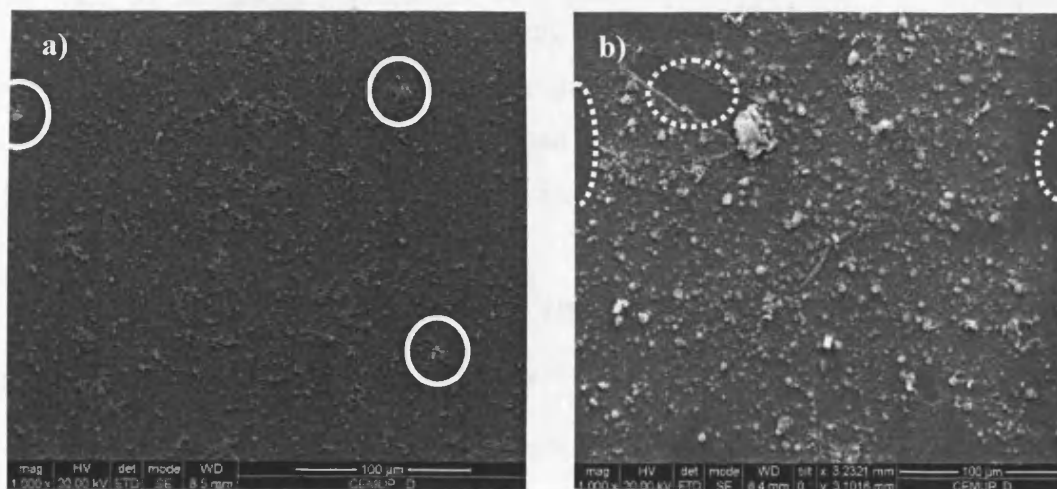


**Figure 7.13:** SEM images of MWCNT-T0 prepared in a)  $0.1 \text{ mol dm}^{-3}$  TBAP/ $\text{CH}_3\text{CN}$  and b)  $0.1 \text{ mol dm}^{-3}$  TBAP/ $\text{CH}_2\text{Cl}_2$ . Solid circles correspond to regions of superficial MWCNT; dashed circles correspond to regions of lower amounts of MWCNT in the surface.

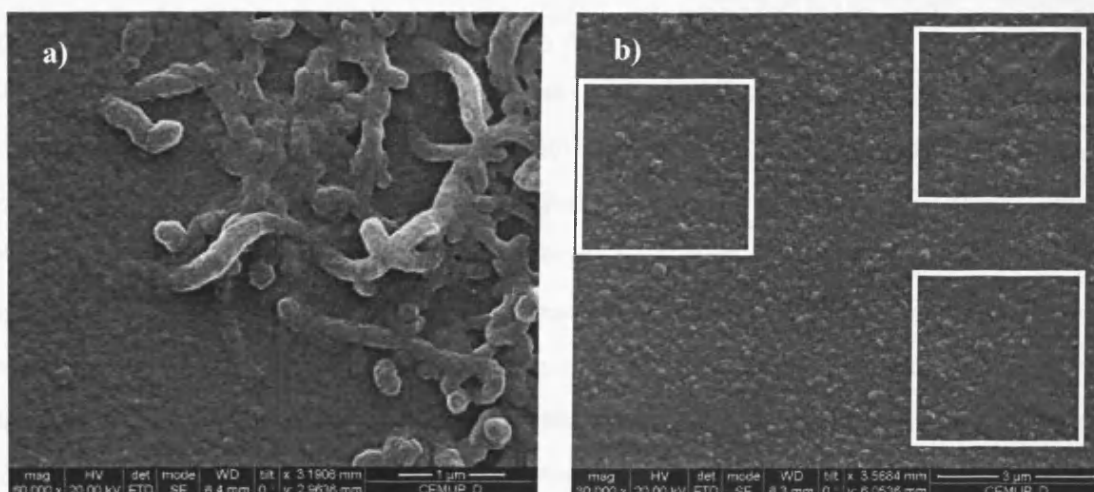


**Figure 7.14:** SEM images of MWCNT-T0 prepared in  $0.1 \text{ mol dm}^{-3}$  TBAP/ $\text{CH}_2\text{Cl}_2$ . a) Carbon nanotubes individually covered are inserted in the polymeric matrix; b) solid squares highlight regions where the presence of nanotubes can be inferred beneath a uniform layer of polymer.

Figure 7.15 shows all the other composites studied, at the same magnification as in Figure 7.14a. The nanotubes seem to be covered with a thinner coating of polymer than in CT0- $\text{CH}_2\text{Cl}_2$ . This effect is more pronounced in composites prepared in  $\text{CH}_3\text{CN}$  (panels a, b, c, d) than in  $\text{CH}_2\text{Cl}_2$  (panels e, f, g). Additionally, in  $\text{CH}_3\text{CN}$  the regions of surface where the carbon nanotubes are found are noticeably more heterogenous, with large islands of carbon nanotubes being trapped within islands of rough polymer (Figure 7.15 panels c, d).

The extent to which the types of structure highlighted in [Figure 7.15a](#) were seen was, amongst the composites prepared, by far the greatest for MWCNT-T0 in CH<sub>2</sub>Cl<sub>2</sub>. Thus, this material appears to have quite different composition (higher MWCNT content), morphology and electronic/electrochemical properties.

### 7.3 CORRELATION OF COMPOSITE ELECTROCHEMICAL PROPERTIES AND MORPHOLOGY

As a prelude to understanding the role of the carbon nanotubes in modulating composite structure and properties, it is worthwhile considering the driving force(s) for their incorporation in the polymer matrix, which is the control sample. The key factors are the solubility of the monomer in the deposition solution and the interactions of the carbon nanotubes with active entities in the solution environment, *i.e.* electrolyte ions and monomer species. The majority of reports of electroactive polymer / carbon nanotube composites involve polypyrrole as the polymer component, which offers the option of high monomer concentration (typically 0.5 mol dm<sup>-3</sup>)<sup>16,19,20,28</sup>. Here, the solubility of monomeric [Ni(3-Mesalophen-b15-c5)] is limited to 0.25x10<sup>-3</sup> mol dm<sup>-3</sup>, *i.e.* a factor of 2000 lower than in previous studies involving polypyrrole composites. As a further constraint, the low quantity of dispersed carbon nanotubes in the deposition solution means that their contribution to the ionic strength is small, so there is still a requirement for additional inert electrolyte<sup>28</sup>. This is significant because, if no additional electrolyte were present, the negatively charged carbon nanotubes would be the only available dopant and electroneutrality would be a strong driving force for their incorporation in the depositing polymer. Despite these challenges, it is clear from the various SEM images that the carbon nanotube incorporation strategy illustrated by [Figure 7.1](#) is successful. In addition, the apparent problems associated with added electrolyte may be alleviated by the fact that both CH<sub>3</sub>CN and CH<sub>2</sub>Cl<sub>2</sub> are aprotic solvents, so the conjugate base groups - present naturally or introduced by the pre-treatments - are not protonated, but remain as negatively charged oxygen-containing functionalities that are electrostatically attracted to the cationic polymer chains.



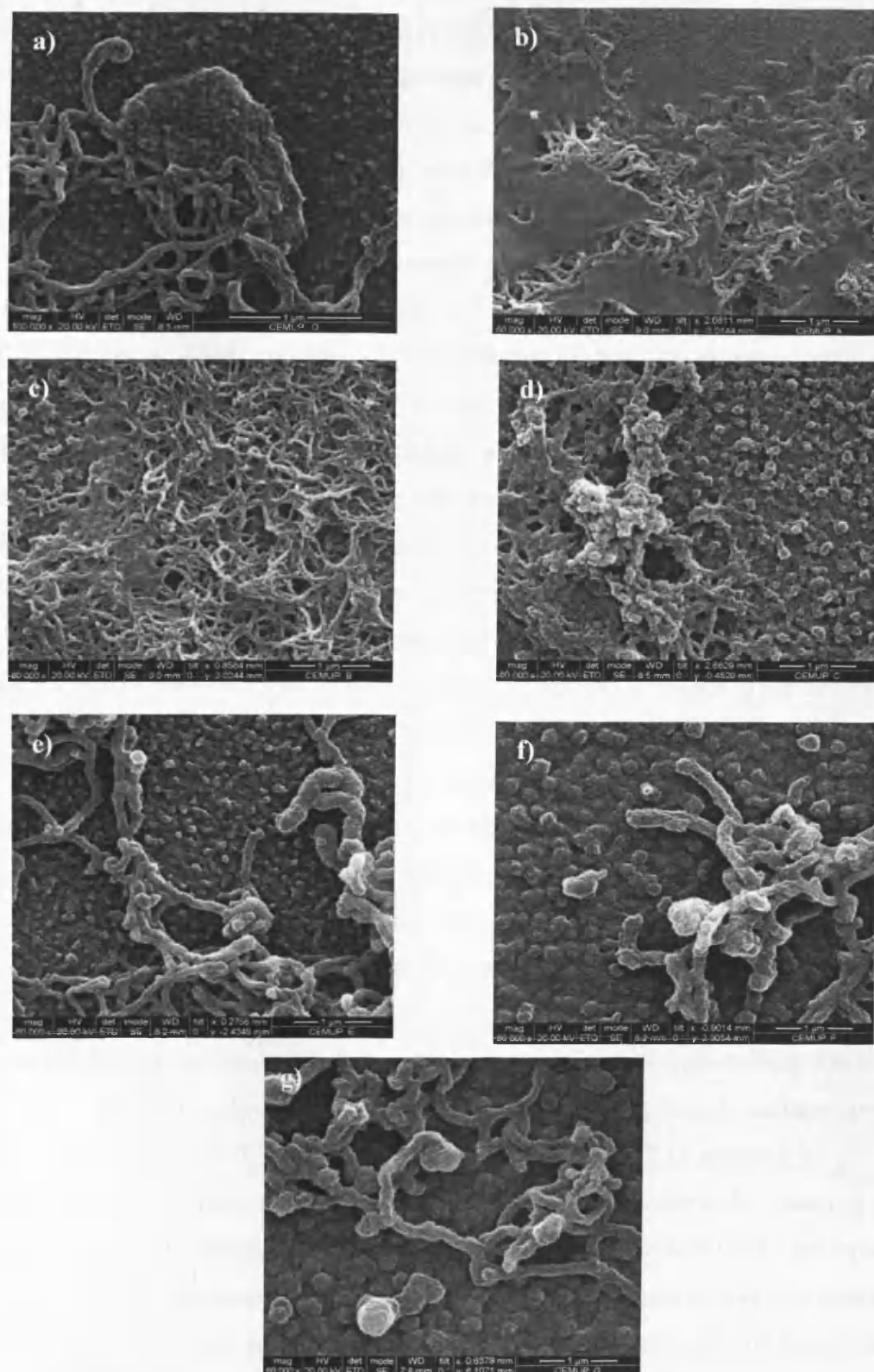


**Figure 7.15:** SEM images of the composites a) MWCNT-T0, b) MWCNT-T1, c) MWCNT-T2 and d) MWCNT-T3 prepared in  $0.1 \text{ mol dm}^{-3}$  TBAP/ $\text{CH}_3\text{CN}$  and e) MWCNT-T1, f) MWCNT-T2, g) MWCNT-T3 prepared in  $0.1 \text{ mol dm}^{-3}$  TBAP/ $\text{CH}_2\text{Cl}_2$ .



Although quantitative determination of carbon nanotube volume fraction in the composites is not possible, an estimate for the upper limit is given. The SEM images show fibrillar structures whose diameter is a factor of two (or more) greater than the diameters of the MWCNTs. If all the composite film were composed of such structures, then the MWCNTs themselves would constitute no more than 25% v/v. Nonetheless, inspection of the images shows that the composites consist of fibrils (polymer-coated MWCNTs) embedded in a polymeric matrix, so the MWCNTs constitute significantly less than 25% v/v of the composite. The outcome of this estimate is that the effect on composite electrical properties exerted by the MWCNTs is disproportionate to their population.

The value of  $C_{DL}$ , which is intimately associated with the structure of the composite/solution interface, increases with the amount of MWCNTs as observed directly on the surface by SEM. This is particularly evident in the case of MWCNT-CT0 in  $\text{CH}_2\text{Cl}_2$  (Figure 7.13b). In spite of SEM being primarily a surface imaging technique, it is possible to infer indirectly the presence beneath the surface of nanotubes via protrusions seen at the surface of the film. This is seen in Figure 7.14b and is related to the decrease in  $R_{CT}$  and increase in  $C_{redox}$  in the presence of MWCNTs within the bulk composite.

In spite of some general trends found for most of the composites, it is interesting to notice some specificity in terms of interactions between the polymeric material and carbon nanotubes. While all the composites in  $\text{CH}_2\text{Cl}_2$  show the nanotubes as individually covered by polymer, keeping their cylindrical shape composites, in  $\text{CH}_3\text{CN}$  there seem to be different types of coverage depending on the nature of surface groups on the walls of the carbon nanotubes: MWCNTs with carboxylic acids and anhydride groups (MWCNT-T1) tend to be covered by a sheet-like layer of uniform and smoother electroactive material (Figure 7.15 panel b), whereas MWCNTs with carbonyl/hydroxyl surface groups (MWCNT-T2 and MWCNT-T3) are covered individually (Figure 7.13 panels c, d).

Small variations in the way the nanotubes are covered by electroactive material may also explain some of the differences found in  $C_{redox}$ . The way the MWCNTs are covered by the polymeric film influences the capacitance of the latter in terms of more accessibility to electrolyte<sup>19</sup>. This is the result of the diverse interactions between different surface groups, electrolyte and polymeric species.

From a purely operational perspective, the most promising formulation is CT0 /  $\text{CH}_2\text{Cl}_2$ . The voltammetric response shows polymer redox chemistry ('doping') at the least

positive potentials as a consequence of the significant decrease in  $R_{CT}$ ; the nanotubes introduce a conductivity path at potentials where the polymer doping level is low. The morphological changes caused by the nanotubes result in an increase in interfacial capacitive charge storage capability.

## CONCLUDING REMARKS

By dispersion of MWCNTs in the deposition solution, it is possible to incorporate them within electropolymerised poly[Ni(3-Mesalophen-b15-c5)] films, to generate MWCNT / poly[Ni(3-Mesalophen-b15-c5)] nanocomposites on Pt or ITO electrode surfaces. Variants of this basic procedure were explored, in which the polymer / nanotube interaction was manipulated by oxygen functionalisation of the nanotubes and the use of different solvent media.

Electrochemical impedance spectra for pure polymer and composites were fitted to a modified Randles electrical equivalent circuit. The charge transfer resistance was decreased by the presence of the MWCNTs – an enhancement of polymer properties within the composite. At relatively low frequencies, the charge transport properties were manifested by a Warburg type element. At the lowest frequencies the response was dominated by the ability of the polymer redox sites to store charge (redox capacitance), which is enhanced by the presence of the MWCNTs. When normalised by the polymer coverage, the redox capacitance  $C_{redox}/\Gamma$  is on the order of  $40 \text{ kF mol}^{-1}$ , consistent with the estimate of capacitance determined from the voltammetric response. The interesting feature is that these two values are acquired on somewhat different timescales, so the implication is that all the redox functionality of the polymer is accessible; again, this is an indication of performance enhancement as a consequence of the presence of MWCNTs.

SEM images of the composites reveal a wide range of morphologies, dependent on the deposition medium and MWCNT pre-treatment. Features seen within the SEM images include relatively smooth polymer, fibrillar structures and heterogeneous regions of variable porosity. The fibrillar structures are consistent with polymer-wrapped MWCNTs; either on or just beneath the surface. Generically, correlation of impedance parameters with SEM images provides a morphological rationale for composite electrical properties.

## REFERENCES:

1. *Handbook of Conducting Polymers*, 2nd ed.; Skotheim, T. A., Elsenbaumer, R. L., Reynolds, J. R, Eds.; Marcel Dekker: New York, 1998.
2. Zarras, P.; Anderson, N.; Webber, C.; Irvin, D. J.; Irvin, J. A.; Guenther, A.; Stenger-Smith, J. D. *Rad. Phys. Chem.* **2003**, *68*, 387.
3. Bredas, J.-L.; Beljonne, D.; Coropceanu, V.; Cornil, J. *Chem. Rev.* **2004**, *104*, 4971.
4. Mortimer, R. J.; Dyer, A. L.; Reynolds, J. R. *Displays* **2006**, *27*, 2.
5. Van Dyke, L. S.; Martin, C. R. *Langmuir* **1990**, *6*, 1118.
6. Bartlett, P. N.; Birkin, P. R.; Ghanem, M. A. *Chem. Commun.* **2000**, 1671.
7. Bartlett, P. N.; Birkin, P. R.; Ghanem, M. A.; Toh, C.-S. *J. Mater. Chem.* **2001**, *11*, 849.
8. Goncharov, A.; Zhukov, A. A.; Bartlett, P. N.; Ghanem, M. A.; Boardman, R.; Fanghor, H.; Groot, P. J. A. *J. Magnet. Magnet. Mater.* **2005**, *286*, 1.
9. Iijima, S. *Nature* **1991**, *354*, 56.
10. *Carbon Nanotubes, Science and Applications*; Han, J., Meyyappan, M., Eds.; CRC Press: New York, 2005.
11. Gong, K.; Dong, Y.; Xiong, S.; Chen, Y.; Mao, L. *Biosens. Bioelec.* **2004**, *20*, 253.
12. Li, J.; Liu, Q.; Liu, Y.; Lui, S.; Yao, S. *Anal. Biochem.* **2005**, *346*, 107.
13. Jia, N.; Liu, L.; Wang, L.; Yan, M.; Jiang, Z. *Electrochim. Acta* **2005**, *51*, 611.
14. Profumo, A.; Fagnoni, M.; Merli, D.; Quartarone, E.; Protti, S.; Dondi, D.; Albin, A. *Anal. Chem.* **2006**, *78*, 4194.
15. Zhang, H.; Cao, G.; Yang, Y. *J. Power Sources* **2007**, *172*, 476.
16. Chen, G. Z.; Schaffer, M. S. P.; Coleby, D.; Dixon, G.; Zhou, W.; Fray, D. J.; Windle, A. H. *Adv. Mater.* **2000**, *12*, 522.
17. Hughes, M.; Chen, G. Z.; Shaffer, M. S. P.; Fray, D. J.; Windle, A. H. *Chem. Mater.* **2002**, *14*, 1610.
18. Huang, J.-E.; Li, X.-H.; Xu, J.-C.; Li, H.-L. *Carbon* **2003**, *41*, 2731.
19. Hughes, M.; Shaffer, M. S. P.; Renouf, A. C.; Singh, C.; Chen, G. Z.; Fray, D. J.; Windle, A. H. *Adv. Mater.* **2002**, *14*, 382.
20. Wang, J.; Dai, J.; Yarlagadda, T. *Langmuir* **2005**, *21*, 9.
21. Snook, G. A.; Chen, G. Z.; Fray, D. J.; Hughes, M.; Shaffer, M. *J. Electroanal. Chem.* **2004**, *568*, 135.

22. Wang, J.; Xu, Y.; Chen, X.; Sun, X. *Compos. Sci. Technol.* **2007**, *67*, 2981.
23. Deng, J.; Ding, X.; Zhang, W.; Peng, Y.; Wang, J.; Long, X.; Li, P.; Chan, A. S. C. *Eur. Polym. J.* **2002**, *38*, 2497.
24. Star, A.; Stoddart, J. F.; Steuerman, D.; Diehl, M.; Boukai, A.; Wong, E. W.; Yang, X.; Chung, S.-W.; Choi, H.; Heath, J. R. *Angew. Chem. Int. Ed.* **2001**, *40*, 1721.
25. Bahr, J. L.; Yang, J.; Kosynkin, D. V.; Bronikowski, M. J.; Smalley, R. E.; Tour, J. M. *J. Am. Chem. Soc.* **2001**, *123*, 6536.
26. Wang, Y.; Iqbal, Z.; Mitra, S. *J. Am. Chem. Soc.* **2006**, *128*, 95.
27. Bahr, J. L.; Tour, J. M. *J. Mater. Chem.* **2002**, *12*, 1952.
28. Hughes, M.; Chen, G. Z.; Shaffer, M. S. P.; Fray, D. J.; Windle, A. H. *Compos. Sci. Technol.* **2004**, *64*, 2325.
29. Tang, L.; Zhu, Y.; Yang, X.; Li, C. *Anal. Chim. Acta* **2007**, *597*, 145.
30. Li, Y.; Wang, P.; Wang, L.; Lin, X. *Biosens. Bioelec.* **2007**, *22*, 3120.
31. Tu, X.; Xie, Q.; Jiang, S.; Yao, S. *Biosens. Bioelec.* **2007**, *22*, 2819.
32. Tsai, Y.-C.; Li, S.-C.; Liao, S.-W. *Biosens. Bioelec.* **2006**, *22*, 495.
33. Qi, H.; Li, X.; Chen, P.; Zhang, C. *Talanta* **2007**, *72*, 1030.
34. Pedersen, C. J. *J. Am. Chem. Soc.* **1967**, *89*, 7017.
35. [http://www.ahwahneetech.com/technology/carbon\\_nanotube.htm](http://www.ahwahneetech.com/technology/carbon_nanotube.htm).
36. Tedim, J.; Goncalves, F.; Pereira, M. F. R.; Figueiredo, J. L.; Moura, C.; Freire, C.; Hillman, A. R. *Electrochim. Acta* **2008**, *53*, 6722.
37. Pereira, M. F. R.; Figueiredo, J. L.; Orfao, J. J. M.; Serp, P.; Kalck, P.; Kihn, Y. *Carbon* **2004**, *42*, 2807.
38. Figueiredo, J. L.; Pereira, M. F. R.; Freitas, M. M. A.; Orfao, J. J. M. *Carbon* **1999**, *37*, 1379.
39. Banerjee, S.; Hemraj-Benny, T.; Wong, S. S. *Adv. Mater.* **2005**, *17*, 17.
40. Ferloni, P.; Mastragostino, M.; Meneghello, L. *Electrochim. Acta*, **1996**, *41*, 27.
41. Randles, J. E. B. *Disc. Farad. Soc.* **1947**, *1*, 11.
42. Warburg, E. *Ann. Phys. Chem.* **1899**, *67*, 493.

## FINAL CONCLUSIONS AND FUTURE DIRECTIONS:

Poly[Ni(3-Mesalophen-b15-c5)] films were prepared by oxidative polymerisation of the [Ni(3-Mesalophen-b15-c5)] monomer. These films exhibit properties of conjugated rather than redox polymers: (i) a coulometric assay showed that the oxidation degree is not an integer and the electrochemical response is ligand-based, (ii) the UV-Vis band profile is consistent with the creation of charge carriers (polarons) upon doping, (iii) analysis of XANES in the Ni K-edge for a similar film, (poly[Ni(3-MeOsaltMe)]), showed that Ni has a formal +2 oxidation state that is kept upon variation of film oxidation state. Furthermore, EXAFS near the Ni K-edge showed that the local structure around Ni remains unchanged with the occurrence of polymerisation, independent of the substituents in R<sub>1</sub> and R<sub>2</sub> positions, which is consistent with the formation of the polymer by linkage of the monomeric units via phenyl rings.

The electrochemical properties of poly[Ni(3-Mesalophen-b15-c5)] films were found to change non-monotonically with increasing  $\Gamma$ ; this is associated with the occurrence of morphological changes. Microscopic techniques showed that thin films ( $\Gamma < 15 \text{ nmol cm}^{-2}$ ) comprise a uniform layer of polymer with small polymer islands on the top. Intermediate films ( $15 < \Gamma / \text{nmol cm}^{-2} < 60$ ) are rougher, and in this case the underlying uniform layer is decorated with larger islands of polymer. For thicker films ( $\Gamma > 100 \text{ nmol cm}^{-2}$ ) the islands become even larger. Acoustic wave measurements, supported by AFM images, showed that the uniform layer is denser whilst the outer and heterogeneous layer is more liquid-like.

The addition of alkali and alkaline earth metal cations to the background electrolyte solution ( $\text{Cs}^+$ ,  $\text{Mg}^{2+}$  and  $\text{Ba}^{2+}$ ) resulted in a change in the film electrochemical response, as well as its spectroscopic properties. These findings are attributed to ion uptake, as proved by (i) XPS, (ii) XAS near the Ba K-edge and (iii) EQCM studies. Additionally, XAS studies showed that, for polymers bearing small and relatively ‘rigid’ receptors (poly[Ni(3-MeOsaltMe)]),  $\text{Ba}^{2+}$  is located *within* the receptor. For films bearing large and flexible crown ether macrocycles  $\text{Ba}^{2+}$  is coordinated to a very low number of donor atoms, which is unexpected considering solution complexation concepts. This low coordination number allows multiple binding to the same or different crowns at the expense of less selectivity, and is expected to affect the polymer mechanical properties. Consequently, poly[Ni(3-

Mesalophen-b15-c5)] films were studied by crystal impedance and the results showed an increase of the loss modulus,  $G''$ , with  $\text{Ba}^{2+}$  uptake, suggesting a rise in the polymer viscosity.

The simple methodology used here for the incorporation of multi-walled carbon nanotubes in the polymeric matrix was proved to be successful. The resulting nanocomposites were found to have differentiated electrical properties with respect to the polymer itself, namely smaller charge transfer resistance and higher redox capacitance  $C_{\text{redox}}/\Gamma$ .

There are two aspects that must be highlighted in this work: the molecular design and the system heterogeneity. Firstly, the concept of molecular design must be considered carefully when one tries to impart or predict the properties of supramolecular systems. Secondly, the heterogeneity is quite often neglected and films are regarded as uniform layers of material, which is not always the case.

Finally, the use of such a wide range of techniques provided different perspectives on the same problem and enabled the elaboration of consistent models, correlating the properties of the poly[Ni(*salen*)] films with their structure, composition and morphology.